Quantum Chemical Approaches to Nonadiabatic Dynamics in Complicated Systems: Nonradiative Relaxation of Excited Molecules and Carrier Behaviors in Halide Perovskites

複雑な系における非断熱動力学への量子化学的アプローチ: 励起分子の無輻射緩和及びハライドペロブスカイト中のキャリア挙動

February 2021

Hiroki URATANI
浦谷 浩輝

Quantum Chemical Approaches to Nonadiabatic Dynamics in Complicated Systems: Nonradiative Relaxation of Excited Molecules and Carrier Behaviors in Halide Perovskites

複雑な系における非断熱動力学への量子化学的アプローチ: 励起分子の無輻射緩和及びハライドペロブスカイト中のキャリア挙動

February 2021

Waseda University
Graduate School of Advanced Science and Engineering
Department of Chemistry and Biochemistry
Research on Electronic State Theory

Hiroki URATANI
浦谷 浩輝

Table of Contents

List of Abbreviations

ADC(2)	algebraic diagrammatic construction scheme to second order
AIE	aggregation-induced emission
AO	atomic orbital
BHHLYP	Becke's half-and-half exchange + Lee–Yang–Parr
CBM	conduction band minimum
CI	configuration interaction
CIS	configuration interaction with singles
CO	canonical orbital
CPA	classical path approximation
CPU	central processing unit
CSF	configuration state function
CX	conical intersection
DC	divide and conquer
DFT	density-functional theory
DFTB	density-functional tight binding
DOF	degree of freedom
DOS	density of states
EC	excitation center
EOM	equation of motion
FC	Franck–Condon

FSSH	fewest-switches surface hopping
FQY	fluorescence quantum yield
GGA	generalized gradient approximation
HOMO	highest occupied molecular orbital
LD	local diabatization
LHP	lead halide perovskite
LR	linear response
LUMO	lowest unoccupied molecular orbital
MaxAD	maximum absolute deviation
MD	molecular dynamics
MECX	minimum-energy conical intersection
MO	molecular orbital
NA-MD	nonadiabatic molecular dynamics
NAC	nonadiabatic coupling
NTO	natural transition orbital
OD	orbital derivative
OLED	organic light-emitting diode
PBE	Perdew–Burke–Ernzerhof
PES	potential energy surface
PSC	perovskite solar cell
QM	quantum mechanical
RHS	right-hand side
RIR	restriction of intramolecular rotation
RMSD	root-mean-square deviation
SCC	self-consistent charge
SF	spin flip
SO	singular orbital

SOC	spin–orbit coupling
SOMO	singly occupied molecular orbital
SVD	singular value decomposition
TD	time dependent
TDA	Tamm–Dancoff approximation
TDNAC	time-derivative nonadiabatic coupling
TPE	tetraphenylethylene
VBM	valence band maximum
VDOS	vibrational density of states
WO	wavefunction overlap

Frequently Used Mathematical Notations

The following indices are used throughout the thesis unless otherwise noted.

$\kappa, \lambda, \mu, \nu$	AOs
i, j, k	occupied MOs
a, b, c	virtual MOs
p, q, r	general MOs
A, B, C, D	atoms
I, J, K, L, M	valence shells
ζ, η, θ, ξ	adiabatic states
s	subsystems in the DC framework
σ, τ	spins

A matrix or a vector is denoted in a bold Roman character (e.g., $\mathbf{A}$), and its elements are indicated in non-bold italics (e.g., A_{pq}). In the spin-dependent context, an upper line is added to an MO index to indicate a β-spin MOs (e.g., $\bar{p}$), and an MO index with a hat (e.g., $\hat{p}$) is used when the spin is not specified, and an MO index with neither an upper line nor a hat (e.g., p) indicates an α-spin MO. In addition, wavefunctions are denoted according to the following rule.

ϕ	one-electron wavefunction
Φ	Slater determinant
ψ	adiabatic-state many-electron wavefunction

Chapter 1

General Introduction

When the Born–Oppenheimer approximation is valid, chemical dynamics can be understood as atomic motions on a single adiabatic PES, which associates the atomic coordinates with potential energy of an adiabatic state. On the contrary, dynamics that involve multiple PESs, i.e., nonadiabatic dynamics, often play a critical role, especially in excited-state phenomena. Because nonadiabatic dynamics are, in general, ultrafast and yet microscopic phenomena, quantum chemistry-based computational simulations are essential tools for studying them, as well as the state-of-the-art spectroscopic techniques. NA-MD, which simulates nonadiabatic dynamics within an MD-like framework by decomposing the electronic and nuclear DOFs into quantum- and classical-mechanical problems, is the most widely used class of computational techniques for nonadiabatic dynamics.

However, while the computational cost of NA-MD is lower than that of other typical nonadiabatic dynamics simulation techniques, e.g., multiconfigurational TD Hartree method, NA-MD is still significantly expensive, limiting its application to relatively simple systems. There are three major contributors to the high computational cost of NA-MD. First, to describe multiple PESs, NA-MD requires excited-state calculations, which consume substantially larger computational time than ground-state calculations. Second, nonadiabaticity is incorporated via NACs among the adiabatic states, whose calculations require additional computational efforts. Third, statistically meaningful results cannot be obtained without simulating a sufficiently large

number of trajectories to approximate the exact nuclear dynamics. For these reasons, conventional quantum chemical approaches have difficulties to study nonadiabatic dynamics in high-complexity systems.

This thesis presents development of computationally efficient NA-MD techniques capable of simulating nonadiabatic dynamics in complicated systems based on the DFTB framework, which is a low-cost semiempirical formulation of DFT. In addition, the methods are applied to tackle several important problems in real systems where such dynamics play a key role. Specifically, the thesis focuses on two cases that are crucial from both fundamental and practical viewpoints: nonradiative relaxation processes of excited molecules and photoexcited-state dynamics of solar cell materials.

The remainder of this thesis is organized as follows.

Chapter 2 reviews the theoretical background of this thesis, i.e., outline of NA-MD methods, and details of DFTB approaches to ground- and excited-state calculations.

Chapter 3 describes novel computational methods for nonadiabatic dynamics in complicated systems. Section 3.1 presents the implementation of the NA-MD method employed throughout this thesis, i.e., FSSH, combined with an excited-state calculation framework based on DFTB, i.e., TD-DFTB. The routine was incorporated into the developmental version of DCDFTBMD code, and the techniques described in Sections 3.2–3.4 were built on this implementation platform. Section 3.2 extends the TD-DFTB/FSSH technique to enable simulations in large systems within a reasonable computational cost by employing a spatial-fragmentation-based linear-scaling framework called the DC technique. Numerical tests show that the developed DC-TD-DFTB/FSSH technique can simulate nonadiabatic dynamics in systems with thousands of atoms, such as in the case of solutions, without a significant increase in computational cost compared with the conventional TD-DFTB/FSSH method. Section 3.3 describes the improvement of the TD-DFTB/FSSH to a different direction; to treat nonadiabatic dynamics involving S_1/S_0 CXs, which are crucial for nonradiative relaxation processes and cannot be correctly described by the conventional TD-DFTB technique, the SF approach is introduced. The developed

method, i.e., SF-TD-DFTB/FSSH, was tested on photoisomerization reactions, and its accuracy was comparable with that of expensive ab initio approaches. Section 3.4, the final section of Chapter 3, combines the approaches developed in Sections 3.2 (DC-TD-DFTB/FSSH) and 3.3 (SF-TD-DFTB/FSSH) to enable nonradiative relaxation dynamics simulations in condensed phases.

Chapters 4 and 5 discuss the first target of the practical application, i.e., nonradiative relaxation of excited molecules. In Chapter 4, as a case study, the SF-TD-DFTB/FSSH technique is applied to investigate the effects of molecular structure on nonradiative relaxation dynamics in tetraphenylethylene and its derivative. The simulations reproduced experimentally observed molecular-structure dependence of excited-state lifetimes. Moreover, the mechanism of the structure dependence was elucidated via combined analyses of NA-MD trajectories, MECX structures, and adiabatic PESs.

Then, Chapter 5 focuses on the effect of the environment on nonradiative relaxation. Using the DC-SF-TD-DFTB/FSSH technique, NA-MD simulations are conducted for the nonradiative relaxation of *trans*-azobenzene in solutions. The trend of excited-state lifetimes vs. the solvents was consistent with experimental results. In addition, the mechanism of solvent dependence is discussed focusing on the solvent viscosity.

Chapters 6 and 7 focus on the second target, i.e., exciton and charge carrier dynamics of solar cell materials. Chapter 6 presents TD-DFTB/FSSH simulations of the photoexcited-state dynamics of LHPs, which are of key importance as materials for a class of solar cells, namely, the perovskite solar cells. The results show that the electronic and nuclear dynamics are strongly coupled with each other in the conversion processes from the photogenerated exciton to band-edge charge carriers, i.e., exciton dissociation, hot carrier cooling, and polaron formation.

Chapter 7 focuses on band-edge carriers, which are generated after the series of nonadiabatic processes discussed in Chapter 6. Previous studies suggest that, at this stage, the polarons, i.e., the carriers, are associated with nanometer-scale structural deformation. In addition, because the most typical LHP, $MAPbI_3$, includes methylammonium cations (MA^+s) as structural

components, the effect of the dipolar orientation of MA^+s on polaron formation has been a long-standing question. Using the DC-based DFTB technique, quantum mechanical MD simulations were conducted for the polarons in $MAPbI_3$ to elucidate the characteristics of the structural deformation. Moreover, based on the energy contribution, the role of the MA^+ rotation is discussed.

Chapter 8 concludes the thesis by summarizing the contribution of this work to the field of nonadiabatic dynamics studies and future perspectives.

Chapter 2

Theoretical Backgrounds

2.1 NA-MD Framework

In the nonrelativistic limit, the total many-body wavefunction Ψ of a system composed of electrons and nuclei is governed by the TD Schrödinger equation:

$$i\hbar\frac{\partial\Psi\left(\mathbf{r},\mathbf{R},t\right)}{\partial t}=\hat{H}\left(\mathbf{r},\mathbf{R}\right)\Psi\left(\mathbf{r},\mathbf{R},t\right), \tag{2.1.1}$$

where $\mathbf{r}$ and $\mathbf{R}$ denote the coordinates of all electrons and nuclei, respectively. The spin DOFs are omitted for simplicity. The Hamiltonian $\hat{H}$ is described as

$$\hat{H}\left(\mathbf{r},\mathbf{R}\right)=\hat{T}_{\mathrm{n}}+\hat{H}_{\mathrm{e}}\left(\mathbf{r},\mathbf{R}\right), \tag{2.1.2}$$

where

$$\hat{T}_{\mathrm{n}}=-\sum_{A}\frac{1}{2m_{A}}\nabla_{\mathbf{R}_{A}}^{2} \tag{2.1.3}$$

$$\hat{H}_{\mathrm{e}}\left(\mathbf{r},\mathbf{R}\right)=-\frac{1}{2m}\nabla_{\mathbf{r}}^{2}+V\left(\mathbf{r},\mathbf{R}\right) \tag{2.1.4}$$

Here, m and m_A denote the masses of electrons and the nucleus of the atom A, respectively. The potential V includes electron–electron, nuclei–electron, and nuclei–nuclei interaction parts.

NA-MD is a general term for methods based on the mixed quantum–classical concept, where the faster, i.e., electronic, and slower, i.e., nuclear, DOFs are treated separately with quantum and classical EOMs, respectively. As such a decomposition is not unique, a variety of NA-MD techniques have been developed.[1–7] Among them, this section focuses on the trajectory surface hopping approach, which is the most typical class of methods and is extensively used throughout this thesis. Prior to the description of trajectory surface hopping, the mean-field approach, which is also important as a practical method and as a background to the trajectory surface hopping, is summarized.

2.1.1 Mean-Field Approach

The mean-field-type NA-MD method, a.k.a. Ehrenfest dynamics, assumes that electrons and nuclei move in the mean fields created by each other. In this ansatz, the total wavefunction Ψ can be factorized as

$$\Psi(\mathbf{r}, \mathbf{R}, t) = \chi(\mathbf{R}, t)\, \Xi(\mathbf{r}, t), \tag{2.1.5}$$

where χ and Ξ denote nuclear and electronic wavefunctions, respectively. As several routes of further derivation have been proposed,[7–9] here, only their essence are summarized. By taking the classical limit for the nuclear wavefunction and its governing EOM, one obtains the classical, Newton-like EOM for the nuclei:

$$\frac{d^2\mathbf{R}_A^{\mathrm{c}}}{dt^2} = -\frac{1}{m_A}\nabla_{\mathbf{R}^{\mathrm{c}}} \left\langle \Xi(\mathbf{r}, t; \mathbf{R}^{\mathrm{c}}) \middle| \hat{H}_{\mathrm{e}}(\mathbf{r}; \mathbf{R}^{\mathrm{c}}) \middle| \Xi(\mathbf{r}, t; \mathbf{R}^{\mathrm{c}}) \right\rangle_{\mathbf{r}}. \tag{2.1.6}$$

Note that $\mathbf{R}$ was replaced with $\mathbf{R}^{\mathrm{c}}$, because it is no longer the *nuclear coordinate as quantum DOFs* but it is the *position of classical nuclei*. For the same reason, Ξ, which was independent

of $\mathbf{R}$, now depends on $\mathbf{R}^{\mathrm{c}}$ in a parametric manner. The EOM for the electronic part is derived from the TD Schrödinger equation for the electronic wavefunction:

$$i\hbar\frac{\partial\Xi\left(\mathbf{r},t;\mathbf{R}^{\mathrm{c}}\left(t\right)\right)}{\partial t}=\hat{H}_{\mathrm{e}}\left(\mathbf{r};\mathbf{R}^{\mathrm{c}}\left(t\right)\right)\Xi\left(\mathbf{r},t;\mathbf{R}^{\mathrm{c}}\left(t\right)\right). \tag{2.1.7}$$

Using an orthonormal many-electron basis set, which is here chosen to be adiabatic states, Ξ can be expanded as follows:

$$\Xi\left(\mathbf{r},t;\mathbf{R}^{\mathrm{c}}\left(t\right)\right)=\sum_{\eta}c_{\eta}\left(t\right)\psi_{\eta}\left(\mathbf{r};\mathbf{R}^{\mathrm{c}}\left(t\right)\right). \tag{2.1.8}$$

Using Eqs. 2.1.7 and 2.1.8, one obtains the EOM for the electronic part, i.e., for the expansion coefficients:

$$i\hbar\frac{\partial c_{\eta}\left(t\right)}{\partial t}=E_{\eta}\left(t\right)c_{\eta}\left(t\right)-i\hbar\sum_{\theta}\sigma_{\eta\theta}\left(t\right)c_{\theta}\left(t\right). \tag{2.1.9}$$

Here, $\sigma_{\eta\theta}$ is called TDNAC and is described as

$$\sigma_{\eta\theta}\left(t\right)=\left\langle \psi_{\eta}\left(\mathbf{r};\mathbf{R}^{\mathrm{c}}\left(t\right)\right)\middle|\frac{d\psi_{\theta}\left(\mathbf{r};\mathbf{R}^{\mathrm{c}}\left(t\right)\right)}{dt}\right\rangle_{\mathbf{r}}. \tag{2.1.10}$$

Note that TDNAC has another common expression:

$$\sigma_{\eta\theta}\left(t\right)=\mathbf{d}_{\eta\theta}\left(t\right)\cdot\frac{d\mathbf{R}^{\mathrm{c}}\left(t\right)}{dt}, \tag{2.1.11}$$

using the NAC vector $\mathbf{d}_{\eta\theta}$:

$$\mathbf{d}_{\eta\theta}\left(t\right)=\left\langle \psi_{\eta}\left(\mathbf{r};\mathbf{R}^{\mathrm{c}}\left(t\right)\right)\middle|\nabla_{\mathbf{R}^{\mathrm{c}}}\psi_{\theta}\left(\mathbf{r};\mathbf{R}^{\mathrm{c}}\left(t\right)\right)\right\rangle_{\mathbf{r}}. \tag{2.1.12}$$

2.1.2 Trajectory Surface Hopping Approach

In the field of molecular science, branching of nuclear wave packets is often crucial, for example, to discuss the yields of multiple products of a photochemical reaction. However, as the mean-field approach assumes a completely localized (delta-function) nuclear wave packet, branching is not allowed. Among several mixed quantum–classical methods that overcome this limitation, which include the multiple spawning technique by Multínez and co-workers,[10] the trajectory surface hopping method is the most popular one owing to its conceptual simplicity, relatively straightforward implementation, and suitable compromise between computational burden and accuracy.

Unlike in the mean-field scheme, in the trajectory surface hopping method,[11] the classical nuclear coordinates are propagated on a specific PES, where hopping to another surface is allowed to take nonadiabaticity into account. Conceptually, the probability distribution of the exact nuclear wave packet is approximated by the ensemble of trajectories, where branching is naturally allowed. For the quantum part, the EOM of the same form as the mean-field approach (Eq. 2.1.9) is typically used.

Tully pointed out that the trajectory surface hopping EOMs can be obtained through essentially the same route as the mean-field approach (Subsection 2.1.1) by starting from a multistate ansatz:

$$\Psi(\mathbf{r}, \mathbf{R}, t) = \sum_{\eta} \chi_{\eta}(\mathbf{R}, t)\, \psi_{\eta}(\mathbf{r}, \mathbf{R}), \tag{2.1.13}$$

instead of the mean-field ansatz (Eq. 2.1.5).[9]

The most widely used trajectory surface hopping algorithm may be the fewest-switches approach,[12] where the hopping probability is calculated such that the number of hopping events is minimized, i.e., according to the following concept:

$$p_{\zeta \to \theta} = \frac{\text{population transmission from state } \zeta \text{ to state } \theta}{\text{population of of state } \zeta}, \tag{2.1.14}$$

where ζ is the index of the currently active state. This leads to the following expression of the probability.

$$p_{\zeta\to\theta} = \max\left[0, \frac{2\delta t}{\left|c_\zeta\right|^2}\sigma_{\zeta\theta}\Re\left(c_\zeta^* c_\theta\right)\right] \tag{2.1.15}$$

2.2 DFTB-Based Approaches to Ground-State Calculations

2.2.1 DFTB[†]

DFTB is a well-established semiempirical quantum chemical calculation scheme, which has been adopted for a wide range of systems, as briefly reviewed elsewhere.[14] The theoretical framework is grounded on the Taylor expansion of Kohn–Sham equations with respect to charge density fluctuation $\delta\rho$ around reference density ρ_0, which is a superposition of the unperturbed atomic charge density. There are three major types of DFTB: DFTB1,[15,16] DFTB2,[17] and DFTB3.[18] In the studies described in this thesis, DFTB2 was employed. In the framework of DFTB2, the total energy E is expressed as[17,19]

$$\begin{aligned} E = &\sum_i^{N_{\mathrm{MO}}} n_i \left\langle \phi_i \middle| \hat{H}_0 \middle| \phi_i \right\rangle + \frac{1}{2}\sum_{I,J}^{N_{\mathrm{shell}}} \Delta q_I \Delta q_J \gamma_{IJ} \\ &+ \frac{1}{2}\sum_A^N \sum_{L,L'\in A} p_{AL} p_{AL'} W_{ALL'} + E_{\mathrm{rep}}, \end{aligned} \tag{2.2.1}$$

where the first, second, third, and fourth terms correspond to the one-electron component; charge density fluctuation contribution, including long-range Coulomb interaction; contribution from spin polarization; and inter-nuclear repulsion plus some ad hoc collection to the total energy, respectively. n_i and ϕ_i are the occupation number and single-particle wavefunction for the i-th MO, respectively. N_{MO} and N_{shell} are the number of MOs and electron shells included in the calculation, respectively. Δq_I is the fluctuation in the Mulliken charge of shell I referenced to that of the neutral isolated atoms. γ_{IJ} is a function of interatomic distance R and the Hubbard

[†]Reproduced from Ref. [13] with permission from the Phys. Chem. Chem. Phys. Owner Societies.

parameters for shells I and J (U_I and U_J, respectively). The Hubbard parameters are given as derivatives of orbital energies with respect to their occupation numbers in free atoms. In the limit of $R \to \infty$, γ_{IJ} approaches $1/R$, i.e., bare Coulomb interaction. When $R = 0$, i.e., shells I and J belong to the same atom, γ_{IJ} is represented with U_I (and U_J), and the second term in Eq. 2.2.1 represents the atomic energy variation originating from the partial electron attachment on (detachment from) the atom, which is related to the chemical hardness. The explicit form of γ_{IJ} is found elsewhere.[17] p_{AL} denotes the spin population of shell L in atom A, which is the difference between the Mulliken populations for up and down spins. The parameter that represents the energetical contribution of spin polarization, $W_{ALL'}$, is computed from the derivative of orbital energies of a free atom with respect to the occupation numbers for up and down spins. E_{rep} is a repulsive potential, which is described as a function of interatomic distance and conceptually includes nuclear repulsion and the other corrections for electronic energy.

ϕ_i is expanded by a set of pseudo-AOs, φ_μ, which is obtained by solving a Kohn–Sham-like equation for an isolated atom:

$$\left[\hat{T} + V_{\mathrm{eff}}[\rho_A] + V_{\mathrm{conf}}\right]\varphi_\mu = \epsilon_\mu \varphi_\mu, \tag{2.2.2}$$

where $\hat{T}$ and $V_{\mathrm{eff}}[\rho_A]$ denote the kinetic operator and the exchange–correlation potential with respect to the atomic charge density ρ_A calculated with the PBE formulation of the GGA (GGA-PBE),[20] respectively. Artificial atom-centered potentials (confinement potentials) $V^{\mathrm{d}}_{\mathrm{conf}}$ and V_{conf} are applied for the calculations of charge density ρ_A and pseudo-AO φ_μ, respectively, to mimic the localized electronic states of the atoms in molecules or solids. In general, the shape of V_{conf} is optimized for each element in an empirical manner.

Through the variational principles, the set of MO coefficients, $\mathbf{c}$, is obtained by solving the following generalized eigenvalue problem:

$$\mathbf{Fc} = \mathbf{Sc}\boldsymbol{\epsilon}^{\mathrm{MO}}, \tag{2.2.3}$$

where the diagonal elements of $\boldsymbol{\epsilon}^{\mathrm{MO}}$ are the MO energy levels. The Fock matrix element $F_{\mu\nu\sigma}$ is given as

$$F_{\mu\nu\sigma} = H^0_{\mu\nu} + \frac{1}{2} S_{\mu\nu} \sum_{K}^{N_{\mathrm{shell}}} (\gamma_{IK} + \gamma_{JK})\, \Delta q_K \pm \frac{1}{2} S_{\mu\nu} \sum_{L'' \in A} (W_{ALL''} + W_{AL'L''})\, p_{AL''}), \tag{2.2.4}$$

where the plus and minus signs correspond to α-spin and β-spin, respectively. Note that the AOs μ and ν belong to the shells I and J, respectively. The third term of Eq. 2.2.4 can be nonzero only if the AOs μ and ν belong to the same atom A, and in this case, they are included in shells L and L', respectively. Eq. 2.2.4 is solved self-consistently until Mulliken charge Δq_I is converged; this procedure is called SCC cycles.

Elements of $\mathbf{H_0}$ and $\mathbf{S}$ matrices are described as

$$S_{\mu\nu} = \left\langle \varphi_\mu \middle| \varphi_\nu \right\rangle, \tag{2.2.5}$$

$$H^0_{\mu\nu} = \begin{cases} \epsilon^0_\mu & \text{if } \mu = \nu \\ \left\langle \phi_\mu \middle| \hat{T} + V_{\mathrm{eff}}[\rho_A + \rho_B] \middle| \phi_\nu \right\rangle & \text{if } A \neq B \;\&\; \mu \neq \nu \\ 0 & \text{otherwise,} \end{cases} \tag{2.2.6}$$

respectively, where ϵ^0_μ denotes the orbital energy eigenvalue of the corresponding AO in the neutral isolated atom without the confinement potential. In actual calculations, $H^0_{\mu\nu}$ and $S_{\mu\nu}$ are obtained from a pre-computed table through Slater–Koster transformation.[21] In the table, which is called Slater–Koster parameter and given for each element pair, $H^0_{\mu\nu}$ and $S_{\mu\nu}$ values for σ-, π-, and δ-type interactions are tabulated as functions of interatomic distance. In addition, the repulsive potential E_{rep} is also a parametric component; E_{rep} is commonly expressed by a set of spline functions of interatomic distance for each element pair.

2.2.2 DC-DFTB[†]

The computational bottleneck of the DFTB method is solving the generalized eigenvalue problem (Eq. 2.2.3), whose computational time scales approximately as $O\left(N^3\right)$. While the DFTB is a computationally efficient method, this scaling still limits the accessible system size to approximately 10^2–10^3 atoms. With this background, an $O(N)$ type DFTB method, DC-DFTB, has been developed to extend the DFTB applications to huge systems. DC[23–26] is a class of fragmentation-based approaches for large-scale quantum chemical calculations,[27–30] among which the fragment MO method[31–33] has been interfaced with DFTB.[34] In addition, the "modified divide-and-conquer" approach, which is also a linear-scaling method based on fragmentation, has been integrated with DFTB and successfully applied to condensed-phase systems.[35–37] The DC technique has been combined with a wide range of techniques including spin-restricted and unrestricted Hartree–Fock,[38,39] Møller–Plesset perturbation theory,[40,41] coupled-cluster,[42,43] and DFTB.[44] In the DC framework, delocalized electronic states over multiple fragments can be described. Moreover, the DC scheme is capable of treating chemical reactions that exceed the boundary of fragments. Taking advantage of these features, the ground-state DC-DFTB has been applied to a variety of problems, where fully quantum mechanical treatment of the whole system is necessary, such as nonlocal proton and hydroxide anion transport in bulk water,[45,46] carrier diffusion in electrolyte solutions for alkali-metal ion batteries,[47,48] chemical CO_2 absorption in amine solutions,[49] polaron formation in a perovskite solar cell material,[13] and proton transfer in bacteriorhodopsin.[50]

In the DC scheme, the target system is spatially divided into mutually exclusive subsets of atoms called subsystems. The subsystem is expressed as $\mathcal{S}^s$, where s is the index that specifies the subsystem. The division is arbitrary; each subsystem can be, for example, a single atom, chemically well-defined atom group (e.g., one amino acid in a protein), or can be automatically defined by a spatial mesh with a constant interval. For each subsystem s, the Hamiltonian matrix and the corresponding MOs are expanded by a set of AOs included in the corresponding

[†]Reproduced from Ref. [22], with the permission of AIP Publishing.

localization region $\mathcal{L}^s$, which incorporates $\mathcal{S}^s$ and the neighboring subsystems called the buffer region, $\mathcal{B}^s$, which is composed of subsystems within the given distance (buffer radius) r_b from $\mathcal{S}^s$. Namely,

$$\mathcal{L}^s = \mathcal{S}^s \cup \mathcal{B}^s. \tag{2.2.7}$$

For each localization region $\mathcal{L}^s$, $\mathcal{S}^s$ is sometimes called the central region, to distinguish it from the buffer region $\mathcal{B}^s$. For each subsystem s, the generalized eigenvalue problem corresponding to Eq. 2.2.3, i.e.,

$$\mathbf{F}^s\mathbf{c}^s = \mathbf{S}^s\mathbf{c}^s\boldsymbol{\epsilon}^s, \tag{2.2.8}$$

is solved. The occupation number f_p^s of each MO in $\mathcal{L}^s$ is determined using the Fermi–Dirac distribution function

$$f_p^s = \frac{\nu}{\exp\left[\beta\left(\epsilon_p^s - \epsilon_\mathrm{F}\right)\right] + 1}, \tag{2.2.9}$$

where $\nu = 2$ for the spin-restricted case. ϵ_F is a Fermi level that is common to all subsystems, which is determined to conserve the total number of electrons in the overall system. The inverse temperature β is given as a controllable parameter. The density matrix for each subsystem s, $\mathbf{D}^s$, is obtained as:

$$D_{\mu\nu}^s = \sum_p f_p^s c_{\mu p}^s c_{\nu p}^s. \tag{2.2.10}$$

The density matrix for the overall system $\mathbf{D}^\mathrm{DC}$ is obtained by merging the subsystem density matrices while avoiding double counting

$$D_{\mu\nu}^\mathrm{DC} = \sum_s P_{\mu\nu} D_{\mu\nu}^s, \tag{2.2.11}$$

where $D^s_{\mu\nu}$ is the element of the density matrix for subsystem s, and $P_{\mu\nu}$ is defined as:

$$P_{\mu\nu} = \begin{cases} 1 & \mu \in \mathcal{S}^s \wedge \nu \in \mathcal{S}^s \\ 1/2 & \mu \in \mathcal{S}^s \wedge \nu \notin \mathcal{S}^s \\ 1/2 & \mu \notin \mathcal{S}^s \wedge \nu \in \mathcal{S}^s \\ 0 & \mu \notin \mathcal{S}^s \wedge \nu \notin \mathcal{S}^s \end{cases}. \tag{2.2.12}$$

The total number of electrons N in the overall system is obtained as:

$$N = \sum_{\mu\nu} D^{\mathrm{DC}}_{\mu\nu} S_{\nu\mu}. \tag{2.2.13}$$

The error arising from the division into the subsystems is controlled by r_b; the error decreases as r_b increases, in general.

2.3 DFTB-Based Approaches to Excited-State Calculations

2.3.1 TD-DFTB[†]

Linear-response formulation of TD-DFTB is an extension of its ground-state counterpart, DFTB, to excited-state calculations. In the TD-DFTB, the η-th excitation energy and response properties are obtained by solving the following non-Hermitian eigenvalue problem, which is called Casida's equation.[51]

$$\begin{bmatrix} \mathbf{A} & \mathbf{B} \\ \mathbf{B}^* & \mathbf{A}^* \end{bmatrix} \begin{bmatrix} \mathbf{X}^\eta \\ \mathbf{Y}^\eta \end{bmatrix} = \omega_\eta \begin{bmatrix} \mathbf{1} & \mathbf{0} \\ \mathbf{0} & -\mathbf{1} \end{bmatrix} \begin{bmatrix} \mathbf{X}^\eta \\ \mathbf{Y}^\eta \end{bmatrix}. \tag{2.3.1}$$

[†]Reproduced from Ref. [22], with the permission of AIP Publishing.

where ω_η is the η-th excitation energy, and the elements of the matrices **A** and **B** are defined as:

$$A_{ia,jb} = \delta_{ij}\delta_{ab}\left(\epsilon_a - \epsilon_i\right) + K_{ia,jb}, \tag{2.3.2}$$

$$B_{ia,jb} = K_{ia,bj}, \tag{2.3.3}$$

where spin indices are omitted. $K_{ia,jb}$ and $K_{ia,bj}$ are coupling matrices. The explicit form of the coupling matrices in the case of the TD-DFTB is found elsewhere.[52] $\mathbf{X}^\eta$ and $\mathbf{Y}^\eta$ are the excitation and de-excitation amplitudes, respectively. For numerical convenience, Eq. 2.3.1 is solved after conversion to the following Hermitian eigenvalue problem:

$$\left(\mathbf{A}-\mathbf{B}\right)^{1/2}\left(\mathbf{A}+\mathbf{B}\right)\left(\mathbf{A}-\mathbf{B}\right)^{1/2}\mathbf{F}^\eta = \omega_\eta^2\mathbf{F}^\eta, \tag{2.3.4}$$

where

$$\mathbf{F}^\eta = \left(\mathbf{A}-\mathbf{B}\right)^{-1/2}\left(\mathbf{X}^\eta + \mathbf{Y}^\eta\right). \tag{2.3.5}$$

The resulting eigenvectors are normalized to satisfy the biorthogonality condition:

$$\sum_{ia}\left(X_{ia}^\eta + Y_{ia}^\eta\right)\left(X_{ia}^\theta - Y_{ia}^\theta\right) = \delta_{\eta\theta}. \tag{2.3.6}$$

The corresponding adabatic electronic wavefunction ψ_η is expressed in a form similar to that in CIS[51]

$$\psi_\eta = \sum_{ia} C_{ia}^\eta \Phi_i^a. \tag{2.3.7}$$

Here, Φ_i^a is the Slater determinant corresponding to the $i \rightarrow a$ excitation configuration. According to the Casida's ansatz,[51]

$$C_{ia}^\eta = X_{ia}^\eta + Y_{ia}^\eta. \tag{2.3.8}$$

2.3.2 DC-TD-DFTB†

DC-TD-DFTB is an extension of DC-DFTB[44] for excited-state calculations, in the same context that TD-DFTB is an extension of DFTB. Two distinct approaches have been employed for the excited-state calculations in the DC framework, i.e., dynamical-polarizability-based[53,54] and eigenvalue-problem-based[55–57] approaches. It should be noted that the dynamical-polarizability-based approach can treat nonlocal excitations such as charge-transfer excitation and transitions among delocalized orbitals.[53,54] Because of the effectiveness in the case of local excitation, the eigenvalue-problem-based approach has been combined with DFTB and applied to MD calculations in excited states.[55–57] In the eigenvalue-based DC-TD-DFTB approach, the excited-state properties are obtained by solving Casida's equation (Eq. 2.3.1) for the subsystem s that includes the excitation center:

$$\begin{bmatrix} \mathbf{A}^s & \mathbf{B}^s \\ \mathbf{B}^{s*} & \mathbf{A}^{s*} \end{bmatrix} \begin{bmatrix} \mathbf{X}^{s,\eta} \\ \mathbf{Y}^{s,\eta} \end{bmatrix} = \omega_\eta \begin{bmatrix} \mathbf{1} & \mathbf{0} \\ \mathbf{0} & -\mathbf{1} \end{bmatrix} \begin{bmatrix} \mathbf{X}^{s,\eta} \\ \mathbf{Y}^{s,\eta} \end{bmatrix}, \tag{2.3.9}$$

where $\mathbf{A}^s$ and $\mathbf{B}^s$ are the counterparts of $\mathbf{A}$ and $\mathbf{B}$, respectively. Here, the MOs are substituted with those obtained from Eq. 2.2.8 for the subsystem s. Similar to the case of TD-DFTB, Eq. 2.3.9 is solved in the form:

$$(\mathbf{A}^s - \mathbf{B}^s)^{1/2} (\mathbf{A}^s + \mathbf{B}^s) (\mathbf{A}^s - \mathbf{B}^s)^{1/2} \mathbf{F}^{s,\eta} = \omega_\eta^2 \mathbf{F}^{s,\eta}, \tag{2.3.10}$$

where

$$\mathbf{F}^{s,\eta} = (\mathbf{A}^s - \mathbf{B}^s)^{-1/2} (\mathbf{X}^{s,\eta} + \mathbf{Y}^{s,\eta}). \tag{2.3.11}$$

The resulting eigenvectors are normalized according to:

$$\sum_{ia} \left(X_{ia}^{s,\eta} + Y_{ia}^{s,\eta}\right)\left(X_{ia}^{s,\theta} - Y_{ia}^{s,\theta}\right) = \delta_{\eta\theta}. \tag{2.3.12}$$

†Reproduced from Ref. [22], with the permission of AIP Publishing.

The corresponding adiabatic wavefunction is described as:

$$\psi_{\eta}^{s} = \sum_{ia} C_{ia}^{s,\eta} \Phi_{i}^{sa}, \tag{2.3.13}$$

where Φ_{i}^{sa} is the Slater determinant for the $i \rightarrow a$ excitation configuration within the localization region $\mathcal{L}^{s}$, and

$$C_{ia}^{s,\eta} = X_{ia}^{s,\eta} + Y_{ia}^{s,\eta}. \tag{2.3.14}$$

2.3.3 SF-TD-DFTB†

In the framework of spin-polarized DFTB,[19] α/β-spin Fock matrices are described by a point-charge-based representation:

$$\begin{aligned} F_{\mu\nu}^{\alpha/\beta} &= H_{\mu\nu}^{0} \\ &+ \frac{1}{2} S_{\mu\nu} \sum_{K} (\gamma_{IK} + \gamma_{JK}) \Delta q_{K} \\ &\pm \frac{1}{2} S_{\mu\nu} \sum_{L'' \in A} (m_{ALL''} + m_{AL'L''}) \, p_{AL''}. \end{aligned} \tag{2.3.15}$$

Here, the one-electron Hamiltonian matrix element $H_{\mu\nu}^{0}$ and the AO overlap matrix element $S_{\mu\nu}$ are computed from pre-calculated tables, which are externally given as a parameter set. The second term on the RHS describes the spin-independent component of the electron-electron interaction with γ_{IK} and Δq_{K}, which are $1/R$-like functions of the interatomic distance[17] and the Mulliken charge of the shell K referenced to that of the isolated neutral atom, respectively. The third term on the RHS of the Eq. 2.3.15 is the spin-dependent part, whose sign is + and − for α and β spins, respectively. $p_{AL''}$ represents the spin polarization, i.e., the α-spin Mulliken charge minus the β-spin one, of shell L'' in atom A. The short-range nature of the electron-electron magnetic interaction allows the spin constant $m_{ALL'}$ to be considered nonzero only for intra-atomic interactions. $m_{ALL'}$ is pre-calculated via Kohn–Sham DFT calculations of an isolated

†Reprinted with permission from Ref. [58]. Copyright 2020 American Chemical Society.

neutral atom by infinitesimally varying the α and β occupation numbers of shell L', i.e., $n^{\alpha}_{L'}$ and $n^{\beta}_{L'}$, respectively:

$$m_{ALL'} = \frac{1}{2}\left(\frac{\partial \epsilon^{\alpha}_{L}}{\partial n^{\alpha}_{L'}} - \frac{\partial \epsilon^{\alpha}_{L}}{\partial n^{\beta}_{L'}}\right). \tag{2.3.16}$$

Here, ϵ^{α}_{L} is the α-spin Kohn–Sham orbital energy level corresponding to the highest occupied valence shell of the atom. The MO coefficients $\mathbf{c}$ are obtained by solving the generalized eigenvalue problem:

$$\mathbf{Fc} = \mathbf{Sc}\epsilon. \tag{2.3.17}$$

In principle, the Fock matrix in Eq. 2.3.17 can be either $\mathbf{F}^{\alpha/\beta}$ themselves, i.e., the spin-unrestricted form, or constructed from them in the restricted open-shell fashion. In this study, the spin-unrestricted-type expression is employed to achieve better convergence of the SCC process.

The SF-TD-DFTB[59] is derived as a DFTB-style approximation to the SF-TD-DFT,[60] which is a modified linear-response TD-DFT where only spin-flipping, i.e., $\alpha \rightarrow \beta$, excitations are allowed. In the SF-TD-DFT/DFTB approach, adiabatic states with the desired spin multiplicity are obtained via spin-flipping excitations from a reference state of higher spin multiplicity, which is chosen to be triplet when focusing on singlet states. Within the TDA,[61] the excitation energy ω_η and the response matrix $\mathbf{X}^{\eta}$ for the state η are obtained as

$$\sum_{j\bar{b}} A_{i\bar{a},j\bar{b}} X^{\eta}_{j\bar{b}} = \omega_\eta X^{\eta}_{i\bar{a}}, \tag{2.3.18}$$

where

$$A_{i\bar{a},j\bar{b}} = F^{\beta}_{\bar{a}\bar{b}}\delta_{ij} - F^{\alpha}_{ij}\delta_{\bar{a}\bar{b}} + K_{i\bar{a},j\bar{b}}. \tag{2.3.19}$$

Here, the coupling matrix **K** is represented in the point-charge-approximated form:

$$K_{i\bar{a},j\bar{b}} = 2\sum_{A} q_A^{i\bar{a}} m_A q_A^{j\bar{b}}. \tag{2.3.20}$$

The transition Mulliken charge for the shell K, $q_K^{\hat{p}\hat{q}}$, is defined as

$$q_K^{\hat{p}\hat{q}} = \frac{1}{2}\sum_{\nu\in A}\sum_{\lambda}\left(c_{\nu\hat{p}} S_{\nu\lambda} c_{\lambda\hat{q}} + c_{\lambda\hat{p}} S_{\lambda\nu} c_{\nu\hat{q}}\right), \tag{2.3.21}$$

and that for the atom A, $q_A^{\hat{p}\hat{q}}$, is the sum of $q_K^{\hat{p}\hat{q}}$ over the shells belonging to the atom A:

$$q_A^{\hat{p}\hat{q}} = \sum_{K\in A} q_K^{\hat{p}\hat{q}}. \tag{2.3.22}$$

The atom-wise spin constant m_A is equal to the $m_{ALL'}$ for the outermost occupied valence of the atom A.

For each state η, the adiabatic wavefunction ψ_η is expressed in a form similar to that in the CIS:

$$\psi_\eta = \sum_{i\bar{a}} C_{i\bar{a}}^{\eta} \Phi_i^{\bar{a}}. \tag{2.3.23}$$

Here, $\Phi_i^{\bar{a}}$ is the Slater determinant for the $i \to \bar{a}$ excitation configuration. Under the TDA, one can set $C_{i\bar{a}}^{\eta} = X_{i\bar{a}}^{\eta}$.

References

[1]J. C. Tully, *J. Chem. Phys.* **137**, 22A301 (2012).

[2]E. Tapavicza, G. D. Bellchambers, J. C. Vincent, and F. Furche, *Phys. Chem. Chem. Phys.* **15**, 18336 (2013).

[3]I. Tavernelli, *Acc. Chem. Res.* **48**, 792 (2015).

[4]E. Brunk and U. Rothlisberger, *Chem. Rev.* **115**, 6217 (2015).

[5]B. F. E. Curchod and T. J. Martínez, *Chem. Rev.* **118**, 3305 (2018).

[6]R. Crespo-Otero and M. Barbatti, *Chem. Rev.* **118**, 7026 (2018).

[7]T. R. Nelson, A. J. White, J. A. Bjorgaard, A. E. Sifain, Y. Zhang, B. Nebgen, S. Fernandez-Alberti, D. Mozyrsky, A. E. Roitberg, and S. Tretiak, *Chem. Rev.* **120**, 2215 (2020).

[8]S.-I. Sawada, A. Nitzan, and H. Metiu, *Phys. Rev. B* **32**, 851 (1985).

[9]J. C. Tully, *Faraday Discuss.* **110**, 407 (1998).

[10]M. Ben-Nun, J. Quenneville, and T. J. Martínez, *J. Phys. Chem. A* **104**, 5161 (2000).

[11]J. C. Tully and R. K. Preston, *J. Chem. Phys.* **55**, 562 (1971).

[12]J. C. Tully, *J. Chem. Phys.* **93**, 1061 (1990).

[13]H. Uratani, C.-P. Chou, and H. Nakai, *Phys. Chem. Chem. Phys.* **22**, 97 (2020).

[14]M. Wahiduzzaman, A. F. Oliveira, P. Philipsen, L. Zhechkov, E. van Lenthe, H. A. Witek, and T. Heine, *J. Chem. Theory Comput.* **9**, 4006 (2013).

[15]W. M. C. Foulkes and R. Haydock, *Phys. Rev. B* **39**, 12520 (1989).

[16]D. Porezag, T. Frauenheim, T. Köhler, G. Seifert, and R. Kaschner, *Phys. Rev. B* **51**, 12947 (1995).

[17]M. Elstner, D. Porezag, G. Jungnickel, J. Elsner, M. Haugk, T. Frauenheim, S. Suhai, and G. Seifert, *Phys. Rev. B* **58**, 7260 (1998).

[18]M. Gaus, Q. Cui, and M. Elstner, *J. Chem. Theory Comput.* **7**, 931 (2011).

[19]C. Köhler, G. Seifert, U. Gerstmann, M. Elstner, H. Overhof, and T. Frauenheim, *Phys. Chem. Chem. Phys.* **3**, 5109 (2001).

[20]J. P. Perdew, K. Burke, and M. Ernzerhof, *Phys. Rev. Lett.* **77**, 3865 (1996).

[21]J. C. Slater and G. F. Koster, *Phys. Rev.* **94**, 1498 (1954).

[22]H. Uratani and H. Nakai, *J. Chem. Phys.* **152**, 224109 (2020).

[23]W. Yang, *Phys. Rev. Lett.* **66**, 1438 (1991).

[24]W. Yang and T.-S. Lee, *J. Chem. Phys.* **103**, 5674 (1995).

[25]M. Kobayashi and H. Nakai, "Divide-and-conquer approaches to quantum chemistry: theory and implementation", in *Linear-scaling techniques in computational chemistry and physics: methods and applications* (2011), pp. 97–127.

[26]M. Kobayashi and H. Nakai, *Phys. Chem. Chem. Phys.* **14**, 7629 (2012).

[27]M. S. Gordon, D. G. Fedorov, S. R. Pruitt, and L. V. Slipchenko, *Chem. Rev.* **112**, 632 (2012).

[28]M. A. Collins and R. P. A. Bettens, *Chem. Rev.* **115**, 5607 (2015).

[29]K. Raghavachari and A. Saha, *Chem. Rev.* **115**, 5643 (2015).

[30]J. M. Herbert, *J. Chem. Phys.* **151**, 170901 (2019).

[31]K. Kitaura, E. Ikeo, T. Asada, T. Nakano, and M. Uebayasi, *Chem. Phys. Lett.* **313**, 701 (1999).

[32]D. G. Fedorov and K. Kitaura, *J. Phys. Chem. A* **111**, 6904 (2007).

[33]D. G. Fedorov, T. Nagata, and K. Kitaura, *Phys. Chem. Chem. Phys.* **14**, 7562 (2012).

[34]Y. Nishimoto, D. G. Fedorov, and S. Irle, *J. Chem. Theory Comput.* **10**, 4801 (2014).

[35]T. J. Giese, H. Chen, T. Dissanayake, G. M. Giambaşu, H. Heldenbrand, M. Huang, E. R. Kuechler, T.-S. Lee, M. T. Panteva, B. K. Radak, and D. M. York, *J. Chem. Theory Comput.* **9**, 1417 (2013).

[36]T. J. Giese, H. Chen, M. Huang, and D. M. York, *J. Chem. Theory Comput.* **10**, 1086 (2014).

[37]T. J. Giese, M. Huang, H. Chen, and D. M. York, *Acc. Chem. Res.* **47**, 2812 (2014).

[38]T. Akama, M. Kobayashi, and H. Nakai, *J. Comput. Chem.* **28**, 2003 (2007).

[39]M. Kobayashi, T. Yoshikawa, and H. Nakai, *Chem. Phys. Lett.* **500**, 172 (2010).

[40]M. Kobayashi, T. Akama, and H. Nakai, *J. Chem. Phys.* **125**, 204106 (2006).

[41]T. Yoshikawa, M. Kobayashi, and H. Nakai, *Theor. Chem. Acc.* **130**, 411 (2011).

[42]M. Kobayashi and H. Nakai, *J. Chem. Phys.* **129**, 044103 (2008).

[43]M. Kobayashi and H. Nakai, *J. Chem. Phys.* **131**, 114108 (2009).

[44]H. Nishizawa, Y. Nishimura, M. Kobayashi, S. Irle, and H. Nakai, *J. Comput. Chem.* **37**, 1983 (2016).

[45]H. Nakai, A. W. Sakti, and Y. Nishimura, *J. Phys. Chem. B* **120**, 217 (2016).

[46]A. W. Sakti, Y. Nishimura, and H. Nakai, *J. Phys. Chem. B* **121**, 1362 (2017).

[47]M. Okoshi, C.-P. Chou, and H. Nakai, *J. Phys. Chem. B* **122**, 2600 (2018).

[48]Q. Zheng, S. Miura, K. Miyazaki, S. Ko, E. Watanabe, M. Okoshi, C.-P. Chou, Y. Nishimura, H. Nakai, T. Kamiya, T. Honda, J. Akikusa, Y. Yamada, and A. Yamada, *Angew. Chem. Int. Ed.* **58**, 14202 (2019).

[49]A. W. Sakti, Y. Nishimura, H. Sato, and H. Nakai, *Bull. Chem. Soc. Jpn.* **90**, 1230 (2017).

[50]J. Ono, M. Imai, Y. Nishimura, and H. Nakai, *J. Phys. Chem. B* **124**, 8524 (2020).

[51]M. E. Casida, *J. Mol. Struct.: THEOCHEM* **914**, 3 (2009).

[52]T. A. Niehaus, S. Suhai, F. Della Sala, P. Lugli, M. Elstner, G. Seifert, and T. Frauenheim, *Phys. Rev. B* **63**, 085108 (2001).

[53]H. Nakai and T. Yoshikawa, *J. Chem. Phys.* **146**, 124123 (2017).

[54]Y. Ikabata, Q. Wang, T. Yoshikawa, A. Ueda, T. Murata, K. Kariyazono, M. Moriguchi, H. Okamoto, Y. Morita, and H. Nakai, *npj Quant. Mater.* **2**, 27 (2017).

[55]N. Komoto, T. Yoshikawa, J. Ono, Y. Nishimura, and H. Nakai, *J. Chem. Theory Comput.* **15**, 1719 (2019).

[56]T. Yoshikawa, N. Komoto, Y. Nishimura, and H. Nakai, *J. Comput. Chem.* **40**, 2778 (2019).

[57]N. Komoto, T. Yoshikawa, Y. Nishimura, and H. Nakai, *J. Chem. Theory Comput.* **16**, 2369 (2020).

[58]H. Uratani, T. Morioka, T. Yoshikawa, and H. Nakai, *J. Chem. Theory Comput.* **16**, 7299 (2020).

[59]M. Inamori, T. Yoshikawa, Y. Ikabata, Y. Nishimura, and H. Nakai, *J. Comput. Chem.* **41**, 1538 (2020).

[60]Y. Shao, M. Head-Gordon, and A. I. Krylov, *J. Chem. Phys.* **118**, 4807 (2003).

[61]S. Hirata and M. Head-Gordon, *Chem. Phys. Lett.* **314**, 291 (1999).

Chapter 3

Development of NA-MD Methods for Complicated Systems

Simulations of nonadiabatic dynamics in complicated systems, e.g., carrier dynamics in solar cell materials and structure-/environment-dependent nonradiative relaxation processes of excited molecules, request sizable model systems to include the details of systems and sufficiently large number of trajectory samples to obtain the statistically reliable outcome. With this background, this chapter presents development of NA-MD methods to satisfy such requirements within the reasonable computational resources. Results of numerical validation for the accuracy and computational cost are also shown.

Section 3.1 describes the implementation of the FSSH technique with the use of TD-DFTB method, which is a low-cost semiempirical excited-state calculation technique. In Section 3.2, by adoption of the DC framework, the TD-DFTB/FSSH technique is further extended to treat huge systems including solutions. Section 3.3 presents the combination of the TD-DFTB/FSSH with the SF approach to obtain the correct description of S_1/S_0 CXs, which play an important role in excited- to ground-state transitions, i.e., nonradiative relaxation phenomena. Section 3.4 describes the combined approach of the techniques presented in Sections 3.2 and 3.3 to simulate the nonradiative relaxation dynamics of excited molecules with including the effects of environments, e.g., solvents.

3.1 Implementation of DFTB-Based NA-MD Method into DCDFTBMD Program[†]

3.1.1 FSSH Algorithm

In the FSSH technique, the electronic wavefunction is propagated quantum mechanically, while the nuclear dynamics is treated classically. For each independent classical trajectory, the TD electronic wavefunction Ξ is expressed as a linear combination of a set of adiabatic electronic wavefunctions:

$$\Xi\left(\mathbf{r}, t; \mathbf{R}(t)\right) = \sum_{\eta} c_{\eta}(t)\psi_{\eta}\left(\mathbf{r}; \mathbf{R}(t)\right), \tag{3.1.1}$$

where t, $\mathbf{r}$, and $\mathbf{R}$ are the time, electronic coordinates, and nuclear coordinates, respectively. According to the TD Schrödinger equation, propagation of the electronic wavefunction is described as:

$$i\hbar\frac{\partial c_{\eta}(t)}{\partial t} = E_{\eta}(t)c_{\eta}(t) - i\hbar\sum_{\theta}\mathbf{d}_{\eta\theta}(t)\cdot\frac{\partial\mathbf{R}(t)}{\partial t}c_{\theta}(t). \tag{3.1.2}$$

Here, $E_{\eta}(t)$ is the potential energy of the adiabatic state η at the time t, and $\mathbf{d}_{\eta\theta}(t)$ is the NAC vector, defined as:

$$\mathbf{d}_{\eta\theta}(t) = \left\langle\psi_{\eta}(t)\,\middle|\,\boldsymbol{\nabla}\psi_{\theta}(t)\right\rangle, \tag{3.1.3}$$

where $\boldsymbol{\nabla}$ indicates the gradient with respect to the nuclear coordinates. The NAC can be simplified as the time-derivative form.

$$\sigma_{\eta\theta}(t) = \mathbf{d}_{\eta\theta}(t)\cdot\frac{\partial\mathbf{R}(t)}{\partial t} = \left\langle\psi_{\eta}(t)\,\middle|\,\frac{\partial\psi_{\theta}(t)}{\partial t}\right\rangle. \tag{3.1.4}$$

$\sigma_{\eta\theta}(t)$ is termed TDNAC. In the standard approach, $\sigma_{\eta\theta}(t)$ is calculated by using the numerical derivative. For CIS type wavefunctions, the numerical evaluation may be performed via either of two distinct methods, i.e., the WO approach[2] or OD approach.[3] While the latter is computationally more efficient in general, the importance of the former should not be overlooked. For

[†]Reproduced from Ref. [1], with the permission of AIP Publishing.

example, in the electronic wavefunction propagation scheme called local diabatization,[4] which has excellent numerical stability in the case where trivial crossings among adiabatic PESs are present, the wavefunction overlap is directly used instead of the TDNAC.

As in adiabatic MD simulations, the nuclear coordinates **R** are propagated according to Newton's equation using the atomic force on the active adiabatic state ξ:

$$\frac{d^2R_A^u}{dt^2} = -\frac{1}{m_A}\left(\frac{\partial \omega_\xi}{\partial R_A^u} + \frac{\partial E_0}{\partial R_A^u}\right), \tag{3.1.5}$$

where R_A^u ($u = x, y, z$) is the coordinate of atom A for the axis u, and m_A is the mass of atom A.

Quantum decoherence is not included in the time propagation according to Eqs. 3.1.2 and 3.1.4. The simplified decay of mixing[5] approach is a straightforward and widely used correction scheme for the decoherence. In this approach, the population of the non-active state θ is damped with the time constant of $\tau_{\theta\xi}$, which is calculated as:

$$\tau_{\theta\xi} = \frac{\hbar}{\left|E_\theta - E_\xi\right|}\left(1 + \frac{\alpha}{E_{\mathrm{kin}}}\right). \tag{3.1.6}$$

Here, α is a constant parameter, the typical value of which is set to 0.1 hartree. E_{kin} is the nuclear kinetic energy.

For each time step of the electronic wavefunction propagation, the probability of hopping from the current active state ξ to another state θ, $p_{\xi\to\theta}$, is computed as:[6]

$$p_{\xi\to\theta} = \max\left[0,\ \frac{2\delta t}{\left|c_\xi\right|^2}\sigma_{\xi\theta}\Re\left(c_\xi^* c_\theta\right)\right], \tag{3.1.7}$$

where δt is the time step for propagating the electronic wavefunction. Based on the hopping probability, the active state at the next step is determined using a uniform random number, which ranges from 0 to 1.

3.1.2 NAC Calculation Algorithms

WO Approach

In the WO approach, TDNAC is approximately computed on the basis of the overlap between the adiabatic state wavefunctions at the subsequent time steps:

$$S_{\eta\theta}(t_1, t_2) = \left\langle \psi_\eta(t_1) \middle| \psi_\theta(t_2) \right\rangle, \tag{3.1.8}$$

where $t_2 = t_1 + \Delta t$. Δt is the time step for propagation of the nuclear coordinates. TDNAC is obtained using the finite difference approximation,[2,7] which, for example, takes the following form:

$$\sigma_{\eta\theta}\left(t_1 + \frac{\Delta t}{2}\right) \to \frac{1}{2\Delta t}\left[S_{\eta\theta}(t_1, t_2) - S_{\theta\eta}(t_1, t_2)\right]. \tag{3.1.9}$$

For CIS type wavefunctions (Eq. 2.3.7), the wavefunction overlap $S_{\eta\theta}(t_1, t_2)$ is expressed as:

$$S_{\eta\theta}(t_1, t_2) = \sum_{ia,jb} C^{\eta}_{ia}(t_1) C^{\theta}_{jb}(t_2) \left\langle \Phi^a_i(t_1) \middle| \Phi^b_j(t_2) \right\rangle, \tag{3.1.10}$$

where the overlap between the Slater determinants on the RHS is calculated using the following relation[8,9]

$$\left\langle \Phi^a_i(t_1) \middle| \Phi^b_j(t_2) \right\rangle = \det\left(\mathbf{\Sigma}[ia, jb]\right). \tag{3.1.11}$$

Here, $\mathbf{\Sigma}[ia, jb]$ is the overlap matrix among the spin orbitals that constitute the Slater determinants $\Phi^a_i(t_1)$ and $\Phi^b_j(t_2)$. Assuming α–α excitation, $\mathbf{\Sigma}[ia, jb]$ is written as:

$$\mathbf{\Sigma}[ia, jb] = \begin{pmatrix} {}^{\alpha\alpha}\mathbf{\Sigma}[ia, jb] & {}^{\alpha\beta}\mathbf{\Sigma}[ia, jj] \\ {}^{\beta\alpha}\mathbf{\Sigma}[ii, jb] & {}^{\beta\beta}\mathbf{\Sigma}[ii, jj] \end{pmatrix}, \tag{3.1.12}$$

where

$$
{}^{\sigma\tau}\mathbf{\Sigma}[ip, jq] =
$$

$$
\begin{pmatrix}
\langle\phi_1(t_1)\,|\,\phi_1(t_2)\rangle\,\langle\sigma\,|\,\tau\rangle & \dots & \overline{\left\langle\phi_1(t_1)\,\middle|\,\phi_q(t_2)\right\rangle\,\langle\sigma\,|\,\tau\rangle} & \dots & \langle\phi_1(t_1)\,\middle|\,\phi_{n_\mathrm{O}}(t_2)\rangle\,\langle\sigma\,|\,\tau\rangle \\
\vdots & & \vdots & & \vdots \\
\underline{\left\langle\phi_p(t_1)\,\middle|\,\phi_1(t_2)\right\rangle\,\langle\sigma\,|\,\tau\rangle} & \dots & \underline{\overline{\left\langle\phi_p(t_1)\,\middle|\,\phi_q(t_2)\right\rangle\,\langle\sigma\,|\,\tau\rangle}} & \dots & \underline{\left\langle\phi_p(t_1)\,\middle|\,\phi_{n_\mathrm{O}}(t_2)\right\rangle\,\langle\sigma\,|\,\tau\rangle} \\
\vdots & & \vdots & & \vdots \\
\langle\phi_{n_\mathrm{O}}(t_1)\,\big|\,\phi_1(t_2)\rangle\,\langle\sigma\,|\,\tau\rangle & \dots & \overline{\left\langle\phi_{n_\mathrm{O}}(t_1)\,\middle|\,\phi_q(t_2)\right\rangle\,\langle\sigma\,|\,\tau\rangle} & \dots & \langle\phi_{n_\mathrm{O}}(t_1)\,\big|\,\phi_{n_\mathrm{O}}(t_2)\rangle\,\langle\sigma\,|\,\tau\rangle
\end{pmatrix},
\tag{3.1.13}
$$

in the spin-restricted case. σ and τ are spin indices, which take either α or β. The i-th row and the j-th column are underlined and overlined, respectively. Each matrix element in Eq. 3.1.13 is calculated as:

$$
\left\langle\phi_p(t_1)\,\middle|\,\phi_q(t_2)\right\rangle = \sum_{\mu\nu} c_{\mu p}(t_1) c_{\nu q}(t_2)\left\langle\chi_\mu(t_1)\,\middle|\,\chi_\nu(t_2)\right\rangle, \tag{3.1.14}
$$

$$
\langle\sigma\,|\,\tau\rangle = \begin{cases} 1 & \sigma = \tau \\ 0 & \sigma \neq \tau \end{cases}, \tag{3.1.15}
$$

where $c_{\mu p}$ is the MO coefficient of the AO basis function χ_μ in the MO p. Because the overlap between spin functions $\langle\sigma\,|\,\tau\rangle$ vanishes when $\sigma \neq \tau$, $\mathbf{\Sigma}[ia, jb]$ is block diagonal with respect to the spin.

$$
\mathbf{\Sigma}[ia, jb] = \begin{pmatrix} {}^{\alpha\alpha}\mathbf{\Sigma}[ia, jb] & \mathbf{0} \\ \mathbf{0} & {}^{\beta\beta}\mathbf{\Sigma}[ii, jj] \end{pmatrix}. \tag{3.1.16}
$$

Hence, the determinant is given as:

$$
\det\left(\mathbf{\Sigma}[ia, jb]\right) = \det\left({}^{\alpha\alpha}\mathbf{\Sigma}[ia, jb]\right) \times \det\left({}^{\beta\beta}\mathbf{\Sigma}[ii, jj]\right). \tag{3.1.17}
$$

It should be noted that Mitrić and co-workers derived a rigorous formulation for overlap between spin-adapted CSFs for singlet excited states[10,11]

$$\begin{aligned}
&\left\langle {}^{\mathrm{CSF}}\Phi_i^a(t_1) \,\middle|\, {}^{\mathrm{CSF}}\Phi_j^b(t_2) \right\rangle = \\
&\det\left({}^{\sigma\sigma}\mathbf{\Sigma}[ia, jb]\right) \times \det\left({}^{\sigma\sigma}\mathbf{\Sigma}[ii, jj]\right) \\
&+ \det\left({}^{\sigma\sigma}\mathbf{\Sigma}[ia, jj]\right) \times \det\left({}^{\sigma\sigma}\mathbf{\Sigma}[ii, jb]\right). \qquad (3.1.18)
\end{aligned}$$

For a sufficiently small nuclear time step Δt where the finite difference approximation (Eq. 3.1.9) is valid, the mutual orthogonality of the occupied and virtual spaces should be approximately conserved between the subsequent time steps, resulting in

$$\det\left({}^{\sigma\sigma}\mathbf{\Sigma}[ia, jj]\right) \approx 0, \qquad (3.1.19)$$

$$\det\left({}^{\sigma\sigma}\mathbf{\Sigma}[ii, jb]\right) \approx 0. \qquad (3.1.20)$$

From this observation, the "bare" Slater determinant overlap (Eq. 3.1.11) and the CSF overlap (Eq. 3.1.18) are considered to give essentially the same results.

The adiabatic wavefunctions have the arbitrariness to the extent of the phase factor $\mathrm{e}^{i\theta}$, which takes 1 or -1 in the real-valued case. The uncertainty in the phase (sign) of the adiabatic wavefunctions affects the sign of TDNAC and introduces severe error in the propagation of the total electronic wavefunction Ξ. For this reason, the sign of $\psi_\eta(t_2)$ is flipped when $S_{\eta\eta}(t_1, t_2)$ is negative, to keep the sign of the adiabatic wavefunctions at adjacent time steps consistent with each other.[7,12]

OD Approach

Another approach called the OD method was developed by Ryabinkin and co-workers.[3] Using Eqs. 2.3.7 and 3.1.4, TDNAC is formally expressed as:

$$\sigma_{\eta\theta}(t) = \sum_{ia\,jb} \left(C^{\eta}_{ia}(t) \frac{\partial C^{\theta}_{jb}(t)}{\partial t} \left\langle \Phi^{a}_{i}(t) \middle| \Phi^{b}_{j}(t) \right\rangle + C^{\eta}_{ia}(t) C^{\theta}_{jb}(t) \left\langle \Phi^{a}_{i}(t) \middle| \frac{\partial \Phi^{b}_{j}(t)}{\partial t} \right\rangle \right), \tag{3.1.21}$$

where the first term on the RHS can be non-zero only if $i = j \wedge a = b$ according to the Slater–Condon rule. Using the following conditions for real-valued orbitals,

$$\left\langle \phi_p(t) \middle| \frac{\partial \phi_p(t)}{\partial t} \right\rangle = 0, \tag{3.1.22}$$

$$\left\langle \phi_p(t) \middle| \phi_q(t) \right\rangle = \delta_{pq}, \tag{3.1.23}$$

one obtains:

$$\left\langle \Phi^{a}_{i}(t) \middle| \frac{\partial \Phi^{b}_{j}(t)}{\partial t} \right\rangle = \delta_{ij} \left\langle \phi_a(t) \middle| \frac{\partial \phi_b(t)}{\partial t} \right\rangle - \mathcal{P}_{ij} \delta_{ab} \left\langle \phi_j(t) \middle| \frac{\partial \phi_i(t)}{\partial t} \right\rangle. \tag{3.1.24}$$

Here, the factor $\mathcal{P}_{ij}$ arises from the arbitrariness in the ordering convention selected for the orbitals constituting the Slater determinants. $\mathcal{P}_{ij} = 1$ in the present case, where an occupied orbital i is substituted by a virtual orbital a without changing the ordering for each Slater determinant

of $i \rightarrow a$ excitation configuration. Using Eq. 3.1.24, TDNAC is further rewritten as

$$\begin{aligned}\sigma_{\eta\theta}(t) = &\sum_{ia} C_{ia}^{\eta}(t)\frac{\partial C_{ia}^{\theta}(t)}{\partial t} \\ &+ \sum_{iab} C_{ia}^{\eta}(t)C_{ib}^{\theta}(t)\left\langle \phi_a(t)\left|\frac{\partial \phi_b(t)}{\partial t}\right.\right\rangle \\ &- \sum_{ija} \mathcal{P}_{ij}C_{ia}^{\eta}(t)C_{ja}^{\theta}(t)\left\langle \phi_j(t)\left|\frac{\partial \phi_i(t)}{\partial t}\right.\right\rangle . \end{aligned} \tag{3.1.25}$$

Finally, TDNAC is numerically computed by applying the finite difference approximation to the derivatives in Eq. 3.1.25 as

$$\frac{\partial C_{ia}^{\theta}(t)}{\partial t} \rightarrow \frac{1}{\Delta t}\left(C_{ia}^{\theta}(t+\Delta t) - C_{ia}^{\theta}(t)\right), \tag{3.1.26}$$

$$\left\langle \phi_p(t)\left|\frac{\partial \phi_q(t)}{\partial t}\right.\right\rangle \rightarrow \frac{1}{\Delta t}\left\langle \phi_p(t)\left|\phi_q(t+\Delta t)\right.\right\rangle . \tag{3.1.27}$$

Note that the phase (sign) of each orbital wavefunction is arbitrary, and the order of the orbital energy levels, on which the orbital indices are based, may change in association with the time propagation of the nuclear coordinates. To keep the sign of the orbitals constant and to track the appropriate orbital, Ref. [3] proposed the use of a permutation matrix $\mathbf{O}$, the elements of which are defined as:

$$O_{pq} = \begin{cases} 1 & \left\langle \phi_p(t)\left|\phi_q(t+\Delta t)\right.\right\rangle > 0.5 \\ -1 & \left\langle \phi_p(t)\left|\phi_q(t+\Delta t)\right.\right\rangle < -0.5 \cdot \\ 0 & \text{otherwise} \end{cases} \tag{3.1.28}$$

The sign and order of the orbitals are permutated based on $\mathbf{O}$, and the CIS coefficients are corrected accordingly, prior to numerical differentiation (Eqs. 3.1.26 and 3.1.27).

3.2 Large-Scale NA-MD Technique with DC Type Excited-State Calculations[†]

3.2.1 Introduction

In the condensed phase, dynamics of nonadiabatic systems is inevitably affected by interactions with the environment, such as solvent molecules or ligands. The nonadiabatic dynamics is modulated by exchange of energy and electrons with the environment. For instance, Marcus theory compactly illustrates that the rate of an electron transfer reaction is controlled by the probability of the nonadiabatic transition and how it is affected by the interaction with the solvent.[13] Atoms (chemical species) are also exchanged if chemical reactions, e.g., proton transfer, are involved. This background strongly suggests the importance of techniques for simulating nonadiabatic dynamics capable of simultaneously treating not only the active site, but also the environment, which is still challenging because of the severe computational cost arising from the system size.

The trajectory surface hopping method[14] is a widely accepted approach for simulating nonadiabatic dynamics, in which the nuclear dynamics involving multiple PESs is approximated in a statistical manner based on a set of classical trajectories. Propagation of each classical nuclear trajectory is performed according to the atomic force calculated from the energy derivative at the current active state, which stochastically hops to another state. Because of its computational efficiency and compatibility with well-established electronic structure methods for excited states such as linear response TD-DFT,[15–19] The trajectory surface hopping is extensively utilized to treat nonadiabatic dynamics in the context of quantum chemistry. There are several variations of trajectory surface hopping techniques, including decoherence-induced-surface hopping[20] and Zhu–Nakamura theory approach.[21–24] Among them, the FSSH method, proposed by Tully,[6] is the most widely used method owing to the suitable compromise between the accuracy and cost.[25,26] The name of the technique originates from its characteristics, where the probability of hopping is calculated to minimize the number of hopping events.

[†]Reproduced from Ref. [1], with the permission of AIP Publishing.

Typically, there are two computational bottlenecks in the FSSH. The first is the calculation of the adiabatic excited-state energy, energy gradient, and the corresponding wavefunctions. The second is the calculation of the NAC terms, which is required to propagate the electronic (quantum) DOFs. In recent years, the available system size of the FSSH has been extended by combination with TD-DFTB method.[10,11,27,28] TD-DFTB[29] is a low-cost semi-empirical excited-state calculation technique that is based on the ground-state counterpart, i.e., the DFTB method.[30–33] Successful application of the TD-DFTB-based FSSH has been reported for a variety of targets, including cycloparaphenylene,[28] polyacene derivatives,[34,35] adenine in a water cluster,[10] and silver nanorods.[36]

This section presents a large-scale NA-MD methodology, in which DC-TD-DFTB is combined with the FSSH method. The rest of this section is organized as follows: Subsection 3.2.2 describes the theoretical aspects, focusing on the formulation of the NAC calculation algorithms in the framework of DC-TD-DFTB. The results of the numerical tests are reported in Subsection 3.2.3. Subsection 3.2.3 describes the details of the computational setup. Subsection 3.2.3 compares the DC-TD-DFTB-based NAC value with that from the conventional (TD-DFTB-based) calculation, and evaluate the accuracy of the proposed method. The advantages of the developed approach for enhancing the numerical stability is also discussed. Moreover, as a pilot application, DC-TD-DFTB-based FSSH simulations are performed for a thymine molecule in acetonitrile solution. Subsection 3.2.3 compares the computational time required for the DC-TD-DFTB-based method versus the conventional method. Subsection 3.2.4 summarizes the study.

3.2.2 Theory

The scope of the theory described in this subsection is limited to singlet excited states with spin-restricted reference. In the present DC-TD-DFTB/FSSH approach, FSSH simulations (Subsection 3.1.1) are conducted using the adiabatic potential energies, adiabatic wavefunctions, and TDNACs, obtained in the framework of DC-TD-DFTB. The DC-TD-DFTB calculations of adi-

abatic potential energies and wavefunctions were described in Subsection 2.3.2. Here, TDNAC calculation algorithms with DC-TD-DFTB are presented.

TDNAC Calculation in DC Scheme: WO Approach

For TD-DFTB without DC (Subsection 3.1.2), the wavefunction overlap is obtained on the basis of the overlap between the Slater determinants for the excitation configurations, which is equal to $\det(\mathbf{\Sigma}[ia, jb])$ (Eq. 3.1.11). In the case of DC-TD-DFTB, the analogue of the matrix $\mathbf{\Sigma}[ia, jb]$ can be defined as:

$$\mathbf{\Sigma}_{\mathrm{DC}}[ia, jb] = \begin{pmatrix} {}^{\alpha\alpha}\mathbf{\Sigma}_{\mathrm{DC}}[ia, jb] & {}^{\alpha\beta}\mathbf{\Sigma}_{\mathrm{DC}}[ia, jj] \\ {}^{\beta\alpha}\mathbf{\Sigma}_{\mathrm{DC}}[ii, jb] & {}^{\beta\beta}\mathbf{\Sigma}_{\mathrm{DC}}[ii, jj] \end{pmatrix}, \tag{3.2.1}$$

where

$${}^{\sigma\tau}\mathbf{\Sigma}_{\mathrm{DC}}[ip, jq] =$$

$$\begin{pmatrix} \langle\phi_1(t_1)\,|\,\phi_1(t_2)\rangle\langle\sigma\,|\,\tau\rangle & \dots & \overline{\left\langle\phi_1(t_1)\,\middle|\,\phi_q(t_2)\right\rangle\langle\sigma\,|\,\tau\rangle} & \dots & \langle\phi_1(t_1)\,\big|\,\phi_{n_{\mathrm{O}}(t_2)}(t_2)\rangle\langle\sigma\,|\,\tau\rangle \\ \vdots & & \vdots & & \vdots \\ \underline{\left\langle\phi_p(t_1)\,\middle|\,\phi_1(t_2)\right\rangle\langle\sigma\,|\,\tau\rangle} & \dots & \overline{\underline{\left\langle\phi_p(t_1)\,\middle|\,\phi_q(t_2)\right\rangle\langle\sigma\,|\,\tau\rangle}} & \dots & \underline{\left\langle\phi_p(t_1)\,\middle|\,\phi_{n_{\mathrm{O}}(t_2)}(t_2)\right\rangle\langle\sigma\,|\,\tau\rangle} \\ \vdots & & \vdots & & \vdots \\ \left\langle\phi_{n_{\mathrm{O}}(t_1)}(t_1)\,\middle|\,\phi_1(t_2)\right\rangle\langle\sigma\,|\,\tau\rangle & \dots & \overline{\left\langle\phi_{n_{\mathrm{O}}(t_1)}(t_1)\,\middle|\,\phi_q(t_2)\right\rangle\langle\sigma\,|\,\tau\rangle} & \dots & \langle\phi_{n_{\mathrm{O}}(t_1)}(t_1)\,\big|\,\phi_{n_{\mathrm{O}}(t_2)}(t_2)\rangle\langle\sigma\,|\,\tau\rangle \end{pmatrix}, \tag{3.2.2}$$

regarding the localization region $\mathcal{L}^s$, which includes the excitation center. Note that n_{O} is time-dependent in the DC scheme, because the buffer region around the excitation center is re-defined for each nuclear time step based on the current atomic coordinates, as schematically shown in Fig. 3.1. In Fig. 3.1(a), the subsystem represented by the red-colored circle is included in $\mathcal{L}^s$ at t_1 and remains included in it at t_2. Fig. 3.1(b) shows the case in which the subsystem is not included at t_1, but is newly included at t_2. On the other hand, in Fig. 3.1(c), the subsystem is included at t_1, but not at t_2. In the following discussion, the situations corresponding to Figs. 3.1(a), 3.1(b), and 3.1(c) are called in-in, out-in, and in-out, respectively.

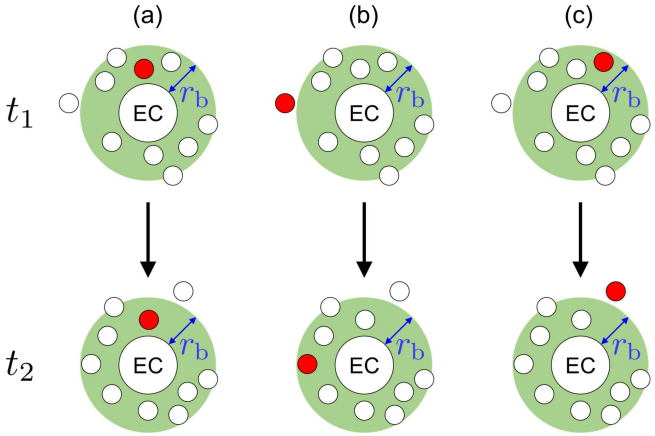

Fig. 3.1: Schematic illustration of buffer region update in the DC scheme. White and red circles indicate subsystems; the area marked as EC is the central region corresponding to the excitation center. Green-colored region is the buffer region with a buffer radius of r_b. (a) Red-colored subsystem is included in the buffer region at t_1, and remains included at t_2 (in-in). (b) Red-colored subsystem is not included in the buffer region at t_1, but is newly included at t_2 (out-in). (c) Red-colored subsystem is included in the buffer region at t_1, but is not included at t_2 (in-out).

When $\mathcal{L}^s(t_1) \neq \mathcal{L}^s(t_2)$, i.e., out-in or in-out subsystems exist, the wavefunction overlap calculations become problematic. In this case, $\mathbf{\Sigma}_{\mathrm{DC}}[ia, jb]$ is not squared in general; thus, $\det(\mathbf{\Sigma}_{\mathrm{DC}}[ia, jb])$ cannot be defined. Even if $\mathbf{\Sigma}_{\mathrm{DC}}[ia, jb]$ becomes squared by coincidence, it is effectively not a regular matrix, i.e., $\det(\mathbf{\Sigma}_{\mathrm{DC}}[ia, jb])$ is essentially zero. This is because the orbitals arising from in-out(out-in) subsystems at $t_1(t_2)$ do not overlap significantly with any orbitals at $t_2(t_1)$; in other words, all the elements in the rows(columns) of $\mathbf{\Sigma}_{\mathrm{DC}}[ia, jb]$ corresponding to these orbitals are approximately zero.

From another perspective, $\mathbf{\Sigma}[ia, jb]$ or $\mathbf{\Sigma}_{\mathrm{DC}}[ia, jb]$ can be seen as a transformation matrix from the space spanned by the orbitals that constitute $\Phi_j^b(t_2)$ to the space spanned by the component orbitals of $\Phi_i^a(t_1)$ (Fig. 3.2). In the case of TD-DFTB without DC, $\det(\mathbf{\Sigma}[ia, jb])$ is always well-defined and generally non-zero because the transformation is one-to-one correspondence. However, in the case of DC-TD-DFTB, the transformation is no longer one-to-one correspondence when $\mathcal{L}^s(t_1) \neq \mathcal{L}^s(t_2)$. The orbitals arising from the out-in subsystems at t_2 do not correspond to any orbitals at t_1. In the case of the in-out subsystems, the opposite is true. Therefore, $\det(\mathbf{\Sigma}_{\mathrm{DC}}[ia, jb])$ is either essentially zero, which is physically meaningless, or undefined.

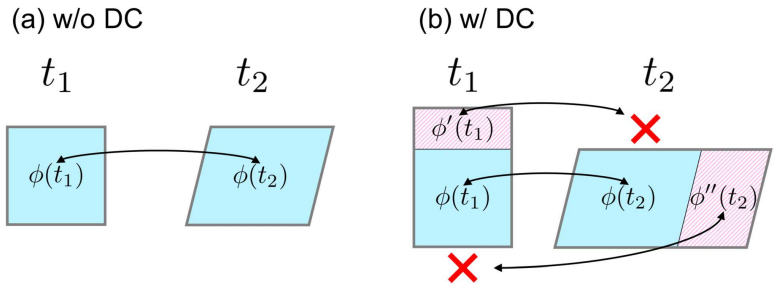

Fig. 3.2: Schematic illustration of the relationship between the orbital space regarding Φ_i^a at t_1 and Φ_j^b at t_2. (a) Without DC, the transformation between the t_1 and t_2 orbital spaces ($\mathbf{\Sigma}[ia, jb]$) can be one-to-one correspondence. (b) With DC, the one-to-one correspondence can be maintained only within the subspace indicated by the blue-colored region. Orbitals in the red-colored region at $t_1(t_2)$ are not mapped to any orbital at $t_2(t_1)$.

Here, one can construct a subspace in which the one-to-one correspondence character of the transformation $\mathbf{\Sigma}_{\mathrm{DC}}[ia, jb]$ can be maintained, where the subspace is called common space, and its complement is called uncommon space, by the following procedure. Let $\mathbf{\Sigma}^{\mathrm{O}}$ and $\mathbf{\Sigma}^{\mathrm{V}}$ be the MO overlap matrices for the occupied and virtual spaces, respectively, where the matrix elements are defined as:

$$\Sigma_{ij}^{\mathrm{O}} = \left\langle \phi_i(t_1) \middle| \phi_j(t_2) \right\rangle, \quad \Sigma_{ab}^{\mathrm{V}} = \langle \phi_a(t_1) | \phi_b(t_2) \rangle . \tag{3.2.3}$$

SVD of the occupied or virtual MO overlap matrices

$$\mathbf{\Sigma}^{\mathrm{O/V}} = \mathbf{U}^{\mathrm{O/V}} \mathbf{\Lambda}^{\mathrm{O/V}} \mathbf{V}^{\mathrm{O/V}\dagger}, \tag{3.2.4}$$

produces sets of orbitals at t_1 and t_2, which are represented by the matrices $\mathbf{U}^{\mathrm{O/V}}$ and $\mathbf{V}^{\mathrm{O/V}}$, respectively, in the canonical MO basis. The obtained orbitals are hereafter called SOs. Each set of orbitals is orthonormal, and spans the same space as spanned by the corresponding (either occupied or virtual, at either t_1 or t_2) set of MOs. Note that the SVD is performed for the occupied and virtual spaces separately. The matrix $\mathbf{\Lambda}^{\mathrm{O/V}}$ contains the set of corresponding singular values

$$\Lambda_{pq}^{\mathrm{O/V}} = \begin{cases} \lambda_p^{\mathrm{O/V}} & p = q \ \wedge \ p \leq n'_{\mathrm{O/V}} \\ 0 & \text{otherwise} \end{cases}, \tag{3.2.5}$$

where $n'_{\mathrm{O/V}} = \min\{n_{\mathrm{O/V}}(t_1), n_{\mathrm{O/V}}(t_2)\}$. The singular values are sorted in descending order: $\lambda_1 > \lambda_2 > \cdots > \lambda_{n'_{\mathrm{O/V}}}$. Here, one can define a new set of SOs that contain only the SOs having singular values close to unity

$$\tilde{\mathbf{U}}^{\mathrm{O/V}} = \begin{pmatrix} \mathbf{u}_1^{\mathrm{O/V}} & \mathbf{u}_2^{\mathrm{O/V}} & \cdots & \mathbf{u}_{\tilde{n}'_{\mathrm{O/V}}}^{\mathrm{O/V}} \end{pmatrix}, \tag{3.2.6}$$

$$\tilde{\mathbf{V}}^{\mathrm{O/V}} = \begin{pmatrix} \mathbf{v}_1^{\mathrm{O/V}} & \mathbf{v}_2^{\mathrm{O/V}} & \cdots & \mathbf{v}_{\tilde{n}'_{\mathrm{O/V}}}^{\mathrm{O/V}} \end{pmatrix}, \tag{3.2.7}$$

where $\mathbf{u}_p^{\mathrm{O/V}}$ and $\mathbf{v}_q^{\mathrm{O/V}}$ are the p-th column vectors in the matrices $\mathbf{U}^{\mathrm{O/V}}$ and $\mathbf{V}^{\mathrm{O/V}}$, respectively, and represent the p-th SOs at t_1 and t_2, respectively. $\tilde{n}'_{\mathrm{O/V}}$ is the number of singular values that satisfy $\lambda_p^{\mathrm{O/V}} > \lambda^{\mathrm{thresh}}$, where $\lambda^{\mathrm{thresh}}$ is a given threshold constant. The common space is defined as the space expanded by the new set of SOs, i.e., $\tilde{\mathbf{U}}^{\mathrm{O/V}}$ or $\tilde{\mathbf{V}}^{\mathrm{O/V}}$.

On the basis of the common/uncommon spaces, the CIS state overlap in the case of DC-TD-DFTB can be calculated as follows. The CIS coefficient matrices at t_1 and t_2 can be represented using the SOs at each time as:

$$\mathbf{C}'^{\eta}(t_1) = \mathbf{U}^{\mathrm{O}}\mathbf{C}^{\eta}(t_1)\mathbf{U}^{\mathrm{V}\dagger}, \tag{3.2.8}$$

$$\mathbf{C}'^{\theta}(t_2) = \mathbf{V}^{\mathrm{O}}\mathbf{C}^{\theta}(t_2)\mathbf{V}^{\mathrm{V}\dagger}, \tag{3.2.9}$$

respectively. Note that $\mathbf{C}'^{\eta}(t)$ is an $n_{\mathrm{O}}(t) \times n_{\mathrm{V}}(t)$ matrix, where $n_{\mathrm{V}}(t)$ is the number of virtual orbitals at the time t. Therefore, the adiabatic wavefunctions at t are represented as:

$$\psi_\eta(t) = \sum_{ia} C'^{\eta}_{ia}(t)\Phi'^{a}_{i}(t), \tag{3.2.10}$$

where $\Phi'^{a}_{i}(t)$ is the Slater determinant for the single excitation configuration from the i-th occupied SO to the a-th virtual SO. Note that the uncommon space arises from the incorporation of out-in or in-out subsystems. The out-in and in-out subsystems cross over the outer boundary of the buffer region around the excitation center in the time step of Δt. This fact indicates that these subsystems are located near the outer boundary, which is expected to be apart from

the excitation center; thus, their contribution to the excitation energy and excitation amplitude can be neglected. Therefore, it can be safely assumed that the excitation character is described within the common space and the uncommon space has negligible contribution. $\tilde{\psi}_\eta(t)$, which is the approximate expression of $\psi_\eta(t)$ within the common space, is defined as

$$\tilde{\psi}_\eta(t) = \sum_{ia} \tilde{C}'^{\eta}_{ia}(t)\tilde{\Phi}'^{a}_{i}(t), \tag{3.2.11}$$

where $\tilde{C}'^{\eta}_{ia}(t) = C'^{\eta}_{ia}(t)$ but the range of orbital indices is restricted to the $1 \leq i \leq \tilde{n}'_{\mathrm{O}}$ and $1 \leq a \leq \tilde{n}'_{\mathrm{V}}$, i.e., $\tilde{\mathbf{C}}'^{\eta}(t)$ is an $\tilde{n}'_{\mathrm{O}} \times \tilde{n}'_{\mathrm{V}}$ matrix. $\tilde{\Phi}'^{a}_{i}(t)$ is the Slater determinant corresponding to the single excitation configuration from the i-th occupied SO to the a-th virtual SO, where the reference configuration $\tilde{\Phi}'(t)$ is constituted by the set of $\tilde{n}'_{\mathrm{O}}$ occupied SOs, which spans the occupied common space at t. The wavefunction overlap in DC-TD-DFTB can be defined as the wavefunction overlap calculated within the common space, namely

$$S^{\mathrm{DC}}_{\eta\theta}(t_1, t_2) = \left\langle \tilde{\psi}_\eta(t_1) \middle| \tilde{\psi}_\theta(t_2) \right\rangle \tag{3.2.12}$$

$$= \sum_{ia,jb} \tilde{C}'^{\eta}_{ia}(t_1)\tilde{C}'^{\theta}_{jb}(t_2) \times \left\langle \tilde{\Phi}'^{a}_{i}(t_1) \middle| \tilde{\Phi}'^{b}_{j}(t_2) \right\rangle, \tag{3.2.13}$$

where the overlap between the Slater determinants is calculated as:

$$\left\langle \tilde{\Phi}'^{a}_{i}(t_1) \middle| \tilde{\Phi}'^{b}_{j}(t_2) \right\rangle = \det\left(\tilde{\mathbf{\Sigma}}'[ia, jb]\right). \tag{3.2.14}$$

The matrix $\tilde{\mathbf{\Sigma}}'[ia, jb]$ is an analogue of $\mathbf{\Sigma}[ia, jb]$, and is defined as

$$\tilde{\mathbf{\Sigma}}'[ia, jb] = \begin{pmatrix} {}^{\alpha\alpha}\tilde{\mathbf{\Sigma}}'[ia, jb] & {}^{\alpha\beta}\tilde{\mathbf{\Sigma}}'[ia, jj] \\ {}^{\beta\alpha}\tilde{\mathbf{\Sigma}}'[ii, jb] & {}^{\beta\beta}\tilde{\mathbf{\Sigma}}'[ii, jj] \end{pmatrix}, \tag{3.2.15}$$

where

$$
{}^{\sigma\tau}\tilde{\mathbf{\Sigma}}'[ip, jq] =
$$

$$
\begin{pmatrix}
\left\langle \phi'_1(t_1) \middle| \phi'_1(t_2) \right\rangle \langle \sigma \,|\, \tau \rangle & \dots & \overline{\left\langle \phi'_1(t_1) \middle| \phi'_q(t_2) \right\rangle \langle \sigma \,|\, \tau \rangle} & \dots & \left\langle \phi'_1(t_1) \middle| \phi'_{\tilde{n}'_\mathrm{O}}(t_2) \right\rangle \langle \sigma \,|\, \tau \rangle \\
\vdots & & \vdots & & \vdots \\
\underline{\left\langle \phi'_p(t_1) \middle| \phi'_1(t_2) \right\rangle \langle \sigma \,|\, \tau \rangle} & \dots & \underline{\overline{\left\langle \phi'_p(t_1) \middle| \phi'_q(t_2) \right\rangle \langle \sigma \,|\, \tau \rangle}} & \dots & \underline{\left\langle \phi'_p(t_1) \middle| \phi'_{\tilde{n}'_\mathrm{O}}(t_2) \right\rangle \langle \sigma \,|\, \tau \rangle} \\
\vdots & & \vdots & & \vdots \\
\left\langle \phi'_{\tilde{n}'_\mathrm{O}}(t_1) \middle| \phi'_1(t_2) \right\rangle \langle \sigma \,|\, \tau \rangle & \dots & \overline{\left\langle \phi'_{\tilde{n}'_\mathrm{O}}(t_1) \middle| \phi'_b(t_2) \right\rangle \langle \sigma \,|\, \tau \rangle} & \dots & \left\langle \phi'_{\tilde{n}'_\mathrm{O}}(t_1) \middle| \phi'_{\tilde{n}'_\mathrm{O}}(t_2) \right\rangle \langle \sigma \,|\, \tau \rangle
\end{pmatrix}. \tag{3.2.16}
$$

Note that $\tilde{\mathbf{\Sigma}}'[ia, jb]$ is a $2\tilde{n}'_\mathrm{O} \times 2\tilde{n}'_\mathrm{O}$ squared matrix of rank $2\tilde{n}'_\mathrm{O}$. The matrix elements in ${}^{\sigma\tau}\tilde{\mathbf{\Sigma}}'[ip, jq]$ can be calculated as

$$
\left\langle \phi'_p(t_1) \middle| \phi'_q(t_2) \right\rangle = \sum_{rs} u_{pr}^{\mathrm{O/V}} v_{qs}^{\mathrm{O/V}} \langle \phi_r(t_1) \,|\, \phi_s(t_2) \rangle \,, \tag{3.2.17}
$$

$$
\langle \sigma \,|\, \tau \rangle = \begin{cases} 1 & \sigma = \tau \\ 0 & \sigma \neq \tau \end{cases}, \tag{3.2.18}
$$

where the superscript O/V over u_{pr} takes O or V when the $\phi'_p(t_1)$ is an occupied or a virtual SO, respectively. The same convention is applied for the superscript over v_{qs} depending on whether $\phi'_q(t_2)$ is occupied or virtual. Because the α–β and β–α parts vanish, $\tilde{\mathbf{\Sigma}}[ia, jb]$ becomes block diagonal and the determinant in Eq. 3.2.14 can be calculated as:

$$
\det\left(\tilde{\mathbf{\Sigma}}'[ia, jb]\right) = \det\left({}^{\alpha\alpha}\tilde{\mathbf{\Sigma}}'[ia, jb]\right) \times \det\left({}^{\beta\beta}\tilde{\mathbf{\Sigma}}'[ii, jj]\right). \tag{3.2.19}
$$

Finally, as done in the case of TD-DFTB (Subsection 3.1.2), TDNAC can be obtained from the wavefunction overlap through the finite difference approximation (Eq. 3.1.9).

In principle, the CPU time for calculation of $S_{\eta\theta}^{\mathrm{DC}}$ according to Eq. 3.2.13 scales as

$O\left(\left[\tilde{n}'_{\mathrm{O}}\right]^5\left[\tilde{n}'_{\mathrm{V}}\right]^2\right)$, because the scaling for the numerical computation of each $\det\left(\tilde{\mathbf{\Sigma}}'_{\mathrm{DC}}[ia, jb]\right)$ is $O\left(\left[\tilde{n}'_{\mathrm{O}}\right]^3\right)$. The scaling of the power of seven suggests severe computational burden even if the DC method is applied. Here, the efficient computation scheme proposed by Sapunar and co-workers[37] for this type of wavefunction overlap, which is based on the NTO concept,[38] is employed. NTOs are orbitals obtained by SVD of the CIS coefficient matrix. For the approximate CIS coefficient matrix within the common space, $\tilde{\mathbf{C}}'^{\eta}$, the corresponding set of NTOs is obtained as:

$$\tilde{\mathbf{C}}'^{\eta} = \grave{\mathbf{U}}^{\eta}\grave{\mathbf{\Lambda}}^{\eta}\grave{\mathbf{V}}^{\eta\dagger}, \tag{3.2.20}$$

where $\grave{\mathbf{U}}^{\eta}$ and $\grave{\mathbf{V}}^{\eta}$ contain the occupied and virtual NTOs, respectively, which are represented by the SOs within the common space, and

$$\grave{\Lambda}^{\eta}_{pq} = \begin{cases} \grave{\lambda}^{\eta}_{p} & p = q \ \wedge \ p \leq \grave{n} \\ 0 & \text{otherwise} \end{cases}, \tag{3.2.21}$$

where $\grave{n}$ is the number of NTOs, and here $\grave{n} = \min\left\{\tilde{n}'_{\mathrm{O}}, \tilde{n}'_{\mathrm{V}}\right\}$. The adiabatic wavefunction is represented as:

$$\tilde{\psi}_{\eta}(t) = \sum_{p} \grave{\lambda}^{\eta}_{p}\grave{\Phi}^{\eta}_{p}, \tag{3.2.22}$$

where $\grave{\Phi}^{\eta}_{p}$ is the Slater determinant corresponding to the single excitation configuration from the p-th occupied NTO to the p-th virtual NTO at the state η. Using the NTO representation, the wavefunction overlap is rewritten as:

$$\begin{aligned} S^{\mathrm{DC}}_{\eta\theta}(t_1, t_2) = &\sum_{p,q} \grave{\lambda}^{\eta}_{p}(t_1)\grave{\lambda}^{\theta}_{q}(t_2) \\ &\times \left\langle \grave{\Phi}^{\eta}_{p}(t_1) \middle| \grave{\Phi}^{\theta}_{q}(t_2) \right\rangle. \end{aligned} \tag{3.2.23}$$

Here, the overlap between the Slater determinants on the RHS is calculated in a manner similar to that used in Eq. 3.2.14, i.e., computing the determinant of the overlap matrix between the

NTOs that constitute $\grave{\Phi}_p(t_1)$ and $\grave{\Phi}_q(t_2)$. Therefore, the scaling becomes $O\left(\grave{n}^2\left[\tilde{n}'_{\mathrm{O}}\right]^3\right)$, which is a significant cut of the computational cost. Note that a set of NTOs is defined for each adiabatic state, i.e., the overall computational cost increases by the square of the number of adiabatic states of interest. Because the number of states is normally significantly smaller than that of the occupied or virtual orbitals, this shortcoming does not obviate the advantage of the NTO-based approach in terms of computational efficiency. The calculation can be further accelerated by neglecting the configurations with small absolute values of the coefficient $\grave{\lambda}_p^{\eta}(t)$ based on a threshold value $\grave{C}^{\mathrm{thresh}}$.

TDNAC Calculation in DC Scheme: OD Approach

For essentially the same reason as that discussed in the case of the WO approach, it is obvious that the OD method cannot be directly applied to the DC-TD-DFTB when $\mathcal{L}^s(t_1) \neq \mathcal{L}^s(t_2)$. Alternatively, TDNAC is calculated within the common space for the case of DC-TD-DFTB.

$$\sigma_{\eta\theta}^{\mathrm{DC}}(t) = \left\langle \tilde{\psi}_{\eta}(t) \middle| \frac{\partial \tilde{\psi}_{\theta}(t)}{\partial t} \right\rangle. \tag{3.2.24}$$

Using a procedure similar to that used for the transformation from Eq. 3.1.21 to Eq. 3.1.25, $\sigma_{\eta\theta}^{\mathrm{DC}}$ can be expressed in the similar form to Eq. 3.1.25, where the CIS coefficients and orbitals are replaced by their counterparts in the common space formalism

$$\begin{aligned}\sigma_{\eta\theta}^{\mathrm{DC}}(t) = &\sum_{ia} \tilde{C}'^{\eta}_{ia}(t) \frac{\partial \tilde{C}'^{\theta}_{ia}(t)}{\partial t} \\ &+ \sum_{iab} \tilde{C}'^{\eta}_{ia}(t) \tilde{C}'^{\theta}_{ib}(t) \left\langle \phi'_a(t) \middle| \frac{\partial \phi'_b(t)}{\partial t} \right\rangle \\ &- \sum_{ija} \mathcal{P}_{ij} \tilde{C}'^{\eta}_{ia}(t) \tilde{C}'^{\theta}_{ja}(t) \left\langle \phi'_j(t) \middle| \frac{\partial \phi'_i(t)}{\partial t} \right\rangle. \end{aligned} \tag{3.2.25}$$

The derivatives of the CIS coefficients and orbitals in Eq. 3.2.25 are numerically calculated using the analogues of Eqs. 3.1.26 and 3.1.27, respectively.

$$\frac{\partial \tilde{C}'^{\theta}_{ia}(t)}{\partial t} \to \frac{1}{\Delta t}\left(\tilde{C}'^{\theta}_{ia}(t+\Delta t) - \tilde{C}'^{\theta}_{ia}(t)\right), \tag{3.2.26}$$

$$\left\langle \phi'_p(t) \middle| \frac{\partial \phi'_q(t)}{\partial t} \right\rangle \to \frac{1}{\Delta t}\left\langle \phi'_p(t) \middle| \phi'_q(t+\Delta t) \right\rangle. \tag{3.2.27}$$

3.2.3 Numerical Tests

Computational Details

The TDNAC calculation algorithms and FSSH routine with TD-DFTB and DC-TD-DFTB methods were implemented in the developmental version of DCDFTBMD code.[39] Benchmark calculations were performed using acetonitrile solutions of thymine (Fig. 3.3) as target systems. Cubic simulation cells were used with application of the periodic boundary condition, where the electrostatic interaction among the atomic Mulliken charges were treated with Ewald summation.[40] Because the calculations were conducted with several different numbers of solvent molecules, hereinafter, the model systems are specified as thymine + $n\,CH_3CN$, where n is the number of acetonitrile molecules in the system. For each model system, n was determined to adjust the density to that of pure acetonitrile based on the given volume of the cell; the resulting density was in the range of 0.7829 to 0.7868 $g\,cm^{-3}$. Initial equilibration was conducted for 2.0 ns or longer with classical MD, followed by an equilibration run with (DC-)DFTB-MD for 2.0 ps. Both equilibration steps were conducted with the NVT ensemble using the time step of 0.5 fs. The classical MD simulations were conducted using GROMACS code[41] with the general AMBER force field.[42] For the DC-(TD-)DFTB calculations, each single molecule was treated as a subsystem, and the thymine molecule was chosen as the excitation center. According to a previous study,[43] the buffer radius r_b was set to 6.0 Å, and all DFTB calculations including excited-state calculations, with or without DC, were performed at the DFTB2 level[33] using the 3OB parameter set.[44] In the excited-state calculations, the two lowest singlet excited states were

solved. The threshold for singular values, λ^{thresh}, was set to 0.99.

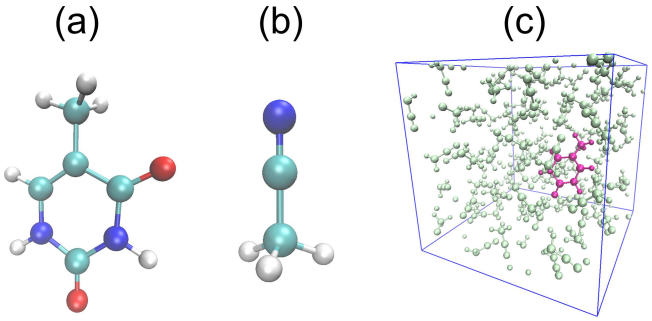

Fig. 3.3: Chemical structures of (a) thymine and (b) acetonitrile molecules. The white, cyan, blue, and red spheres indicate H, C, N, and O, respectively. (c) Snapshot of thymine acetonitrile solution system obtained in DFTB-MD run with *NVT* ensemble. The system contains one thymine molecule (magenta) and 89 acetonitrile molecules (light green) in the 2 nm × 2 nm × 2 nm periodic box, indicated by blue solid lines.

Accuracy of DC-based Treatment

For the thymine + 89 CH_3CN system, the time course change of the TDNAC calculated using TD-DFTB and DC-TD-DFTB are compared in Fig. 3.4 for the WO and OD methods. The WO-based TDNAC calculations were performed in the NTO representation with or without the DC scheme.[37] The threshold for the absolute value of the CIS coefficients, $\grave{C}^{\text{thresh}}$, was set to 1.0×10^{-2}. For the OD-based TDNAC calculations, the SO representation was used for both DC-TD-DFTB and TD-DFTB. The nuclear trajectory was pre-determined and externally given, and thus was exactly the same in all of the four (TD-DFTB or DC-TD-DFTB, and WO or OD) aforementioned conditions. The trajectory was obtained by a ground-state DFTB-MD simulation using the *NVT* ensemble with a time step of 0.5 fs. Note that this treatment was only applied to the numerical validation of TDNAC itself; in the FSSH simulations, which are reported later in this subsection, the nuclear coordinates were propagated according to the atomic force on the PES of the active state at each nuclear time step. In Fig. 3.4, the TD-DFTB result (blue, solid line) and the DC-TD-DFTB result (orange, dotted line) overlap with each other, indicating satisfactory agreement of these two results. Hence, it can be concluded that the TDNAC determined with DC-TD-DFTB is sufficiently accurate compared with that obtained using TD-DFTB. In addition, from Fig. 3.4, it can be deduced that the WO and OD results are consistent with each other. Note that the common-space-based method can treat

the case of $\mathcal{L}^s(t_1) \neq \mathcal{L}^s(t_2)$ in DC-TD-DFTB calculations, where the conventional TDNAC calculation method cannot be applied. In the DC-TD-DFTB calculation, this situation arose 147 times within the simulation time of 500 fs for the given trajectory, as illustrated in Fig. 3.5, suggesting the importance of the present treatment of TDNAC.

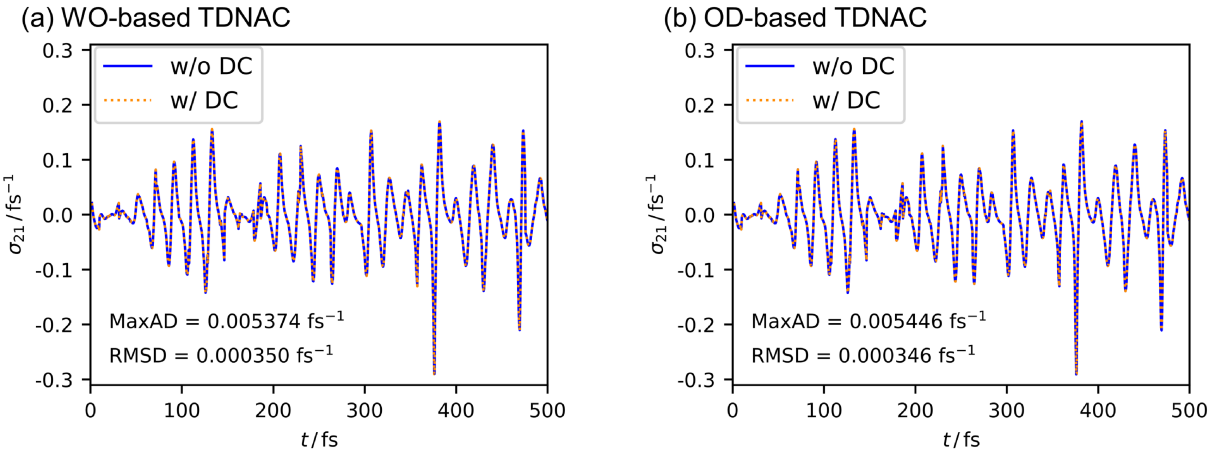

Fig. 3.4: Time course change of σ_{21} calculated using TD-DFTB (blue, solid) and DC-TD-DFTB (orange, dotted), using (a) WO method and (b) OD method, along with pre-determined nuclear trajectory. The MaxAD and RMSD of the DC-TD-DFTB results versus the TD-DFTB results are also shown.

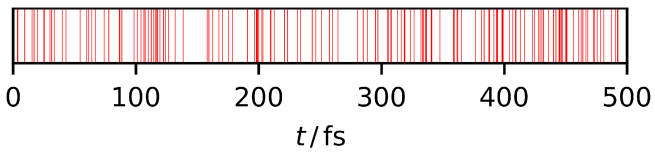

Fig. 3.5: Times at which $\mathcal{L}^s(t_1) \neq \mathcal{L}^s(t_2)$ are indicated by red vertical lines.

FSSH simulations for the thymine+89 CH_3CN system were performed using TD-DFTB and DC-TD-DFTB, without a thermostat. The initial state was chosen to be S_2, and the simplified decay of mixing method was employed for decoherence correction with $\alpha = 0.1$ hartree. The nuclear time step Δt was set to 0.5 fs. The simulations were conducted by using the TDNAC calculated by each of the WO and OD methods. 1740 independent trajectories were simulated for each condition. The set of initial geometries and velocities was collected from the ground-state DFTB-MD or DC-DFTB-MD, for the TD-DFTB-based and DC-TD-DFTB-based simulations, respectively, using the NVT ensemble. The interval between each initial condition was 50 fs or longer. The time course change of the fraction of S_1 and S_2 is shown in Fig. 3.6. According to a previous study,[45] the 95% confidence interval was obtained by using the bootstrap method.

In the bootstrap method, the original data set is resampled N-times with replacement. The uncertainty of a statistical quantity Q can be measured based on a set of N different values of Q obtained from the resampled data sets. In this work, the number of resampling, N, was set to 10^4. As shown in Fig. 3.6, the agreement of the TD-DFTB (solid lines) and DC-TD-DFTB (dashed lines) results was reasonably good for both WO and OD cases. In addition, Fig. 3.7 presents the time course change of potential energy and total (potential plus kinetic) energy for a representative trajectory with DC. Fig. 3.7(a) demonstrates that the DC-TD-DFTB trajectory yields the smooth potential energy, and Fig. 3.7(b) indicates conservation of the total energy at the acceptable level.

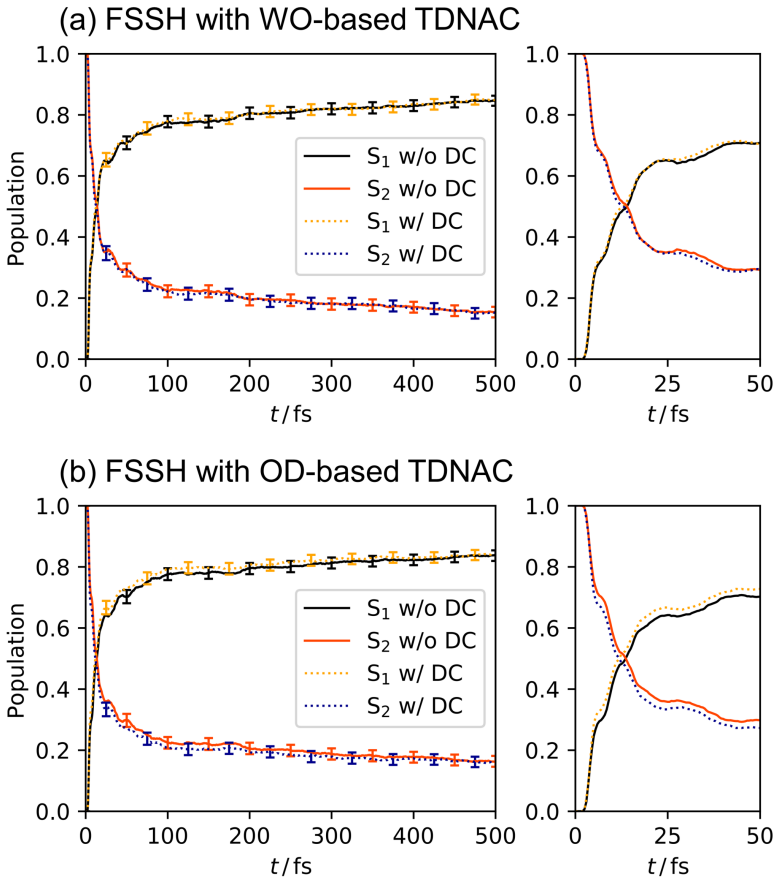

Fig. 3.6: Time course change of S_1 and S_2 populations in FSSH simulations with TD-DFTB (solid) and DC-TD-DFTB (dashed), averaged over 1740 trajectories. Error bars indicate 95% confidence interval obtained with the bootstrap method with resampling of 10^4 times (left). Enlarged views for 0–50 fs are also shown (right). Results obtained with WO method (a) and OD method (b) are indicated.

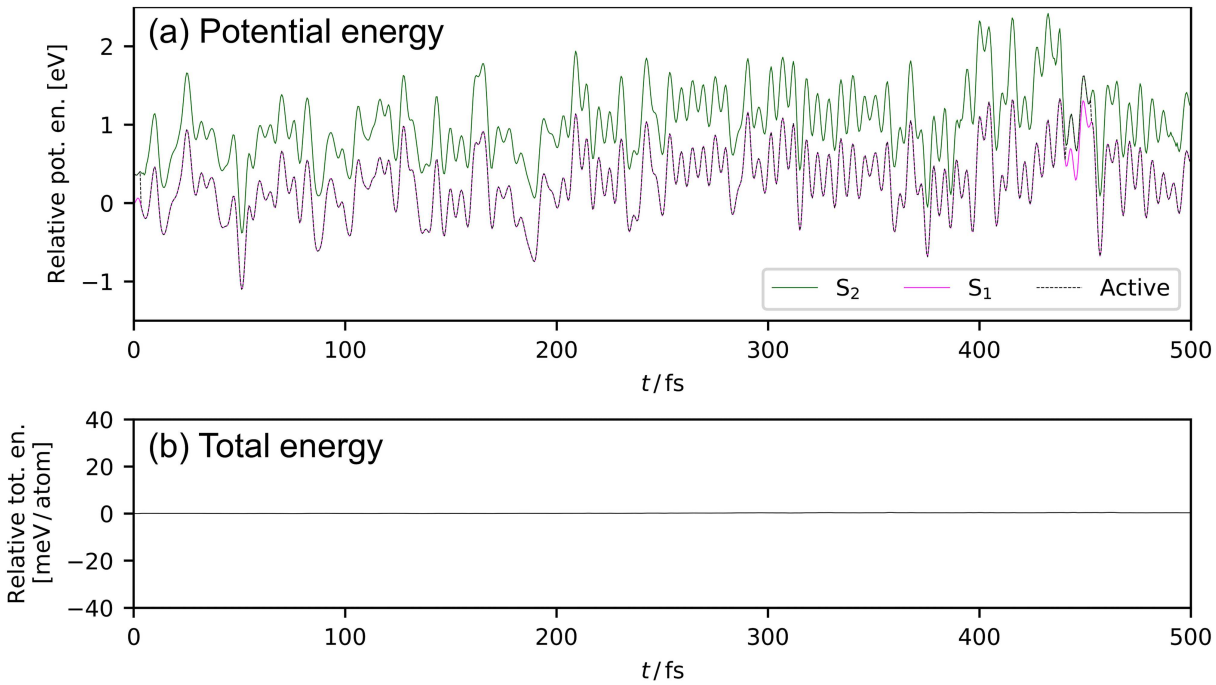

Fig. 3.7: Time course change of (a) potential energy and (b) total energy in a representative trajectory with DC. The potential energy is referenced to that of S_1 state at $t = 0$. The total energy is referenced to the value at $t = 0$.

Efficacy of Singular Orbitals for OD-based TDNAC Calculations

For the OD-based TDNAC calculations, the permutation matrix (**O**) plays a critical role; for each orbital p at t_1, a corresponding orbital q at t_2 must be uniquely assigned by the permutation matrix. This condition is satisfied if and only if the determinant of the permutation matrix is 1 or -1. For the thymine + 89 CH_3CN system and using TD-DFTB without DC, the determinants of the permutation matrix were calculated in the conventional (canonical MO) representation and in the SO representation for various sizes of the time step Δt. The results are listed in Table 3.1, where "Success" indicates that the determinant was 1 or -1; otherwise "Fail" is indicated. The SOs were calculated for TD-DFTB by using the same procedure as used for the DC-TD-DFTB. Table 3.1 indicates that the canonical-MO-based permutation matrix collapses at $\Delta t = 2.0\times10^{-4}$ fs, suggesting that an impossibly small time step is required in the conventional approach. This is because many canonical MOs are found within a very narrow energy window in large systems such as thymine + 89 CH_3CN. This pseudo-degeneracy entails strong mixing among the canonical MOs, even due to the small perturbation originating from the nuclear

displacement in the time step Δt. On the other hand, Table 3.1 shows that the singular-orbital-based permutation matrix is stable up to $\Delta t = 2.0$ fs, which suggests that the construction of the permutation matrix is no longer the factor limiting the size of Δt. In contrast with the canonical MOs, the character of each SO is maintained as long as the orbital space is not drastically changed. Therefore, the present singular-orbital-based approach not only enables the TDNAC calculations in the DC-TD-DFTB, but also overcomes the problem of tracking canonical MOs. In other words, even without the DC scheme, the SO approach is beneficial for OD-based TDNAC calculations, in the sense that Δt can be significantly increased without loss of the numerical stability.

Table 3.1: TD-DFTB results for orbital permutation matrix construction for thymine + 89 CH_3CN system with varying Δt.

Δt / fs	SO	canonical MO (conventional)
5×10^{-5}	Success	Success
1×10^{-4}	Success	Success
2×10^{-4}	Success	Fail
5×10^{-4}	Success	Fail
1×10^{-3}	Success	Fail
2×10^{-3}	Success	Fail
5×10^{-3}	Success	Fail
1×10^{-2}	Success	Fail
2×10^{-2}	Success	Fail
5×10^{-2}	Success	Fail
1×10^{-1}	Success	Fail
2×10^{-1}	Success	Fail
5×10^{-1}	Success	Fail
1	Success	Fail
2	Success	Fail
5	Fail	Fail

Computational Time

The CPU time per nuclear time step for the excitation energy and energy gradient, WO-based TDNAC, and OD-based TDNAC were measured with varying the number of solvent molecules n; the results are shown in Fig. 3.8. The calculations were performed on Intel Xeon Gold 6154 processors. Each data point is the average of the results of eleven runs. Note that the excitation

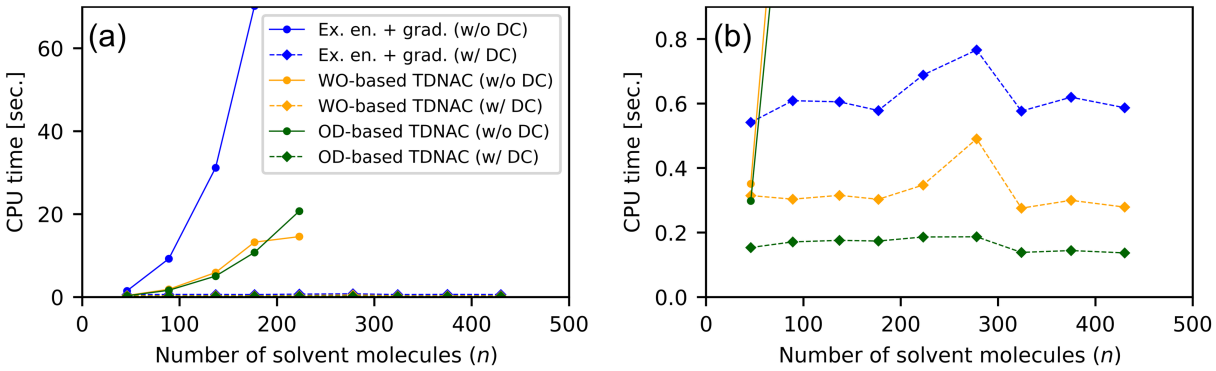

Fig. 3.8: (a) CPU time per nuclear time step for excitation energy and gradient, WO-based TDNAC and OD-based TDNAC are indicated by blue, orange, and green, respectively. TD-DFTB and DC-TD-DFTB results are indicated by circles with solid lines and lozenges with dashed lines, respectively. (b) Enlarged view for the CPU time range of 0 to 0.9 sec.

energy and gradient are always necessary, while one can choose either the WO or OD approach for the TDNAC calculations. The TD-DFTB results are indicated by circles with solid lines. The corresponding DC-TD-DFTB results are indicated by lozenges with dashed lines. As shown in Fig. 3.8, the CPU time for the DC-TD-DFTB calculations is significantly less than that for the TD-DFTB calculations. In addition, while the CPU time in the case of TD-DFTB increases sharply with n, in the case of DC-TD-DFTB the CPU time is constant irrespective of n, suggesting that DC-TD-DFTB can treat excited states and TDNAC in large systems without increasing the computational cost. Note that in the case of DC-TD-DFTB, the ground-state energy and energy gradient are obtained with DC-DFTB, where the computational cost scales linearly with the system size. In addition, the DC-DFTB algorithm is efficient for massively parallelized computations because each subsystem is solved separately.[39,46] Therefore, it is suggested that the DC-TD-DFTB-based FSSH simulations can be applied to huge systems with manageable computational cost.

3.2.4 Conclusion

The DC-TD-DFTB method, which is an extension of the TD-DFTB method for the DC framework, enables large-scale excited-state calculation with low computational cost. In the present study, algorithms for TDNAC calculations with the DC-TD-DFTB method were developed, based on the concept of common/uncommon orbital spaces constructed using SVD of the over-

lap matrix among MOs in the subsequent time steps. The DC-TD-DFTB-based TDNAC calculation algorithm was presented for each of WO and OD approaches. Sufficient accuracy was obtained compared to the corresponding results obtained with the conventional method, i.e., TD-DFTB, in both cases. Moreover, it was found that the SVD-based approach improves the numerical stability of the OD-based TDNAC calculations in the circumstances where the canonical MOs are pseudo-degenerated, which commonly occurs in medium-sized or larger systems; this benefit is relevant not only for the DC-based scheme but also for conventional, non-DC calculations. The developed DC-TD-DFTB-based TDNAC calculation algorithms were combined with the FSSH technique. DC-TD-DFTB-based FSSH simulations of the excited-state dynamics of the thymine molecule in acetonitrile solutions were conducted, and reasonable results were obtained. The benchmark calculation results indicate that the CPU time required by the DC-TD-DFTB-based approach is drastically less than that of the conventional TD-DFTB, and does not increase when the system size is extended. Hence, it can be concluded that the DC-TD-DFTB-based approach enables huge-scale FSSH simulations, which incorporates not only an excitation center but also its environment, within affordable computational resources without loss of accuracy.

3.3 Efficient NA-MD Scheme Capable of Simulating Nonradiative Relaxation Processes via SF-TD-DFTB Method[†]

3.3.1 Introduction

The nonadiabatic dynamics of photoexcited chemical species play a key role in multifarious systems from fundamental and/or pragmatic points of view, e.g., photoactive proteins,[48] solar cells,[49] and molecular machines.[50] NA-MD methods,[26] in which trajectory surface hopping[14,25] may be the most popular example in the field of molecular science, provide practical ways to study nonadiabatic phenomena in such highly complex chemical systems via computational simulations. The NA-MD techniques are based on mixed quantum–classical approach, which decomposes problems of electronic and nuclear DOFs into quantum mechanical and classical mechanical hierarchies, respectively. The quantum mechanical, i.e., electronic, part can be treated with a variety of electronic structure calculation methods developed in the field of quantum chemistry, which include multiconfigurational self-consistent field, multireference CI, and ADC(2).[51,52] In particular, linear-response TD-DFT, which is considered a standard tool for excited-state calculations, is important also as an option for the electronic structure technique to combine with NA-MD.[15,19,45,53,54] Notably, the tight-binding formulation of DFT with semiempirical parametrization, DFTB,[30–33,55] and its TD extension, TD-DFTB,[56] have been established as efficient quantum chemical calculation techniques with accuracies comparable with that of (TD-)DFT. Owing to the low computational cost, adoption of the TD-DFTB method has extended the size of target systems in NA-MD simulations within affordable computational resources.[1,11,27,28,34,35,57–59]

It is widely recognized that single-reference methods, e.g., TD-DFT and ADC(2), present difficulties in situations where multireference character is pronounced, such as S_1/S_0 CXs,[52,60] which, in particular, play a critical role in nonradiative relaxation processes of photoexcited species. The TD-DFTB, as a single-reference method derived from the TD-DFT, has similar

[†]Reprinted with permission from Ref. [47]. Copyright 2020 American Chemical Society.

limitations.[28,58] To solve this problem, the SF approach[61,62] is one of the well-established methods. The SF version of the TD-DFT, SF-TD-DFT,[63] utilizes a high-spin reference state, which is triplet if the singlet states are of interest. The eigenstates of the desired spin multiplicity are obtained via the spin-flipping excitation from the reference state, which yields not only single-excitation configurations, but also double-excitation configurations. Because the SF-TD-DFT can conveniently include the multireference character within minor modifications to the theoretical and programmatic infrastructures of the normal TD-DFT, the SF-TD-DFT has been widely used to search for CX structures[64–70] and perform (nonadiabatic) dynamics simulations,[71–76] as an alternative to single-reference methods in situations where they do not provide the correct description.

This section presents a computationally efficient NA-MD method capable of describing dynamics that involve S_1/S_0 CXs. To this end, the semiempirically approximated version of the SF-TD-DFT, i.e., SF-TD-DFTB, which has been introduced as the DFTB-counterpart of the SF-TD-DFT,[77] was combined with the FSSH technique. The remainder of this section is organized as follows. Subsection 3.3.2 describes the theoretical aspects of the proposed method, i.e., NA-MD based on the SF-TD-DFTB. Subsection 4.3 discusses the results of numerical tests. The accuracy of the proposed technique is discussed therein via comparisons with results of previous studies. Subsection 3.3.4 summarizes the study.

3.3.2 Theory

Analytical Energy Gradient

In the SF-TD-DFTB/FSSH technique, the nuclear coordinates are propagated according to the atomic force obtained from the reference-state and excitation energy gradients. Because the reference-state gradient is nothing but the ordinary open-shell SCC-DFTB gradient, of which the analytical implementation is already available in the DCDFTBMD program,[39] this section only presents the formulation of the excitation energy gradient. Because the derivation is lengthy, the

details are described in Appendix A.1, and only the final results are presented below. Although only the spin-unrestricted case is discussed, the derivation of the gradient in the restricted open-shell case is also shown in Appendix A.2. The Lagrangian approach[78,79] enables one to obtain the analytical gradient of the excitation energy ω (the adiabatic state index η is omitted hereinafter for simplicity) avoiding explicit calculations of the derivatives of MO coefficients with respect to the nuclear coordinates, which are extremely costly. The Lagrangian L for the SF-TD-DFTB with the spin-unrestricted reference is defined as

$$\begin{aligned} L\left[\mathbf{X}, \omega, \mathbf{C}, \mathbf{Z}^{\alpha}, \mathbf{Z}^{\beta}, \mathbf{W}^{\alpha}, \mathbf{W}^{\beta}\right] &= G\left[\mathbf{X}, \omega\right] \\ &+ \sum_{ia} Z_{ia}^{\alpha} F_{ia}^{\alpha} - \sum_{p \leq q} W_{pq}^{\alpha} \left(S_{pq}^{\alpha} - \delta_{pq}\right) \\ &+ \sum_{\bar{i}\bar{a}} Z_{\bar{i}\bar{a}}^{\beta} F_{\bar{i}\bar{a}}^{\beta} - \sum_{\bar{p} \leq \bar{q}} W_{\bar{p}\bar{q}}^{\beta} \left(S_{\bar{p}\bar{q}}^{\beta} - \delta_{\bar{p}\bar{q}}\right). \end{aligned} \tag{3.3.1}$$

where L and G are variational with respect to the quantities in the square brackets. The second and fourth terms on the RHS denote the condition that the α- and β-spin MOs are variational for the reference state, respectively. The third and fifth terms are the orthonormal conditions for the α- and β-spin MOs, respectively. The energy functional G is

$$G\left[\mathbf{X}, \omega\right] = \sum_{i\bar{a}, j\bar{b}} X_{i\bar{a}} A_{i\bar{a}, j\bar{b}} X_{j\bar{b}} - \omega \left(\sum_{i\bar{a}} X_{i\bar{a}} X_{i\bar{a}} - 1 \right). \tag{3.3.2}$$

Prior to further explanation, the coupling-like matrices are defined as

$$K^{\mathrm{c}}_{\hat{p}\hat{q}, \hat{r}\hat{s}} = \sum_{IJ} q_I^{\hat{p}\hat{q}} \gamma_{IJ} q_J^{\hat{r}\hat{s}}, \tag{3.3.3}$$

$$K^{\mathrm{m}}_{\hat{p}\hat{q}, \hat{r}\hat{s}} = \sum_{A} \sum_{L \in A} \sum_{L' \in A} q_L^{\hat{p}\hat{q}} m_{ALL'} q_{L'}^{\hat{r}\hat{s}}, \tag{3.3.4}$$

$$K^{\mathrm{sf}}_{\hat{p}\hat{q}, \hat{r}\hat{s}} = \sum_{A} q_A^{\hat{p}\hat{q}} m_A q_A^{\hat{r}\hat{s}}. \tag{3.3.5}$$

In addition, the following notations are introduced:

$$H^{+\alpha}_{\hat{p}\hat{q}}\left[\mathbf{V}\right] = \sum_{\hat{r}\hat{s}} \left(2K^{\mathrm{c}}_{\hat{p}\hat{q},\hat{r}\hat{s}} + 2K^{\mathrm{m}}_{\hat{p}\hat{q},\hat{r}\hat{s}}\right) V_{\hat{r}\hat{s}}, \tag{3.3.6}$$

$$H^{+\beta}_{\hat{p}\hat{q}}\left[\mathbf{V}\right] = \sum_{\hat{r}\hat{s}} \left(2K^{\mathrm{c}}_{\hat{p}\hat{q},\hat{r}\hat{s}} - 2K^{\mathrm{m}}_{\hat{p}\hat{q},\hat{r}\hat{s}}\right) V_{\hat{r}\hat{s}}, \tag{3.3.7}$$

$$\mathcal{K}_{\hat{p}\hat{q}} = \sum_{i\bar{a}} 2K^{\mathrm{sf}}_{\hat{p}\hat{q},i\bar{a}} X_{i\bar{a}}, \tag{3.3.8}$$

where $\mathbf{V}$ is an arbitrary vector. The stationary condition of L with respect to the MO coefficients:

$$\frac{\partial L}{\partial c_{\mu\hat{p}}} = 0. \tag{3.3.9}$$

leads to the Z-vector equation to obtain $\mathbf{Z}^{\alpha}$ and $\mathbf{Z}^{\beta}$:

$$\begin{pmatrix} \mathbf{J}^{\alpha\alpha} & \mathbf{J}^{\alpha\beta} \\ \mathbf{J}^{\beta\alpha} & \mathbf{J}^{\beta\beta} \end{pmatrix} \begin{pmatrix} \mathbf{Z}^{\alpha} \\ \mathbf{Z}^{\beta} \end{pmatrix} = - \begin{pmatrix} \mathbf{U}^{\alpha} \\ \mathbf{U}^{\beta} \end{pmatrix}. \tag{3.3.10}$$

where the orbital Hessian matrix elements are

$$J^{\alpha\alpha}_{ia,jb} = \left(\epsilon_a - \epsilon_i\right)\delta_{ij}\delta_{ab} + 2K^{\mathrm{c}}_{ia,jb} + 2K^{\mathrm{m}}_{ia,jb}, \tag{3.3.11}$$

$$J^{\alpha\beta}_{ia,\bar{j}\bar{b}} = 2K^{\mathrm{c}}_{ia,\bar{j}\bar{b}} - 2K^{\mathrm{m}}_{ia,\bar{j}\bar{b}}, \tag{3.3.12}$$

$$J^{\beta\alpha}_{\bar{i}\bar{a},jb} = 2K^{\mathrm{c}}_{\bar{i}\bar{a},jb} - 2K^{\mathrm{m}}_{\bar{i}\bar{a},jb}, \tag{3.3.13}$$

$$J^{\beta\beta}_{\bar{i}\bar{a},\bar{j}\bar{b}} = \left(\epsilon_{\bar{a}} - \epsilon_{\bar{i}}\right)\delta_{\bar{i}\bar{j}}\delta_{\bar{a}\bar{b}} + 2K^{\mathrm{c}}_{\bar{i}\bar{a},\bar{j}\bar{b}} + 2K^{\mathrm{m}}_{\bar{i}\bar{a},\bar{j}\bar{b}}. \tag{3.3.14}$$

The RHS of Eq. 3.3.10 is expressed as

$$U^{\alpha}_{ia} = H^{+\alpha}_{ia}\left[\mathbf{T}^{\alpha}\right] + H^{+\beta}_{ia}\left[\mathbf{T}^{\beta}\right] + \sum_{\bar{b}} 2X_{i\bar{b}}\mathcal{K}_{a\bar{b}}, \tag{3.3.15}$$

$$U^{\beta}_{\bar{i}\bar{a}} = H^{+\alpha}_{\bar{i}\bar{a}}\left[\mathbf{T}^{\beta}\right] + H^{+\beta}_{\bar{i}\bar{a}}\left[\mathbf{T}^{\alpha}\right] + \sum_{j} 2X_{j\bar{a}}\mathcal{K}_{j\bar{i}}. \tag{3.3.16}$$

Here, the unrelaxed difference density matrices for the α-spin and β-spin were defined as

$$T^{\alpha}_{pq} = \begin{cases} -\sum_{\bar{a}} X_{i\bar{a}} X_{j\bar{a}} & (p,q) = (i,j) \\ 0 & \text{otherwise} \end{cases}, \tag{3.3.17}$$

$$T^{\beta}_{\bar{p}\bar{q}} = \begin{cases} \sum_{i} X_{i\bar{a}} X_{i\bar{b}} & (\bar{p},\bar{q}) = (\bar{a},\bar{b}) \\ 0 & \text{otherwise} \end{cases}, \tag{3.3.18}$$

respectively. From $\mathbf{T}^{\alpha/\beta}$ and $\mathbf{Z}^{\alpha/\beta}$, the relaxed difference density matrices, $\mathbf{P}^{\alpha/\beta}$, are obtained as

$$\mathbf{P}^{\alpha} = \mathbf{T}^{\alpha} + \mathbf{Z}^{\alpha}, \tag{3.3.19}$$

$$\mathbf{P}^{\beta} = \mathbf{T}^{\beta} + \mathbf{Z}^{\beta}, \tag{3.3.20}$$

where Z^{α}_{pq} is zero unless $(p,q) = (i,a)$, and $Z^{\beta}_{\bar{p}\bar{q}}$ is zero unless $(\bar{p},\bar{q}) = (\bar{i},\bar{a})$. $\mathbf{W}^{\alpha}$ and $\mathbf{W}^{\beta}$ are calculated as

$$W^{\alpha}_{ij} = \frac{1}{1+\delta_{ij}}\Big[H^{+\alpha}_{ij}\left[\mathbf{P}^{\alpha}\right] + H^{+\beta}_{ij}\left[\mathbf{P}^{\beta}\right] - 2\sum_{\bar{c}} X_{i\bar{c}}X_{j\bar{c}} - 2\omega T^{\alpha}_{ij}\Big], \tag{3.3.21}$$

$$W^{\alpha}_{ia} = H^{+\alpha}_{ia}\left[\mathbf{P}^{\alpha}\right] + H^{+\beta}_{ia}\left[\mathbf{P}^{\beta}\right] + \epsilon^{\alpha}_{a}Z^{\alpha}_{ia} + \sum_{\bar{b}} 2X_{i\bar{b}}\mathcal{K}_{a\bar{b}}, \tag{3.3.22}$$

$$W^{\alpha}_{ai} = 0, \tag{3.3.23}$$

$$W^{\alpha}_{ab} = 0, \tag{3.3.24}$$

$$W^{\beta}_{\bar{i}\bar{j}} = \frac{1}{1+\delta_{\bar{i}\bar{j}}}\Big[H^{+\alpha}_{\bar{i}\bar{j}}\left[\mathbf{P}^{\beta}\right] + H^{+\beta}_{\bar{i}\bar{j}}\left[\mathbf{P}^{\alpha}\right]\Big], \tag{3.3.25}$$

$$W^{\beta}_{\bar{i}\bar{a}} = H^{+\alpha}_{\bar{i}\bar{a}}\left[\mathbf{P}^{\beta}\right] + H^{+\beta}_{\bar{i}\bar{a}}\left[\mathbf{P}^{\alpha}\right] + \epsilon^{\beta}_{\bar{a}}Z^{\beta}_{\bar{i}\bar{a}} + \sum_{j} 2X_{j\bar{a}}\mathcal{K}_{j\bar{i}}, \tag{3.3.26}$$

$$W^{\beta}_{\bar{a}\bar{i}} = 0, \tag{3.3.27}$$

$$W^{\beta}_{\bar{a}\bar{b}} = \frac{1}{1+\delta_{\bar{i}\bar{j}}}\left[2\omega T^{\beta}_{\bar{a}\bar{b}} + 2\sum_{k}\epsilon^{\alpha}_{k}X_{k\bar{a}}X_{k\bar{b}}\right]. \tag{3.3.28}$$

Derivative of the Lagrangian (Eq. 3.3.1) with respect to nuclear coordinates gives the explicit form of the gradient:

$$\begin{aligned}
\frac{\partial \omega}{\partial \mathbf{R}} &= \frac{\partial L}{\partial \mathbf{R}} \\
&= \sum_{\mu\nu} \left(\frac{dH^{0}_{\mu\nu}}{d\mathbf{R}} + \frac{dH^{\mathrm{c}}_{\mu\nu}}{d\mathbf{R}} \right) \left(\mathcal{P}^{\alpha}_{\mu\nu} + \mathcal{P}^{\beta}_{\mu\nu} \right) \\
&+ \sum_{\mu\nu} \frac{dH^{\mathrm{x}}_{\mu\nu}}{d\mathbf{R}} \left(\mathcal{P}^{\alpha}_{\mu\nu} - \mathcal{P}^{\beta}_{\mu\nu} \right) \\
&- \sum_{\mu\nu} \mathcal{W}_{\mu\nu} \frac{dS_{\mu\nu}}{d\mathbf{R}} \\
&+ \frac{1}{2} \sum_{\mu\nu\lambda\kappa} \left(\frac{dS_{\mu\nu}}{d\mathbf{R}} S_{\lambda\kappa} + S_{\mu\nu} \frac{dS_{\lambda\kappa}}{d\mathbf{R}} \right) \\
&\times (m_A \delta_{AC} + m_B \delta_{AD} + m_B \delta_{BC} + m_B \delta_{BD}) \\
&\times \mathcal{X}_{\mu\nu} \mathcal{X}_{\lambda\kappa}. \qquad (3.3.29)
\end{aligned}$$

Here, the following “AO representation” was employed.

$$\mathcal{P}^{\alpha}_{\mu\nu} = \sum_{pq} c_{\mu p} P^{\alpha}_{pq} c_{\nu q}, \qquad (3.3.30)$$

$$\mathcal{P}^{\beta}_{\mu\nu} = \sum_{\bar{p}\bar{q}} c_{\mu \bar{p}} P^{\beta}_{\bar{p}\bar{q}} c_{\nu \bar{q}}, \qquad (3.3.31)$$

$$\mathcal{W}_{\mu\nu} = \sum_{pq} c_{\mu p} W^{\alpha}_{pq} c_{\nu q} + \sum_{\bar{p}\bar{q}} c_{\mu \bar{p}} W^{\beta}_{\bar{p}\bar{q}} c_{\nu \bar{q}}, \qquad (3.3.32)$$

$$\mathcal{X}_{\mu\nu} = \sum_{i\bar{a}} c_{\mu i} X_{i\bar{a}} c_{\nu \bar{a}}. \qquad (3.3.33)$$

As $\mathbf{H}^{\mathrm{c}}$ and $\mathbf{H}^{\mathrm{x}}$ represent the spin-independent and spin-dependent parts of the Fock matrix, respectively, their derivatives are calculated as

$$\begin{aligned}
\frac{dH^{\mathrm{c}}_{\mu\nu}}{d\mathbf{R}} &= \frac{1}{2}\frac{dS_{\mu\nu}}{d\mathbf{R}}\sum_{M}\left(\gamma_{IM}+\gamma_{JM}\right)\Delta q_M \\
&+ \frac{1}{2}S_{\mu\nu}\sum_{M}\left(\frac{d\gamma_{IM}}{d\mathbf{R}}+\frac{d\gamma_{JM}}{d\mathbf{R}}\right)\Delta q_M \\
&+ \frac{1}{2}S_{\mu\nu}\sum_{M}\left(\gamma_{IM}+\gamma_{JM}\right) \\
&\times \sum_{\lambda\in M}\sum_{\kappa}\left(D^{\alpha}_{\kappa\lambda}+D^{\beta}_{\kappa\lambda}\right)\frac{dS_{\kappa\lambda}}{d\mathbf{R}}, \qquad (3.3.34) \\
\frac{dH^{\mathrm{x}}_{\mu\nu}}{d\mathbf{R}} &= \frac{1}{2}\frac{dS_{\mu\nu}}{d\mathbf{R}}\sum_{L''\in A}\left(m_{ALL''}+m_{AL'L''}\right)p_{L''} \\
&+ \frac{1}{2}S_{\mu\nu}\sum_{L''\in A}\left(m_{ALL''}+m_{AL'L''}\right) \\
&\times \sum_{\lambda\in M}\sum_{\kappa}\left(D^{\alpha}_{\kappa\lambda}-D^{\beta}_{\kappa\lambda}\right)\frac{dS_{\kappa\lambda}}{d\mathbf{R}}. \qquad (3.3.35)
\end{aligned}$$

TDNAC

The TDNAC calculation algorithm is developed on the basis of the OD approach of Ryabinkin et al.,[3] with some modification to improve the numerical stability. The OD approach is based on the analytical time-derivative expression of TDNAC under the CIS type wavefunction ansatz, which is expressed using the time-derivative coupling of MOs. Using the same derivation approach as that described in Ref. [3], a similar formula for the SF-CIS type wavefunctions can be obtained:

$$\begin{aligned}
\sigma_{\eta\theta}(t) &= \sum_{i\bar{a}} C^{\eta}_{i\bar{a}}(t)\frac{\partial C^{\theta}_{i\bar{a}}(t)}{\partial t} \\
&+ \sum_{i\bar{a}\bar{b}} C^{\eta}_{i\bar{a}}(t)\,C^{\theta}_{i\bar{b}}(t)\left\langle \phi_{\bar{a}}(t)\left|\frac{\partial\phi_{\bar{b}}(t)}{\partial t}\right.\right\rangle \\
&- \mathcal{P}_{ij}\sum_{ij\bar{a}} C^{\eta}_{i\bar{a}}(t)\,C^{\theta}_{j\bar{a}}(t)\left\langle \phi_{j}(t)\left|\frac{\partial\phi_{i}(t)}{\partial t}\right.\right\rangle, \qquad (3.3.36)
\end{aligned}$$

where the phase factor $\mathcal{P}_{ij}$ depends on the choice of ordering rule in the Slater determinants for single-excitation configurations. In the present case, an α-spin occupied orbital i is replaced by a β-spin virtual orbital $\bar{a}$ without reordering to construct an $i \rightarrow \bar{a}$ excitation configuration Slater determinant, namely

$$\Phi_i^{\bar{a}} = \left|\phi_1 \cdots \phi_{i-1}\phi_{\bar{a}}\phi_{i+1} \cdots \phi_{N^\alpha}\phi_{\bar{1}} \cdots \phi_{\bar{N}^\beta}\right|. \tag{3.3.37}$$

In this case, $\mathcal{P}_{ij} = 1$, regardless of i and j. The value of TDNAC is obtained by calculating the derivative of CIS coefficients and the time-derivative coupling of MOs by applying the following finite-difference approximations on the analytical derivative coupling terms in Eq. 3.3.36.

$$\frac{\partial C_{i\bar{a}}^{\eta}(t)}{\partial t} \approx \frac{1}{\Delta t}\left(C_{i\bar{a}}^{\eta}(t+\Delta t) - C_{i\bar{a}}^{\eta}(t)\right), \tag{3.3.38}$$

$$\left\langle \phi_{\hat{p}}(t) \middle| \frac{\partial \phi_{\hat{q}}(t)}{\partial t} \right\rangle \approx \frac{1}{\Delta t}\left\langle \phi_{\hat{p}}(t) \middle| \phi_{\hat{q}}(t+\Delta t) \right\rangle. \tag{3.3.39}$$

Although the analytical form of TDNAC (Eq. 3.3.36) is invariant with respect to orbital rotation within the occupied or virtual spaces for each spin, the numerical behavior does change upon rotation because of the finite-difference approximations (Eqs. 3.3.38 and 3.3.39). In the CO expression, signs and energetic ordering of orbitals may change with the nuclear dynamics and must be corrected to keep tracking the orbital with the same character; this is not necessarily a trivial task and may limit the size of the time step, especially when the COs are quasi-degenerate. The approach in the present study, which is hereafter called the SVD-OD method, has been previously introduced in the context of fragmentation-based NA-MD calculations.[1] The SVD-OD approach utilizes a set of unitary-transformed MOs called SOs $\left\{\phi_{\hat{p}}^{\mathrm{S}}\right\}$, instead of COs $\left\{\phi_{\hat{p}}^{\mathrm{C}}\right\}$.

$$\phi_i^{\mathrm{S}}(t) = \sum_j \phi_j^{\mathrm{C}}(t)\, U_{ji}^{\alpha\mathrm{O}}(t), \tag{3.3.40}$$

$$\phi_{\bar{a}}^{\mathrm{S}}(t) = \sum_{\bar{b}} \phi_{\bar{b}}^{\mathrm{C}}(t)\, U_{\bar{b}\bar{a}}^{\beta\mathrm{V}}(t). \tag{3.3.41}$$

The transformation matrices to convert the COs to the SOs, $\mathbf{U}^{\alpha\mathrm{O}/\beta\mathrm{V}}(t)$, are constructed for each nuclear time step via SVD:

$$\mathbf{\Sigma}^{\alpha\mathrm{O}}(t, t+\Delta t) = \mathbf{U}^{\alpha\mathrm{O}}(t)\,\mathbf{\Lambda}^{\alpha\mathrm{O}}(t, t+\Delta t)\,\mathbf{U}^{\alpha\mathrm{O}}(t+\Delta t)^{\dagger}, \tag{3.3.42}$$

$$\mathbf{\Sigma}^{\beta\mathrm{V}}(t, t+\Delta t) = \mathbf{U}^{\beta\mathrm{V}}(t)\,\mathbf{\Lambda}^{\beta\mathrm{V}}(t, t+\Delta t)\,\mathbf{U}^{\beta\mathrm{V}}(t+\Delta t)^{\dagger}, \tag{3.3.43}$$

where the matrices $\mathbf{\Lambda}^{\alpha\mathrm{O}}(t, t+\Delta t)$ and $\mathbf{\Lambda}^{\beta\mathrm{V}}(t, t+\Delta t)$ contain the $\hat{p}$-th singular values as their $(\hat{p}, \hat{p})$ elements. $\mathbf{\Sigma}^{\alpha\mathrm{O}}(t, t+\Delta t)$ and $\mathbf{\Sigma}^{\beta\mathrm{V}}(t, t+\Delta t)$ are the overlap matrices between the COs at t and those at $t+\Delta t$, i.e.,

$$\Sigma_{ij}^{\alpha\mathrm{O}}(t, t+\Delta t) = \left\langle \phi_i^{\mathrm{C}}(t) \middle| \phi_j^{\mathrm{C}}(t+\Delta t) \right\rangle, \tag{3.3.44}$$

$$\Sigma_{\bar{a}\bar{b}}^{\beta\mathrm{V}}(t, t+\Delta t) = \left\langle \phi_{\bar{a}}^{\mathrm{C}}(t) \middle| \phi_{\bar{b}}^{\mathrm{C}}(t+\Delta t) \right\rangle. \tag{3.3.45}$$

In the present case, where the number of occupied and virtual MOs does not change with time, the SVD is equivalent to the diagonalization. The CO-based CIS coefficient matrix for each state η, $\mathbf{C}^{\eta,\mathrm{C}}(t)$, is also transformed into the SO-based expression:

$$\mathbf{C}^{\eta,\mathrm{S}}(t) = \mathbf{U}^{\alpha\mathrm{O}}(t)^{\dagger}\mathbf{C}^{\eta,\mathrm{C}}(t)\,\mathbf{U}^{\beta\mathrm{V}}(t). \tag{3.3.46}$$

The TDNAC values are obtained via Eq. 3.3.36 using the SO-based CIS coefficients $\mathbf{C}^{\eta,\mathrm{S}}(t)$ and the SOs $\left\{\phi_{\hat{p}}^{\mathrm{S}}\right\}$. Because the construction of SOs (Eqs. 3.3.42 and 3.3.43) is performed for each time step, the characters of SOs $\phi_{\hat{p}}^{\mathrm{S}}(t)$ and $\phi_{\hat{p}}^{\mathrm{S}}(t+\Delta t)$ are kept similar to each other without suffering from the sign flips, reordering, and intermixing of COs. As discussed in Ref. [1], the use of SOs avoids the tracking problem of COs and allows one to safely employ a comparable-sized nuclear time step to that typically used in adiabatic MD simulations, i.e., 0.25-0.5 fs, even with the presence of quasi-degenerate COs.

It should be noted that there exists another method to obtain the TDNAC, called the WO approach, which is based on the finite-difference approximation using the overlap between the

adiabatic many-electron wavefunctions[2,9,37,80]

$$\sigma_{\eta\theta}(t) \approx \frac{1}{2\Delta t}\left(\left\langle \psi_\eta(t) \middle| \psi_\theta(t+\Delta t)\right\rangle - \left\langle \psi_\theta(t) \middle| \psi_\eta(t+\Delta t)\right\rangle\right). \tag{3.3.47}$$

While the WO approach was also implemented, the SVD-OD approach is used for the calculations presented later because of its computational efficiency.

Identification of Target States

In SF-based dynamics simulations, the adiabatic states of interest must be identified carefully. In general, adiabatic states obtained via the SF approach are spin-contaminated because the SF excitation does not necessarily generate a complete set of configurations to make a spin-pure configuration state function.[81–83] Note that this origin of spin contamination is independent of the spin contamination in the reference state introduced by the spin-unrestricted approach, and thus cannot be eliminated even if one uses the restricted open-shell instead. Because the singlet ($\left\langle S^2\right\rangle = 0$) and triplet ($\left\langle S^2\right\rangle = 2$) states in the SF approach are occasionally mixed with each other because of the spin contamination, it is difficult to find the desired states, i.e., S_0 and S_1, on the basis of only $\left\langle S^2\right\rangle$. In the present study, the T_{SF}-index method proposed by Maeda et al.,[68] was employed. The T_{SF}-index method has been successfully applied to CX searches,[68,77] ab initio MD,[71,72] and FSSH simulations.[75,76] The T_{SF} value is calculated for each state as the sum of $\left\langle S^2\right\rangle$ and the squared CIS coefficients for the four excitation configurations among the SOMOs. From the lowest three roots, the one with the largest T_{SF} value is characterized as triplet (T_1), and the remaining two are picked up as S_0 and S_1. Only the S_0 and S_1 states are considered in the FSSH algorithm.

3.3.3 Numerical Tests

Computational Cost

The CPU time required to calculate the SF excitation energy and its analytical gradient was measured for the SF-TD-DFT and SF-TD-DFTB using phenyl-substituted ethylenes as the target molecules with increasing the number of phenyl rings from zero to four (Fig. 3.9(a)). The ethylenic double bonds of the molecules were twisted with a dihedral angle of 60° to mimic the intermediate situations between the stable geometries at S_0 and the S_1/S_0 CXs. In both SF-TD-DFTB and SF-TD-DFT calculations, the lowest 10 roots were solved, and the gradient was calculated for the lowest one. The SF-TD-DFT calculations were conducted on the GAMESS program[84,85] using 6-31G(d,p) and STO-3G basis sets with BHHLYP exchange–correlation functional,[86] which is typically combined with SF-TD-DFT calculations. The results are presented in Fig. 3.9(b), indicating that the SF-TD-DFTB (green solid line with cross marks) is 10^2-10^3 and 10^3-10^4 times faster than the SF-TD-DFT calculations with STO-3G (orange solid line with circles) and 6-31G(d,p) (blue solid line with lozenges), respectively. In addition, Fig. 3.9(b) shows the CPU time for calculating the TDNAC using the SF-TD-DFTB with the SVD-OD approach (black dashed line with cross marks). The CPU time is approximately one order of magnitude lower than that of the excitation energy and gradient (green solid line with cross marks), suggesting that the TDNAC calculation with the SVD-OD approach is not the computational bottleneck for SF-TD-DFTB-based NA-MD simulations.

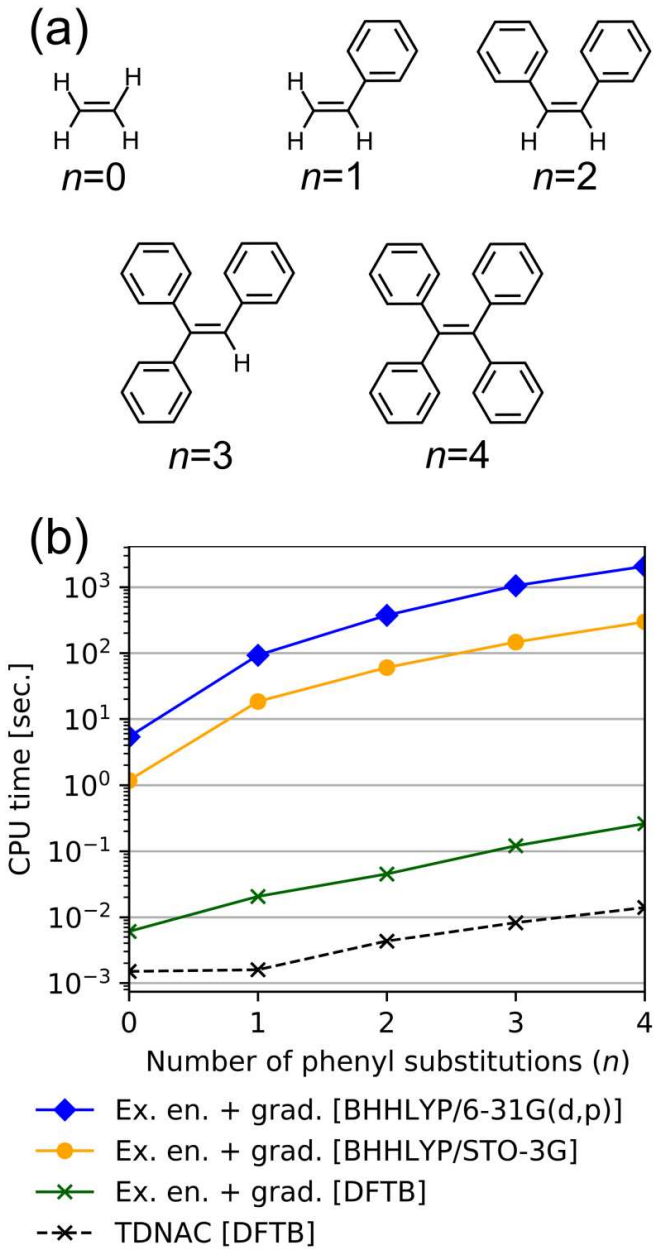

Fig. 3.9: (a) Ethylene derivatives with n phenyl substitutions. (b) CPU time for calculating SF excitation energy and gradient vs n using BHHLYP/6-31G(d,p) (blue solid line with lozenges), BHHLYP/STO-3G (orange solid line with circles), and DFTB (green solid lines with cross marks). CPU time for TDNAC calculation using DFTB with SVD-OD approach is also shown by black dashed lines with cross marks.

cis ↔ *trans* Photoisomerization of Azobenzene

The proposed method was tested on the photoexcitation-invoked ultrafast *cis* ↔ *trans* isomerization reactions of azobenzene, which are prototypical targets of nonadiabatic chemical dynamics studies with respect to both experiments and computational simulations. Azobenzene molecules undergo both *cis* → *trans* and *trans* → *cis* isomerization after being excited to S_1,

which has the n $\rightarrow \pi^*$ character.[87]

The populations of HOMO $\rightarrow$ LUMO excitation configurations at S_1 calculated with the SF-TD-DFTB were 99.98% and 99.80% for *cis*-azobenzene and *trans*-azobenzene, respectively, on the optimized geometries at S_0. The HOMOs and the LUMOs, i.e., the lower and higher SOMOs in the triplet reference states, respectively, are visualized in Fig. 3.10. Only the α-spin MOs are shown because the shapes of the β-spin MOs did not substantially differ from the α-spin ones. Fig. 3.10 shows that the HOMOs and the LUMOs have the N-lone-pair character and the π^* character, respectively, indicating that the SF-TD-DFTB correctly captured the excitation character of S_1 for *cis*- and *trans*-azobenzene.

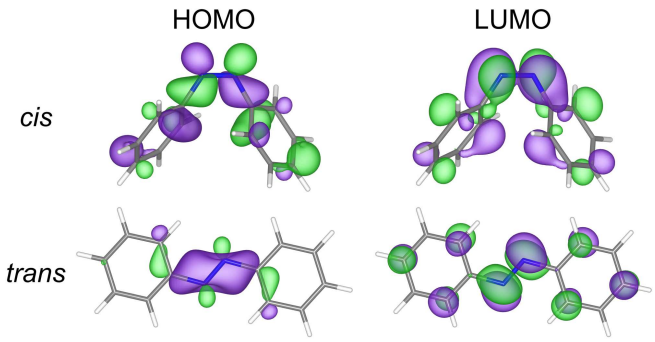

Fig. 3.10: HOMO of *cis*-azobenzene (upper left), LUMO of *cis*-azobenzene (upper right), HOMO of *trans*-azobenzene (lower left), and LUMO of *trans*-azobenzene (lower, right) are indicated by purple and green iso-surfaces. H, C, and N atoms are represented by white, gray, and blue sticks, respectively. Rendered using the visualization software VESTA[88] with an isosurface level of 0.04.

Fig. 3.11 presents the time-course change of the S_1 population in the FSSH simulation starting from each isomer. The 95% confidence interval obtained using the bootstrap method is also shown.

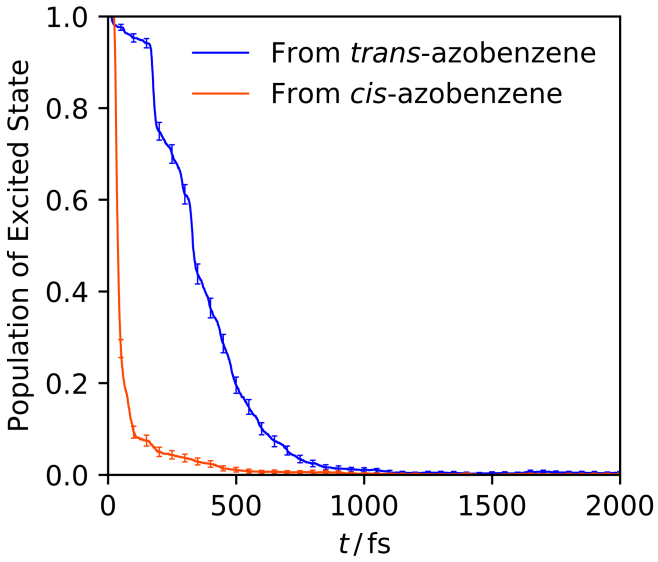

Fig. 3.11: Time-course changes of S_1 populations for *trans*-azobenzene (blue) and *cis*-azobenzene (red). Error bars indicate 95% confidence interval.

Tables 3.2 and 3.3 show the calculated photoisomerization quantum yields and excited-state lifetimes for *cis*- and *trans*-azobenzene, respectively, with previous computational and experimental results for comparison. The *cis* and *trans* products were distinguished based on the dihedral angle of the N=N bond at the final geometry of each trajectory. The dihedral angle was defined in the range from 0° to 180°. The trajectories that ended up with > 90° were classified as *trans* products, and the rest were treated as *cis* products. The S_1 lifetimes were estimated via single-exponential fitting of the decay curves in Fig. 3.11. For *cis*-azobenzene (Table 3.2), the photoisomerization quantum yield obtained by the present simulations (41.5%) is reasonable compared with the experimental value (41%-58%). This result is also comparable with the previous ab initio results, i.e., from 34 ± 10% to 65%. In addition, the S_1 lifetime obtained by the present simulations (54.1 fs) is consistent with the previous simulation results, which vary from 52.7 ± 0.6 to 121 fs. Table 3.3 indicates that the quantum yield for *trans*-azobenzene (32.6%) is reasonable compared with the experimental results (23%-35%) and the previous ab initio computational results (from 11%-16% to 33 ± 5%), as well as the semiempirical results (from 17% to 46 ± 8%). The S_1 lifetime of *trans*-azobenzene obtained from the present calculations is 0.380 ps. While this is a shorter estimation than the previous ab initio results, which range from 0.81 ± 0.10 to 2.218 ± 0.010 ps, the present result falls within the experimentally

Table 3.2: Quantum yields of photoisomerization and excited-state lifetimes of *cis*-azobenzene upon $S_0 \rightarrow S_1$ excitation.

Ref.	Electronic structure method	Dynamics method	*cis* → *trans* quantum yield (%)	S_1 lifetime (fs)
This work	SF-TD-DFTB	FSSH	41.5	54.1
[89]	SA5-CASSCF(6e,4o)	FSSH	45	6×10^1
[23]	SA2-CASSCF(6e,6o)	ZN[a]	39 ± 4	53.1 ± 3.0
[90]	SA3-CASSCF(10e,8o)	FSSH	65	67
[74]	SF-TD-DFT(BHHLYP)	FSSH	34 ± 10	52.7 ± 0.6
[74]	SF-TD-DFT(BHHLYP)	ZN[a]	43 ± 7	63.1 ± 0.1
[74]	TD-DFT(BHHLYP)	ZN[a]	34 ± 9	62.0 ± 0.9
[54]	TD-DFT(BLYP)	FSSH	58	121
[91]	Semiempirical(AM1)/ CASCI(4e,6o)	FSSH	61 ± 3	N/A[c]
[91]	Semiempirical(AM1)/ CASCI(4e,6o)	FMS[b]	68 ± 11	N/A[c]
[92]	Semiempirical(OM2)/ MRCI	FSSH	58	60-116
[87]	Experiment		41-58[d]	N/A[c]
[93]	Experiment		N/A[c]	170

[a]Surface hopping with Zhu–Nakamura-theory-based hopping probability.
[b]Full multiple spawning.
[c]No data available.
[d]Depending on solvents.

observed range (0.26-2.02 ps). Notably, the previous studies, computational or experimental, consistently result in lower photoisomerization quantum yield and longer S_1 lifetime for *cis*-azobenzene (Table 3.2) compared with those of *trans*-azobenzene (Table 3.3). The results in the present study also follow this trend.

3.3.4 Conclusion

This section presented an approach that combined the FSSH algorithm and the approximate SF-TD-DFT in the DFTB framework, i.e., the SF-TD-DFTB. The analytical gradient of excited-state energy was derived, and the TDNAC calculation algorithm was presented as the SF version of the SVD-OD approach. The computational time of the SF-TD-DFTB was approximately 10^2-10^3 and 10^3-10^4 times lower than that of the SF-TD-DFT with 6-31G(d,p) and STO-3G basis sets, respectively, demonstrating the computational efficiency of the present approach. In addi-

Table 3.3: Quantum yields of photoisomerization and excited-state lifetimes of *trans*-azobenzene upon $S_0 \rightarrow S_1$ excitation.

Ref.	Electronic structure method	Dynamics method	*trans* → *cis* quantum yield (%)	S_1 lifetime (ps)
This work	SF-TD-DFTB	FSSH	32.6	0.380
[89]	SA5-CASSCF(6e,4o)	FSSH	28 ± 14	1.86
[23]	SA2-CASSCF(6e,6o)	ZN[a]	33 ± 5	0.81 ± 0.10
[74]	SF-TD-DFT(BHHLYP)	ZN[a]	11-16	2.218 ± 0.010
[74]	TD-DFT(BHHLYP)	ZN[a]	13 ± 16	1.039 ± 0.009
[91]	Semiempirical(AM1)/ CASCI(4e,6o)	FSSH	33 ± 3	N/A[c]
[91]	Semiempirical(AM1)/ CASCI(4e,6o)	FMS[b]	46 ± 8	N/A[c]
[94]	Semiempirical(OM2)/ MRCI	FSSH	17	0.258
[87]	Experiment		23-35	N/A[c]
[95]	Experiment		N/A[c]	0.26-2.02[d]

[a]Surface hopping with Zhu–Nakamura-theory-based hopping probability.
[b]Full multiple spawning.
[c]No data available.
[d]Depending on solvents and pump/probe wavelengths. For each condition, the original literature presents multiple time constants with their relative weights obtained via multiexponential fitting. The average lifetimes, i.e., the weighted-average values, are indicated in this table.

tion, as a test of numerical performance, FSSH simulations were conducted for the *cis* ↔ *trans* photoisomerization reactions of azobenzene. The S_1 lifetime and the quantum yield of the product for the *cis* → *trans* reaction were estimated to be 41.5% and 54.1 fs, respectively. The results for the *trans* → *cis* reaction were 32.6% and 0.380 ps, respectively. Agreement of these results with the experimental values was at the comparable level with that of the previous ab-initio-based NA-MD results, suggesting that the use of the simplified method, i.e., the SF-TD-DFTB, does not significantly deteriorate the accuracy of NA-MD simulations.

3.4 NA-MD Method with Combined DC and SF-TD-DFTB Approach for Condensed-Phase Nonradiative Relaxation Phenomena

3.4.1 Introduction

Nonradiative relaxation, in which excited species decay to the ground state via internal conversion without emitting photons, holds the key to various photochemistry-related problems that are interested in both fundamental and industrial contexts. For example, nonradiative relaxation is one of the factors controlling aggregation-induced emission phenomena,[96] the luminescence quantum yield of OLEDs,[97] and the photoelectric conversion efficiency of solar cells.[98] Importantly, many of the nonradiative-relaxation-related phenomena of interest occur in the condensed phase. For instance, spectroscopic experiments are typically conducted in the liquid or solid phase. Moreover, most commercial photoelectronic devices consist of condensed matter; for example, the core components of OLEDs are amorphous organic layers, which are mixtures of electron-/hole-transporting molecules (host materials) and luminescent molecules.[99]

The importance of the nonradiative relaxation dynamics motivates the research community toward a microscopic understanding, where computational approaches should play a key role. In particular, hybrid approaches of quantum mechanical treatment of electrons and classical treatment of nuclei, i.e., NA-MD methods,[26] including trajectory surface hopping,[6,14,25] are established as efficient and yet reasonably accurate tools to explore nonadiabatic dynamics. However, computational simulations of condensed-phase nonradiative relaxation dynamics are challenging for two reasons. First, nonradiative relaxation involves S_1/S_0 CXs, which have a strong multireference character and cannot be correctly described with ordinary single-reference excited-state calculation techniques such as linear-response TD-DFT.[52,60] Second, in general, chemical phenomena in condensed phases are strongly affected by the environment, e.g., by solvent molecules; explicit consideration of the environment imposes a very high com-

putational cost, which makes it difficult or even impossible.

Regarding the first problem, to mitigate the drawbacks of single-reference methods while retaining their advantages, i.e., simplicity of formulation and low computational cost, SF approach[61,62] is widely accepted. The SF method in effect incorporates a multireference character into the single-reference framework by using spin-flipping excitation from a high-spin reference state. TD-DFT in the SF framework (SF-TD-DFT)[63] is a standard tool for exploring S_1/S_0 CXs[64–70] and dynamics involving them.[71–76] Notably, a tight-binding approximated version of SF-TD-DFT, i.e., SF-TD-DFTB, was proposed recently. Its accuracy is reportedly comparable to that of conventional ab initio electronic structure methods (including SF-TD-DFT), but its computational cost is several orders of magnitude lower.[47,70]

The root of the second difficulty, i.e., the high computational cost, is the high-order scaling of the computational time required for typical excited-state calculation methods with system size. Fragmentation-based frameworks,[100–103] e.g., the fragment MO method,[104–108] are frequently used for calculations of large systems because the cost scales only linearly. Among them, the DC technique[109–115] has been successful in practical applications. Because the DC method naturally allows interfragment exchange of electrons and atoms, DC-based approaches have been used to investigate multifaceted chemical problems that involve 10^3–10^4 atoms: the proton and hydroxide ion transfer dynamics in water[116,117] and in a protein,[118] ion diffusion in electrolyte solutions for batteries,[119] and polaron formation in a perovskite solar cell material.[120] Furthermore, the DC method has been extended to excited-state (adiabatic and nonadiabatic) MD simulations.[1,43,121,122]

This section proposes an efficient trajectory surface hopping approach suitable for treating condensed-phase nonradiative relaxation dynamics by combining the SF-TD-DFTB and DC techniques.

3.4.2 Theory

Method Overview

Tully's FSSH (Subsection 3.1.1)[6] was employed as the NA-MD framework. In the FSSH scheme, the electronic and nuclear DOFs are simultaneously propagated according to the TD Schrödinger equation and the classical EOM, respectively. The adiabatic-state wavefunctions, energies, and energy gradients were obtained on the fly using the DC-SF-TD-DFTB method, which is described below. The TDNACs among the adiabatic states were calculated using an OD approach based on SVD, called SVD-OD method, which is also presented in this section.

DC-SF-TD-DFTB

Here, the DC-based SF-TD-DFTB calculation method, DC-SF-TD-DFTB, is presented. The method of excited-state calculations based on SF-TD-DFTB technique was described in Subsection 2.3.3. Two strategies for DC-based excited-state calculations have been reported: the dynamical polarizability approach for nonlocal excitation[123–125] and the EC approach for local excitation.[43,115,121,122] Here, the latter, which has been adopted in excited-state MD simulations, was employed. In the DC-SF-TD-DFTB approach, the SF-TD-DFTB eigenequation (Eq. 2.3.18) is solved for a specific localization region that includes the EC, which is referred to hereafter as the ECL region. Other localization regions are treated in the same way as in the ground-state DC-DFTB method. To adapt the EC approach to the SF(-TD-DFTB) method, the ECL region must have the spin multiplicity that is appropriate as the reference state. Therefore, an additional approximation is made in the proposed approach; a shifted Fermi level $\epsilon^{\sigma}_{\mathrm{F,ECL}}$ is adopted for the ECL region, and the other localization regions share the common Fermi level $\epsilon^{\sigma}_{\mathrm{F,out}}$, as in the conventional DC scheme. The Fermi levels of the ECL region and the other regions are related to each other through the shift quantity Δ:

$$\epsilon^{\sigma}_{\mathrm{F,ECL}} = \epsilon^{\sigma}_{\mathrm{F,out}} \pm \Delta, \tag{3.4.1}$$

where ± is + and − for $\sigma = \alpha$ and $\sigma = \beta$, respectively. For each SCC iteration, Δ is determined on the fly to satisfy both of the following conditions.

1. $N^{\alpha}_{\mathrm{ECL}} - N^{\beta}_{\mathrm{ECL}} = \Delta N$, where $N^{\sigma}_{\mathrm{ECL}}$ is the number of σ-spin electrons in the ECL region, and ΔN is the expected difference in the number of α- and β-spin electrons for the desired spin multiplicity; for example, $\Delta N = 2$ for triplet.

2. $N^{\sigma} = N^{\sigma}_{0}$.

Note that the value of Δ is uniquely determined from the above conditions, because the numbers of α- and β-spin electrons in each subsystem are monotonic with respect to the α- and β-spin Fermi levels, respectively.

TDNAC Calculation: SVD-OD Approach

The TDNAC calculation method for the DC-SF-TD-DFTB approach is presented in the following. The method is based on the SVD-OD algorithm, which was originally developed for the DC-TD-DFTB technique,[1] but is rewritten as the SF version according to the author's previous study.[47] A major obstacle to TDNAC calculations in the DC framework is that atoms may enter or exit the buffer region of the ECL region because of changes in the atomic coordinates with time; such events change the dimensionality of the adiabatic wavefunctions in the ECL region (Eq. 2.3.23), making the TDNAC values meaningless or undefined.[1] In the SVD-OD method, which has been introduced to avoid this problem, SOs $\left\{\phi^{\mathrm{S}}_{i}\right\}$ are constructed by the unitary transformation of the MOs $\{\phi_i\}$:

$$\phi^{\mathrm{S}}_{i}(t) = \sum_{j} \phi_j(t)\, U_{ji}(t)\,, \tag{3.4.2}$$

$$\phi^{\mathrm{S}}_{i}(t+\Delta t) = \sum_{j} \phi_j(t+\Delta t)\, U_{ji}(t+\Delta t)\,, \tag{3.4.3}$$

where the transformation matrices $\mathbf{U}(t)$ and $\mathbf{U}(t+\Delta t)$ are obtained by SVD:

$$\mathbf{\Sigma}(t, t+\Delta t) = \mathbf{U}(t)\,\mathbf{\Lambda}(t, t+\Delta t)\,\mathbf{U}(t+\Delta t)^{\dagger}. \tag{3.4.4}$$

Here, the element (k,k) of the matrix $\mathbf{\Lambda}(t, t+\Delta t)$ is the singular value $\lambda_k(t, t+\Delta t)$ ($0 \leq \lambda_k(t, t+\Delta t) \leq 1$) corresponding to the k-th singular vector. The singular values and singular vectors are sorted in descending order, i.e., $\lambda_1 > \lambda_2 > \cdots$. The matrix $\mathbf{\Sigma}(t, t+\Delta t)$ is the MO overlap matrix between the times t and $t+\Delta t$:

$$\Sigma_{ij}(t, t+\Delta t) = \left\langle \phi_i(t) \middle| \phi_j(t+\Delta t) \right\rangle. \tag{3.4.5}$$

Note that SOs are separately constructed for the α-occupied, α-virtual, β-occupied, and β-virtual spaces, although here only the α-occupied case is shown as an example. As the singular value $\lambda_k(t, t+\Delta t)$ measures the similarity of the SOs $\phi_k^{\mathrm{S}}(t)$ and $\phi_k^{\mathrm{S}}(t+\Delta t)$, the SOs with singular values close to unity, i.e., larger than a threshold value $\lambda_{\mathrm{thresh}}$, are picked up to expand the common space; the other SOs are discarded. The adiabatic wavefunctions are re-expressed within the common space as

$$\tilde{\psi}_\eta(t) = \sum_{i}^{\tilde{N}_{\mathrm{O}}^{\alpha}} \sum_{\bar{a}}^{\tilde{N}_{\mathrm{V}}^{\beta}} \mathscr{X}_{i\bar{a}}^{\eta}(t)\,\tilde{\Phi}_i^{\bar{a}}(t). \tag{3.4.6}$$

Here, $\mathscr{X}_{i\bar{a}}^{\eta}$ is an SO-based expression of the response matrix $X_{j\bar{b}}^{\eta}$:

$$\mathscr{X}_{i\bar{a}}^{\eta}(t) = \sum_{j\bar{b}} U_{ij}(t)\,X_{j\bar{b}}^{\eta}(t)\,U_{\bar{b}\bar{a}}^{\dagger}(t). \tag{3.4.7}$$

$\tilde{N}_{\mathrm{O}}^{\alpha}$ and $\tilde{N}_{\mathrm{V}}^{\beta}$ are the numbers of α-spin occupied and β-spin virtual SOs that expand the common space, respectively. $\tilde{\Phi}_i^{\bar{a}}$ is the SO-based Slater determinant of the $i \to \bar{a}$ excitation configuration

and is expressed within the common space:

$$\tilde{\Phi}_i^{\bar{a}} = \left| \phi_1^{\mathrm{S}} \cdots \phi_{i-1}^{\mathrm{S}} \phi_{\bar{a}}^{\mathrm{S}} \phi_{i+1}^{\mathrm{S}} \cdots \phi_{\tilde{N}_{\mathrm{O}}^{\alpha}}^{\mathrm{S}} \phi_{\bar{1}}^{\mathrm{S}} \cdots \phi_{\tilde{N}_{\mathrm{O}}^{\beta}}^{\mathrm{S}} \right|. \tag{3.4.8}$$

On the basis of this expression, the TDNAC is calculated using the analytical time-derivative form for CIS type wavefunctions:[3]

$$\begin{aligned}
\sigma_{\eta\theta}(t) = & \sum_{i}^{\tilde{N}_{\mathrm{O}}^{\alpha}} \sum_{\bar{a}}^{\tilde{N}_{\mathrm{V}}^{\beta}} \mathscr{X}_{i\bar{a}}^{\eta}(t) \frac{\partial \mathscr{X}_{i\bar{a}}^{\theta}(t)}{\partial t} \\
& + \sum_{i}^{\tilde{N}_{\mathrm{O}}^{\alpha}} \sum_{\bar{a}}^{\tilde{N}_{\mathrm{V}}^{\beta}} \sum_{\bar{b}}^{\tilde{N}_{\mathrm{V}}^{\beta}} \mathscr{X}_{i\bar{a}}^{\eta}(t) \mathscr{X}_{i\bar{b}}^{\theta}(t) \left\langle \phi_{\bar{a}}^{\mathrm{S}}(t) \middle| \frac{\partial \phi_{\bar{b}}^{\mathrm{S}}(t)}{\partial t} \right\rangle \\
& - \mathcal{P}_{ij} \sum_{i}^{\tilde{N}_{\mathrm{O}}^{\alpha}} \sum_{j}^{\tilde{N}_{\mathrm{O}}^{\alpha}} \sum_{\bar{a}}^{\tilde{N}_{\mathrm{V}}^{\beta}} \mathscr{X}_{i\bar{a}}^{\eta}(t) \mathscr{X}_{j\bar{a}}^{\theta}(t) \left\langle \phi_{j}^{\mathrm{S}}(t) \middle| \frac{\partial \phi_{i}^{\mathrm{S}}(t)}{\partial t} \right\rangle.
\end{aligned} \tag{3.4.9}$$

Here, the phase factor $\mathcal{P}_{ij}$ is unity when the SOs in the Slater determinants are ordered as described in Eq. 3.4.8, i.e., when ϕ_i^{S} in the reference configuration is replaced by $\phi_{\bar{a}}^{\mathrm{S}}$ (without reordering) to construct the Slater determinant for the $i \to \bar{a}$ configuration. The time derivatives in Eq. 3.4.9 are calculated using the finite-difference approximation:

$$\frac{\partial \mathscr{X}_{i\bar{a}}^{\eta}(t)}{\partial t} \approx \frac{1}{\Delta t} \left(\mathscr{X}_{i\bar{a}}^{\eta}(t + \Delta t) - \mathscr{X}_{i\bar{a}}^{\eta}(t) \right), \tag{3.4.10}$$

$$\left\langle \phi_p^{\mathrm{S}}(t) \middle| \frac{\partial \phi_q^{\mathrm{S}}(t)}{\partial t} \right\rangle \approx \frac{1}{\Delta t} \left\langle \phi_p^{\mathrm{S}}(t) \middle| \phi_q^{\mathrm{S}}(t + \Delta t) \right\rangle. \tag{3.4.11}$$

Adiabatic State Tracking

The SF approach generally does not yield the spin-complete set of configurations. In particular, when the singlet states are of interest, i.e., the reference state is triplet, a spin-complete description can be obtained only within the two-electron–four-orbital space among the α HOMO, α LUMO, β HOMO, and β LUMO; all the other excitations lack some of the configurations needed to make the spin eigenfunctions.[81–83] As a result, the adiabatic states in the SF framework are spin-contaminated, and a large number of unphysical mixed singlet–triplet states, i.e.,

$\left\langle S^2 \right\rangle \approx 1$ states, are found. Hence, it is a nontrivial task to identify the correct singlet states from the obtained roots. The T_{SF} index method,[68] which is typically used for this purpose, is based on the T_{SF} value calculated from the $\left\langle S^2 \right\rangle$ and CIS coefficients, where $T_{\mathrm{SF}} \approx 0$ for singlet states and $T_{\mathrm{SF}} \approx 2$ for triplet states in general. Although the T_{SF} index method is a robust approach when the desired states are expected to be found in lowest a few roots, this is not necessarily the case when the DC-SF-TD-DFTB approach is used because the environment, e.g., solvent molecules, is explicitly included. Alternatively, the procedure illustrated in Fig. 3.12 was employed. Fig. 3.12 shows a flowchart for determining the indices of the roots, $\theta_x(t)$, corresponding to the correct S_x states at time t. The present scheme uses $\left\langle S^2 \right\rangle$ as the criterion if possible. When $\left\langle S^2 \right\rangle$-based selection becomes problematic, the scheme identifies the states of the next time step so that they are energetically close to, and have a large TDNAC with, the states of the current time step, to maintain the state characters. The routine is repeated for every nuclear time step.

3.4.3 Numerical Tests

This subsection presents and discusses the results of benchmark calculations using the developed method. The method was implemented in the development version of the DCDFTBMD code,[39] and all the DFTB calculations were performed using this program with the 3OB parameter set.[44] Dispersion correction was included via Grimme's D3 scheme[126] using Becke–Johnson damping.[127] Time steps for integrating the TD Schrödinger equation (Eq. 3.1.2) and the Newton's equation (Eq. 3.1.5) were set to 0.01 and 0.5 fs, respectively. For the DC-based calculations, $r_{\mathrm{buf}} = 4.0$ Å and $\mathscr{B} = 800\,\mathrm{hartree}^{-1}$ were employed, and each molecule was treated as a subsystem. The threshold for singular values in the SVD-OD method ($\lambda_{\mathrm{thresh}}$) was set to 0.95. Classical MD calculations for preliminary equilibration were performed using the GROMACS code.[41]

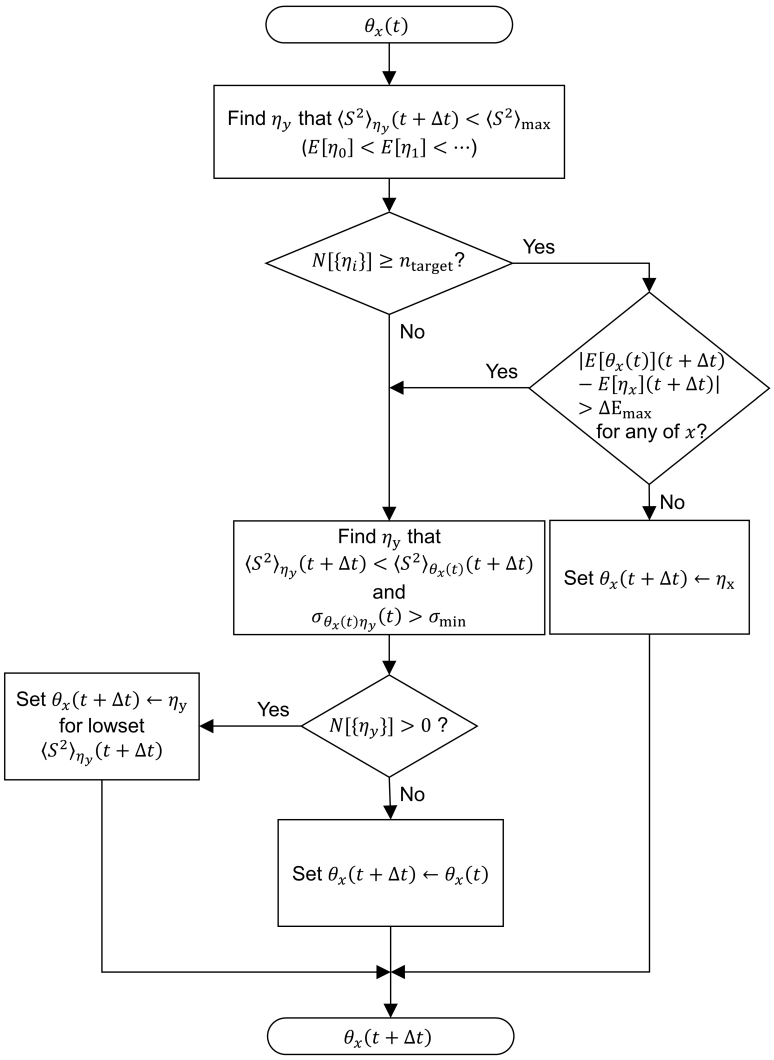

Fig. 3.12: Flowchart of singlet state identification scheme. $\theta_x(t)$ is the index of the root corresponding to the S_x state at time t. n_{target} is the number of adiabatic states of interest. $\langle S^2\rangle_{\max}$, $\Delta E_{\max}$, and $\sigma_{\min}$ are threshold parameters.

Accuracy of DC Approach

The accuracy of the DC-SF-TD-DFTB approach is compared with that of the SF-TD-DFTB approach without the DC scheme. The target system is an acetonitrile solution of thymine, which is composed of one thymine molecule and 89 acetonitrile molecules within a 2 nm×2 nm×2 nm periodic box. The time-course changes in the TDNAC between the S_1 and S_0 states were calculated using SF-TD-DFTB and DC-SF-TD-DFTB over the same predetermined nuclear trajectory constructed using a DFTB-MD run. The DFTB-MD simulation was conducted under the NVT ensemble at $T = 298.15$ K using an Andersen thermostat[128] after an equilibration run of 2.0 ps following pre-equilibration by a classical MD simulation. Figure 3.13 shows the SF-TD-

DFTB (blue solid line) and DC-SF-TD-DFTB results (orange dotted line), which agree well with each other. The results suggest that the error originating from fragmentation is negligibly small in the context of nonadiabatic dynamics simulations.

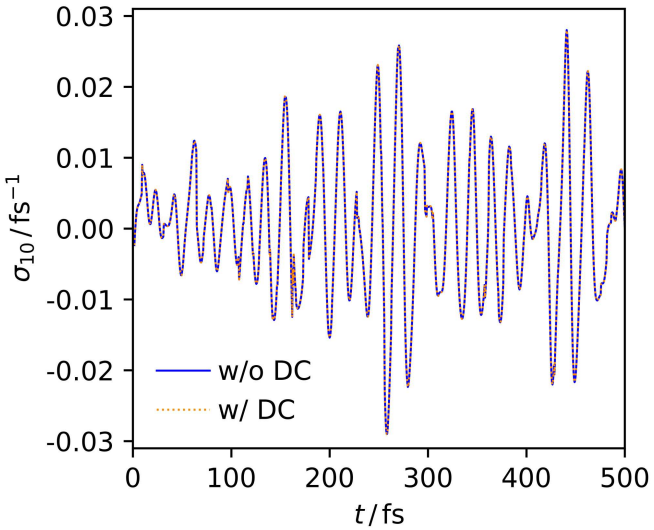

Fig. 3.13: Time-course changes in TDNAC between S_1 and S_0 states (σ_{10}) for a predetermined nuclear trajectory of a thymine + 89 acetonitrile system, calculated using SF-TD-DFTB without DC (blue solid line) and DC-SF-TD-DFTB (orange dotted line).

Computational Cost

Figure 3.14 shows the measured CPU times for the (DC-)SF-TD-DFTB calculations of the excitation energy, excitation energy gradient, and TDNAC for acetonitrile solution models of thymine with various numbers of solvent molecules, n. Each data point in Fig. 3.14 represents the averaged result of 11 trials. The SF-TD-DFTB results (solid lines with circles) show a rapid increase with n. By contrast, the DC-SF-TD-DFTB results (dashed lines with lozenges) are essentially constant as n is increased, suggesting that the DC-SF-TD-DFTB approach can simulate systems with hundreds of molecules without a significant increase in the computational burden.

3.4.4 Conclusion

The SF-TD-DFTB/FSSH technique has been established as an efficient NA-MD technique capable of treating the nonradiative relaxation processes of excited molecules.[47] In the present

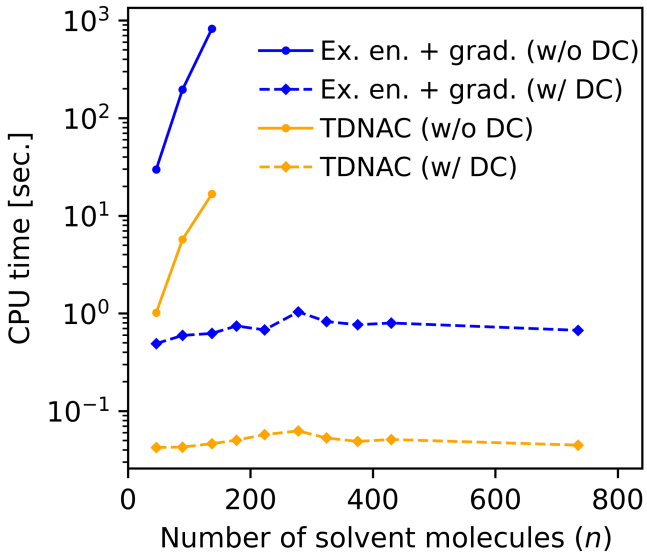

Fig. 3.14: CPU time required to calculate excitation energy and its gradient (blue) and TDNAC (orange) versus the number of solvent molecules (n) for acetonitrile solutions of thymine. Results with and without the use of DC are shown by dashed lines with lozenges and solid lines with circles, respectively.

study, this strategy was extended to simulations of condensed-phase nonradiative relaxation processes by introducing the DC fragmentation scheme, which enables the explicit quantum-mechanical treatment of entire systems including environmental species, without a prohibitively high computational cost. Numerical tests using acetonitrile solutions of thymine showed that the S_1/S_0 TDNACs obtained using the DC-SF-TD-DFTB method and the conventional method, i.e., SF-TD-DFTB, were in good agreement, indicating that the proposed approach is reasonably accurate. In addition, although the CPU time required for the SF-TD-DFTB method increased sharply with increasing number of solvent molecules, that required for the DC-SF-TD-DFTB calculations remained constant at a manageable level even when the system contained several hundreds of molecules.

References

[1]H. Uratani and H. Nakai, *J. Chem. Phys.* **152**, 224109 (2020).

[2]S. Hammes-Schiffer and J. C. Tully, *J. Chem. Phys.* **101**, 4657 (1994).

[3]I. G. Ryabinkin, J. Nagesh, and A. F. Izmaylov, *J. Phys. Chem. Lett.* **6**, 4200 (2015).

[4]F. Plasser, G. Granucci, J. Pittner, M. Barbatti, M. Persico, and H. Lischka, *J. Chem. Phys.* **137**, 22A514 (2012).

[5]G. Granucci and M. Persico, *J. Chem. Phys.* **126**, 134114 (2007).

[6]J. C. Tully, *J. Chem. Phys.* **93**, 1061 (1990).

[7]A. V. Akimov, *J. Phys. Chem. Lett.* **9**, 6096 (2018).

[8]P.-O. Löwdin, *Phys. Rev.* **97**, 1474 (1955).

[9]F. Plasser, M. Ruckenbauer, S. Mai, M. Oppel, P. Marquetand, and L. González, *J. Chem. Theory Comput.* **12**, 1207 (2016).

[10]R. Mitrić, U. Werner, M. Wohlgemuth, G. Seifert, and V. Bonačić-Koutecký, *J. Phys. Chem. A* **113**, 12700 (2009).

[11]A. Humeniuk and R. Mitrić, *Comput. Phys. Commun.* **221**, 174 (2017).

[12]L. Wang, J. Qiu, X. Bai, and J. Xu, *WIREs. Comput. Mol. Sci.* **10**, e1435 (2020).

[13]R. A. Marcus, *J. Chem. Phys.* **24**, 966 (1956).

[14]J. C. Tully and R. K. Preston, *J. Chem. Phys.* **55**, 562 (1971).

[15]E. Tapavicza, I. Tavernelli, and U. Rothlisberger, *Phys. Rev. Lett.* **98**, 023001 (2007).

[16]U. Werner, R. Mitrić, T. Suzuki, and V. Bonačić-Koutecký, *Chem. Phys.* **349**, 319 (2008).

[17]M. Barbatti, J. Pittner, M. Pederzoli, U. Werner, R. Mitrić, V. Bonačić-Koutecký, and H. Lischka, *Chem. Phys.* **375**, 26 (2010).

[18]D. Fazzi, M. Barbatti, and W. Thiel, *Phys. Chem. Chem. Phys.* **17**, 7787 (2015).

[19]D. Fazzi, M. Barbatti, and W. Thiel, *J. Am. Chem. Soc.* **138**, 4502 (2016).

[20]H. M. Jaeger, S. Fischer, and O. V. Prezhdo, *J. Chem. Phys.* **137**, 22A545 (2012).

[21]C. Zhu, H. Kamisaka, and H. Nakamura, *J. Chem. Phys.* **116**, 3234 (2002).

[22]W. C. Chung, S. Nanbu, and T. Ishida, *J. Phys. Chem. B* **116**, 8009 (2012).

[23]L. Yu, C. Xu, Y. Lei, C. Zhu, and Z. Wen, *Phys. Chem. Chem. Phys.* **16**, 25883 (2014).

[24]K. Hanasaki, M. Kanno, T. A. Niehaus, and H. Kono, *J. Chem. Phys.* **149**, 244117 (2018).

[25]M. Barbatti, *WIREs. Comput. Mol. Sci.* **1**, 620 (2011).

[26]T. R. Nelson, A. J. White, J. A. Bjorgaard, A. E. Sifain, Y. Zhang, B. Nebgen, S. Fernandez-Alberti, D. Mozyrsky, A. E. Roitberg, and S. Tretiak, *Chem. Rev.* **120**, 2215 (2020).

[27]S. Pal, D. J. Trivedi, A. V. Akimov, B. Aradi, T. Frauenheim, and O. V. Prezhdo, *J. Chem. Theory Comput.* **12**, 1436 (2016).

[28]L. Stojanović, S. G. Aziz, R. H. Hilal, F. Plasser, T. A. Niehaus, and M. Barbatti, *J. Chem. Theory Comput.* **13**, 5846 (2017).

[29]T. A. Niehaus, S. Suhai, F. Della Sala, P. Lugli, M. Elstner, G. Seifert, and T. Frauenheim, *Phys. Rev. B* **63**, 085108 (2001).

[30]W. M. C. Foulkes and R. Haydock, *Phys. Rev. B* **39**, 12520 (1989).

[31]D. Porezag, T. Frauenheim, T. Köhler, G. Seifert, and R. Kaschner, *Phys. Rev. B* **51**, 12947 (1995).

[32]G. Seifert, D. Porezag, and T. Frauenheim, *Int. J. Quant. Chem.* **58**, 185 (1996).

[33]M. Elstner, D. Porezag, G. Jungnickel, J. Elsner, M. Haugk, T. Frauenheim, S. Suhai, and G. Seifert, *Phys. Rev. B* **58**, 7260 (1998).

[34]E. Titov, A. Humeniuk, and R. Mitrić, *Phys. Chem. Chem. Phys.* **20**, 25995 (2018).

[35]E. Posenitskiy, M. Rapacioli, B. Lepetit, D. Lemoine, and F. Spiegelman, *Phys. Chem. Chem. Phys.* **21**, 12139 (2019).

[36]F. Alkan and C. M. Aikens, *J. Phys. Chem. C* **122**, 23639 (2018).

[37]M. Sapunar, T. Piteša, D. Davidović, and N. Došlić, *J. Chem. Theory Comput.* **15**, 3461 (2019).

[38]R. L. Martin, *J. Chem. Phys.* **118**, 4775 (2003).

[39]Y. Nishimura and H. Nakai, *J. Comput. Chem.* **40**, 1538 (2019).

[40]P. P. Ewald, *Ann. Phys.* **369**, 253 (1921).

[41]M. J. Abraham, T. Murtola, R. Schulz, S. Páll, J. C. Smith, B. Hess, and E. Lindahl, *SoftwareX* **1-2**, 19 (2015).

[42]J. Wang, R. M. Wolf, J. W. Caldwell, P. A. Kollman, and D. A. Case, *J. Comput. Chem.* **25**, 1157 (2004).

[43]N. Komoto, T. Yoshikawa, J. Ono, Y. Nishimura, and H. Nakai, *J. Chem. Theory Comput.* **15**, 1719 (2019).

[44]M. Gaus, A. Goez, and M. Elstner, *J. Chem. Theory Comput.* **9**, 338 (2013).

[45]S. M. Parker, S. Roy, and F. Furche, *Phys. Chem. Chem. Phys.* **21**, 18999 (2019).

[46]H. Nishizawa, Y. Nishimura, M. Kobayashi, S. Irle, and H. Nakai, *J. Comput. Chem.* **37**, 1983 (2016).

[47]H. Uratani, T. Morioka, T. Yoshikawa, and H. Nakai, *J. Chem. Theory Comput.* **16**, 7299 (2020).

[48]H. Kuramochi, S. Takeuchi, K. Yonezawa, H. Kamikubo, M. Kataoka, and T. Tahara, *Nat. Chem.* **9**, 660 (2017).

[49]J. Jankowska, R. Long, and O. V. Prezhdo, *ACS Energy Lett.* **2**, 1588 (2017).

[50]N. Koumura, R. W. J. Zijlstra, R. A. van Delden, N. Harada, and B. L. Feringa, *Nature* **401**, 152 (1999).

[51]M. Barbatti, M. Ruckenbauer, F. Plasser, J. Pittner, G. Granucci, M. Persico, and H. Lischka, *WIREs. Comput. Mol. Sci.* **4**, 26 (2013).

[52]F. Plasser, R. Crespo-Otero, M. Pederzoli, J. Pittner, H. Lischka, and M. Barbatti, *J. Chem. Theory Comput.* **10**, 1395 (2014).

[53]E. Tapavicza, I. Tavernelli, U. Rothlisberger, C. Filippi, and M. E. Casida, *J. Chem. Phys.* **129**, 124108 (2008).

[54]A. J. Neukirch, L. C. Shamberger, E. Abad, B. J. Haycock, H. Wang, J. Ortega, O. V. Prezhdo, and J. P. Lewis, *J. Chem. Theory Comput.* **10**, 14 (2014).

[55]M. Gaus, Q. Cui, and M. Elstner, *J. Chem. Theory Comput.* **7**, 931 (2011).

[56]T. A. Niehaus, S. Suhai, F. Della Sala, P. Lugli, M. Elstner, G. Seifert, and T. Frauenheim, *Phys. Rev. B* **63**, 085108 (2001).

[57]X. Gao, Q. Peng, Y. Niu, D. Wang, and Z. Shuai, *Phys. Chem. Chem. Phys.* **14**, 14207 (2012).

[58]T. Tran, A. Prlj, K.-H. Lin, D. Hollas, and C. Corminboeuf, *Phys. Chem. Chem. Phys.* **21**, 9026 (2019).

[59]H. Uratani and H. Nakai, *J. Phys. Chem. Lett.* **11**, 4448 (2020).

[60]B. G. Levine, C. Ko, J. Quenneville, and T. J. MartÍnez, *Mol. Phys.* **104**, 1039 (2006).

[61]A. I. Krylov, *Chem. Phys. Lett.* **338**, 375 (2001).

[62]A. I. Krylov, *Chem. Phys. Lett.* **350**, 522 (2001).

[63]Y. Shao, M. Head-Gordon, and A. I. Krylov, *J. Chem. Phys.* **118**, 4807 (2003).

[64]N. Minezawa and M. S. Gordon, *J. Phys. Chem. A* **113**, 12749 (2009).

[65]N. Minezawa and M. S. Gordon, *J. Phys. Chem. A* **115**, 7901 (2011).

[66]N. Minezawa and M. S. Gordon, *J. Chem. Phys.* **137**, 034116 (2012).

[67]Y. Harabuchi, S. Maeda, T. Taketsugu, N. Minezawa, and K. Morokuma, *J. Chem. Theory Comput.* **9**, 4116 (2013).

[68]S. Maeda, Y. Harabuchi, T. Taketsugu, and K. Morokuma, *J. Phys. Chem. A* **118**, 12050 (2014).

[69]H. Nakai, M. Inamori, Y. Ikabata, and Q. Wang, *J. Phys. Chem. A* **122**, 8905 (2018).

[70]M. Inamori, Y. Ikabata, T. Yoshikawa, and H. Nakai, *J. Chem. Phys.* **152**, 144108 (2020).

[71]Y. Harabuchi, K. Keipert, F. Zahariev, T. Taketsugu, and M. S. Gordon, *J. Phys. Chem. A* **118**, 11987 (2014).

[72]Y. Harabuchi, R. Yamamoto, S. Maeda, S. Takeuchi, T. Tahara, and T. Taketsugu, *J. Phys. Chem. A* **120**, 8804 (2016).

[73]L. Yue, Z. Lan, and Y.-J. Liu, *J. Phys. Chem. Lett.* **6**, 540 (2015).

[74]L. Yue, Y. Liu, and C. Zhu, *Phys. Chem. Chem. Phys.* **20**, 24123 (2018).

[75]N. Minezawa and T. Nakajima, *J. Chem. Phys.* **150**, 204120 (2019).

[76]N. Minezawa and T. Nakajima, *J. Chem. Phys.* **152**, 024119 (2020).

[77]M. Inamori, T. Yoshikawa, Y. Ikabata, Y. Nishimura, and H. Nakai, *J. Comput. Chem.* **41**, 1538 (2020).

[78]F. Furche and R. Ahlrichs, *J. Chem. Phys.* **117**, 7433 (2002).

[79]D. Heringer, T. A. Niehaus, M. Wanko, and T. Frauenheim, *J. Comput. Chem.* **28**, 2589 (2007).

[80]S. Lee, E. Kim, S. Lee, and C. H. Choi, *J. Chem. Theory Comput.* **15**, 882 (2019).

[81]J. S. Sears, C. D. Sherrill, and A. I. Krylov, *J. Chem. Phys.* **118**, 9084 (2003).

[82]Z. Li and W. Liu, *J. Chem. Phys.* **136**, 024107 (2012).

[83]T. Tsuchimochi, *J. Chem. Phys.* **143**, 144114 (2015).

[84]M. W. Schmidt, K. K. Baldridge, J. A. Boatz, S. T. Elbert, M. S. Gordon, J. H. Jensen, S. Koseki, N. Matsunaga, K. A. Nguyen, S. Su, T. L. Windus, M. Dupuis, and J. A. Montgomery Jr, *J. Comput. Chem.* **14**, 1347 (1993).

[85]M. S. Gordon and M. W. Schmidt, "Chapter 41 - advances in electronic structure theory: gamess a decade later", in *Theory and applications of computational chemistry*, edited by C. E. Dykstra, G. Frenking, K. S. Kim, and G. E. Scuseria (Elsevier, Amsterdam, 2005), pp. 1167 –1189.

[86]A. D. Becke, *J. Chem. Phys.* **98**, 1372 (1993).

[87]H. M. D. Bandara and S. C. Burdette, *Chem. Soc. Rev.* **41**, 1809 (2012).

[88]K. Momma and F. Izumi, *J. Appl. Crystallogr.* **44**, 1272 (2011).

[89]Y. Ootani, K. Satoh, A. Nakayama, T. Noro, and T. Taketsugu, *J. Chem. Phys.* **131**, 194306 (2009).

[90]M. Pederzoli, J. Pittner, M. Barbatti, and H. Lischka, *J. Phys. Chem. A* **115**, 11136 (2011).

[91]A. Toniolo, C. Ciminelli, M. Persico, and T. J. Martínez, *J. Chem. Phys.* **123**, 234308 (2005).

[92]O. Weingart, Z. Lan, A. Koslowski, and W. Thiel, *J. Phys. Chem. Lett.* **2**, 1506 (2011).

[93]T. Nägele, R. Hoche, W. Zinth, and J. Wachtveitl, *Chem. Phys. Lett.* **272**, 489 (1997).

[94]J. A. Gámez, O. Weingart, A. Koslowski, and W. Thiel, *J. Chem. Theory Comput.* **8**, 2352 (2012).

[95]C.-W. Chang, Y.-C. Lu, T.-T. Wang, and E. W.-G. Diau, *J. Am. Chem. Soc.* **126**, 10109 (2004).

[96]J. Mei, N. L. C. Leung, R. T. K. Kwok, J. W. Y. Lam, and B. Z. Tang, *Chem. Rev.* **115**, 11718 (2015).

[97]D. Y. Kondakov, J. R. Sandifer, C. W. Tang, and R. H. Young, *J. Appl. Phys.* **93**, 1108 (2003).

[98]J. Benduhn, K. Tvingstedt, F. Piersimoni, S. Ullbrich, Y. Fan, M. Tropiano, K. A. McGarry, O. Zeika, M. K. Riede, C. J. Douglas, S. Barlow, S. R. Marder, D. Neher, D. Spoltore, and K. Vandewal, *Nat. Energy* **2**, 17053 (2017).

[99]H. Kaji, H. Suzuki, T. Fukushima, K. Shizu, K. Suzuki, S. Kubo, T. Komino, H. Oiwa, F. Suzuki, A. Wakamiya, Y. Murata, and C. Adachi, *Nat. Commun.* **6**, 8476 (2015).

[100]M. S. Gordon, D. G. Fedorov, S. R. Pruitt, and L. V. Slipchenko, *Chem. Rev.* **112**, 632 (2012).

[101]M. A. Collins and R. P. A. Bettens, *Chem. Rev.* **115**, 5607 (2015).

[102]K. Raghavachari and A. Saha, *Chem. Rev.* **115**, 5643 (2015).

[103]J. M. Herbert, *J. Chem. Phys.* **151**, 170901 (2019).

[104]K. Kitaura, E. Ikeo, T. Asada, T. Nakano, and M. Uebayasi, *Chem. Phys. Lett.* **313**, 701 (1999).

[105]D. G. Fedorov and K. Kitaura, *J. Phys. Chem. A* **111**, 6904 (2007).

[106]D. G. Fedorov, T. Nagata, and K. Kitaura, *Phys. Chem. Chem. Phys.* **14**, 7562 (2012).

[107]Y. Nishimoto, D. G. Fedorov, and S. Irle, *J. Chem. Theory Comput.* **10**, 4801 (2014).

[108]Y. Mochizuki, S. Koikegami, S. Amari, K. Segawa, K. Kitaura, and T. Nakano, *Chem. Phys. Lett.* **406**, 283 (2005).

[109]W. Yang, *Phys. Rev. Lett.* **66**, 1438 (1991).

[110]W. Yang and T.-S. Lee, *J. Chem. Phys.* **103**, 5674 (1995).

[111]T. Akama, M. Kobayashi, and H. Nakai, *J. Comput. Chem.* **28**, 2003 (2007).

[112]M. Kobayashi, T. Yoshikawa, and H. Nakai, *Chem. Phys. Lett.* **500**, 172 (2010).

[113]M. Kobayashi and H. Nakai, "Divide-and-conquer approaches to quantum chemistry: theory and implementation", in *Linear-scaling techniques in computational chemistry and physics: methods and applications* (2011), pp. 97–127.

[114]M. Kobayashi and H. Nakai, *Phys. Chem. Chem. Phys.* **14**, 7629 (2012).

[115]T. Yoshikawa, M. Kobayashi, A. Fujii, and H. Nakai, *J. Phys. Chem. B* **117**, 5565 (2013).

[116]H. Nakai, A. W. Sakti, and Y. Nishimura, *J. Phys. Chem. B* **120**, 217 (2016).

[117]A. W. Sakti, Y. Nishimura, and H. Nakai, *J. Phys. Chem. B* **121**, 1362 (2017).

[118]J. Ono, M. Imai, Y. Nishimura, and H. Nakai, *J. Phys. Chem. B* **124**, 8524 (2020).

[119]M. Okoshi, C.-P. Chou, and H. Nakai, *J. Phys. Chem. B* **122**, 2600 (2018).

[120]H. Uratani, C.-P. Chou, and H. Nakai, *Phys. Chem. Chem. Phys.* **22**, 97 (2020).

[121]T. Yoshikawa, N. Komoto, Y. Nishimura, and H. Nakai, *J. Comput. Chem.* **40**, 2778 (2019).

[122]N. Komoto, T. Yoshikawa, Y. Nishimura, and H. Nakai, *J. Chem. Theory Comput.* **16**, 2369 (2020).

[123]H. Nakai and T. Yoshikawa, *J. Chem. Phys.* **146**, 124123 (2017).

[124]Y. Ikabata, Q. Wang, T. Yoshikawa, A. Ueda, T. Murata, K. Kariyazono, M. Moriguchi, H. Okamoto, Y. Morita, and H. Nakai, *npj Quant. Mater.* **2**, 27 (2017).

[125]T. Yoshikawa, J. Yoshihara, and H. Nakai, *J. Chem. Phys.* **152**, 024102 (2020).

[126]S. Grimme, J. Antony, S. Ehrlich, and H. Krieg, *J. Chem. Phys.* **132**, 154104 (2010).

[127]E. R. Johnson and A. D. Becke, *J. Chem. Phys.* **123**, 024101 (2005).

[128]H. C. Andersen, *J. Chem. Phys.* **72**, 2384 (1980).

Chapter 4

Structure Dependence of Nonradiative Relaxation Mechanism of Excited Molecules: Case Studies on Tetraphenylethylene and Its Derivative[†]

4.1 Introduction

TPE and its derivative (2OTPE) (Fig. 4.1), which were experimentally studied by Shi et al.[2] while exploring the mechanism of the AIE, illustratively exemplify the molecular-structure dependence of nonradiative relaxation dynamics. The term AIE denotes a class of phenomena, in which some types of molecules that are not fluorescent in the solution phase exhibit substantially strong fluorescence in aggregate form.[3] From the general perspective, the AIE phenomena are ascribed to the hindrance of specific intramolecular DOFs that lead to nonradiative decay from the excited state. In particular, the RIR has been proposed as one of the typical mechanisms.[4] The RIR concept is based on the viewpoint that the propeller-like rotation of aromatic rings around the single bond plays a critical role in nonradiative decay; in the aggregate form,

[†]Reprinted with permission from Ref. [1]. Copyright 2020 American Chemical Society.

the rotation should be sterically hindered by the presence of surrounding molecules, resulting in an excited-state lifetime that is long enough for fluorescence to be observed. The TPE molecule (Fig. 4.1, left) has torsional DOFs about the four single bonds between the phenyl rings and the ethylene unit. Conversely, in the 2OTPE molecule (Fig. 4.1, right), the geminal phenyl rings are bridged with O atoms, so that the propeller-like rotation of these rings is prohibited. They reported that TPE is not fluorescent in the solution phase but exhibits fluorescence in the crystal phase. On the contrary, 2OTPE has substantial FQY in both solution and crystal. From the phenomenological point of view, this result suggests that locking the torsional rotation about the phenyl–ethylene single bonds elongates the excited-state lifetime of this class of molecules, in line with the RIR concept. However, thus far, limited knowledge is available regarding the detailed pathway of the nonradiative decay of these molecules (in particular, 2OTPE) and the manner in which the restriction of phenyl ring rotation affects it.

In this chapter, using the SF-TD-DFTB/FSSH technique, which was described in Section 3.3, the nonradiative decay processes of TPE and 2OTPE are simulated in the gas phase. The obtained excited-state lifetime for 2OTPE is longer than that for TPE in several orders of magnitude, being consistent with the abovementioned experimental results on FQY. In addition, the underlying mechanism of the difference in the excited-state lifetimes between TPE and 2OTPE is discussed in detail from the points of view of NA-MD trajectories, MECX structures, and potential energy landscapes.

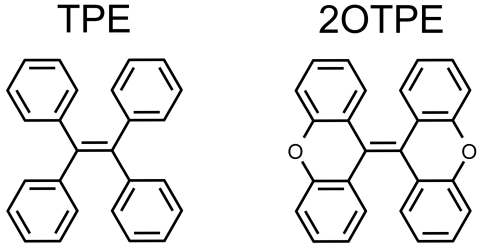

Fig. 4.1: Structures of TPE (left) and 2OTPE (right).[2]

4.2 Computational Details

All the DFTB calculations were performed using DCDFTBMD code[5] with the 3OB parameter set.[6] SF-TD-DFTB/FSSH simulations were started from the S_1 state and performed without a thermostat. For each target system, 2000 independent trajectories were collected to obtain statistical convergence. These trajectories differ from each other with respect to the initial geometry, initial velocity, and the seed for random numbers. Time steps of 0.25 and 0.01 fs were adopted for numerical integration of the EOM for the nuclei (Eq. 3.1.5) and the TD electronic Schrödinger equation (Eq. 3.1.2), respectively. The dispersion correction was included using Grimme's D3 scheme[7] with Becke–Johnson damping.[8] The initial structures and velocities for FSSH simulations were sampled from closed-shell DFTB-MD trajectories in the S_0 state under the *NVT* ensemble with the temperature controlled to 298.15 K using the Andersen thermostat,[9] following equilibration runs of 50 ps. The intervals between subsequent samplings were 250 fs or longer.

4.3 Results and Discussion

Figure 4.2 shows the time trace of S_1 populations obtained by the FSSH simulations for TPE and 2OTPE, indicating that the $S_1 \rightarrow S_0$ decay of TPE (magenta) occurred on a subpicosecond time scale, while that of 2OTPE (black) was significantly slower. The S_1 lifetimes of TPE and 2OTPE estimated by single-exponential fitting were 0.742 and 119 ps, respectively. These results are qualitatively consistent with the experimentally observed FQY of these molecules in solution (Table 4.1). Note that the FQY of a molecule is determined in general by the competition between the spontaneous emission and other nonradiative decay channels; in other words, the slower nonradiative relaxation suggests the higher FQY.

Table 4.1: FQY (%) of TPE and 2OTPE in solution and in crystal. Data taken from Ref. [2].

	Solution	Crystal
TPE	$\sim 0^a$	24.6
2OTPE	30.1	30.8

[a]Not detected.

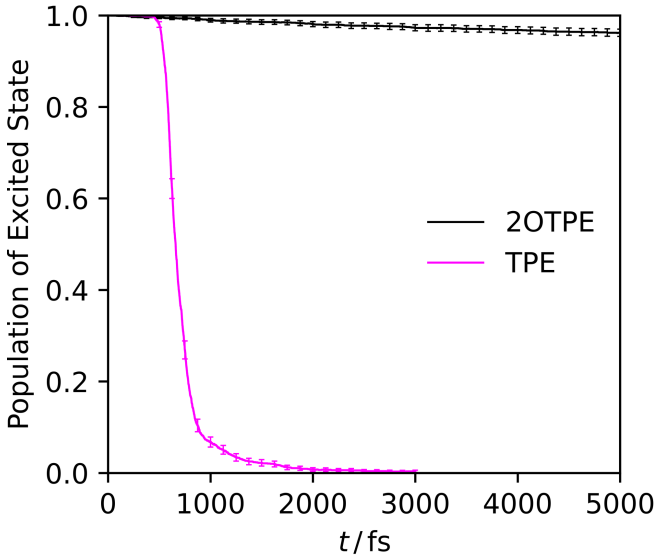

Fig. 4.2: Time-course changes of S_1 populations for TPE (magenta) and 2OTPE (black). Error bars indicate 95% confidence interval.

Typically, nonradiative decay pathways are understood in a schematic picture whereby the molecules move through the MECXs from the excited state(s) to the ground state. Figure 4.3 shows the MECX structures of TPE and 2OTPE optimized with the combined use of the SF-TD-DFTB and the branching-plane updating method.[10] The optimized structures at S_0 are also shown for comparison. There has been a debate on the principal pathway of the $S_1 \rightarrow S_0$ decay of TPE. On the one hand, it has been suggested that the decay involves a twist of the ethylenic C=C bond by approximately 90°.[11–15] On the other hand, some researchers have proposed a different path via quasi C−C bond formation between the vicinal phenyl rings.[16–18] Another path has been proposed, where the propeller-like torsion of phenyl rings around the ethylene-phenyl single bonds plays a key role.[19,20] Two MECXs for TPE, which are hereafter termed twist-type and cycle-type MECXs (Figs. 4.3(c) and 4.3(d), respectively), were found. The similar twist- and cycle-type MECX structures were also recognized for 2OTPE (Figs. 4.3(e) and 4.3(f), respectively). Figure 4.3 indicates the two DOFs that characterize the twist and cycle MECXs,

i.e., the twisting angle of the C=C bond (φ, $0^\circ \leq \varphi \leq 90^\circ$) and the minimum distance between the vicinal phenyl rings (d), respectively. In Fig. 4.3, the twist-type and cycle-type MECXs have twisted ethylenic C=C bonds with $\varphi \approx 90^\circ$ and closely contacted vicinal phenyl rings ($d \approx 1.7$ Å), respectively, suggesting that the twist-type and cycle-type MECXs correspond to the abovementioned "C=C bond twisting" path and the "quasi C−C bond formation" paths, respectively.

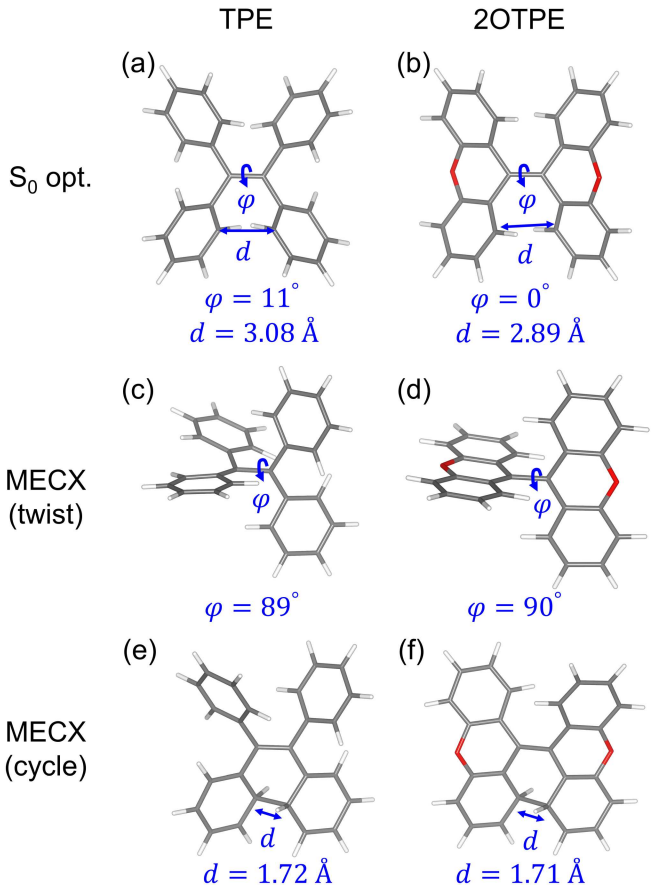

Fig. 4.3: (a), (b): S_0 stable geometry of TPE and 2OTPE, respectively. (c), (d): twist-type MECX of TPE and 2OTPE, respectively. (e), (f): cycle-type MECX of TPE and 2OTPE, respectively. Optimized with SF-TD-DFTB. C, H, and O atoms are represented by gray, white, and red sticks, respectively. Twisting angle of ethylenic C=C bond (φ) and minimum distance between vicinal phenyl rings (d) are also shown.

For each FSSH trajectory, φ and d at the moment of the $S_1 \rightarrow S_0$ transition are indicated as a circle in Fig. 4.4. The S_1/S_0 energy gap is also represented by the color of the circle. For TPE (Fig. 4.4(a)), most of the $S_1 \rightarrow S_0$ transitions occurred with a significant twist of the C=C bond ($\varphi > 60^\circ$) and a narrow S_1/S_0 energy gap (< 1.0 eV), suggesting that the twist-MECX route is dominant for the nonradiative decay of TPE. In the case of 2OTPE (Fig. 4.4(b)), the number

of trajectories passing through the twist-MECX route, which is characterized by $\varphi \approx 90°$, is significantly decreased compared with that for TPE. The plot also indicates that the $S_1 \rightarrow S_0$ transitions of 2OTPE mostly occurred in the region of $\varphi < 30°$ and 2.5 Å $< d <$ 3.0 Å, where the S_1/S_0 gap is substantially large (> 1.0 eV). This result suggests that the structural dynamics toward the twist-MECX is hindered in the case of 2OTPE, resulting in its long S_1 lifetime. Notably, the cycle-MECX route did not become the main pathway while the twist-MECX route was impeded.

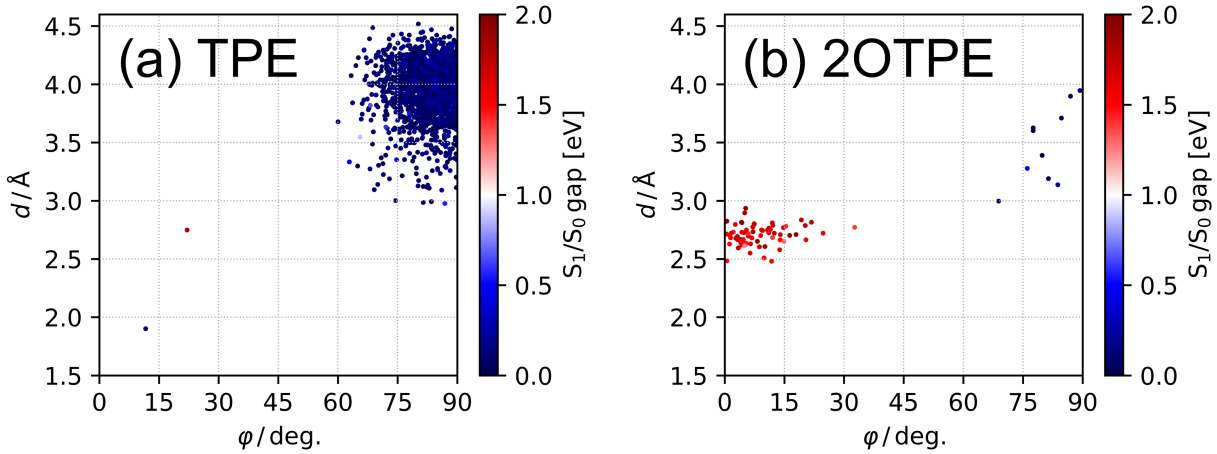

Fig. 4.4: Distribution of ϕ, d, and the S_1/S_0 energy gap at the $S_1 \rightarrow S_0$ transitions, obtained from FSSH simulations for TPE (a) and 2OTPE (b). φ and d are represented by positions of circles, and the S_1/S_0 energy gap is indicated by their colors.

S_1 potential energy profiles with respect to φ and d are shown in Fig. 4.5. Each data point in the profiles was obtained by structural relaxation on the S_1 PES with fixing the DOF corresponding to the horizontal axis, i.e., φ or d. The potential profiles for d (Figs. 4.5(c) and 4.5(d) for TPE and 2OTPE, respectively) suggest that there are large (1.50 and 0.51 eV for TPE and 2OTPE, respectively) energy barriers in the pathways from the FC-like point (d = 3.08 Å and d = 2.89 Å for TPE and 2OTPE, respectively) to the cycle-type MECXs ($d \approx$ 1.7 Å), which explains the reason why the cycle-MECXs were not the main routes for $S_1 \rightarrow S_0$ decay in the present FSSH simulations.

Conversely, in Fig. 4.5(a), it is clear that the C=C bond twisting of TPE is driven from the FC-like point (φ = 11°) toward the twist-MECX (φ = 89°). Because the potential energy difference between the starting point (φ = 11°) and the S_1 minimum (φ = 52°) is approximately

0.3 eV, this energetically downhill process may provide the molecule with sufficient kinetic energy to overcome the small barrier at $\varphi = 85°$ (0.057 eV). The rapid $S_1 \rightarrow S_0$ decay of TPE and the dominant role of the twist-type MECX route can be understood from this result.

For the C=C bond twisting of 2OTPE (Fig. 4.5(b)), two different potential energy profiles were obtained, depending on the conformations shown in Fig. 4.6, which are hereafter called the louver-type and seesaw-type. In the louver-type conformation, the two Ph−O−Ph units are in parallel, like slats in a louver window. The seesaw-type conformation has a staggered arrangement of the two Ph−O−Ph units. The S_0 stable geometry of 2OTPE (Fig. 4.3(b)) has the louver-type conformation, and this has also been experimentally confirmed in Ref. [2] by X-ray diffraction measurements. The twist-type and cycle-type MECXs (Figs. 4.3(d) and 4.3(f), respectively) have the seesaw-type and louver-type conformations, respectively. Note that such conformational isomers are not present for TPE, in which the phenyl rings are allowed to rotate around the ethylene-phenyl single bonds. The potential energy profiles about the twisting angle φ for louver- and seesaw-type conformations of 2OTPE are shown in Fig. 4.5(b) with blue and orange lines, respectively. The plot for louver breaks off at $\varphi = 44°$ because louver-type energy minima were not found for $\varphi > 44°$. The potential energy profiles indicate that the C=C bond twisting of 2OTPE from the FC-like point ($\varphi = 0°$ with the louver-type conformation) is an energetically uphill process, which may be ascribed to the steric repulsion between the two Ph−O−Ph units. In addition, because the molecule has the louver-type conformation at the FC point, the twist-type MECX cannot be accessed without transformation to the seesaw-type conformation, which may need to overcome some additional energy barriers. The infrequency of the $S_1 \rightarrow S_0$ decay via the twist-type MECX for 2OTPE (Fig. 4.4(b)) can be understood from this point of view, suggesting that the effect of locking phenyl rings on the excited-state lifetime is indirect, in the sense that it blocks the twisting motion of the ethylenic C=C bond, which is the main nonradiative decay pathway of TPE.

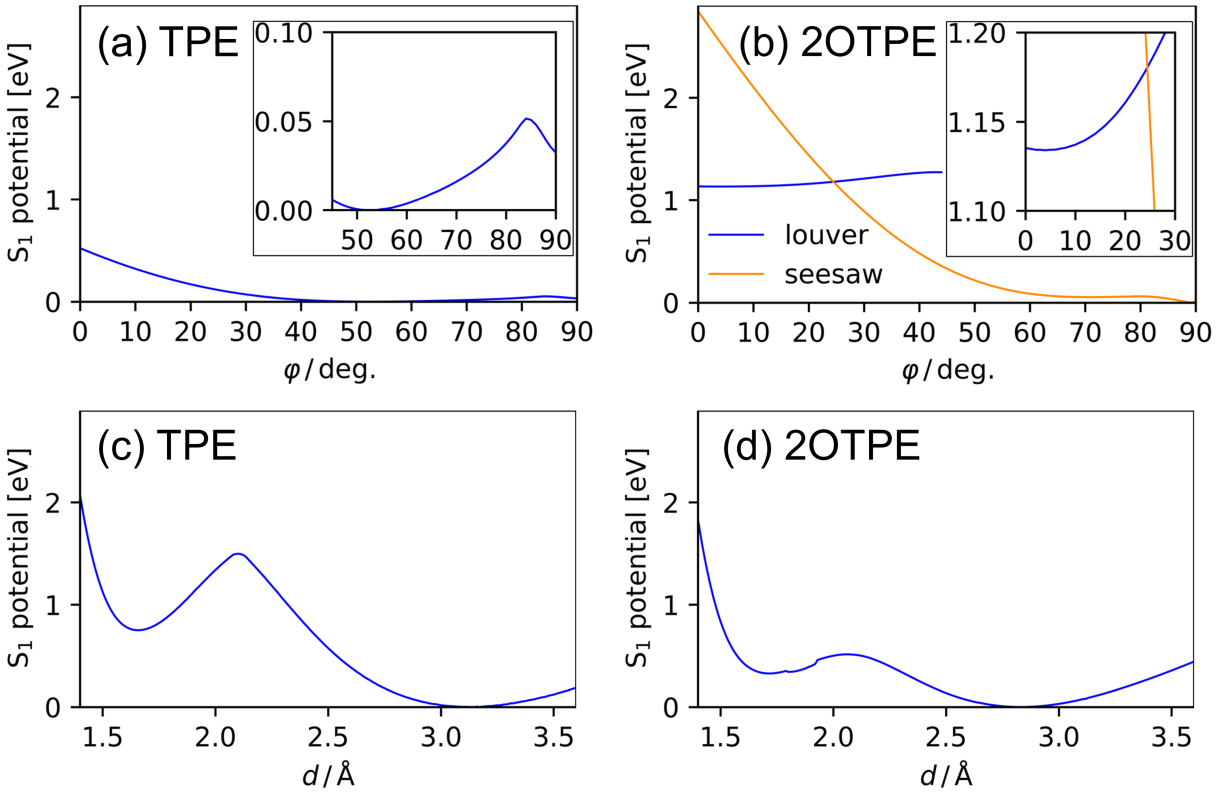

Fig. 4.5: Potential energy profiles on S_1 obtained using constrained geometry optimization. (a), (b): Scanned with φ for TPE and 2OTPE, respectively. (c), (d): Scanned with d for TPE and 2OTPE, respectively.

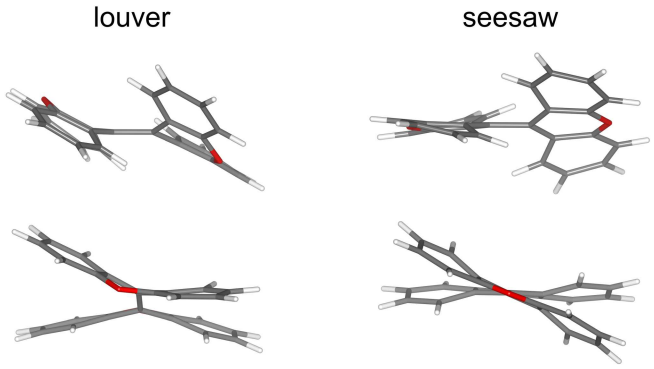

Fig. 4.6: Structures of louver (left) and seesaw (right) conformers of 2OTPE at $\varphi = 25°$.

Figure 4.7 presents the time trace of potential energies, φ, and d for representative FSSH trajectories. In the twist-type MECX route for TPE (Fig. 4.7(a)), φ increased in an essentially monotonic manner from $t = 0$, accompanied by a decrease in the S_1 potential energy. Finally, the molecule underwent the $S_1 \rightarrow S_0$ transition at the CX with $\varphi \approx 90°$ ($t = 621$ fs). Conversely, Fig. 4.7(b) shows an example of the $S_1 \rightarrow S_0$ decay trajectory of 2OTPE without passing through any CXs, which was the main nonradiative relaxation route in the present FSSH simulations. The $S_1 \rightarrow S_0$ transition (at $t = 966$ fs) occurred jumping over the large en-

ergy gap (1.61 eV). It can also be seen that the time-course changes of φ and d do not show any characteristic behavior other than thermal fluctuations, suggesting that this type of nonradiative relaxation process may not be linked to a specific mode of structural dynamics. In addition, an example of the twist-type MECX route for 2OTPE, which was the minor pathway, is also shown (Fig. 4.7(c)). Figure 4.7(c) indicates that φ tended to increase with time until $t \approx 1000$ fs. On the contrary, the S_1 potential energy did not substantially change until $t \approx 600$ fs, indicating a lack of driving force, but started to decrease at $t \approx 600$ fs. This result contrasts with the case of TPE (Fig. 4.7(a)), where the increase in φ toward the twist-type MECX and the decrease in the S_1 potential energy were synchronized. The molecular structures around $t = 600$ fs are visualized in Fig. 4.8, in which the molecule initially had the louver conformation but transformed to the seesaw conformation at $t = 600$ fs. Keeping in mind the S_1 potential energy profile (Fig. 4.5(b)), where the C=C bond twisting of 2OTPE is slightly unfavorable in the louver conformation but is favorable in the seesaw conformation, it can be concluded that the change in the tendency of the S_1 potential energy in Fig. 4.7(c) at $t \approx 600$ fs is a result of the louver $\rightarrow$ seesaw transformation.

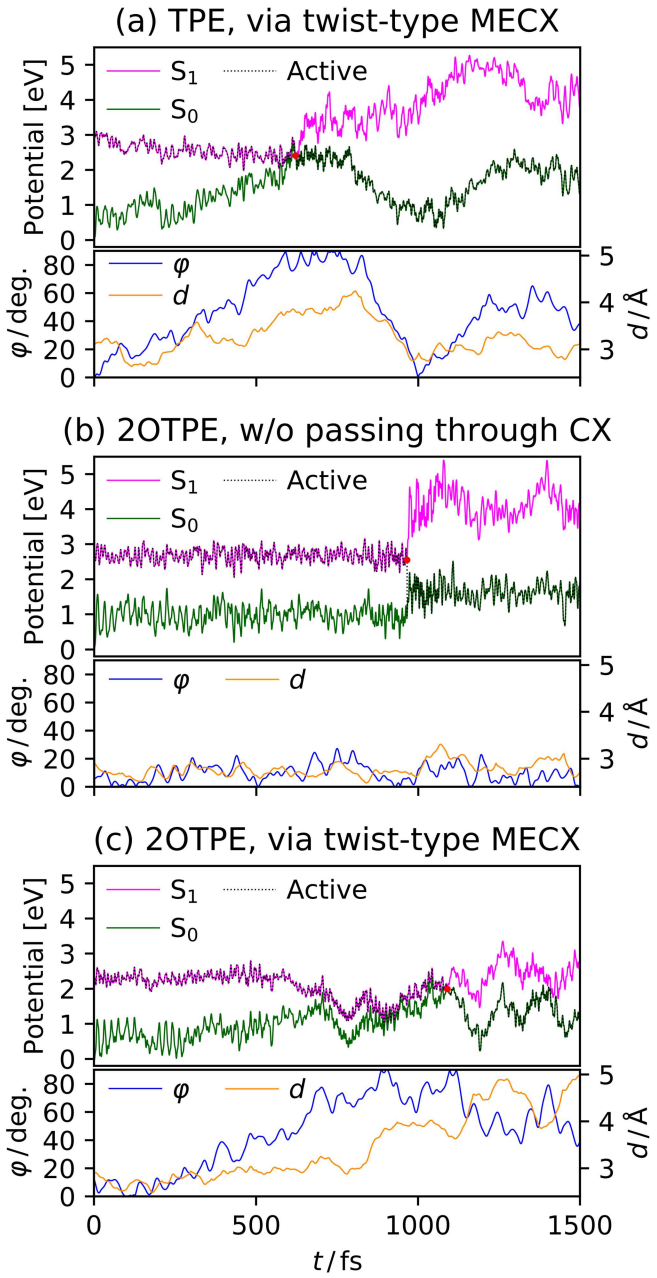

Fig. 4.7: Time trace of potential energies, φ, and d for representative trajectories that exhibited $S_1 \rightarrow S_0$ transitions. (a) TPE, via twist-type MECX. (b) 2OTPE, via twist-type MECX. (c) 2OTPE, not passing through CXs. S_0 potential energy at $t = 0$ is set to zero. Red circles indicate $S_1 \rightarrow S_0$ transitions.

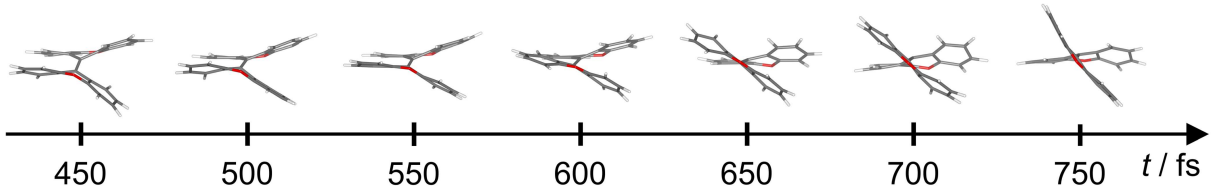

Fig. 4.8: Snapshots of 2OTPE molecular structures in the example trajectory presented in Fig. 4.7(c). C, H, and O atoms are represented by gray, white, and red sticks, respectively.

4.4 Conclusion

This chapter reported a practical application of the developed SF-TD-DFTB/FSSH method, targeting the nonradiative relaxation processes of the photoexcited TPE and its derivative where the phenyl rings are bridged with O atoms (2OTPE), in the context of exploring the essence of the RIR mechanism of AIE. The present FSSH simulations estimated the excited-state lifetimes of TPE and 2OTPE at subpicoseconds and > 100 ps, respectively, in agreement with the tendency of the experimental FQY in solution. The simulations also clarified that the main pathway of the nonradiative decay of TPE is characterized by the twist of the C=C bond, while the nonradiative decay via this route was barely observed in the case of 2OTPE. This is because locking the phenyl rings makes a significant difference in the S_1 potential energy landscape of 2OTPE from that of TPE. For TPE, the twisting motion around the C=C bond is energetically favorable in S_1. Conversely, because the S_0 stable structure of 2OTPE has a conformation in which the two Ph−O−Ph units are arranged in parallel, the twisting motion around the C=C bond in S_1 becomes energetically uphill because of the steric repulsion between the two Ph−O−Ph units.

References

[1]H. Uratani, T. Morioka, T. Yoshikawa, and H. Nakai, *J. Chem. Theory Comput.* **16**, 7299 (2020).

[2]J. Shi, N. Chang, C. Li, J. Mei, C. Deng, X. Luo, Z. Liu, Z. Bo, Y. Q. Dong, and B. Z. Tang, *Chem. Commun.* **48**, 10675 (2012).

[3]J. Mei, N. L. C. Leung, R. T. K. Kwok, J. W. Y. Lam, and B. Z. Tang, *Chem. Rev.* **115**, 11718 (2015).

[4]J. Chen, C. C. W. Law, J. W. Y. Lam, Y. Dong, S. M. F. Lo, I. D. Williams, D. Zhu, and B. Z. Tang, *Chem. Mater.* **15**, 1535 (2003).

[5]Y. Nishimura and H. Nakai, *J. Comput. Chem.* **40**, 1538 (2019).

[6]M. Gaus, A. Goez, and M. Elstner, *J. Chem. Theory Comput.* **9**, 338 (2013).

[7]S. Grimme, J. Antony, S. Ehrlich, and H. Krieg, *J. Chem. Phys.* **132**, 154104 (2010).

[8]E. R. Johnson and A. D. Becke, *J. Chem. Phys.* **123**, 024101 (2005).

[9]H. C. Andersen, *J. Chem. Phys.* **72**, 2384 (1980).

[10]S. Maeda, K. Ohno, and K. Morokuma, *J. Chem. Theory Comput.* **6**, 1538 (2010).

[11]B. I. Greene, *Chem. Phys. Lett.* **79**, 51 (1981).

[12]E. Lenderink, K. Duppen, and D. A. Wiersma, *J. Phys. Chem.* **99**, 8972 (1995).

[13]G.-J. Zhao, K.-L. Han, Y.-B. Lei, and Y.-S. Dou, *J. Chem. Phys.* **127**, 094307 (2007).

[14]S. Kayal, K. Roy, and S. Umapathy, *J. Chem. Phys.* **148**, 024301 (2018).

[15]K. Kokado, T. Machida, T. Iwasa, T. Taketsugu, and K. Sada, *J. Phys. Chem. C* **122**, 245 (2018).

[16]A. Prlj, N. Došlić, and C. Corminboeuf, *Phys. Chem. Chem. Phys.* **18**, 11606 (2016).

[17]Y.-J. Gao, X.-P. Chang, X.-Y. Liu, Q.-S. Li, G. Cui, and W. Thiel, *J. Phys. Chem. A* **121**, 2572 (2017).

[18]T. Tran, A. Prlj, K.-H. Lin, D. Hollas, and C. Corminboeuf, *Phys. Chem. Chem. Phys.* **21**, 9026 (2019).

[19]D. A. Shultz and M. A. Fox, *J. Am. Chem. Soc.* **111**, 6311 (1989).

[20]N. B. Shustova, T.-C. Ong, A. F. Cozzolino, V. K. Michaelis, R. G. Griffin, and M. Dincă, *J. Am. Chem. Soc.* **134**, 15061 (2012).

Chapter 5

Environment Dependence of Nonradiative Relaxation Mechanism of Excited Molecules: Case Studies on *trans*-Azobenzene Solutions

5.1 Introduction

Solvent dependence of nonradiative relaxation processes of *trans*-azobenzene is an illustrative example of the importance of the environment for nonadiabatic dynamics. Upon photoexcitation to the S_1 ($n \rightarrow \pi^*$) state, *trans*-azobenzene undergoes nonradiative relaxation associated with an isomerization reaction to the *cis* isomer, which passes through S_1/S_0 CXs. Two paths for this reaction have been proposed: rotation and inversion mechanisms, whose key DOFs are the C−N=N−C torsional angle and N=N−C bond angle, respectively.[1–3] Using fluorescence anisotropy measurements, Chang and co-workers[3] proposed that the isomerization route depends on the solvent viscosity. The rotation mechanism is dominant in low-viscosity solvents, e.g., hexane, but it is hindered in high-viscosity solvents, e.g., ethylene glycol, and the inversion

route makes a significant contribution in such situations.

With this background, in this chapter, DC-SF-TD-DFTB/FSSH simulations are conducted for the nonradiative relaxation processes of $n \rightarrow \pi^*$ excited *trans*-azobenzene in hexane, in ethylene glycol, and in the gas phase. Tendency in the resulting excited-state lifetimes, which depend on the solvents, is consistent with the experimental results. The solvent dependence of the results is discussed from the viewpoint of viscosity of the solvents.

5.2 Computational Details

All the DFTB calculations were performed using the DCDFTBMD code[4] with the 3OB parameter set.[5] Dispersion correction was included via Grimme's D3 scheme[6] using Becke–Johnson damping.[7] Time steps for integrating the TD Schrödinger equation (Eq. 3.1.2) and Newton's equation (Eq. 3.1.5) were set to 0.01 and 0.5 fs, respectively. For the DC-based calculations, $r_{\mathrm{buf}} = 4.0\,\text{Å}$ and $\mathscr{B} = 800\,\mathrm{hartree}^{-1}$ were employed, and each molecule was treated as a subsystem. The threshold for singular values in the SVD-OD method ($\lambda_{\mathrm{thresh}}$) was set to 0.95. Classical MD calculations for preliminary equilibration were performed using the GROMACS code.[8] Each solution model (Fig. 5.1) was a $3\,\mathrm{nm} \times 3\,\mathrm{nm} \times 3\,\mathrm{nm}$ periodic box containing a *trans*-azobenzene molecule as the solute with 122 hexane molecules or 289 ethylene glycol molecules as the solvent, where the *trans*-azobenzene molecule was treated as the EC (Fig. 5.1). The number of solvent molecules was determined to reproduce the room-temperature density of pure solvents, i.e., 0.66 and $1.11\,\mathrm{g\,mL}^{-1}$ for hexane and ethylene glycol, respectively. In the gas-phase model, which was an isolated *trans*-azobenzene molecule, the periodic boundary condition was not applied. The initial geometries and velocities for the FSSH simulations were sampled from ground-state DFTB-MD trajectories under the NVT ensemble at $T = 298.15\,\mathrm{K}$ using an Andersen thermostat,[9] which followed 10 ps of equilibration runs. The solution models were pre-equilibrated using classical MD before the DFTB-MD equilibration. The interval between sampling was at least 100 fs. The FSSH simulations were started from the S_1 state,

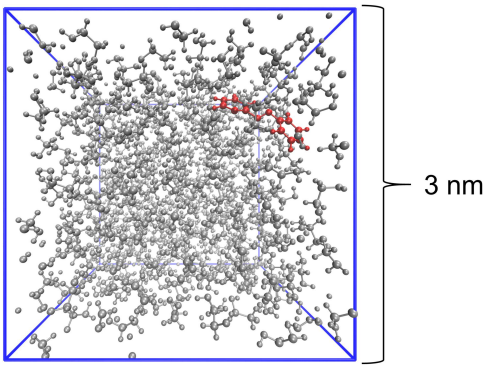

Fig. 5.1: Snapshot of 3 nm × 3 nm × 3 nm periodic model structure (ethylene glycol solution). Solute (*trans*-azobenzene) and solvent molecules are represented by red and gray, respectively.

which has been characterized as n → π^* in SF-TD-DFTB calculations of *trans*-azobenzene,[10] and were conducted without any thermostats or barostats. The threshold values for state tracking, i.e., $\left\langle S^2 \right\rangle_{\max}$, $\Delta E_{\max}$, and $\sigma_{\min}$, were set to 0.5, 1.0×10^{-2} hartree, and 5.0×10^{-3} a.u., respectively. Excluding trajectories that resulted in convergence failure, 2000 valid trajectories were obtained for each of the hexane solution, ethylene glycol solution, and gas-phase model, out of 5637, 2405, and 2000 trials, respectively.

5.3 Results and Discussion

Figure 5.2 shows the time-course changes in the excited-state population under each condition, which indicates that the $S_1 \rightarrow S_0$ decay is slower in solution than in the gas phase. Table 5.1 summarizes the excited-state lifetimes of *trans*-azobenzene in the solutions as estimated experimentally[3] and calculated in the present FSSH simulations. The experimental values are the weighted-averaged lifetimes of multiple decay components. The FSSH lifetimes were calculated by single-exponential fitting of the decay curves in Fig. 5.2. As indicated in Table 5.1, the experimentally observed excited-state lifetimes in hexane are shorter than those in ethylene glycol. The present FSSH results are also consistent with this trend.

For further analysis of the nonradiative relaxation pathways, here, the C−N=N−C torsional angle (θ) and the N=N−C bond angle (ϕ), are defined as shown in Figs. 5.3(a) and 5.3(b), respectively. Because two N=N−C angles can be defined for each azobenzene molecule, ϕ

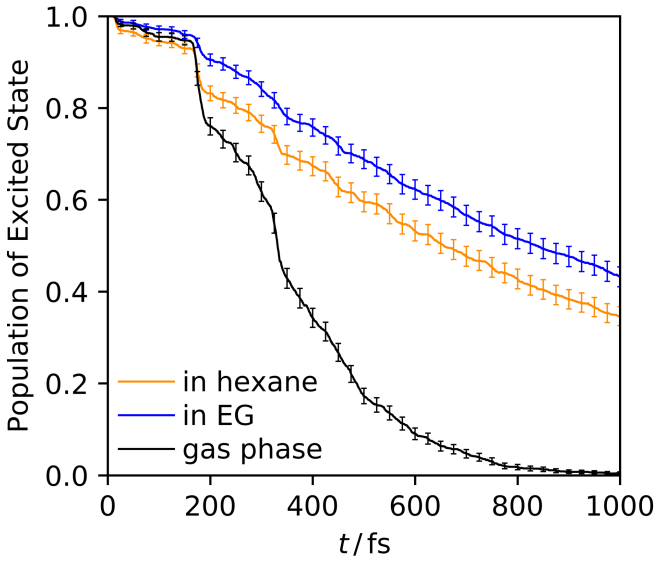

Fig. 5.2: Time-course changes in excited-state populations of *trans*-azobenzene in hexane (orange), in ethylene glycol (blue), and without a solvent (black). Error bars indicate 95% confidence intervals.

Table 5.1: Experimental and calculated excited-state lifetimes of *trans*-azobenzene.

	Experiment (Ref. [3])			FSSH (present)
Solvent	Ex. [nm][a]	Fl. [nm][b]	τ_{ave}/ps[c]	τ/ps[d]
hexane	400	600	0.56	0.98 ± 0.05[e]
	440	520	0.26	
	440	600	0.63	
	480	600	0.47	
	440	680	0.89	
	480	680	1.10	
Ethylene glycol	440	680	1.88	1.29 ± 0.08[e]
	480	680	2.02	
None (gas phase)	-	-	-	0.38 ± 0.01[e]

[a]Excitation wavelength.
[b]Fluorescence wavelength.
[c]Weighted average of multiple decay components.
[d]Obtained from single-exponential fitting of excited-state population decay curves (Fig. 5.2).
[e]95% confidence interval.

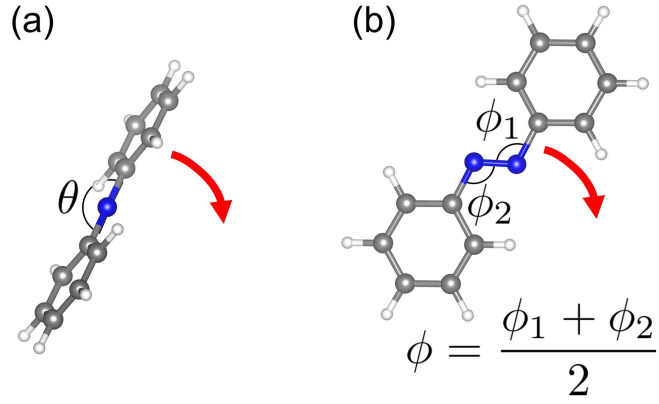

Fig. 5.3: (a) Illustration of C−N=N−C torsional angle, θ, where the N=N bond is perpendicular to the screen. (b) Illustration of N=N−C bond angle, ϕ. Red arrows in (a) and (b) indicate rotation and inversion channels, respectively. Gray, white, and blue spheres represent C, H, and N atoms, respectively.

is defined as their average. The values of θ and ϕ at the $S_1 \rightarrow S_0$ transitions are plotted in Figs. 5.4(a), 5.4(b), and 5.4(c) for the hexane solution, ethylene glycol solution, and gas-phase results, respectively. The time of the transition (t_{hop}) for each trajectory is indicated by the color of the circle, and the green circles indicate θ and ϕ at $t = 0$, i.e., the values taken from the ground-state NVT ensembles. The blue crosses represent θ and ϕ for the S_0 stable structure, the MECX corresponding to inversion, and the MECX corresponding to rotation (Figs. 5.5(a), 5.5(b), and 5.5(c), respectively) of gas-phase *trans*-azobenzene from SF-TD-DFTB calculations combined with the branching-plane updating method.[11]

Figures 5.4(a), 5.4(b), and 5.4(c) indicate that $S_1 \rightarrow S_0$ transitions are associated with increases in both θ and ϕ compared with the $t = 0$ values, which are distributed around the S_0 stable geometry (S_0 min.). The values of θ and ϕ at the $S_1 \rightarrow S_0$ transitions are broadly dispersed, suggesting that the inversion channel, i.e., S_0 min. $\rightarrow$ MECX (inversion), and the rotation channel, i.e., S_0 min. $\rightarrow$ MECX (rotation), are not clearly distinguished, and thus each trajectory has a mixture of the characteristics of these two channels. For convenience in the following qualitative discussion, the transitions with $\theta < 135^\circ$ are classified as rotation and the other transitions are classified as inversion.

Table 5.2 summarizes the contribution of each channel, i.e.,

$$\frac{[\text{the number of transitions classified as each channel}]}{[\text{total number of trajectories}]} \tag{5.3.1}$$

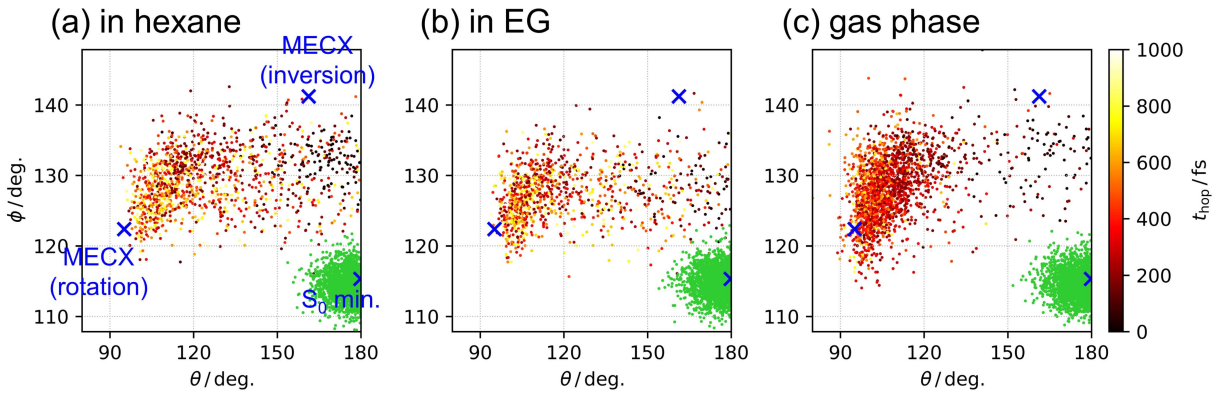

Fig. 5.4: Each black, red, or yellow circle indicates θ and ϕ at the $S_1 \rightarrow S_0$ transition for each trajectory, where the color represents the time of transition (t_{hop}). θ and ϕ at $t = 0$ for each trajectory are also plotted as green circles. Blue crosses indicate θ and ϕ at S_0 min. or MECXs. Results (a) in hexane, (b) in ethylene glycol, and (c) without a solvent.

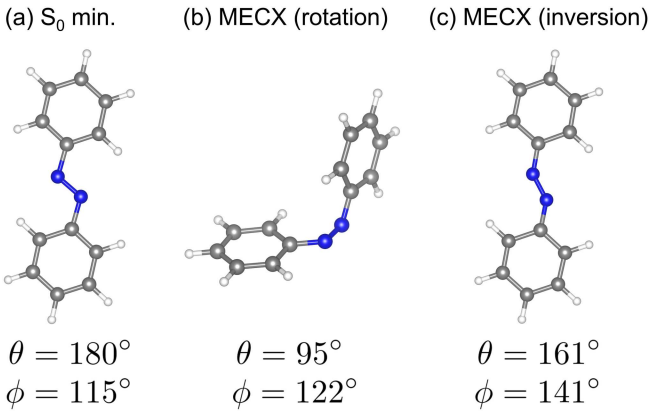

Fig. 5.5: (a) S_0 stable geometry, (b) S_1/S_0 MECX corresponding to rotation, and (c) S_1/S_0 MECX corresponding to inversion, optimized using SF-TD-DFTB.

Table 5.2: Fractions of rotation and inversion channels among all (2000) trajectories, with 95% confidence intervals.

Solvent	rotation	inversion
hexane	48.4 ± 2.2%	20.5 ± 1.8%
Ethylene glycol	45.4 ± 2.2%	14.8 ± 1.6%
None (gas phase)	93.1 ± 1.1%	6.7 ± 1.1%

Note that the denominator is the *total* number of trajectories, i.e., 2000, regardless of whether they underwent $S_1 \rightarrow S_0$ transitions within 1 ps. Table 5.2 indicates that the contribution of the rotation channel follows the order ethylene glycol solution (45.4 ± 2.2%) < hexane solution (48.4 ± 2.2%) < gas phase (93.1 ± 1.1%), where the error ranges indicated by ± are the 95% confidence intervals obtained via the bootstrap method. This result clarifies that rotation is hindered by the presence of solvents and suggests that this effect is stronger in the high-viscosity solvent (ethylene glycol) than in the low-viscosity one (hexane). In addition, Table 5.2 shows that the contributions of the inversion path in the ethylene glycol solution (14.8 ± 1.6%) and in the hexane solution (20.5 ± 1.8%) are larger than that in the gas phase (6.7 ± 1.1%), which implies that the suppression of rotation by the solvents increased the relative importance of the inversion channel. The smaller contribution of inversion in the ethylene glycol solution (14.8 ± 1.6%) compared to that in the hexane solution (20.5 ± 1.8%) suggests that not only the rotation channel but also the inversion channel depends on the solvent viscosity.

5.4 Conclusion

The DC-SF-TD-DFTB/FSSH simulations showed that the presence of solvents elongates the excited-state lifetime of *trans*-azobenzene compared with that in the gas phase. In addition, the lifetime in ethylene glycol, a high-viscosity solvent, was longer than that in hexane, a low-viscosity solvent, which is consistent with previous experimental results.[3] The longer excited-state lifetime in solutions compared to that in the gas phase was found to be ascribed to suppression of the rotation mechanism (twisting of the N=N bond) by the presence of solvents. In addition, the results suggested that the difference between the lifetimes in the hexane and

ethylene glycol solutions results from the solvent viscosity dependence of both the rotation and inversion (rotation around the N=N−C angle) channels.

References

[1]H. M. D. Bandara and S. C. Burdette, *Chem. Soc. Rev.* **41**, 1809 (2012).

[2]Y. Ootani, K. Satoh, A. Nakayama, T. Noro, and T. Taketsugu, *J. Chem. Phys.* **131**, 194306 (2009).

[3]C.-W. Chang, Y.-C. Lu, T.-T. Wang, and E. W.-G. Diau, *J. Am. Chem. Soc.* **126**, 10109 (2004).

[4]Y. Nishimura and H. Nakai, *J. Comput. Chem.* **40**, 1538 (2019).

[5]M. Gaus, A. Goez, and M. Elstner, *J. Chem. Theory Comput.* **9**, 338 (2013).

[6]S. Grimme, J. Antony, S. Ehrlich, and H. Krieg, *J. Chem. Phys.* **132**, 154104 (2010).

[7]E. R. Johnson and A. D. Becke, *J. Chem. Phys.* **123**, 024101 (2005).

[8]M. J. Abraham, T. Murtola, R. Schulz, S. Páll, J. C. Smith, B. Hess, and E. Lindahl, *SoftwareX* **1-2**, 19 (2015).

[9]H. C. Andersen, *J. Chem. Phys.* **72**, 2384 (1980).

[10]H. Uratani, T. Morioka, T. Yoshikawa, and H. Nakai, *J. Chem. Theory Comput.* **16**, 7299 (2020).

[11]S. Maeda, K. Ohno, and K. Morokuma, *J. Chem. Theory Comput.* **6**, 1538 (2010).

Chapter 6

Coupled Structural–Electronic Dynamics of Photoexcited Lead Iodide Perovskites[†]

6.1 Introduction

The opto-electronic properties of LHPs have drawn attention in the context of solar-cell applications.[2–4] Nowadays, the usage of LHPs has been widened to include not only solar cells but also, for example, light-emitting devices.[5] As a basis for rational material design, the excited-state dynamics of this class of materials must be understood from a fundamental point of view. Driven by this motivation, experimental evidences have been accumulated to characterize the behavior of the photoexcited LHPs, mostly by means of time-resolved spectroscopy techniques. It has been revealed that the excitons promptly dissociates into free carriers with the small energy barrier comparable to the thermal energy at the room temperature.[6–9] In addition, hot carrier cooling process in LHPs has interested many physical chemists, because of the possibility of surpassing Schockley–Queisser limit of the efficiency by harvesting the hot carriers.[10–16] Character of polarons in LHPs, which may involve the charge carrier properties, has been also deeply discussed.[17–19]

As well as the experiments, quantum-chemistry-based simulations are powerful tools, which

[†]Reprinted with permission from Ref. [1]. Copyright 2020 American Chemical Society.

are especially advantageous to gain microscopic insights. In LHPs, photogenerated charge carriers cause structural deformation in their surroundings, which acts back on the electronic state, resulting in polaron formation.[17,18] Polaron formation has been mainly studied using adiabatic ground-state quantum chemical calculations, including MD. For instance, Neukirch and co-workers investigated the character of polarons in LHPs based on structures optimized at the Kohn–Sham DFT level.[20,21] Quantum mechanical MD simulations of the polaron formation process have also been reported.[22–24] In these studies, the relationship between the charge distribution and the structural deformation was discussed within the adiabatic regime.

The other aspect of charge carrier dynamics involves nonadiabatic processes, where electronic dynamics must be explicitly treated. Hot carrier cooling is such a phenomenon; the charge carriers relax to the band edge by dissipating the excess energy via electron–phonon interactions.[15] In addition, treatment of non-radiative recombination of positive and negative charge carriers also requires a nonadiabatic framework.[25] In typical computational approaches for problems of this type, the electronic dynamics are simulated under the CPA[26] because of its efficiency. CPA assumes that the nuclear dynamics are governed purely by the thermal kinetic energy and not affected by the electronic dynamics. In practical computations, the nuclear trajectories are generated using adiabatic MD simulations, and the electronic wavefunction is propagated on the pre-determined nuclear trajectories. Based on this approach, Long, Prezhdo, and co-workers conducted a series of studies covering a wide range of situations including the presence of grain boundaries,[27] doped chlorine,[28] defects,[29] A-site cation substitution,[30,31] and oxygen species.[32] Some of these studies are summarized in their review papers.[25,33] Madjet et al. focused on the dependence of the hot carrier cooling rate on the A-site cation species.[34] Kilin and co-workers investigated the electronic dynamics in LHP nanoclusters from the viewpoint of quantum confinement,[35] spin–orbit coupling,[36,37] and polaron excited states.[38] Wang and co-workers elucidated the effect of interstitial iodine on hot carrier cooling.[39]

In real situations, the electronic and structural DOFs should be coupled with each other. The nuclear motion modulates the propagation of the electronic wavefunction, and the change

in the electronic wavefunction affects the atomic motion through the force acting on the nuclei. However, the adiabatic MD and the CPA approaches ignore the former and the latter effects, respectively. For this reason, to the best of the author's knowledge, the interplay between these two dynamics has not been fully investigated to date. In this work, the nonadiabatic dynamics of photogenerated charge carriers in LHPs was simulated by incorporating the two-way interaction between the electronic and structural DOFs by means of FSSH[40] without CPA. To make the simulations practical with the realistic quantity of computational resources, the excitation energy, excited state wavefunctions, and force acting on the nuclei were obtained using the LR-TD-DFTB method,[41] which is a parametrically approximate analogue of LR-TD-DFT.

6.2 Computational Details

LR-TD-DFTB is an extension of the DFTB method[42,43] to excited-state calculations in the same way as DFT has been extended to LR-TD-DFT. DFTB is a computational method to treat the electronic structure and atomic dynamics at low computational cost but comparable accuracy to that of DFT by introducing some empirical parametrization. In particular, the efficacy of DFTB to describe the electronic character and structural dynamics of LHPs has been established by previous studies.[24,44] The nonadiabatic dynamics were treated by the FSSH technique. For each FSSH trajectory, the electronic wavefunction was described as a linear combination of adiabatic wavefunctions, and the nuclear dynamics were approximated as a classical trajectory. The electronic wavefunction and nuclear geometry were propagated simultaneously according to TD Schrödinger equation and Newton's equation, respectively. The force acting on the nuclei was calculated on-the-fly at the active adiabatic state, which stochastically hops to another state according to the population variation in the electronic wavefunction. The fully quantum electronic–nuclear dynamics were approximated by a swarm of independent FSSH trajectories.

All DFTB and LR-TD-DFTB calculations were performed at the closed-shell SCC-DFTB (DFTB2) level[43] under periodic boundary conditions. Only singlet excited states were solved in

the LR-TD-DFTB calculations. The developmental version of the DCDFTBMD code,[45] in which the TD-DFTB/FSSH technique was implemented, was used for all DFTB calculations unless otherwise noted. For visualization, VESTA software was utilized.[46]

The parameters for DFTB are composed of two parts: the electronic part defined for each element and the repulsive part given for each pair of elements. The parameter set was newly constructed for I, Pb, Cs, and the element pairs regarding them using ADPT program package.[47] For other elements and element pairs, the 3OB parameter set[48,49] was employed. Further details of the parameter optimization are described in Appendix B. As shown in Appendix B, the band gap and vibrational spectra of lead iodide perovskites calculated by DFTB with the constructed parameter set agreed well with the DFT results obtained using the PBE exchange–correlation functional.[50] Because previous studies, e.g., Refs. [25, 27–34, 39] have established that PBE provides reasonable results for the nonadiabatic dynamics of LHPs, PBE is considered to be a suitable reference to evaluate the accuracy of the DFTB parametrization in the context of the present study. While the effect of SOC on the rate of hot carrier cooling and non-radiative recombination has been discussed in several previous studies,[36,37,51,52] the SOC was not considered in the present calculations. It is widely recognized that PBE reproduces the experimental band gap of the lead iodide perovskites well when the SOC is not included. This is because of the cancellation of the neglect of SOC and the self-interaction error inherent in the generalized gradient approximation. It should be noted that PBE has been used without including the SOC for the nonadiabatic dynamics in Refs. [25, 27–34, 39], of which the results were not unreasonable.

In this study, $2\times2\times2$ supercells of tetragonal $CsPbI_3$ and $MAPbI_3$ (MA = CH_3NH_3), which are composed of 160 and 384 atoms, respectively, were constructed and utilized as model systems. These structures are depicted in Fig. 6.1. In the FSSH simulations, the propagation of the electronic wavefunction was performed using the LD method.[53] Because the LD method requires the calculation of the overlap between the adiabatic wavefunctions at adjacent nuclear time steps, the OD approach was employed for this purpose.[54] The decoherence effect was

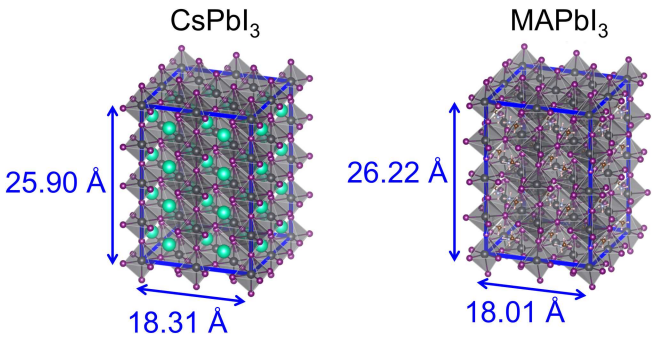

Fig. 6.1: Tetragonal $2 \times 2 \times 2$ supercell structures employed for calculations as model systems. Simulation cells of $CsPbI_3$ and $MAPbI_3$ systems are composed of 160 and 384 atoms, respectively. The gray, purple, green, brown, blue, and pink spheres represent Pb, I, Cs, C, N, and H atoms, respectively. The cell boundary is indicated by blue solid lines.

Table 6.1: Number of solved adiabatic states (N_{state}).

System	E_{init}	N_{state}
$CsPbI_3$	E_0	10
$CsPbI_3$	$E_0 + 0.4\,\text{eV}$	100
$MAPbI_3$	E_0	15
$MAPbI_3$	$E_0 + 0.4\,\text{eV}$	90

approximately included with the simplified decay of mixing technique,[55] which is typically combined with LR-TD-DFTB-based FSSH.[56,57] The initial conditions (nuclear geometries and velocities) for FSSH simulations were sampled from the ground-state DFTB-MD trajectory in the *NVE* ensemble, which was followed by a thermalization run of 4 ps with the temperature adjusted to 298.15 K by rescaling the velocity every 200 fs. The interval between the subsequent sampling was at least 100 fs. A nuclear time step of 0.05 fs was employed for the FSSH simulations. The initial adiabatic states for the FSSH were chosen on the basis of the initial excitation energy, E_{init}. To compare the band-edge and hot carrier dynamics, two different initial conditions were considered: $E_{\text{init}} = E_0$, and $E_{\text{init}} = E_0 + 0.4\,\text{eV}$. E_0 is the lowest excitation energy averaged over the initial geometries, and their values are 1.83 and 1.70 eV for $CsPbI_3$ and $MAPbI_3$, respectively. The conditions of $E_{\text{init}} = E_0$ and $E_{\text{init}} = E_0 + 0.4\,\text{eV}$ correspond to the band-edge and hot carriers, respectively. For each condition, 201 or more FSSH trajectories were collected and the results were averaged to obtain reasonable statistical convergence. The number of solved adiabatic states are listed in Table 6.1. Each FSSH trajectory ran for 500 fs.

6.3 Results and Discussion

6.3.1 Exciton Dissociation and Charge Localization

The population of positive and negative charge carriers are described in density-matrices-like forms:

$$\mathbf{\Gamma}^{+} = (\mathbf{X} + \mathbf{Y})\,(\mathbf{X} + \mathbf{Y})^{\dagger}\,, \tag{6.3.1}$$

$$\mathbf{\Gamma}^{-} = (\mathbf{X} + \mathbf{Y})^{\dagger}\,(\mathbf{X} + \mathbf{Y})\,, \tag{6.3.2}$$

respectively. Here, $\mathbf{X}$ and $\mathbf{Y}$ are the excitation and de-excitation amplitudes, respectively. The dimension of both $\mathbf{X}$ and $\mathbf{Y}$ is $N_{\mathrm{occ}} \times N_{\mathrm{vir}}$, where N_{occ} and N_{vir} are the numbers of occupied and virtual MOs, respectively. Using Mulliken charge analysis, the atomic population of positive and negative charge carriers can be obtained as

$$q_A^{+/-} = \sum_{\mu \in A} \left(\mathbf{D}^{+/-}\mathbf{S}\right)_{\mu\mu}\,. \tag{6.3.3}$$

Here, $\mathbf{S}$ is the overlap matrix of AOs. A and μ are the indices of atoms and AOs. $+/-$ takes $+$ and $-$ for the value regarding positive and negative charge carriers, which are calculated from $\mathbf{\Gamma}^{+}$ and $\mathbf{\Gamma}^{-}$, respectively, and this usage is hereafter used in this chapter. $\mathbf{D}^{+}$ and $\mathbf{D}^{-}$ are defined as

$$\mathbf{D}^{+} = \mathbf{C}^{\mathrm{O}}\mathbf{\Gamma}^{+}\mathbf{C}^{\mathrm{O}\dagger}, \tag{6.3.4}$$

$$\mathbf{D}^{-} = \mathbf{C}^{\mathrm{V}}\mathbf{\Gamma}^{-}\mathbf{C}^{\mathrm{V}\dagger}, \tag{6.3.5}$$

where $\mathbf{C}^{\mathrm{O}}$ and $\mathbf{C}^{\mathrm{V}}$ are the MO coefficient matrices for occupied and virtual orbitals, respectively.

The charge separation can be measured from the spatial overlap between the positive and negative charge carriers. Here, the amount of spatial overlap was quantified as the inner product

of the atomic population of positive and negative charge carriers, s:

$$s = \sum_A q_A^+ q_A^- . \tag{6.3.6}$$

The calculated time-course changes of s are presented in Fig. 6.2(a). The decay patterns of s suggest that the time scale of the exciton dissociation is around 10^1–10^2 fs, which seems consistent with the experimental result (ca. 50 fs).[9] The visualized spatial distribution of charge carriers is shown in Fig. 6.2(b) for a representative trajectory of $CsPbI_3$ in the case of $E_{\text{init}} = E_0 + 0.4\,\text{eV}$. At $t = 0\,\text{fs}$, the positive (red) and negative (blue) charge carriers are delocalized and overlapped each other, whereas the carriers are dissociated at $t = 300\,\text{fs}$.

Spatial delocalization of the charge carriers was quantified by index $d^{+/-}$, which is defined as[24]

$$d^{+/-} = \left[\sum_A \left(q_A^{+/-} \right)^2 \right]^{-1} . \tag{6.3.7}$$

$d^{+/-}$ can be interpreted as the number of atoms that characterizes the locality of the charge carrier density. Fig. 6.2(c) shows the time-course change of $d^{+/-}$. $d^{+/-}$ rapidly decreases within the characteristic time in the order of 10^1–10^2 fs, which is similar to the time scale of the decrease in s, indicating that the charge carriers are localized concurrently with the exciton dissociation. This result implies that exciton dissociation and polaron formation are mutually coupled processes.

6.3.2 Energetics of Charge Carriers

The energies of the positive and negative charge carriers are obtained from the excitation energy decomposition as follows. In LR-TD-DFTB, the excitation energy, E, is described as

$$E = \langle \mathbf{X} + \mathbf{Y} \,|\, (\mathbf{A} + \mathbf{B}) \,|\, \mathbf{X} + \mathbf{Y} \rangle , \tag{6.3.8}$$

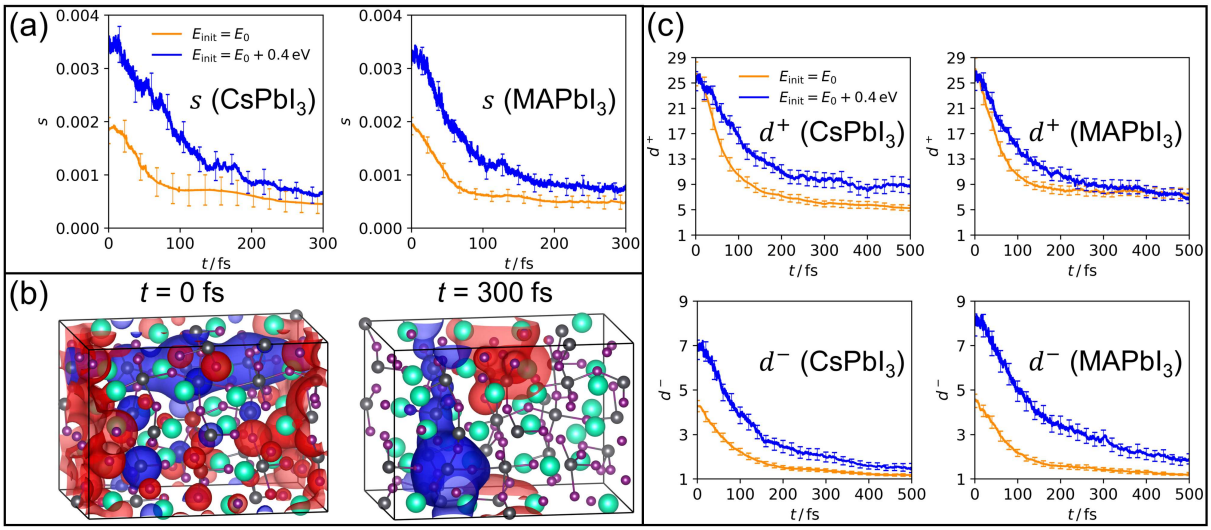

Fig. 6.2: (a) Time-course changes of the averaged spatial overlap, s, between positive and negative charge carriers. Error bars indicate the 95% confidence interval. (b) Snapshots of the spatial charge carrier distribution for a representative trajectory of $CsPbI_3$ with $E_{init} = E_0 + 0.4\,eV$. Positive and negative charge carriers are represented by red and blue isosurfaces, respectively. (c) Time-course changes of averaged charge delocalization indices d^+ (for positive charge carrier) and d^- (for negative charge carrier). Error bars indicate the 95% confidence interval.

where

$$(A+B)_{ia,jb} = \delta_{ij}\delta_{ab}\left(\epsilon_a - \epsilon_i\right) + \left(K_{ia,jb} + K_{ia,bj}\right). \tag{6.3.9}$$

Here, (i, j) and (a, b) are the indices of occupied and virtual MOs, respectively. ϵ_p is the energy level of the p-th MO. $K_{ia,jb}$ and $K_{ia,bj}$ are the coupling matrices, whose explicit form in the case of LR-TD-DFTB can be found elsewhere.[41] Using Eqs. 6.3.1, 6.3.2, 6.3.8, and 6.3.9, the excitation energy can be decomposed into three terms:

$$E = E^+ + E^- + E', \tag{6.3.10}$$

where

$$E^+ = -\sum_i \epsilon_i \Gamma^+_{ii}, \tag{6.3.11}$$

$$E^- = \sum_a \epsilon_a \Gamma^-_{aa}, \tag{6.3.12}$$

$$E' = \left\langle \mathbf{X}+\mathbf{Y} \middle| \left(K_{ia,jb} + K_{ia,bj}\right) \middle| \mathbf{X}+\mathbf{Y} \right\rangle. \tag{6.3.13}$$

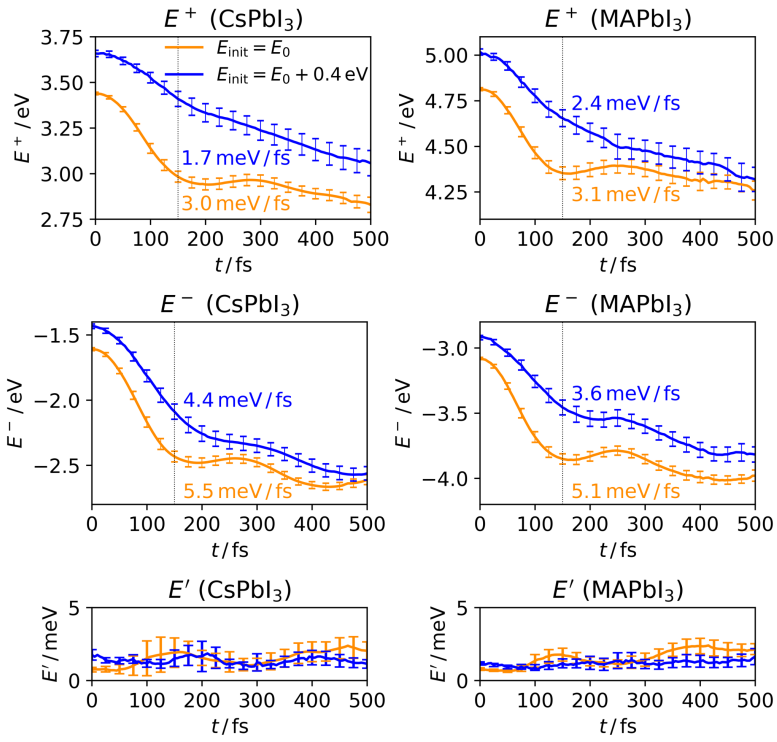

Fig. 6.3: Time-course changes of averaged E^+, E^-, and E'. Energy decay rates for the time range of 0 fs $\leq t \leq$ 150 fs are also shown with the corresponding colors. Error bars indicate the 95% confidence interval.

The time-course changes of E^+, E^-, and E' are plotted in Fig. 6.3. Note that, in Fig. 6.3, the unit of E' is the milielectronvolt (meV), whereas the unit of E^+ and E^- is the electronvolt (eV). Figure 6.3 suggests that the third term, E', is negligibly small in absolute value compared to those of E^+ and E^-. Because E^+ arises from the occupied orbital energy and occupation (Eq. 6.3.11) and E^- from the virtual orbital energy and occupation (Eq. 6.3.12), E^+ and E^- can be interpreted as the energies of the positive and the negative charge carriers, respectively. Figure 6.3 also presents the initial energy decay rates measured for the time range from $t = 0$ fs to $t = 150$ fs, where the decay patterns are quasi-linear. The calculated initial energy decay rates fall within the range of 1.7 to 5.5 meV / fs, which is reasonable compared to the experimental results (3.0 and 4.6 meV / fs for $CsPbI_3$ and $MAPbI_3$, respectively[19]).

Figure 6.4(a) shows the averaged time-course changes of the orbital occupations with positive and negative charge carriers. Here, the occupations are defined as Γ^+_{pp} and Γ^-_{pp}, respectively, where p is the MO index. In the case of band-edge carriers ($E_{\text{init}} = E_0$), the orbital occupations are dominated by the HOMO and the LUMO, and the occupations of the remaining orbitals are

approximately zero. On the other hand, in the case of hot carriers ($E_{\mathrm{init}} = E_0 + 0.4\,\mathrm{eV}$), the situation changes. At $t = 0\,\mathrm{fs}$, the occupations are distributed over multiple MOs including those deeper than the HOMO and shallower than LUMO. As time t, the occupations gradually cumulate to the HOMO and LUMO, indicating the relaxation of hot carriers. In addition, Fig. 6.4(b) shows the averaged time-course changes of the orbital energies around the band edge, which reflect the structural deformation in response to the existence of carriers, i.e., polaron formation. The occupied/virtual orbitals become shallower/deeper, resulting in the stabilization of positive/negative carriers. Overall, the change in the orbital occupation (Fig. 6.4(a)) and the orbital energies (Fig. 6.4(b)) suggest that hot carrier cooling and polaron formation simultaneously involve the decay of the carrier energy (Fig. 6.3).

Time-course changes of the adiabatic potential energy for representative trajectories are presented in Fig. 6.4(c). Nonadiabatic transitions are not observed in the case of $E_{\mathrm{init}} = E_0$, suggesting that band edge carriers behave adiabatically. This result supports the validity of the previous treatment of *band-edge* carriers with adiabatic MD simulations.[22–24] On the other hand, the dynamics in the case of $E_{\mathrm{init}} = E_0 + 0.4\,\mathrm{eV}$, i.e., hot carriers, features a large number of nonadiabatic transitions.

6.3.3 Structural Deformation

According to the previous study,[24] the structural deformation associated with the polaron formation can be measured using the following index,

$$Z_{+/-} = \frac{\sum_A q_A^{+/-} Z_A}{\sum_A q_A^{+/-}}, \tag{6.3.14}$$

where Z_A is an arbitrary structural quantity of interest, e.g., bond length, regarding the atom A. $Z_{+/-}$, which is the weighted average of Z_A about $q_A^{+/-}$, represents the value of Z_A in the region where the positive/negative charge carrier is localized. Because most of the positive and negative charge carrier populations are located on I and Pb atoms, respectively, the index A in

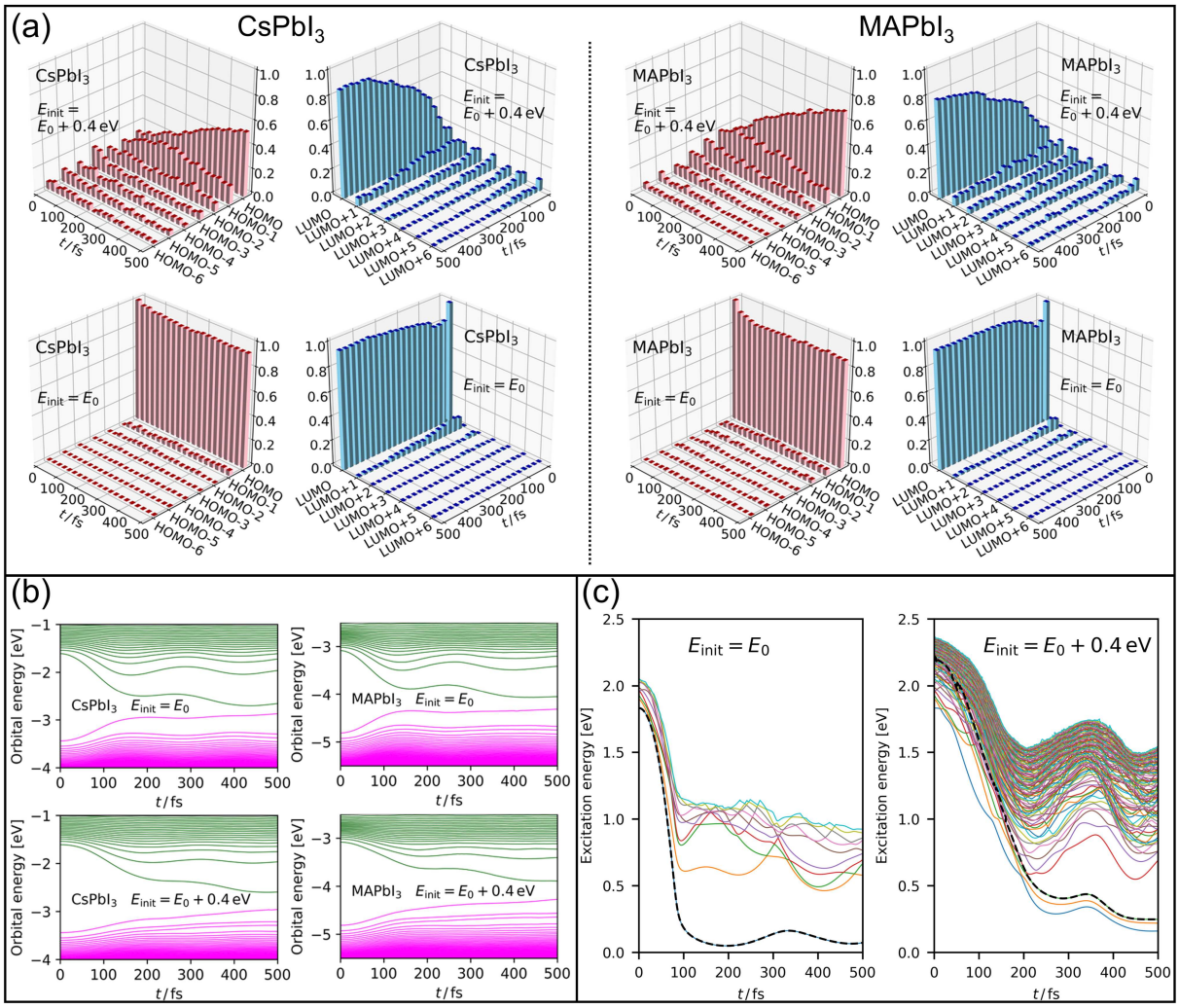

Fig. 6.4: (a) Time-course changes of averaged orbital population of positive (red) and negative (blue) charge carriers. (b) Time-course changes of averaged orbital energies. Magenta and green lines indicate occupied and virtual orbital energies, respectively. (c) Time-course changes of adiabatic potential energy for representative trajectories of $CsPbI_3$.

Eq. 6.3.14 runs over I and Pb atoms for negative and positive charge carriers, respectively.

The time-course change of the Pb–I bond length was calculated in the region where the charge carriers are localized. In other words, $Z_{+/-}$ in Eq. 6.3.14 was computed by substituting the Pb–I distance $r_{\mathrm{Pb–I}}$ for Z_A. The definition of $r_{\mathrm{Pb–I}}$ is illustrated in Fig. 6.5(a). The results are shown in Fig. 6.5(b). For both positive and negative charge carriers, the Pb–I bond length increases with time. This result can be qualitatively understood from an electrostatic point of view. Whereas Pb and I are partially cationic and anionic, respectively, the positive and negative charge carriers are located on I and Pb atoms, respectively. Thus, the Pb–I bond elongation reduces the Coulombic repulsion between the negative charge carriers and I atoms, and between the positive charge carriers and Pb atoms.

The structural motion of another component of LHPs, i.e., the A-site cations, were analyzed using a similar approach utilizing Eq. 6.3.14. Fig. 6.5(c) shows the time-course changes of $r_{\mathrm{I–A}}(r_{\mathrm{Pb–A}})$, which are the distances between the A-site cation and I(Pb) in the region where the charge carriers populate, as depicted in Fig. 6.5(a). Note that the position of each MA cation is defined as its centroid. In the case of positive charge carriers, the distance between the A-site cations and I atoms increases with time, reflecting the Coulombic interaction between the A-site cations and the positive charge carrier. The same explanation can be applied to the decrease in the distance between the A-site cations and Pb atoms in the case of negative charge carriers. In addition, Fig. 6.5(d) indicates the time-course change of angle θ of the MA cations (in $MAPbI_3$). As depicted in Fig. 6.5(a), θ is defined as the angle between the I(Pb) $\rightarrow$ MA vector and the dipole moment vector $\boldsymbol{\mu}$ of the MA cation. θ increases and decreases in the case of positive and negative charge carriers, respectively, suggesting that the MA cations rotate in a direction favorable in terms of the electrostatic charge–dipole interactions.

Notably, the sub-picoseconds time scales of the structural deformation shown in Figs. 6.5(b)–6.5(d) are consistent with the experimentally observed characteristic time of the polaron formation (ca. 400 fs[19]).

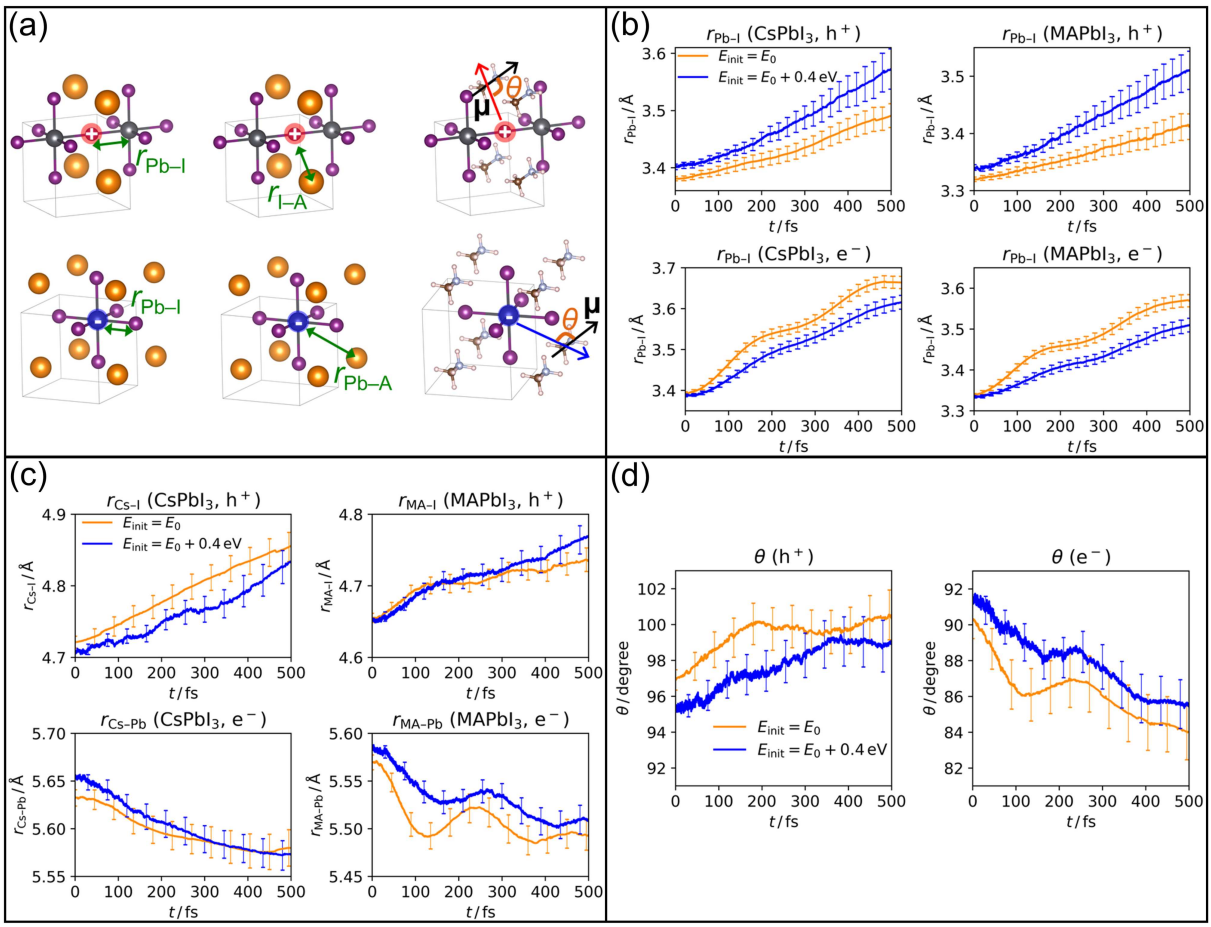

Fig. 6.5: (a) Schematic illustration of the definition of structural quantities under discussion. Atoms on which positive and negative charge carriers populate are indicated as red and blue circles, respectively. Orange spheres represent A-site cations. $\boldsymbol{\mu}$ is the electric dipole moment vector of MA cation. The red arrows are vectors connecting I and the centers of MA cations. The blue arrows are vectors connecting Pb and the centers of the MA cations. (b)–(d) Time-course change of structural quantities in the region where positive (h^+) and negative (e^-) charge carriers are localized, as calculated using Eq. 6.3.14. Error bars indicate the 95% confidence interval. (b) Pb–I bond length, (c) distance between A-site cation and I (for positive charge carrier) or Pb (for negative charge carrier), and (d) angle θ of MA cations.

6.4 Conclusion

In summary, the excited-state dynamics of two representative LHPs, $CsPbI_3$ and $MAPbI_3$, were simulated using the LR-TD-DFTB-based FSSH technique. The mutual dependence of electronic and nuclear dynamics was incorporated in the simulations. Exciton dissociation, decay of the carrier energy, and polaron formation were observed at similar time scales. In addition, these time scales are in reasonable agreement with the experimental results. The calculation results suggest that two factors simultaneously involve the decay of the carrier energy: the relaxation of positive/negative carriers to the HOMO/LUMO and the variation of the orbital energy invoked by the structural deformation. The systems behave adiabatically when the initial excitation energy is at its lowest ($E_{\mathrm{init}} = E_0$), i.e., band-edge carriers, whereas a large number of nonadiabatic transitions were observed in the case of hot carriers ($E_{\mathrm{init}} = E_0 + 0.4\,\mathrm{eV}$). The structural deformation was observed in both the inorganic framework (Pb and I) and A-site cations (Cs^+ or MA^+). Regarding the inorganic framework, the Pb–I bond length increased for both positive and negative charge carriers. For A-site cations, the distance between the A-site cation and Pb, where the negative charge carriers populate, decreased with time. On the other hand, the distance between the A-site cation and I, i.e., the center of positive charge carrier, increased. In addition, the rotational dynamics of dipolar MA^+ were observed in the direction that reduces the electrostatic charge–dipole interaction between MA^+ and the charge carriers. These behaviors suggest that the structural deformation associated with polaron formation is mainly governed by the interatomic electrostatic interaction. The results reported herein shed light on the importance of coupling between the structural and the electronic dynamics in the photoexcited states of LHPs.

References

[1]H. Uratani and H. Nakai, *J. Phys. Chem. Lett.* **11**, 4448 (2020).

[2]A. Kojima, K. Teshima, Y. Shirai, and T. Miyasaka, *J. Am. Chem. Soc.* **131**, 6050 (2009).

[3]J.-H. Im, C.-R. Lee, J.-W. Lee, S.-W. Park, and N.-G. Park, *Nanoscale* **3**, 4088 (2011).

[4]H.-S. Kim, C.-R. Lee, J.-H. Im, K.-B. Lee, T. Moehl, A. Marchioro, S.-J. Moon, R. Humphry-Baker, J.-H. Yum, J. E. Moser, M. Grätzel, and N.-G. Park, *Sci. Rep.* **2**, 591 (2012).

[5]S. Colella, M. Mazzeo, A. Rizzo, G. Gigli, and A. Listorti, *J. Phys. Chem. Lett.* **7**, 4322 (2016).

[6]Y. Yamada, T. Nakamura, M. Endo, A. Wakamiya, and Y. Kanemitsu, *IEEE J. Photovolt.* **5**, 401 (2015).

[7]L. Q. Phuong, Y. Yamada, M. Nagai, N. Maruyama, A. Wakamiya, and Y. Kanemitsu, *J. Phys. Chem. Lett.* **7**, 2316 (2016).

[8]S. A. March, C. Clegg, D. B. Riley, D. Webber, I. G. Hill, and K. C. Hall, *Sci. Rep.* **6**, 39139 (2016).

[9]A. Jha, H.-G. Duan, V. Tiwari, P. K. Nayak, H. J. Snaith, M. Thorwart, and R. J. D. Miller, *ACS Photonics* **5**, 852 (2018).

[10]G. Xing, N. Mathews, S. Sun, S. S. Lim, Y. M. Lam, M. Grätzel, S. Mhaisalkar, and T. C. Sum, *Science* **342**, 344 (2013).

[11]M. B. Price, J. Butkus, T. C. Jellicoe, A. Sadhanala, A. Briane, J. E. Halpert, K. Broch, J. M. Hodgkiss, R. H. Friend, and F. Deschler, *Nat. Commun.* **6**, 8420 (2015).

[12]H. Zhu, K. Miyata, Y. Fu, J. Wang, P. P. Joshi, D. Niesner, K. W. Williams, S. Jin, and X.-Y. Zhu, *Science* **353**, 1409 (2016).

[13]Z. Guo, Y. Wan, M. Yang, J. Snaider, K. Zhu, and L. Huang, *Science* **356**, 59 (2017).

[14]J. Fu, Q. Xu, G. Han, B. Wu, C. H. A. Huan, M. L. Leek, and T. C. Sum, *Nat. Commun.* **8**, 1300 (2017).

[15]M. Li, J. Fu, Q. Xu, and T. C. Sum, *Adv. Mater.* **31**, 1802486 (2019).

[16]X. T. Nguyen, D. Timmer, Y. Rakita, D. Cahen, A. Steinhoff, F. Jahnke, C. Lienau, and A. De Sio, *J. Phys. Chem. Lett.* **10**, 5414 (2019).

[17]X.-Y. Zhu and V. Podzorov, *J. Phys. Chem. Lett.* **6**, 4758 (2015).

[18]K. Miyata, D. Meggiolaro, M. T. Trinh, P. P. Joshi, E. Mosconi, S. C. Jones, F. De Angelis, and X.-Y. Zhu, *Sci. Adv.* **3**, e1701217 (2017).

[19]S. A. Bretschneider, I. Ivanov, H. I. Wang, K. Miyata, X. Zhu, and M. Bonn, *Adv. Mater.* **30**, 1707312 (2018).

[20]A. J. Neukirch, W. Nie, J.-C. Blancon, K. Appavoo, H. Tsai, M. Y. Sfeir, C. Katan, L. Pedesseau, J. Even, J. J. Crochet, G. Gupta, A. D. Mohite, and S. Tretiak, *Nano Lett.* **16**, 3809 (2016).

[21]L. Zhou, C. Katan, W. Nie, H. Tsai, L. Pedesseau, J. J. Crochet, J. Even, A. D. Mohite, S. Tretiak, and A. J. Neukirch, *J. Phys. Chem. Lett.* **10**, 3516 (2019).

[22]F. Ambrosio, J. Wiktor, F. De Angelis, and A. Pasquarello, *Energy Environ. Sci.* **11**, 101 (2018).

[23]F. Ambrosio, D. Meggiolaro, E. Mosconi, and F. De Angelis, *ACS Energy Lett.* **4**, 2013 (2019).

[24]H. Uratani, C.-P. Chou, and H. Nakai, *Phys. Chem. Chem. Phys.* **22**, 97 (2020).

[25]J. Jankowska, R. Long, and O. V. Prezhdo, *ACS Energy Lett.* **2**, 1588 (2017).

[26]A. V. Akimov and O. V. Prezhdo, *J. Chem. Theory Comput.* **9**, 4959 (2013).

[27]R. Long, J. Liu, and O. V. Prezhdo, *J. Am. Chem. Soc.* **138**, 3884 (2016).

[28]J. Liu and O. V. Prezhdo, *J. Phys. Chem. Lett.* **6**, 4463 (2015).

[29]W. Li, J. Liu, F.-Q. Bai, H.-X. Zhang, and O. V. Prezhdo, *ACS Energy Lett.* **2**, 1270 (2017).

[30]J. He, W.-H. Fang, and R. Long, *J. Phys. Chem. Lett.* **9**, 4834 (2018).

[31]J. He, W.-H. Fang, R. Long, and O. V. Prezhdo, *ACS Energy Lett.* **3**, 2070 (2018).

[32]J. He, W.-H. Fang, R. Long, and O. V. Prezhdo, *J. Am. Chem. Soc.* **141**, 5798 (2019).

[33]W. Li, R. Long, J. Tang, and O. V. Prezhdo, *J. Phys. Chem. Lett.* **10**, 3788 (2019).

[34]M. E. Madjet, G. R. Berdiyorov, F. El-Mellouhi, F. H. Alharbi, A. V. Akimov, and S. Kais, *J. Phys. Chem. Lett.* **8**, 4439 (2017).

[35]D. J. Vogel, A. Kryjevski, T. Inerbaev, and D. S. Kilin, *J. Phys. Chem. Lett.* **8**, 3032 (2017).

[36]A. Forde, T. Inerbaev, and D. Kilin, *J. Phys. Chem. C* **122**, 26196 (2018).

[37]A. Forde, T. Inerbaev, E. K. Hobbie, and D. S. Kilin, *J. Am. Chem. Soc.* **141**, 4388 (2019).

[38]A. Forde, T. Inerbaev, and D. Kilin, *J. Phys. Chem. C* **124**, 1027 (2020).

[39]S. Banerjee, J. Kang, X. Zhang, and L.-W. Wang, *J. Chem. Phys.* **152**, 091102 (2020).

[40]J. C. Tully, *J. Chem. Phys.* **93**, 1061 (1990).

[41]T. A. Niehaus, S. Suhai, F. Della Sala, P. Lugli, M. Elstner, G. Seifert, and T. Frauenheim, *Phys. Rev. B* **63**, 085108 (2001).

[42]D. Porezag, T. Frauenheim, T. Köhler, G. Seifert, and R. Kaschner, *Phys. Rev. B* **51**, 12947 (1995).

[43]M. Elstner, D. Porezag, G. Jungnickel, J. Elsner, M. Haugk, T. Frauenheim, S. Suhai, and G. Seifert, *Phys. Rev. B* **58**, 7260 (1998).

[44]F. Bi, S. Markov, R. Wang, Y. Kwok, W. Zhou, L. Liu, X. Zheng, G. Chen, and C. Yam, *J. Phys. Chem. C* **121**, 11151 (2017).

[45]Y. Nishimura and H. Nakai, *J. Comput. Chem.* **40**, 1538 (2019).

[46]K. Momma and F. Izumi, *J. Appl. Crystallogr.* **44**, 1272 (2011).

[47]C.-P. Chou, Y. Nishimura, C.-C. Fan, G. Mazur, S. Irle, and H. A. Witek, *J. Chem. Theory Comput.* **12**, 53 (2016).

[48]M. Gaus, A. Goez, and M. Elstner, *J. Chem. Theory Comput.* **9**, 338 (2013).

[49]M. Kubillus, T. Kubař, M. Gaus, J. Řezáč, and M. Elstner, *J. Chem. Theory Comput.* **11**, 332 (2015).

[50]J. P. Perdew, K. Burke, and M. Ernzerhof, *Phys. Rev. Lett.* **77**, 3865 (1996).

[51]F. Zheng, L. Z. Tan, S. Liu, and A. M. Rappe, *Nano Lett.* **15**, 7794 (2015).

[52]W. Li, L. Zhou, O. V. Prezhdo, and A. V. Akimov, *ACS Energy Lett.* **3**, 2159 (2018).

[53]F. Plasser, G. Granucci, J. Pittner, M. Barbatti, M. Persico, and H. Lischka, *J. Chem. Phys.* **137**, 22A514 (2012).

[54]I. G. Ryabinkin, J. Nagesh, and A. F. Izmaylov, *J. Phys. Chem. Lett.* **6**, 4200 (2015).

[55]G. Granucci and M. Persico, *J. Chem. Phys.* **126**, 134114 (2007).

[56]L. Stojanović, S. G. Aziz, R. H. Hilal, F. Plasser, T. A. Niehaus, and M. Barbatti, *J. Chem. Theory Comput.* **13**, 5846 (2017).

[57]E. Posenitskiy, M. Rapacioli, B. Lepetit, D. Lemoine, and F. Spiegelman, *Phys. Chem. Chem. Phys.* **21**, 12139 (2019).

Chapter 7

Nanometer-Scale Polaron Formation in Methylammonium Lead Iodide Perovskite[†]

7.1 Introduction

The opto-electronic applicability of LHP materials was first recognized in the context of utilization for photovoltaics, called PSCs, which realized an exceptionally high photoconversion efficiency.[2,3] Recently, the field of LHP application has grown to include other types of devices, such as light-emitting diodes[4] and phototransistors.[5] LHPs have the general formula $APbX_3$, where A and X denote monovalent cations and halide anions, respectively. The most typical and first LHP used in PSCs is methylammonium lead iodide perovskite ($MAPbI_3$), where an organic molecular cation—methylammonium ($CH_3NH_3^+$, MA^+)—is chosen as cation A.[2] From structural viewpoint, LHP has two components. One is an inorganic framework, which is formally PbX_3^-, composed of corner-sharing PbX_6 octahedra. Because the DOS around the VBM and CBM is dominated by the PbX_3^- framework, the charge carriers are located on this structural part. The other is a sublattice constructed by the A cations, which fill the vacancies

[†]Reproduced from Ref. [1] with permission from the Phys. Chem. Chem. Phys. Owner Socieries.

and compensate for the net negative charge of the PbX_3^- framework. While the A cations have no significant contribution to DOS around the band edge, their indirect effect on the electronic structure through their electrostatic or structural role has been recognized.[6]

The unique properties of charge carriers in LHPs, such as long diffusion length, long lifetime, and low electron–hole recombination rate,[7–12] have been considered to be key to the remarkable performance of LHP-based opto-electronic devices such as PSCs. Therefore, the physics underlying these properties, particularly polarons, i.e., charges wearing structural deformation caused by the polarization potential,[13] has been extensively studied experimentally and theoretically. The polaron formation process, which is a structural motion responding the additional (negative or positive) charge coupled with its electronic state, is a fundamental knowledge needed to unveil the abovementioned charge carrier properties. However, the understanding in this regard is still limited. In particular, some researchers have proposed the importance of rotational motion of organic molecular cations such as MA^+,[14–18] while others have focused on the role of structural deformation in the PbX_3^- frameworks[19–21] rather than the organic molecular cations. This issue has been focused on in conjunction with the recent progress in the opto-electronic applications of LHPs using various cations such as formamidinium (FA^+), Cs^+, and Rb^+.[22–24]

A commonly used model of polarons was proposed by Frölich.[25] In this picture, the lattice is polarized by the Coulomb potential of the charge carrier to produce the polarization potential. This polarization potential acts back on the charge carrier toward self-consistency. Zheng and Wang[26] constructed a model Hamiltonian, which includes the polarization potential as the screened Coulomb potential, as well as the effects of the thermal disorder of the MA^+ and the PbI_3^- lattice as artificial stochastic potential fluctuation. An electronic wavefunction was propagated based on this Hamiltonian. Their simulations were performed with a sufficiently large spatial scale to describe the whole electronic wavefunctions of polarons, whose radii are estimated to be several nanometres.[21,27] The simulations indicated that not only the polarization potential but also the thermal disorder significantly affect the spatial distribution of the

wavefunction, the polaron binding energy, and the transport properties. Note that their model Hamiltonian approach cannot describe atomic motions, although nanoscale simulations can be performed.

In contrast, from the atomistic viewpoint, the mechanism of polaron formation has been investigated for several years using first-principles DFT calculations, which are frequently combined with MD simulations. Neukirch et al.[28] compared the stable geometries of $MAPbI_3$ and $CsPbI_3$ between neutral and charged states, using zero-dimensional cluster models. Yin et al.[29] used DFT-based MD simulations to analyse the structural dynamics of LHP clusters, which are monomers or dimers of PbX_6 octahedral units, with the existence of charge carriers. For bulk LHPs, Miyata et al.[21] compared their time-resolved spectroscopy measurements with DFT calculations in the negatively or positively charged state. In addition, DFT-based MD simulations in the presence of charge carriers were reported by Ambrosio et al.[30,31] These studies[21,28–31] clarified the relationship between charge localization and explicit atomic motions: for example, modulations in Pb–X bond length and the rotation of MA^+.

In the present study, the polaron formation mechanism was studied from both nanoscale and atomistic viewpoints. To capture both real atomic motions and spatial size of the polarons simultaneously, QM-MD simulations were performed for the polaron formation process in $MAPbI_3$ with large model systems, which is beyond the reach of the conventional DFT technique. To overcome the computational burden arising from the system size, this study employed a combined approach of DC method[32–39] and DFTB method,[40–43] referred to as DC-DFTB,[44–46] which is a linear scaling QM technique. Its parallelized implementation, that is, DCDFTBMD code,[46] can perform QM-MD simulations of systems containing thousands of atoms by using parallel computation resources.

The rest of this chapter is organized as follows. Section 7.2 explains the numerical details of the simulations. The results are reported and discussed in Section 7.3. On the basis of the simulations, the extent of charge localization is evaluated (Subsection 7.3.1). Next, the relationship between charge localization and structural deformation is discussed (Subsection

7.3.2). Moreover, the process of structural deformation is discussed in detail by focusing on the early stage of polaron formation (Subsection 7.3.3). From the energetical viewpoint, the importance of the role of PbI_3^- framework and MA cations is discussed (Subsection 7.3.4). Finally, the conclusion is presented in Section 7.4.

7.2 Computational Details

7.2.1 Details of Parameter Fitting

In the DFTB parametrization process, the shape of V_{conf} (Eq. 2.2.2) is subjected to optimization for each element. For the $MAPbI_3$ system, H, Pb, C, I, and N are needed to be parametrized. For H, C, N, and I, the V_{conf} proposed in the previous studies[47,48] was employed. V_{conf} for Pb was newly constructed. The modified Woods–Saxon potential[49] was employed:

$$V_{\mathrm{conf}}(r) = \frac{W}{1 + \exp\left[-a(r - r_0)\right]}, \tag{7.2.1}$$

where the parameters W, a, and r_0 were subjected to optimization. These parameters were tuned to reproduce the band structure of the Pb pure metal obtained by DFT calculations with the PBE formulation of the GGA (GGA-PBE).[50] The obtained set of parameters are listed in Appendix C.2. In the calculations, 5d, 6s, and 6p shells were included for Pb; 5s and 5p for I; and 2s and 2p for H, C, and N. Regarding Pb and I, the Hubbard parameters were calculated for each of the s, p, and d (for Pb) shells, and these shell-dependent values were used. For the other elements, the common Hubbard parameters for s and p shells, which are only dependent on the type of element, were used as described in the literature.[47]

In addition, the repulsive potential E_{rep} was parametrized. E_{rep} is defined for each element pair as a function of interatomic distance, which is typically described by a set of spline functions. As done for V_{conf}, the previously reported E_{rep} was used for element pairs among H, C, N, and I.[47,48] For the Pb–I pair, a new repulsive potential was constructed. In this study, the

fourth-order spline function form was adopted. The function is piecewisely defined as

$$c_0 + c_1(R - R_0) + c_2(R - R_0)^2 + c_3(R - R_0)^3 + c_4(R - R_0)^4, \tag{7.2.2}$$

for each distance range that starts from R_0 and ends at the starting point of the next range or at a sufficiently far cutoff point. In a region shorter than the first starting point, the exponential form was used with adjustable parameters a_1, a_2, and a_3.

$$\exp\left[-a_1 R + a_2\right] + a_3. \tag{7.2.3}$$

The values of the parameters defining the set of functions were fitted to reproduce the atomic forces calculated by GGA-PBE for a set of disordered structures. Note that the repulsive potentials for Pb–(H, Pb, C, N) pairs were omitted because repulsive potentials are only necessary only for a short interatomic distance within the bonding regions; throughout the simulations, for these element pairs such as Pb–C, interatomic distances are so long that the repulsive potential is not meaningful.

To obtain the set of optimized parameters and solve Eq. 2.2.2, the ADPT program package[51] was utilized. All reference GGA-PBE calculations were conducted with VASP code,[52–55] treating the core electrons by using the projector augmented-wave method.[56]

Using the obtained parameter set, the VDOS was calculated and is shown in Fig. 7.1, with the GGA-PBE result as a comparison. The VDOS was obtained by the Fourier transform of velocity autocorrelation functions calculated from MD runs. The DFTB-MD and GGA-PBE-MD runs for VDOS calculations were performed for 15 ps with a time step of 0.25 fs without any geometrical constraint, using $2 \times 2 \times 2$ supercells, whose building block is the optimized tetragonal cell with each method. Prior to the production runs, the equilibration runs were performed at room temperature in the reported scheme.[20] Note that these computational conditions were employed only for VDOS calculations and not for the polaron formation simulations described in detail in the next section. Figure 7.1 shows that the VDOS calculated with DFTB (blue)

agrees with that obtained using GGA-PBE (grey), indicating that DFTB calculations with the constructed parameter set well-reproduce the GGA-PBE results in terms of structural dynamics.

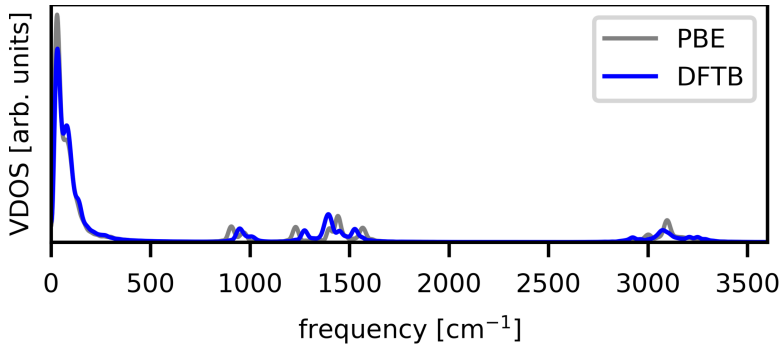

Fig. 7.1: Calculated VDOS from unconstrained *NVE*-MD runs. GGA-PBE and DFTB results are shown by grey and blue lines, respectively.

7.2.2 Calculation Setup

All DFTB calculations, with or without the DC technique, were performed in the orbitally resolved DFTB2[43] level under the periodic boundary condition, using the abovementioned parameter set, unless otherwise noted. As the building block of the simulation cell, the tetragonal unit cell of $MAPbI_3$, which includes four formula units (48 atoms), was optimized with DFTB without DC, as implemented in DFTB+ code[57] using the Γ-centered $6 \times 6 \times 6$ k-point mesh. In this process, both the atomic coordinates and cell parameters were optimized. A slight deviation from the perfect tetragonal unit cell shape was eliminated in the reported manner,[20] which essentially does not affect the cell length (change in the length was smaller than 0.001 Å). The simulation cells were constructed by repeating the optimized unit cell of $MAPbI_3$ four times along each dimension. They contained 3072 atoms and had lattice parameters of $a = b = 36.83$ Å, $c = 53.79$ Å, and $\alpha = \beta = \gamma = 90°$.

DC-DFTB-MD calculations were conducted using the DCDFTBMD program.[44–46] To adopt the DC technique, each unit cell was treated as a subsystem; one simulation cell contained 64 subsystems. For each subsystem, the neighboring subsystems within 8 Å were included as buffer regions. Figure 7.2 compares the averaged wall clock time for one SCC cycle with and without DC in this system in the neutral state. Using the sufficiently large number of CPU

cores, DC-DFTB has the advantage of the order of magnitude compared to DFTB without DC, enabling MD simulations of this system within a feasible computation time.

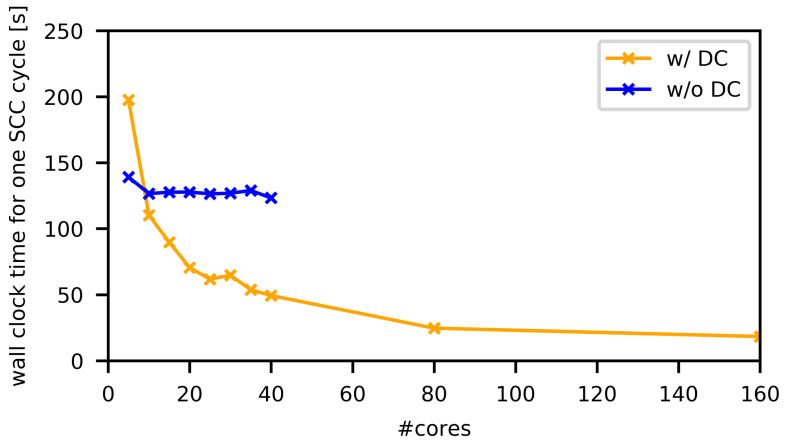

Fig. 7.2: Averaged wall clock time for one SCC cycle with (orange) and without (blue) DC technique on Intel Xeon Gold 6148 (40 cores per computation node). Calculations without DC were parallelized with OpenMP. DC calculations were performed with MPI/OpenMP hybrid parallelization, where five OpenMP threads and #cores/5 MPI processes were used.

Prior to the simulations of the polaron formation process, the system was equilibrated in the charge-neutral state with an *NVT* run of over 6 ps at 298.15 K, followed by an *NVE* run of over 2 ps. Then, the polaron formation process for a negative (positive) charge was initiated by resetting the net system charge -1 (+1) and restarting an *NVE* run. Spin-polarized calculations were conducted in the charged systems. Time steps of 2 and 4 fs were adopted for the *NVE* and *NVT* runs, respectively, with constraints of C–H and N–H bond lengths using the RATTLE method.[58]

7.3 Results and Discussion

7.3.1 Spatial Distribution of Charge Carriers

Throughout this section, the atomic spin population for each atom is defined as its α-spin Mulliken charge minus β-spin one; here, the number of α-spin electrons is larger than that of β-spin ones. The atomic spin population obtained for a snapshot, as depicted in Fig. 7.3, shows that the negative (positive) charge is located on Pb (I) atoms. The results are consistent with the

orbital nature of VBM and CBM, where the p-orbitals of I atoms and those of Pb atoms have a dominant contribution, respectively.

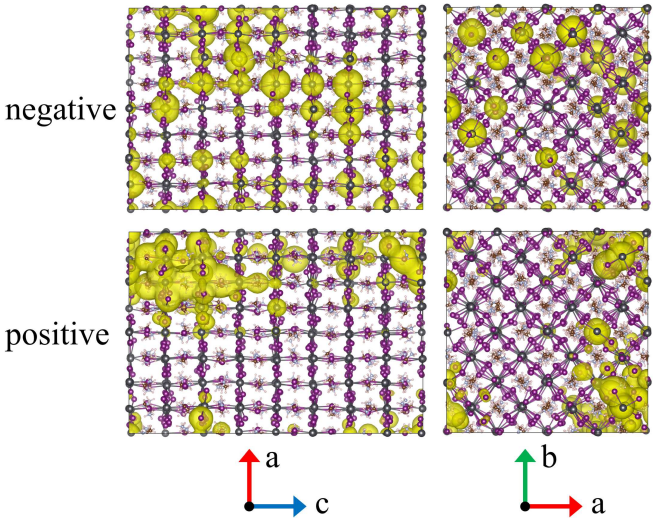

Fig. 7.3: Atomic spin population corresponding to a negative (positive) charge is shown as a yellow iso-surface for a snapshot. For visualization, the atomic spin population values are converted into density at each spatial grid point by multiplying the atom-centered Slater functions. The pink, grey, brown, purple, and blue spheres indicate H, Pb, C, I, and N atoms, respectively.

The radius of the charge carrier was estimated as follows. The number of atoms d, over which an electron or a hole is delocalized, was evaluated as

$$d = \frac{1}{\sum_A p_A^2}, \tag{7.3.1}$$

where p_A is the spin population on the atom A. In Eq. 7.3.1, the index A runs over all atoms (regardless of their type) in the cell. Once d was obtained, the volume V of the negative (positive) charge carrier was estimated as

$$V = V_{\text{cell}} d/n, \tag{7.3.2}$$

where $V_{\text{cell}} = 1.14\,\text{nm}$ is the volume of a tetragonal unit cell of $MAPbI_3$ and $n = 4$ ($n = 12$) is the number of Pb (I) atoms in the unit cell. Finally, the radius of the charge carrier r_{deloc} was evaluated as that of a sphere of volume V. Figure 7.4 shows the time-course change in the radii of negative and positive charge densities. The averaged radii were estimated as 1.1 and 0.9 nm for the negative and positive charge carriers, respectively. Note that the estimated radii

are smaller than the estimation by Frölich model.[21] This is attributable to the structural disorder arising from the thermal motion, which is not considered in the Frölich model; the effect of the thermal motion will be more deeply discussed later.

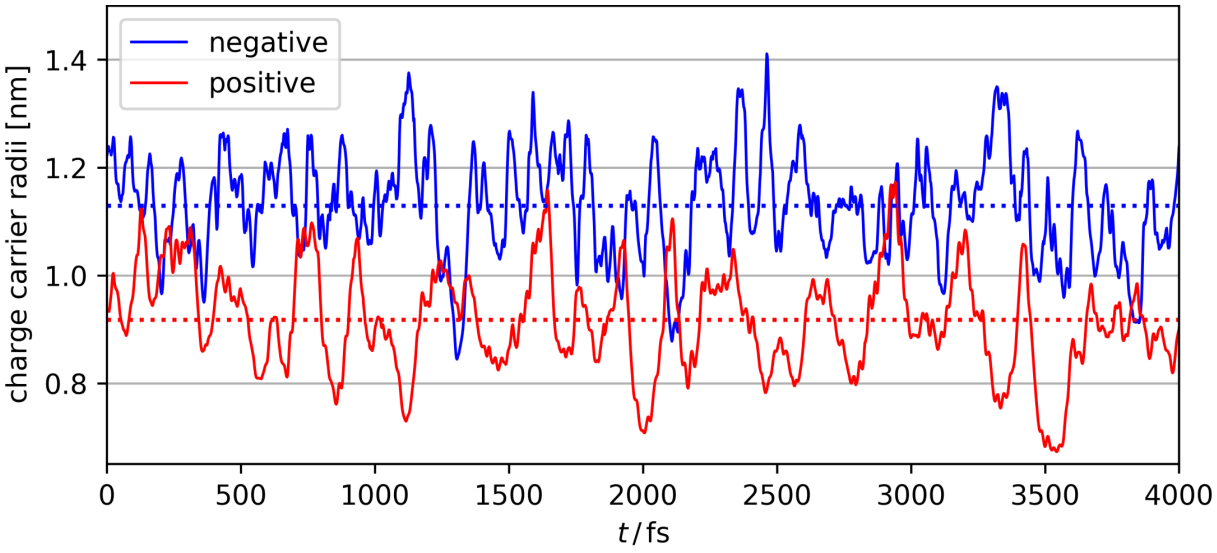

Fig. 7.4: Time course change of negative (blue) and positive (red) charge carrier radii. Averaged values are shown with dashed lines.

7.3.2 Structural Dynamics

Figure 7.5(a) and 7.5(b) show a comparison of the time-course changes in the averaged Pb–I bond lengths in the region where the charge is localized (charged region) and the rest (non-charged region). The averaged values in the charged and non-charged regions are defined as

$$X_{\text{charged}} = \frac{\sum_A p_A X_A}{\sum_A p_A}, \tag{7.3.3}$$

$$X_{\text{non-charged}} = \frac{\sum_A X_A}{N_A}, \tag{7.3.4}$$

respectively, where p_A is the spin population on the atom A. The index A runs over all Pb atoms in the case of the negative excess charge and all I atoms in the case of the positive excess charge. X_A is a structural quantity, which is the target of comparison between the charged and non-charged regions, defined for the atom A (e.g., averaged length of bonds involving the atom A).

In Fig. 7.5(a), X_A is defined as the average length of six Pb–I bonds around the atom A, which is a Pb atom (Fig. 7.6(a)). In Fig. 7.5(b), the average length of two I–Pb bonds around the atom A, which is an I atom (Fig. 7.6(b)), is used as X_A. From Figs. 7.5(a) and 7.5(b), a longer Pb–I bond length is observed in the charged region compared to that in the non-charged region. From the electrostatic viewpoint, the elongation of Pb–I distance, which is observed in both cases of negative and positive excess charges, can be considered as the result of Coulombic repulsion between the negative (positive) excess charge and I^- (Pb^{2+}). In addition, because CBM has antibonding nature between the AOs of Pb and I,[59] the CBM energy level is deepened with the Pb–I distance, stabilizing the negative excess charge.

In the case of the positive excess charge, the distance between I atom and its nearest-neighbor I atom is shorter in the charged region than that in the non-charged region (Fig. 7.5(c)). Here, X_A is defined as the distance between the atom A, which is an I atom, and its nearest-neighbor I atom (Fig. 7.6(c)). This behaviour is considered to originate from the antibonding interaction between the p-orbitals of these I atoms, which raises the valence bands near the VBM.

Figure 7.5(d) shows the time-course change of the averaged Pb–MA distance in the case of negative excess charge, where X_A is defined as the averaged distance between the atom A, which is a Pb atom, and the neighboring eight MA cations (Fig. 7.6(d)). The position of an MA cation is defined as the geometrical center. As indicated in Fig. 7.5(d), the Pb–MA distance in the charged region is shorter than that in the non-charged region. Similarly, Fig. 7.5(e) shows the averaged I–MA distance in the case of positive excess charge, where X_A is the averaged distance between the atom A, which is an I atom, and the neighboring four MA cations (Fig. 7.6(e)). Figure 7.5(e) indicates that the longer I–MA distance tends to be observed in the charged region compared to the non-charged region. Because the excess negative (positive) charge is located on the Pb (I) atoms, these tendencies are suggested to originate from the Coulombic interaction between the excess negative (positive) charge and MA cations.

Figure 7.5(f) (7.5(g)) compares the angle θ of MA cations in charged and non-charged re-

gions for the case of excess negative (positive) charge. The angle θ, which is used as X_A here, is defined as the averaged angle between the MA $\rightarrow$ Pb (MA $\rightarrow$ I) vectors and the C $\rightarrow$ N vectors in the corresponding MA cations (Figs. 7.6(f) and 7.6(g)). Note that the direction of C $\rightarrow$ N vector is approximately equal to that of the electric dipole moment of the MA cation. The average is taken over the nearest eight (four) MA cations around the Pb (I) atom. In the presence of negative excess charge (Fig. 7.5(f)), θ in the charged region is smaller than that in the non-charged region. Hence, in the charged region, the MA cations tend to direct their electric dipole moment to the neighboring Pb atom, on which the negative excess charge is populated. On the other hand, in the case of positive excess charge (Fig. 7.5(g)), a larger θ is observed in the charged region compared to the non-charged region. These tendencies can be interpreted as the minimization of charge–dipole interaction energy between the excess negative (positive) charge and the electric dipole moment of the MA cations. Therefore, the dipolar rotation of the MA cations is suggested to occur in the polaron formation process.

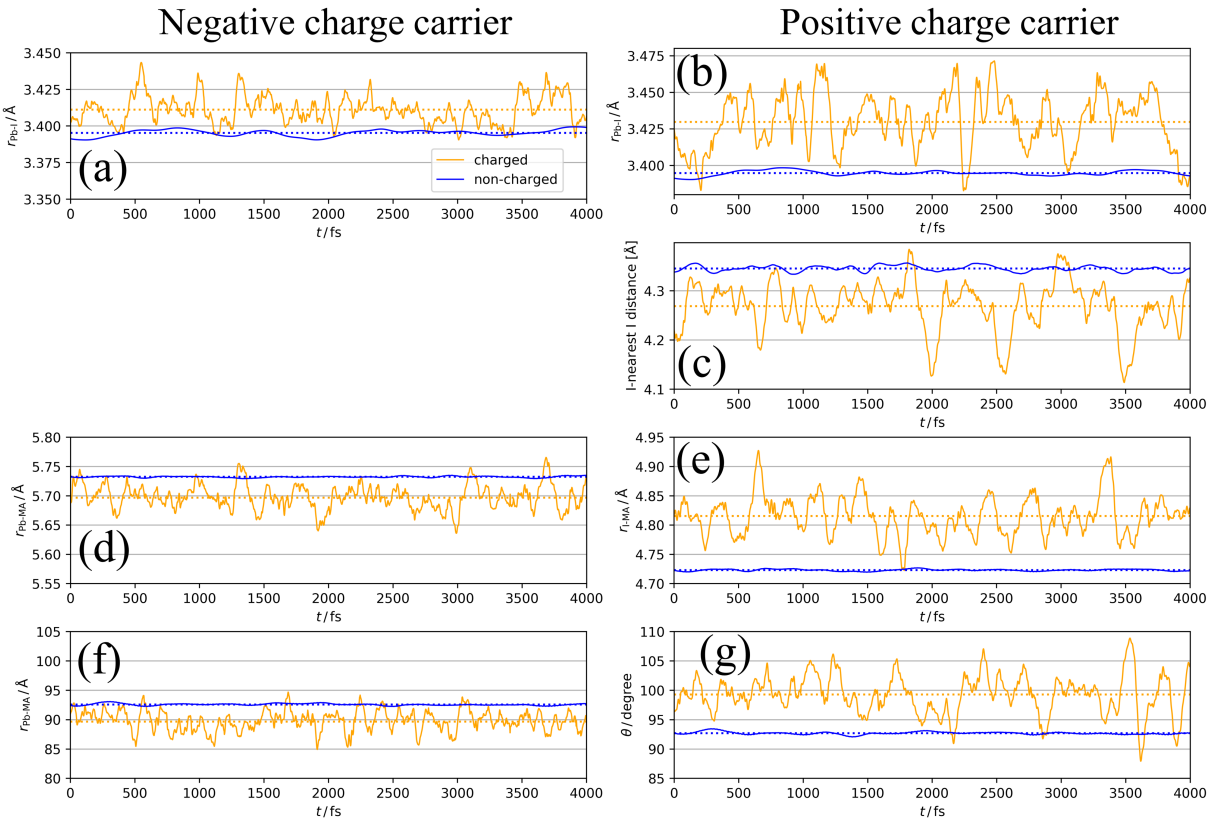

Fig. 7.5: Time course changes of (a) Pb–I distance for negative charge, (b) Pb–I distance for positive charge, (c) I–nearest I distance for positive charge, (d) Pb–MA distance for negative charge, (e) I–MA distance for positive charge, (f) angle of MA cations θ for negative charge, (g) angle of MA cations for positive charge. θ is defined as the angle between C→N vector and MA→Pb/I vector. Orange and blue lines indicate the values in charged and non-charged regions, respectively. Averaged values are shown in dashed lines.

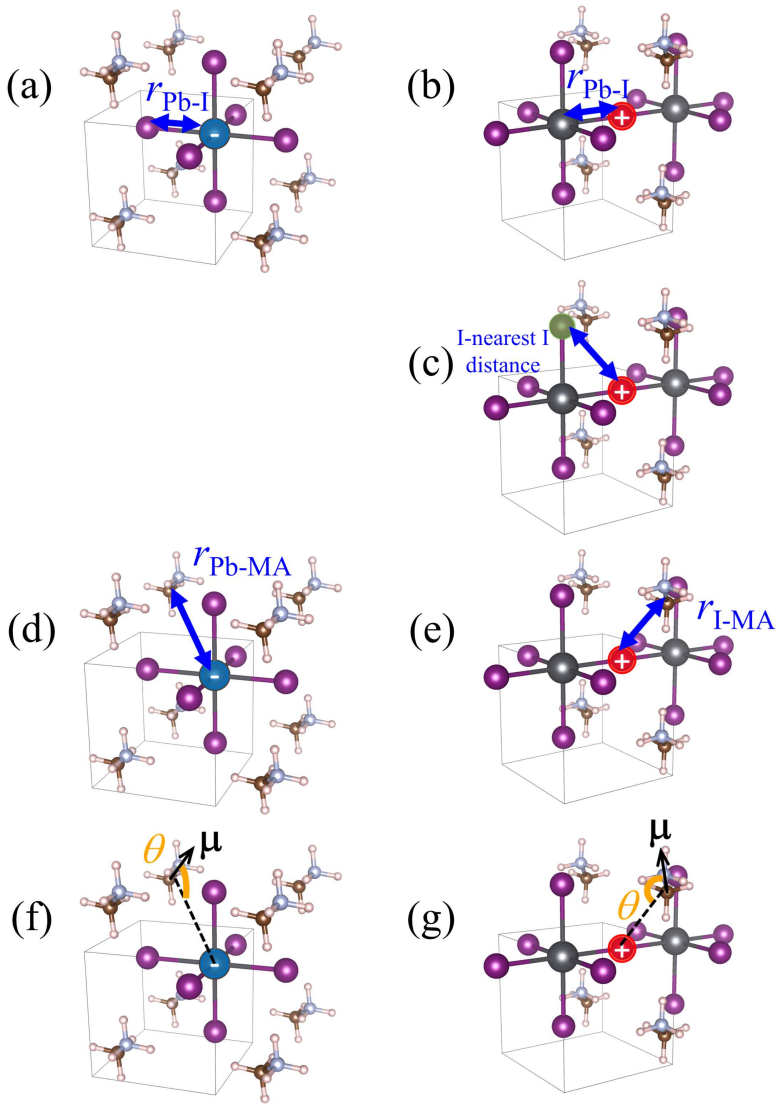

Fig. 7.6: Schematic illustration of the definition of structural quantities under discussion. (a),(b): Pb–I distance in the case of negative and positive charges, respectively. (c): I–nearest I distance in the case of positive charge. The iodine atom indicated by green circle is the closest one to the iodine atom indicated by red circle, in each snapshot. (d): Pb–MA distance in the case of negative charge. (e) I–MA distance in the case of positive charge. (f),(g): Angle of MA cation θ in the case of negative and positive charges, respectively. μ is the C→N vector of the MA cation, which approximates the electrostatic dipole moment of the MA cation.

7.3.3 Early Stage of Polaron Formation: Disorder and Relaxation Effects

Figure 7.7(a)–7.7(g) show the structural deformation in the early stage (until 100 fs from the charge injection) of polaron formation; for one-hundred 100-fs trajectories, in other words, the 100-fs trajectories starting from one-hundred different initial snapshots, the same analyses as that conducted in the previous subsection were performed and the results were averaged. These initial snapshots were obtained from the neutral *NVE* run, which is described in the

computational details (Subsection 7.2.2). The first initial snapshot was obtained at 500 fs from the beginning of the NVE run, and the others were subsequently sampled every 100 fs. For example, the Pb–I bond length shown in Figs. 7.7(a) and 7.7(b) has the followings tendencies.

1. At $t = 0$, that is, the time of the excess negative (positive) charge injection, the Pb–I bond length in the charged region is larger than that in the non-charged region.

2. The Pb–I bond length in the charged region further increases as the time t passes (while the Pb–I bond length in the non-charged region does not change significantly).

The former (1) suggests that the excess charge is localized by thermal fluctuation in the structure; the injected charge localizes in the region where Pb–I bond length is already long. On the other hand, the latter (2) indicates that the excess charge affects the lattice structure, resulting in further elongation of Pb–I bonds at $t > 0$. Similar tendencies are found for the I–nearest I distance (Fig. 7.7(c)), the Pb(I)–MA distance (Figs. 7.7(d) and 7.7(e)), and the angle of MA (Figs. 7.7f and 7.7(g)). These results suggest that, in the polaron formation process, the charge carriers are first localized by the thermal structural fluctuation, and after that, further structural deformation is caused by the relaxation of the charge carriers. Hereafter, the former (1) effect and the latter (2) effect are called as disorder effect and relaxation effect, respectively. Note that this finding, obtained from the QM-MD simulations, is consistent with that of a model Hamiltonian study by Zheng and Wang.[26] In their Hamiltonian, the effects of the rotation of MA cations and the lattice vibration of the PbI_3^- framework were mimicked by artificial potential fluctuations and the polarization potential was described by screened Coulomb potential. In the Flölich Hamiltonian, which is commonly used to model the polarons in LHPs,[21] the former (thermal fluctuation) effect is neglected and only the latter (polarization potential) is considered. They compared the resulting wavefunction and its time evolution with turning on and off each (thermal fluctuation and polarization potential) effect, and concluded that both effects are relevant to polaron formation.

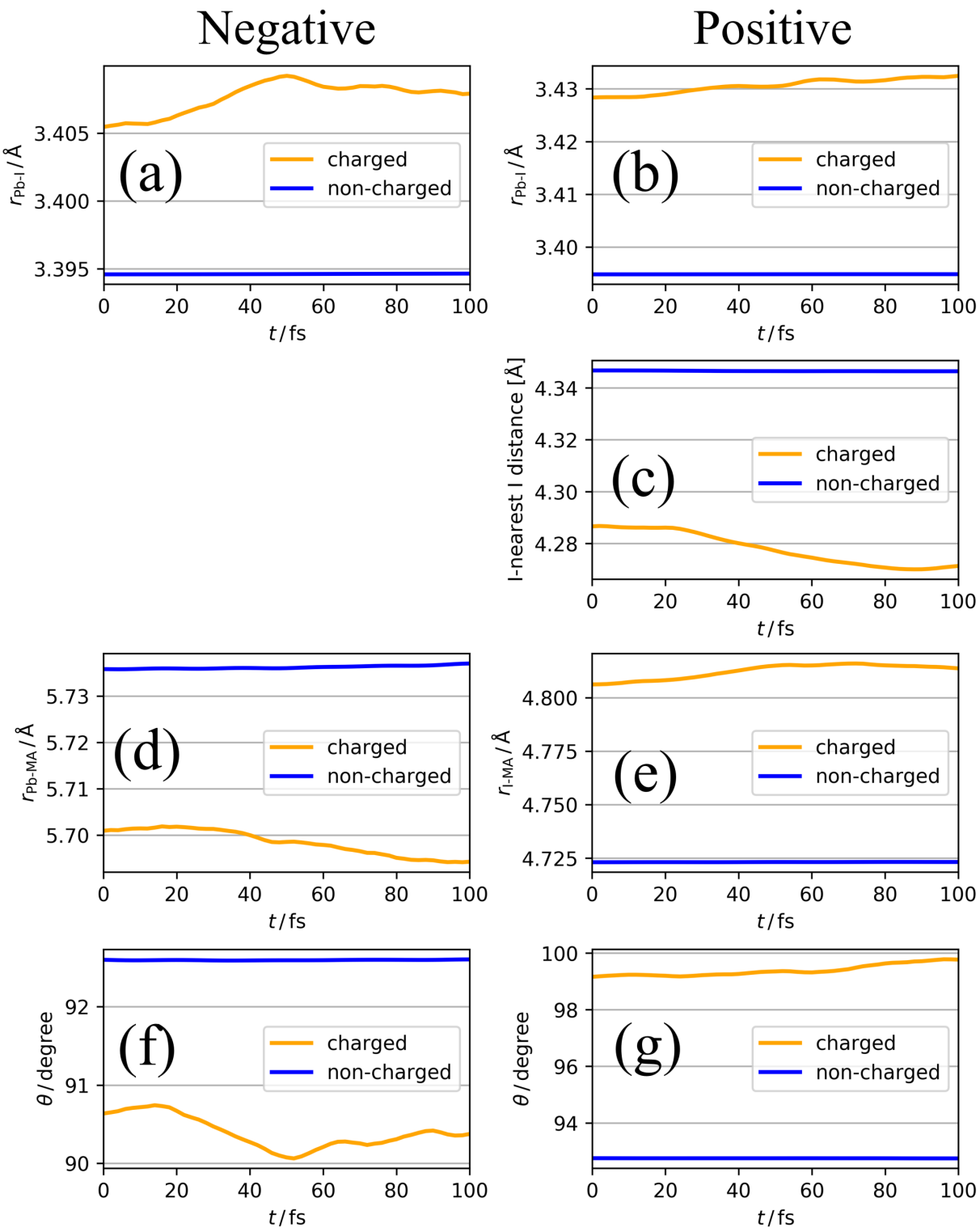

Fig. 7.7: Averaged time course changes of (a) Pb–I distance for negative charge, (b) Pb–I distance for positive charge, (c) I–nearest I distance for positive charge, (d) Pb–MA distance for negative charge, (e) I–MA distance for positive charge, (f) angle of MA cations θ for negative charge, (g) angle of MA cations for positive charge. θ is defined as the angle between C→N vector and MA→Pb/I vector. Orange and blue lines indicate the values in charged and non-charged regions, respectively.

7.3.4 Energetic Contribution for Polaron Formation: PbI_3^- Framework versus MA Cations

This subsection discusses the importance of each structural part, i.e., the PbI_3^- framework and the MA cations, regarding polaron formation, from the energetical viewpoint. Because the polaron formation was showed to be understood as a process involving two effects, that is, disorder and relaxation, in what follows, these effects are discussed separately.

Disorder Effect

The stabilization energy of the charge carriers by the disorder effect, E^d, is described as

$$E^d = \left\langle E^{\text{carrier}}(\mathbf{R}) \right\rangle_{\text{neutral}} - E^{\text{carrier}}(\mathbf{R}_0), \tag{7.3.5}$$

where $E^{\text{carrier}}(\mathbf{R})$ is the energy of the charge carrier, defined as the total energy of the charged state with geometry $\mathbf{R}$ minus the total energy of the neutral state with the same geometry $\mathbf{R}$. The average $\langle \ldots \rangle_{\text{neutral}}$ is taken over the NVE trajectory at neutral state to separate out the relaxation effect. $\mathbf{R}_0$ is the geometry without any thermal fluctuation. Because the model system is initially constructed as a $4 \times 4 \times 4$ supercell of the optimized unit cell of the tetragonal $MAPbI_3$, here, this initial supercell structure is defined as $\mathbf{R}_0$. The sample points used to calculate the average $\langle \ldots \rangle_{\text{neutral}}$ are the same as the initial snapshots obtained as described in the previous subsection (7.3.3). $E^d = -235 \pm 4$ and -267 ± 5 meV (95% confidence interval) are obtained in case of the negative and positive charges, respectively.

To separately evaluate the contribution of the PbI_3^- framework and the MA cations for E^d, the atomic decomposition scheme of the total energy in the spirit of the energy density analysis[60] was utilized. The first term in the energy expression (Eq. 2.2.1), which corresponds to the orbital interaction contribution, can be decomposed into the atomic contribution ($E_A^{H_0}$):

$$E_A^{H_0} = \sum_{\mu \in A} (\mathbf{H_0 S})_{\mu\mu}\,, \tag{7.3.6}$$

where A and μ are the indices of atoms and AOs, respectively. The second term, which arises from the charge fluctuation, can also be re-written in the atom-decomposed fashion:

$$E_A^{\mathrm{SCC}} = \frac{1}{2} \sum_{I \in A} \sum_{J}^{N_{\mathrm{shell}}} \Delta q_I \Delta q_J \gamma_{IJ}. \tag{7.3.7}$$

Next, the third, spin-polarization term, can be decomposed straightforwardly.

$$E_A^{\mathrm{spin}} = \frac{1}{2} \sum_{l,l' \in A} p_{Al} p_{Al'} W_{All'}. \tag{7.3.8}$$

Because the fourth term, E_{rep}, only depends on the geometry, it does not contribute to E^d. Therefore, the atomic energy contribution can be evaluated as the sum of $E_A^{H_0}$, E_A^{SCC}, and E_A^{spin}. Tables 7.1 and 7.2 show the contribution of the PbI_3^- framework and MA cations with respect to each term, indicating that $E_A^{H_0}$ contribution of the PbI_3^- framework is the largest. This result implies that the disorder effect is mainly attributed to orbital interaction in the PbI_3^- framework.

Table 7.1: Component of E^{d} for negative charge carrier (95% confidence interval).

	E_A^{H0}	E_A^{SCC}	E_A^{spin}
PbI_3^-	102.7 ± 2.1%	−25.9 ± 2.2%	2.0 ± 0.1%
MA^+	3.0 ± 0.4%	18.2 ± 1.6%	0.0 ± 0.0%

Table 7.2: Component of E^{d} for positive charge carrier (95% confidence interval).

	E_A^{H0}	E_A^{SCC}	E_A^{spin}
PbI_3^-	50.3 ± 2.1%	5.3 ± 2.6%	1.4 ± 0.1%
MA^+	9.0 ± 0.5%	34.0 ± 1.9%	0.0 ± 0.0%

Relaxation Effect

For the relaxation effect, the contribution of the PbI_3^- framework and MA cations for the internal reorganization energy in the Marcus theory,[61] which measures the energy variation resulting

from the structural relaxation in response to the addition or subtraction of an electron, is evaluated in the following scheme. The contribution of the atom A ($\Delta w_A(t)$) for the reorganization energy is defined as follows.

$$\Delta w_A(t) = \int_{\mathbf{R}(t_0)}^{\mathbf{R}(t)} [\mathbf{F}_A^{\mathrm{c}}(\mathbf{R}) - \mathbf{F}_A^{\mathrm{n}}(\mathbf{R})] \cdot d\mathbf{R}, \tag{7.3.9}$$

where $\mathbf{F}_A^{\mathrm{c}}(\mathbf{R})$ and $\mathbf{F}_A^{\mathrm{n}}(\mathbf{R})$ are the atomic forces acting on the atom A in the charged and neutral states, respectively, at the geometry $\mathbf{R}$. The integration is performed along an MD trajectory from t_0 to t. Note that the ordinary expression of reorganization energy is obtained by integrating the RHS of Eq. 7.3.9 from a neutral optimized geometry to a charged optimized geometry and summing over A. In this sense, $\Delta w_A(t)$ can be considered as the atomic contribution for the reorganization energy. Here, one can compare Δw_A with respect to the PbI_3^- framework and MA cations, that is, Δw_A summed over the PbI_3^- framework and MA cations, respectively. Δw_A is calculated with the MD trajectories of the polaron formation process initiated at t_0 and run for 100 fs. The obtained Δw is averaged over the 100 trajectories, and the averaged value ($\langle \Delta w_A \rangle$) is shown in Fig. 7.8, which indicates that the contribution from the PbI_3^- framework is dominant, while that from the MA cations is small. This result suggests that the polaron stabilization by the relaxation effect is mainly ascribed to the structural deformation of the PbI_3^- frameworks, and that the contribution of motion of MA cations is not the most important component. To understand this result, note that the MA cations are composed of much lighter elements than Pb and I, and thus, the change in dynamics of the MA cations can be pronounced even if the acting force is small.

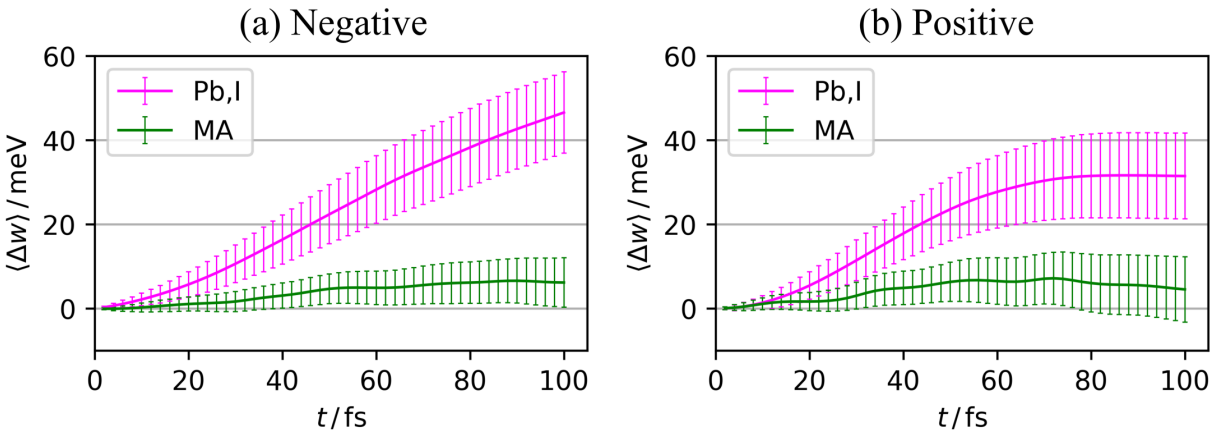

Fig. 7.8: $\langle \Delta w \rangle$ of the PbI_3^- framework (magenta) and MA cations (green) in the case of (a) negative and (b) positive charge carriers. The error bars indicate 95% confidence interval.

7.4 Conclusion

Using the DC-DFTB scheme, the full-QM-level MD simulations were performed for the polaron formation process in $MAPbI_3$ with 3072 atom supercells. The simulations provided comparable results with a nanoscale model Hamiltonian study,[26] and also gave atomic-scale information as well as the first-principles studies.[21,28–30]

The structural dynamics of both PbI_3^- framework and MA cations were found to involve the polaron formation process in $MAPbI_3$. For the PbI_3^- framework, elongation of Pb–I bonds was observed. Particularly in the case of positive polarons, the distances between I atoms and their nearest-neighbor I atoms decreased. For the MA cations, both translational and rotational motions were observed. With respect to translational motion, the distance between Pb (I) atom and the neighboring MA cation increased (decreased) in the case of negative (positive) polaron formation. The rotational motion was characterized by a change in the angle between the dipole moment of an MA cation and the corresponding MA→Pb (MA→I) vector. In the case of negative polaron, the angle decreased, indicating that the dipole moment was directed towards the Pb atoms, where the excess negative charge was located. On the other hand, in the case of positive polaron, the angle increased, indicating that the dipole moment reoriented to avoid the I atoms, on which the excess positive charge was populated.

In addition, this chapter clarified that the polaron formation process, which is characterized by the abovementioned structural deformations, underwent two steps. The first step, called the disorder effect, was the charge localization and its stabilization by thermal motion of the structure. The second one, called relaxation effect, was the further structural deformation caused by the injected charge.

For each of these two steps, the energetical contribution of the PbI_3^- framework and MA cations was evaluated. These analyses were performed with the atomic energy decomposition scheme and the decomposition of the reorganization energy into the work that each atom does, for the disorder effect and relaxation effect, respectively. The results suggested that for both effects, the PbI_3^- framework had the primary contribution, implying that the nature of polarons in LHPs is, to a significant extent, determined by the inorganic frameworks. This conclusion can be one possible explanation of the reason why the carrier diffusion length, carrier lifetime, and electron–hole recombination rate are not significantly dependent on the cation species,[62] while the dipolar rotation of MA cations themselves is actually observed in this study.

References

[1]H. Uratani, C.-P. Chou, and H. Nakai, *Phys. Chem. Chem. Phys.* **22**, 97 (2020).

[2]A. Kojima, K. Teshima, Y. Shirai, and T. Miyasaka, *J. Am. Chem. Soc.* **131**, 6050 (2009).

[3]J.-H. Im, C.-R. Lee, J.-W. Lee, S.-W. Park, and N.-G. Park, *Nanoscale* **3**, 4088 (2011).

[4]S. D. Stranks and H. J. Snaith, *Nature Nanotechnol.* **10**, 391 (2015).

[5]X. Y. Chin, D. Cortecchia, J. Yin, A. Bruno, and C. Soci, *Nat. Commun.* **6**, 7383 (2015).

[6]J. M. Frost and A. Walsh, *Acc. Chem. Res.* **49**, 528 (2016).

[7]S. D. Stranks, V. M. Burlakov, T. Leijtens, J. M. Ball, A. Goriely, and H. J. Snaith, *Phys. Rev. Applied* **2**, 034007 (2014).

[8]G. Xing, N. Mathews, S. Sun, S. S. Lim, Y. M. Lam, M. Grätzel, S. Mhaisalkar, and T. C. Sum, *Science* **342**, 344 (2013).

[9]C. Wehrenfennig, G. E. Eperon, M. B. Johnston, H. J. Snaith, and L. M. Herz, *Adv. Mater.* **26**, 1584 (2014).

[10]Y. Zhao, A. M. Nardes, and K. Zhu, *J. Phys. Chem. Lett.* **5**, 490 (2014).

[11]H. Oga, A. Saeki, Y. Ogomi, S. Hayase, and S. Seki, *J. Am. Chem. Soc.* **136**, 13818 (2014).

[12]Q. Dong, Y. Fang, Y. Shao, P. Mulligan, J. Qiu, L. Cao, and J. Huang, *Science* **347**, 967 (2015).

[13]G. D. Mahan, *Many-particle physics* (Plenum Press, New York, 1990).

[14]J. M. Frost, K. T. Butler, and A. Walsh, *APL Mater.* **2**, 081506 (2014).

[15]J. Ma and L.-W. Wang, *Nano Lett.* **15**, 248 (2015).

[16]C. Quarti, E. Mosconi, and F. De Angelis, *Phys. Chem. Chem. Phys.* **17**, 9394 (2015).

[17]S. Liu, F. Zheng, N. Z. Koocher, H. Takenaka, F. Wang, and A. M. Rappe, *J. Phys. Chem. Lett.* **6**, 693 (2015).

[18]F. Bi, S. Markov, R. Wang, Y. Kwok, W. Zhou, L. Liu, X. Zheng, G. Chen, and C. Yam, *J. Phys. Chem. C* **121**, 11151 (2017).

[19]O. Yaffe, Y. Guo, L. Z. Tan, D. A. Egger, T. Hull, C. C. Stoumpos, F. Zheng, T. F. Heinz, L. Kronik, M. G. Kanatzidis, J. S. Owen, A. M. Rappe, M. A. Pimenta, and L. E. Brus, *Phys. Rev. Lett.* **118**, 136001 (2017).

[20]H. Uratani and K. Yamashita, *J. Phys. Chem. C* **121**, 26648 (2017).

[21]K. Miyata, D. Meggiolaro, M. T. Trinh, P. P. Joshi, E. Mosconi, S. C. Jones, F. De Angelis, and X.-Y. Zhu, *Sci. Adv.* **3**, e1701217 (2017).

[22]N. Pellet, P. Gao, G. Gregori, T.-Y. Yang, M. K. Nazeeruddin, J. Maier, and M. Grätzel, *Angew. Chem. Int. Ed.* **53**, 3151 (2014).

[23]D. P. McMeekin, G. Sadoughi, W. Rehman, G. E. Eperon, M. Saliba, M. T. Hörantner, A. Haghighirad, N. Sakai, L. Korte, B. Rech, M. B. Johnston, L. M. Herz, and H. J. Snaith, *Science* **351**, 151 (2016).

[24]O. A. Syzgantseva, M. Saliba, M. Grätzel, and U. Rothlisberger, *J. Phys. Chem. Lett.* **8**, 1191 (2017).

[25]H. Fröhlich, *Adv. Phys.* **3**, 325 (1954).

[26]F. Zheng and L. wang Wang, *Energy Environ. Sci.* **12**, 1219 (2019).

[27]X.-Y. Zhu and V. Podzorov, *J. Phys. Chem. Lett.* **6**, 4758 (2015).

[28]A. J. Neukirch, W. Nie, J.-C. Blancon, K. Appavoo, H. Tsai, M. Y. Sfeir, C. Katan, L. Pedesseau, J. Even, J. J. Crochet, G. Gupta, A. D. Mohite, and S. Tretiak, *Nano Lett.* **16**, 3809 (2016).

[29]J. Yin, P. Maity, M. De Bastiani, I. Dursun, O. M. Bakr, J.-L. Brédas, and O. F. Mohammed, *Sci. Adv.* **3**, e1701793 (2017).

[30]F. Ambrosio, J. Wiktor, F. De Angelis, and A. Pasquarello, *Energy Environ. Sci.* **11**, 101 (2018).

[31]F. Ambrosio, D. Meggiolaro, E. Mosconi, and F. De Angelis, *ACS Energy Lett.* **4**, 2013 (2019).

[32]W. Yang, *Phys. Rev. Lett.* **66**, 1438 (1991).

[33]W. Yang and T.-S. Lee, *J. Chem. Phys.* **103**, 5674 (1995).

[34]T. Akama, M. Kobayashi, and H. Nakai, *J. Comput. Chem.* **28**, 2003 (2007).

[35]M. Kobayashi, T. Yoshikawa, and H. Nakai, *Chem. Phys. Lett.* **500**, 172 (2010).

[36]M. Kobayashi, T. Kunisada, T. Akama, D. Sakura, and H. Nakai, *J. Chem. Phys.* **134**, 034105 (2011).

[37]M. Kobayashi and H. Nakai, "Divide-and-conquer approaches to quantum chemistry: theory and implementation", in *Linear-scaling techniques in computational chemistry and physics: methods and applications* (2011), pp. 97–127.

[38]M. Kobayashi and H. Nakai, *Phys. Chem. Chem. Phys.* **14**, 7629 (2012).

[39]T. Yoshikawa and H. Nakai, "a Linear-Scaling Divide-and-Conquer Quantum Chemical Method for Open-Shell Systems and Excited States", in *Fragmentation: toward accurate calculations on complex molecular systems*, edited by M. Gordon (Wiley, 2017), pp. 299–323.

[40]W. M. C. Foulkes and R. Haydock, *Phys. Rev. B* **39**, 12520 (1989).

[41]D. Porezag, T. Frauenheim, T. Köhler, G. Seifert, and R. Kaschner, *Phys. Rev. B* **51**, 12947 (1995).

[42]G. Seifert, D. Porezag, and T. Frauenheim, *Int. J. Quant. Chem.* **58**, 185 (1996).

[43]M. Elstner, D. Porezag, G. Jungnickel, J. Elsner, M. Haugk, T. Frauenheim, S. Suhai, and G. Seifert, *Phys. Rev. B* **58**, 7260 (1998).

[44]H. Nishizawa, Y. Nishimura, M. Kobayashi, S. Irle, and H. Nakai, *J. Comput. Chem.* **37**, 1983 (2016).

[45]Y. Nishimura and H. Nakai, *J. Comput. Chem.* **39**, 105 (2018).

[46]Y. Nishimura and H. Nakai, *J. Comput. Chem.* **40**, 1538 (2019).

[47]M. Gaus, A. Goez, and M. Elstner, *J. Chem. Theory Comput.* **9**, 338 (2013).

[48]M. Kubillus, T. Kubař, M. Gaus, J. Řezáč, and M. Elstner, *J. Chem. Theory Comput.* **11**, 332 (2015).

[49]H. A. Witek, C. Köhler, T. Frauenheim, K. Morokuma, and M. Elstner, *J. Phys. Chem. A* **111**, 5712 (2007).

[50]J. P. Perdew, K. Burke, and M. Ernzerhof, *Phys. Rev. Lett.* **77**, 3865 (1996).

[51]C.-P. Chou, Y. Nishimura, C.-C. Fan, G. Mazur, S. Irle, and H. A. Witek, *J. Chem. Theory Comput.* **12**, 53 (2016).

[52]G. Kresse and J. Hafner, *Phys. Rev. B* **47**, 558 (1993).

[53]G. Kresse and J. Hafner, *Phys. Rev. B* **49**, 14251 (1994).

[54]G. Kresse and J. Furthmüller, *Comp. Mater. Sci.* **6**, 15 (1996).

[55]G. Kresse and J. Furthmüller, *Phys. Rev. B* **54**, 11169 (1996).

[56]P. E. Blöchl, *Phys. Rev. B* **50**, 17953 (1994).

[57]B. Aradi, B. Hourahine, and T. Frauenheim, *J. Phys. Chem. A* **111**, 5678 (2007).

[58]H. C. Andersen, *J. Comp. Phys.* **52**, 24 (1983).

[59]M. G. Goesten and R. Hoffmann, *J. Am. Chem. Soc.* **140**, 12996 (2018).

[60]H. Nakai, *Chem. Phys. Lett.* **363**, 73 (2002).

[61]R. A. Marcus and N. Sutin, *Biochim. Biophys. Acta* **811**, 265 (1985).

[62]H. Zhu, M. T. Trinh, J. Wang, Y. Fu, P. P. Joshi, K. Miyata, S. Jin, and X.-Y. Zhu, *Adv. Mater.* **29**, 1603072 (2017).

Chapter 8

General Conclusion

This thesis described computationally efficient NA-MD methods capable of simulating nonadiabatic dynamics in complicated systems, and applications of the methods to challenging real-world problems.

The methodological development was described in detail in Chapter 3. Based on the TD-DFTB/FSSH approach, three extended methods were proposed: DC-TD-DFTB/FSSH, SF-TD-DFTB/FSSH, and DC-SF-TD-DFTB/FSSH. The computational efficiency of the developed methods extends the capability of the NA-MD approach in two aspects. First, the available size of model systems is significantly increased such that the nonadiabatic dynamics center, e.g., the chromophore, and the environment, e.g., solvent molecules, can be treated on equal footing. This characteristic enables realistic modeling of the target systems. Second, reduction of the cost for running each NA-MD trajectory means that one can sample trajectories of larger number within the same quantity of computational resources. This point is particularly important from the perspective of the resolution and credibility of NA-MD results because NA-MD is a statistical approach to approximate the exact wave-packet dynamics; while the use of the semiempirical method, i.e., DFTB, may more or less sacrifice the *accuracy*, it has a significant advantage in terms of *precision*. The author hopes that this achievement will produce paradigm shift in nonadiabatic dynamics studies; the NA-MD approach is no longer a supplementary tool that provides complementary information to experiments, but can be considered as a class of

"observation techniques" on the same plane as the spectroscopic methods.

This concept was proven by the practical applications described in Chapters 4–7, where the developed methods were applied to investigate nonadiabatic dynamics in real, complicated systems, which have been difficult to be accessed by conventional NA-MD approaches.

Chapters 4 and 5 demonstrated the way the present methods can be used to elucidate the molecular-structure and environment dependence of the nonradiative relaxation dynamics of excited molecules. Nonradiative relaxation is of general importance in the energy-conversion processes associated with the emission or absorption of light, which are key functions of, for example, light-emitting diodes, solar cells, and light-driven molecular machines. Although the fundamental physics underlying the functionalities of these materials are simple and conveniently understood by "toy models," such approaches are not always appropriate for practical material design, where fine tuning of the properties via structural and environmental modifications is required. The developed methods, which enable to incorporate the details of the systems into NA-MD simulations, may pave the way to tune the properties computationally. In addition, material design, that is, finding materials that exhibit the desired properties, is an inverse problem, which requires trial and error to obtain the appropriate solutions. At present, the most robust strategy for this class of problems is simply increasing the number of trials, which can be achieved by the computational efficiency of the proposed methods, whereas informatics-based approaches may be promising future solutions.

Chapter 6 presented the first coupled structural–electronic dynamics simulations in photoexcited lead iodide perovskite systems, which are of interest in the context of photovoltaic applications. The results clarified the crucial role of the mutual dependence of the structural and electronic dynamics, suggesting that the simulations, which were realized by the TD-DFTB/FSSH approach, are an important step in understanding the photoexcited-state dynamics of this class of materials. The presented computational scheme and the results may enable a critical appraisal of conventional theoretical and computational approaches to this class of materials, where the mutual dependence of electronic and nuclear dynamics is ignored for ease

of treatment. Finally, in Chapter 7, the DC-DFTB-MD simulations probed nanoscale polarons in the methylammonium lead iodide perovskite material, which are formed after the series of nonadiabatic processes studied in Chapter 6. The MD simulations provided complementary information to the NA-MD calculations in terms of spatial and time scales. The study illustrates how the combined use of the NA-MD and MD approaches can help unravel the entire picture of the excited-state dynamics of complicated chemical systems.

Note that this thesis implies some remaining issues. First, at present the applicability of the DC-based excited-state dynamics methods is limited to local excitations, where the excitation is localized and its the position can be identified trivially. Hence, a further algorithmic breakthrough is needed to cover phenomena involving spatially nonlocal excitations, for example, the entire process from photoexcitation to the generation of completely dissociated band-edge carriers in semiconductors. Second, the thesis only focused on the internal conversion among singlet states. Additional methodological effort is required to extend the methods to discuss higher spin states and intersystem-crossing-mediated phenomena, e.g., thermally activated delayed fluorescence. Third, as the methods proposed and used in this thesis are based on the DFTB, their performance is limited in principle by that of DFTB. Although the applicability of DFTB has been extensively examined in recent years, it is, at least in part, an open question. In particular, heavy-element compounds may be challenging targets. Because the (DC-based) NA-MD itself is a class of general frameworks in the sense that the computational method for the electronic part can be chosen arbitrarily, the numerical performance of DFTB in the NA-MD context is worth comparing with a variety of first-principles or semiempirical electronic structure methods.

The author believes that the works described in this thesis will help the research community pioneer the unexplored frontiers of nonadiabatic dynamics.

Appendices

A Derivation of Analytical Energy Gradient for SF-TD-DFTB

A.1 Spin-Unrestricted Case

The energy functional G is defined as

$$G\left[\mathbf{X}, \omega\right] = \sum_{i\bar{a}, j\bar{b}} X_{i\bar{a}} A_{i\bar{a}, j\bar{b}} X_{j\bar{b}} - \omega \left(\sum_{i\bar{a}} X_{i\bar{a}} X_{i\bar{a}} - 1 \right). \tag{A1}$$

Here, the matrix $\mathbf{A}$ is written as

$$A_{i\bar{a}, j\bar{b}} = F^{\beta}_{\bar{a}\bar{b}} \delta_{ij} - F^{\alpha}_{ij} \delta_{\bar{a}\bar{b}} + K_{i\bar{a}, j\bar{b}}. \tag{A2}$$

The excitation energy ω and the response matrix $\mathbf{X}$ are obtained by variational minimization of G, which leads to the following eigenvalue problem.

$$\mathbf{AX} = \omega \mathbf{X}. \tag{A3}$$

The Lagrangian L for the spin-unrestricted case has the following form:

$$\begin{aligned} L\left[\mathbf{X},\omega,\mathbf{C},\mathbf{Z}^{\alpha},\mathbf{Z}^{\beta},\mathbf{W}^{\alpha},\mathbf{W}^{\beta}\right] &= G\left[\mathbf{X},\omega\right] \\ &+ \sum_{ia} Z_{ia}^{\alpha} F_{ia}^{\alpha} - \sum_{p\leq q} W_{pq}^{\alpha}\left(S_{pq}^{\alpha} - \delta_{pq}\right) \\ &+ \sum_{\bar{i}\bar{a}} Z_{\bar{i}\bar{a}}^{\beta} F_{\bar{i}\bar{a}}^{\beta} - \sum_{\bar{p}\leq\bar{q}} W_{\bar{p}\bar{q}}^{\beta}\left(S_{\bar{p}\bar{q}}^{\beta} - \delta_{\bar{p}\bar{q}}\right). \end{aligned} \tag{A4}$$

As L is variational with respect to the MO coefficients, one obtains

$$\sum_{\mu} \frac{\partial L}{\partial c_{\mu\hat{p}}} c_{\mu\hat{q}} = 0. \tag{A5}$$

In addition, the following matrix $\mathbf{Q}$ is defined.

$$Q_{\hat{p}\hat{q}} = \sum_{\mu} \frac{\partial G}{\partial c_{\mu\hat{p}}} c_{\mu\hat{q}}. \tag{A6}$$

For convenience in further derivation, the following relations for $\mathbf{F}^{\alpha}$ should be noted.

$$\sum_{\mu} \frac{\partial F_{rs}^{\alpha}}{\partial c_{\mu i}} c_{\mu q} = \delta_{ir} F_{qs}^{\alpha} + \delta_{is} F_{rq}^{\alpha} + 2K_{iq,rs}^{\mathrm{c}} + 2K_{iq,rs}^{\mathrm{m}}, \tag{A7}$$

$$\sum_{\mu} \frac{\partial F_{rs}^{\alpha}}{\partial c_{\mu\bar{i}}} c_{\mu\bar{q}} = 2K_{\bar{i}\bar{q},rs}^{\mathrm{c}} - 2K_{\bar{i}\bar{q},rs}^{\mathrm{m}}, \tag{A8}$$

$$\sum_{\mu} \frac{\partial F_{rs}^{\alpha}}{\partial c_{\mu a}} c_{\mu q} = \delta_{ar} F_{qs}^{\alpha} + \delta_{as} F_{rq}^{\alpha}, \tag{A9}$$

$$\sum_{\mu} \frac{\partial F_{rs}^{\alpha}}{\partial c_{\mu\bar{a}}} c_{\mu\bar{q}} = 0. \tag{A10}$$

For $\mathbf{F}^{\beta}$, the spin-inverted counterparts of these equations hold. In addition, the following notations are introduced, as in Section 3.3.

$$K^{\mathrm{c}}_{\hat{p}\hat{q},\hat{r}\hat{s}} = \sum_{IJ} q_I^{\hat{p}\hat{q}} \gamma_{IJ} q_J^{\hat{r}\hat{s}}, \tag{A11}$$

$$K^{\mathrm{m}}_{\hat{p}\hat{q},\hat{r}\hat{s}} = \sum_{A} \sum_{L\in A} \sum_{L'\in A} q_L^{\hat{p}\hat{q}} m_{ALL'} q_{L'}^{\hat{r}\hat{s}}, \tag{A12}$$

$$K^{\mathrm{sf}}_{\hat{p}\hat{q},\hat{r}\hat{s}} = \sum_{A} q_A^{\hat{p}\hat{q}} m_A q_A^{\hat{r}\hat{s}}, \tag{A13}$$

$$H^{+\alpha}_{\hat{p}\hat{q}}\left[\mathbf{V}\right] = \sum_{\hat{r}\hat{s}} \left(2K^{\mathrm{c}}_{\hat{p}\hat{q},\hat{r}\hat{s}} + 2K^{\mathrm{m}}_{\hat{p}\hat{q},\hat{r}\hat{s}}\right) V_{\hat{r}\hat{s}}, \tag{A14}$$

$$H^{+\beta}_{\hat{p}\hat{q}}\left[\mathbf{V}\right] = \sum_{\hat{r}\hat{s}} \left(2K^{\mathrm{c}}_{\hat{p}\hat{q},\hat{r}\hat{s}} - 2K^{\mathrm{m}}_{\hat{p}\hat{q},\hat{r}\hat{s}}\right) V_{\hat{r}\hat{s}}, \tag{A15}$$

$$\mathcal{K}_{\hat{p}\hat{q}} = \sum_{i\bar{a}} 2K^{\mathrm{sf}}_{\hat{p}\hat{q},i\bar{a}}.X_{i\bar{a}} \tag{A16}$$

where $\mathbf{V}$ is an arbitrary vector.

One can derive explicit forms of Eqs. A5 and A6 by exploiting the relations of Eqs. A7-A10 and the condition of Eq. A3.

In the $(\hat{p},\hat{q}) = (i,j)$ case,

$$W^{\alpha}_{ij} = \frac{1}{1+\delta_{ij}} \left(Q_{ij} + H^{+\alpha}_{ij}\left[\mathbf{Z}^{\alpha}\right] + H^{+\beta}_{ij}\left[\mathbf{Z}^{\beta}\right]\right), \tag{A17}$$

$$Q_{ij} = -2\omega T^{\alpha}_{ij} - 2\sum_{\bar{c}} \epsilon^{\beta}_{\bar{c}} X_{i\bar{c}} X_{j\bar{c}} + H^{+\alpha}_{ij}\left[\mathbf{T}^{\alpha}\right] + H^{+\beta}_{ij}\left[\mathbf{T}^{\beta}\right]. \tag{A18}$$

In the $(\hat{p},\hat{q}) = (i,a)$ case,

$$W^{\alpha}_{ia} = Q_{ia} + \epsilon_a Z^{\alpha}_{ia} + H^{+\alpha}_{ia}\left[\mathbf{Z}^{\alpha}\right] + H^{+\beta}_{ia}\left[\mathbf{Z}^{\beta}\right], \tag{A19}$$

$$Q_{ia} = H^{+\alpha}_{ia}\left[\mathbf{T}^{\alpha}\right] + H^{+\beta}_{ia}\left[\mathbf{T}^{\beta}\right] + \sum_{\bar{b}} 2X_{i\bar{b}}\mathcal{K}_{a\bar{b}}. \tag{A20}$$

In the $(\hat{p},\hat{q}) = (a,i)$ case,

$$W^{\alpha}_{ia} = Q_{ai} + \epsilon_i Z^{\alpha}_{ia}, \tag{A21}$$

$$Q_{ai} = 0. \tag{A22}$$

In the $(\hat{p}, \hat{q}) = (a, b)$ case,

$$W^{\alpha}_{ab} = \frac{1}{1 + \delta_{ab}} Q_{ab}, \tag{A23}$$

$$Q_{ab} = 0. \tag{A24}$$

In the $(\hat{p}, \hat{q}) = (\bar{i}, \bar{j})$ case,

$$W^{\beta}_{\bar{i}\bar{j}} = \frac{1}{1 + \delta_{\bar{i}\bar{j}}} \left(Q_{\bar{i}\bar{j}} + H^{+\beta}_{\bar{i}\bar{j}} [\mathbf{Z}^{\alpha}] + H^{+\alpha}_{\bar{i}\bar{j}} \left[\mathbf{Z}^{\beta} \right] \right), \tag{A25}$$

$$Q_{\bar{i}\bar{j}} = H^{+\beta}_{\bar{i}\bar{j}} [\mathbf{T}^{\alpha}] + H^{+\alpha}_{\bar{i}\bar{j}} \left[\mathbf{T}^{\beta} \right]. \tag{A26}$$

In the $(\hat{p}, \hat{q}) = (\bar{i}, \bar{a})$ case,

$$W^{\beta}_{\bar{i}\bar{a}} = Q_{\bar{i}\bar{a}} + \epsilon_{\bar{a}} Z^{\beta}_{\bar{i}\bar{a}} + H^{+\beta}_{\bar{i}\bar{a}} [\mathbf{Z}^{\alpha}] + H^{+\alpha}_{\bar{i}\bar{a}} \left[\mathbf{Z}^{\beta} \right], \tag{A27}$$

$$Q_{\bar{i}\bar{a}} = H^{+\alpha}_{\bar{i}\bar{a}} \left[\mathbf{T}^{\beta} \right] + H^{+\beta}_{\bar{i}\bar{a}} [\mathbf{T}^{\alpha}]. \tag{A28}$$

In the $(\hat{p}, \hat{q}) = (\bar{a}, \bar{i})$ case,

$$W^{\beta}_{\bar{i}\bar{a}} = Q_{\bar{a}\bar{i}} + \epsilon_{\bar{i}} Z^{\beta}_{\bar{i}\bar{a}}, \tag{A29}$$

$$Q_{\bar{a}\bar{i}} = \sum_{j} 2 X_{j\bar{a}} \mathcal{K}_{j\bar{i}}. \tag{A30}$$

In the $(\hat{p}, \hat{q}) = (\bar{a}, \bar{b})$ case,

$$W^{\beta}_{\bar{a}\bar{b}} = \frac{1}{1 + \delta_{\bar{a}\bar{b}}} Q_{\bar{a}\bar{b}}, \tag{A31}$$

$$Q_{\bar{a}\bar{b}} = 2\omega T^{\beta}_{\bar{a}\bar{b}} + 2 \sum_{k} \epsilon_k X_{k\bar{a}} X_{k\bar{b}}. \tag{A32}$$

Thus, $\mathbf{W}^{\alpha}$, $\mathbf{W}^{\beta}$, and $\mathbf{Q}$ can be obtained.

By eliminating W^{α}_{ia} from Eqs. A19 and A21, one can derive the α part of the Z-vector equation:

$$(\epsilon_a - \epsilon_i) Z^{\alpha}_{ia} + H^{+\alpha}_{ia} [\mathbf{Z}^{\alpha}] + H^{+\beta}_{ia} \left[\mathbf{Z}^{\beta} \right] = - (Q_{ia} - Q_{ai}). \tag{A33}$$

Similarly, by eliminating $W^{\beta}_{\bar{i}\bar{a}}$ from Eqs. A27 and A29, one can derive the β part:

$$(\epsilon_{\bar{a}} - \epsilon_{\bar{i}})\, Z^{\beta}_{\bar{i}\bar{a}} + H^{+\beta}_{\bar{i}\bar{a}}\left[\mathbf{Z}^{\alpha}\right] + H^{+\alpha}_{\bar{i}\bar{a}}\left[\mathbf{Z}^{\beta}\right] = -\left(Q_{\bar{i}\bar{a}} - Q_{\bar{a}\bar{i}}\right). \tag{A34}$$

The set of Z-vector equations (Eqs. A33 and A34) can be rewritten as a single matrix equation:

$$\begin{pmatrix} \mathbf{J}^{\alpha\alpha} & \mathbf{J}^{\alpha\beta} \\ \mathbf{J}^{\beta\alpha} & \mathbf{J}^{\beta\beta} \end{pmatrix} \begin{pmatrix} \mathbf{Z}^{\alpha} \\ \mathbf{Z}^{\beta} \end{pmatrix} = - \begin{pmatrix} \mathbf{U}^{\alpha} \\ \mathbf{U}^{\beta} \end{pmatrix}, \tag{A35}$$

where

$$J^{\alpha\alpha}_{ia,jb} = (\epsilon_a - \epsilon_i)\,\delta_{ij}\delta_{ab} + 2K^{\mathrm{c}}_{ia,jb} + 2K^{\mathrm{m}}_{ia,jb}, \tag{A36}$$

$$J^{\alpha\beta}_{ia,\bar{j}\bar{b}} = 2K^{\mathrm{c}}_{ia,\bar{j}\bar{b}} - 2K^{\mathrm{m}}_{ia,\bar{j}\bar{b}}, \tag{A37}$$

$$J^{\beta\alpha}_{\bar{i}\bar{a},jb} = 2K^{\mathrm{c}}_{\bar{i}\bar{a},jb} - 2K^{\mathrm{m}}_{\bar{i}\bar{a},jb}, \tag{A38}$$

$$J^{\beta\beta}_{\bar{i}\bar{a},\bar{j}\bar{b}} = (\epsilon_{\bar{a}} - \epsilon_{\bar{i}})\,\delta_{\bar{i}\bar{j}}\delta_{\bar{a}\bar{b}} + 2K^{\mathrm{c}}_{\bar{i}\bar{a},\bar{j}\bar{b}} + 2K^{\mathrm{m}}_{\bar{i}\bar{a},\bar{j}\bar{b}}, \tag{A39}$$

and

$$U^{\alpha}_{ia} = H^{+\alpha}_{ia}\left[\mathbf{T}^{\alpha}\right] + H^{+\beta}_{ia}\left[\mathbf{T}^{\beta}\right] + \sum_{\bar{b}} 2X_{i\bar{b}}\mathcal{K}_{a\bar{b}}, \tag{A40}$$

$$U^{\beta}_{\bar{i}\bar{a}} = H^{+\alpha}_{\bar{i}\bar{a}}\left[\mathbf{T}^{\beta}\right] + H^{+\beta}_{\bar{i}\bar{a}}\left[\mathbf{T}^{\alpha}\right] - \sum_{j} 2X_{j\bar{a}}\mathcal{K}_{j\bar{i}}. \tag{A41}$$

The geometric derivative of the Lagrangian gives the excitation energy gradient:

$$\begin{aligned}
\frac{\partial \omega}{\partial \mathbf{R}} &= \frac{\partial L}{\partial \mathbf{R}} \\
&= \sum_{\mu\nu} \left(\frac{dH^0_{\mu\nu}}{d\mathbf{R}} + \frac{dH^{\mathrm{c}}_{\mu\nu}}{d\mathbf{R}} \right) \left(\mathcal{P}^{\alpha}_{\mu\nu} + \mathcal{P}^{\beta}_{\mu\nu} \right) + \sum_{\mu\nu} \frac{dH^{\mathrm{x}}_{\mu\nu}}{d\mathbf{R}} \left(\mathcal{P}^{\alpha}_{\mu\nu} - \mathcal{P}^{\beta}_{\mu\nu} \right) \\
&- \sum_{\mu\nu} \mathcal{W}_{\mu\nu} \frac{dS_{\mu\nu}}{d\mathbf{R}} \\
&+ \frac{1}{2} \sum_{\mu\nu\lambda\kappa} \left(\frac{dS_{\mu\nu}}{d\mathbf{R}} S_{\lambda\kappa} + S_{\mu\nu} \frac{dS_{\lambda\kappa}}{d\mathbf{R}} \right) (m_A \delta_{AC} + m_B \delta_{AD} + m_B \delta_{BC} + m_B \delta_{BD}) \, \mathcal{X}_{\mu\nu} \mathcal{X}_{\lambda\kappa}, \qquad \text{(A42)}
\end{aligned}$$

where $\mathcal{P}^{\alpha/\beta}_{\mu\nu}$, $\mathcal{W}_{\mu\nu}$, and $\mathcal{X}_{\mu\nu}$ are "AO-based" representations of the relaxed difference density matrices $\mathbf{P}^{\alpha/\beta}$, the energy-weighted difference density matrix $\mathbf{W}$, and the response matrix $\mathbf{X}$, respectively:

$$\mathcal{P}^{\alpha}_{\mu\nu} = \sum_{pq} c_{\mu p} P^{\alpha}_{pq} c_{\nu q}, \qquad \text{(A43)}$$

$$\mathcal{P}^{\beta}_{\mu\nu} = \sum_{\bar{p}\bar{q}} c_{\mu \bar{p}} P^{\beta}_{\bar{p}\bar{q}} c_{\nu \bar{q}}, \qquad \text{(A44)}$$

$$\mathcal{W}_{\mu\nu} = \sum_{pq} c_{\mu p} \mathbf{W}_{pq} c_{\nu q}, \qquad \text{(A45)}$$

$$\mathcal{X}_{\mu\nu} = \sum_{i\bar{a}} c_{\mu i} X_{i\bar{a}} c_{\nu \bar{a}}. \qquad \text{(A46)}$$

Here, in the spin-unrestricted case, $\mathbf{P}^{\alpha/\beta}$ and $\mathbf{W}$ are defined as follows.

$$\mathbf{P}^{\alpha} = \mathbf{T}^{\alpha} + \mathbf{Z}^{\alpha}, \qquad \text{(A47)}$$

$$\mathbf{P}^{\beta} = \mathbf{T}^{\beta} + \mathbf{Z}^{\beta}, \qquad \text{(A48)}$$

$$\mathbf{W} = \mathbf{W}^{\alpha} + \mathbf{W}^{\beta}. \qquad \text{(A49)}$$

A.2 Restricted Open-Shell Case

In the restricted open-shell formulation, α-spin and β-spin MOs share common spatial one-electron functions. According to the occupation numbers, the MOs are grouped into three

sets: called core (C), open (O), and virt (V), which are doubly occupied, singly occupied, and unoccupied, respectively, where the total wavefunction is invariant with respect to the orbital rotation within each group. In this section, distinct indices are used for the core, open, and virt MOs:

- core: i, j, k, l
- open: x, y, z, w
- virt: a, b, c, d
- general MOs: p, q, r, s

The set of MOs is given as the solution of the generalized eigenvalue problem with respect to the effective Fock matrix $\mathbf{F}$, which is defined as follows in the MO-based representation.

$$\mathbf{F} = \begin{pmatrix} A_{\mathrm{CC}}\mathbf{F}^{\alpha}_{\mathrm{CC}} + B_{\mathrm{CC}}\mathbf{F}^{\beta}_{\mathrm{CC}} & \mathbf{F}^{\beta}_{\mathrm{CO}} & \left(\mathbf{F}^{\alpha}_{\mathrm{CV}} + \mathbf{F}^{\beta}_{\mathrm{CV}}\right)/2 \\ \mathbf{F}^{\beta}_{\mathrm{OC}} & A_{\mathrm{OO}}\mathbf{F}^{\alpha}_{\mathrm{OO}} + B_{\mathrm{OO}}\mathbf{F}^{\beta}_{\mathrm{OO}} & \mathbf{F}^{\alpha}_{\mathrm{OV}} \\ \left(\mathbf{F}^{\alpha}_{\mathrm{VC}} + \mathbf{F}^{\beta}_{\mathrm{VC}}\right)/2 & \mathbf{F}^{\alpha}_{\mathrm{VO}} & A_{\mathrm{VV}}\mathbf{F}^{\alpha}_{\mathrm{VV}} + B_{\mathrm{VV}}\mathbf{F}^{\beta}_{\mathrm{VV}} \end{pmatrix}. \tag{A50}$$

Here, $\mathbf{F}^{\sigma}_{\mathrm{XY}}$ is the XY (X and Y stand for C, O, or V) block of the MO-based Fock matrix for the spin σ. A_{XX} and B_{XX} are arbitrary parameters satisfying $A_{\mathrm{XX}} + B_{\mathrm{XX}} = 1$. The nondiagonal blocks of $\mathbf{F}$ vanish when the MOs satisfy the variational principle. Hence, the Lagrangian L is defined as[1]

$$L\left[\mathbf{X}, \omega, \mathbf{C}, \mathbf{Z}, \mathbf{W}\right] = G\left[\mathbf{X}, \omega\right] + \sum_{kz} Z^{\mathrm{CO}}_{kz} F_{kz} + \sum_{zc} Z^{\mathrm{OV}}_{zc} F_{zc} + \sum_{kc} Z^{\mathrm{CV}}_{kc} F_{kc} - \sum_{rs, r \leq s} W_{rs}\left(S_{rs} - \delta_{rs}\right). \tag{A51}$$

For clarity, the definitions of the energy functional G and unrelaxed difference density matrices $\mathbf{T}^{\alpha/\beta}$ are rewritten as follows in the context of restricted open-shell.

$$G = \sum_{qs}^{\mathrm{O\oplus V}} \sum_{pr}^{\mathrm{C\oplus O}} X_{pq} A_{pq,rs} X_{rs} - \omega \left(\sum_{q}^{\mathrm{O\oplus V}} \sum_{p}^{\mathrm{C\oplus O}} X_{pq} X_{pq} - 1 \right), \tag{A52}$$

$$T^{\alpha}_{pr} = \begin{cases} -\sum_{q}^{\mathrm{O\oplus V}} X_{pq} X_{rq} & (p,r) \in \mathrm{C} \oplus \mathrm{O} \\ 0 & \text{otherwise} \end{cases}, \tag{A53}$$

$$T^{\beta}_{qs} = \begin{cases} \sum_{p}^{\mathrm{C\oplus O}} X_{pq} X_{ps} & (q,s) \in \mathrm{O} \oplus \mathrm{V} \\ 0 & \text{otherwise} \end{cases}. \tag{A54}$$

In addition, as the α- and β-spin MOs are identical under the restricted open-shell formulation, the relations of Eqs. A7-A10 become

$$\sum_{\mu} \frac{\partial F^{\sigma}_{rs}}{\partial c_{\mu p}} c_{\mu q} = \delta_{pr} F^{\sigma}_{qs} + \delta_{ps} F^{\sigma}_{rq} + H^{\sigma}_{pq,rs}, \tag{A55}$$

$$H^{\sigma}_{pq,rs} = \begin{cases} 4K^{\mathrm{c}}_{iq,rs} & (p = i) \\ 2K^{\mathrm{c}}_{xq,rs} + 2K^{\mathrm{m}}_{xq,rs} & (p = x \wedge \sigma = \alpha) \\ 2K^{\mathrm{c}}_{xq,rs} - 2K^{\mathrm{m}}_{xq,rs} & (p = x \wedge \sigma = \beta) \\ 0 & (p = a) \end{cases}. \tag{A56}$$

Furthermore, the total unrelaxed difference density matrix

$$\mathbf{T} = \mathbf{T}^{\alpha} + \mathbf{T}^{\beta}, \tag{A57}$$

the total Z-vector

$$Z_{pq} = \begin{cases} Z_{ix}^{\mathrm{CO}} & (p,q) = (i,x) \\ Z_{xa}^{\mathrm{OV}} & (p,q) = (x,a) \\ Z_{ia}^{\mathrm{CV}} & (p,q) = (i,a) \\ 0 & \text{otherwise} \end{cases}, \tag{A58}$$

and the following notation

$$H_{pq}^{+}\left[\mathbf{V}\right] = H_{pq}^{+\alpha}\left[\mathbf{V}\right] + H_{pq}^{+\beta}\left[\mathbf{V}\right], \tag{A59}$$

are defined.

The explicit forms of Eqs. A5 and A6 are obtained as follows.

In the $(p,q) = (i,j)$ case,

$$W_{ij} = \frac{1}{1+\delta_{ij}}\left(Q_{ij} + H_{ij}^{+}\left[\mathbf{Z}\right]\right), \tag{A60}$$

$$Q_{ij} = H_{ij}^{+}\left[\mathbf{T}\right] - 2\sum_{qs}^{\mathrm{O}\oplus\mathrm{V}} X_{iq}F_{qs}^{\beta}X_{js} - 2\omega T_{ij}^{\alpha}. \tag{A61}$$

In the $(p,q) = (x,y)$ case,

$$W_{xy} = \frac{1}{1+\delta_{xy}}\left(Q_{xy} + H_{xy}^{+\beta}\left[\mathbf{Z}^{\mathrm{CO}}\right] + H_{xy}^{+\alpha}\left[\mathbf{Z}^{\mathrm{OV}}\right] + \frac{1}{2}H_{xy}^{+}\left[\mathbf{Z}^{\mathrm{CV}}\right]\right), \tag{A62}$$

$$Q_{xy} = H_{xy}^{+\alpha}\left[\mathbf{T}^{\alpha}\right] + H_{xy}^{+\beta}\left[\mathbf{T}^{\beta}\right] - 2\sum_{qs}^{\mathrm{O}\oplus\mathrm{V}} X_{xq}F_{qs}^{\beta}X_{ys} + 2\sum_{pr}^{\mathrm{C}\oplus\mathrm{O}} X_{rx}F_{rp}^{\alpha}X_{py} + 2\omega T_{xy}^{\beta} - 2\omega T_{xy}^{\alpha}. \tag{A63}$$

In the $(p,q) = (a,b)$ case,

$$W_{ab} = \frac{1}{1+\delta_{ab}}Q_{ab}, \tag{A64}$$

$$Q_{ab} = 2\omega T_{ab}^{\beta} + 2\sum_{pr}^{\mathrm{C}\oplus\mathrm{O}} X_{pa}F_{pr}^{\alpha}X_{rb}. \tag{A65}$$

In the $(p, q) = (i, x)$ case,

$$W_{ix} = Q_{ix} + H^{+}_{ix}[\mathbf{Z}] + \sum_{z} Z^{\mathrm{CO}}_{iz} F^{\beta}_{zx} + \frac{1}{2} \sum_{c} Z^{\mathrm{CV}}_{ic} F^{\beta}_{cx}, \tag{A66}$$

$$Q_{ix} = H^{+}_{ix}[\mathbf{T}] - 2 \sum_{qs}^{\mathrm{O}\oplus\mathrm{V}} X_{iq} F^{\beta}_{qs} X_{xs} - 2\omega T^{\alpha}_{ix}. \tag{A67}$$

In the $(p, q) = (x, i)$ case,

$$W_{ix} = Q_{xi} + H^{+\beta}_{xi}\left[\mathbf{Z}^{\mathrm{CO}}\right] + H^{+\alpha}_{xi}\left[\mathbf{Z}^{\mathrm{OV}}\right] + \frac{1}{2} H^{+}_{xi}\left[\mathbf{Z}^{\mathrm{CV}}\right] + \sum_{k} Z^{\mathrm{CO}}_{kx} F^{\beta}_{ki} + \sum_{c} Z^{\mathrm{OV}}_{xc} F^{\alpha}_{ci}, \tag{A68}$$

$$\begin{aligned} Q_{xi} =& H^{+\alpha}_{xi}[\mathbf{T}^{\alpha}] + H^{+\beta}_{xi}\left[\mathbf{T}^{\beta}\right] + 2 \sum_{p}^{\mathrm{C}\oplus\mathrm{O}} X_{px} \mathcal{K}_{pi} + 2 \sum_{q}^{\mathrm{O}\oplus\mathrm{V}} X_{xq} \mathcal{K}_{qi} \\ &+ 2 \sum_{k} T^{\alpha}_{xk} F^{\alpha}_{ki} + 2 \sum_{z} T_{xz} F^{\alpha}_{zi} + 2 \sum_{c} T^{\beta}_{xc} F^{\beta}_{ci}. \end{aligned} \tag{A69}$$

In the $(p, q) = (x, a)$ case,

$$W_{xa} = Q_{xa} + H^{+\beta}_{xa}\left[\mathbf{Z}^{\mathrm{CO}}\right] + H^{+\alpha}_{xa}\left[\mathbf{Z}^{\mathrm{OV}}\right] + \frac{1}{2} H^{+}_{xa}\left[\mathbf{Z}^{\mathrm{CV}}\right] + \sum_{k} Z^{\mathrm{CO}}_{kx} F^{\beta}_{ka} + \sum_{c} Z^{\mathrm{OV}}_{xc} F^{\alpha}_{ca}, \tag{A70}$$

$$Q_{xa} = H^{+\alpha}_{xa}[\mathbf{T}^{\alpha}] + H^{+\beta}_{xa}\left[\mathbf{T}^{\beta}\right] + 2 \sum_{q}^{\mathrm{O}\oplus\mathrm{V}} X_{xq} \mathcal{K}_{qa} + 2 \sum_{pr}^{\mathrm{C}\oplus\mathrm{O}} X_{px} F^{\alpha}_{pr} X_{ra} + 2 \sum_{k} T^{\alpha}_{xk} F^{\alpha}_{ka} + 2\omega T^{\beta}_{xa}. \tag{A71}$$

In the $(p, q) = (a, x)$ case,

$$W_{xa} = Q_{ax} + \sum_{z} Z^{\mathrm{OV}}_{za} F^{\alpha}_{zx} + \frac{1}{2} \sum_{k} Z^{\mathrm{CV}}_{ka} F^{\alpha}_{kx}, \tag{A72}$$

$$Q_{ax} = 2 \sum_{p}^{\mathrm{C}\oplus\mathrm{O}} X_{pa} \mathcal{K}_{px} + 2 \sum_{q}^{\mathrm{O}\oplus\mathrm{V}} T^{\beta}_{aq} F^{\beta}_{qx}. \tag{A73}$$

In the $(p, q) = (i, a)$ case,

$$W_{ia} = Q_{ia} + H^{+}_{ia}[\mathbf{Z}] + \sum_{z} Z^{\mathrm{CO}}_{iz} F^{\beta}_{za} + \frac{1}{2} \sum_{c} Z^{\mathrm{CV}}_{ic} \left(F^{\alpha}_{ca} + F^{\beta}_{ca} \right), \tag{A74}$$

$$Q_{ia} = H^{+}_{ia}[\mathbf{T}] + 2 \sum_{q}^{\mathrm{O} \oplus \mathrm{V}} X_{iq} \mathcal{K}_{qa} + 2 \sum_{k} T^{\alpha}_{ik} F^{\alpha}_{ka}. \tag{A75}$$

In the $(p, q) = (a, i)$ case,

$$W_{ia} = Q_{ai} + \sum_{z} Z^{\mathrm{OV}}_{za} F^{\alpha}_{zi} + \frac{1}{2} \sum_{k} Z^{\mathrm{CV}}_{ka} \left(F^{\alpha}_{ki} + F^{\beta}_{ki} \right), \tag{A76}$$

$$Q_{ai} = 2 \sum_{p}^{\mathrm{C} \oplus \mathrm{O}} X_{pa} \mathcal{K}_{pi} + 2 \sum_{c} T^{\beta}_{ac} F^{\beta}_{ci}. \tag{A77}$$

From Eqs. A66 and A68, the Z-vector equation for the (core, open) part is obtained as

$$\begin{aligned} &\sum_{z} Z^{\mathrm{CO}}_{iz} F^{\beta}_{zx} - \sum_{k} F^{\beta}_{ik} Z^{\mathrm{CO}}_{kx} + \frac{1}{2} \sum_{c} Z^{\mathrm{CV}}_{ic} F^{\beta}_{cx} - \sum_{c} Z^{\mathrm{OV}}_{xc} F^{\alpha}_{ci} \\ &+ H^{+\alpha}_{ix} \left[\mathbf{Z}^{\mathrm{CO}} \right] + H^{+\beta}_{ix} \left[\mathbf{Z}^{\mathrm{OV}} \right] + \frac{1}{2} H^{+}_{ix} \left[\mathbf{Z}^{\mathrm{CV}} \right] = -\left(Q_{ix} - Q_{xi} \right). \end{aligned} \tag{A78}$$

In a similar manner, Eqs. A70 and A72 yield the Z-vector equation for the (open, virt) part, that is,

$$\begin{aligned} &\sum_{c} Z^{\mathrm{OV}}_{xc} F^{\alpha}_{ca} - \sum_{z} F^{\alpha}_{xz} Z^{\mathrm{OV}}_{za} + \sum_{k} F^{\beta}_{ak} Z^{\mathrm{CO}}_{kx} - \frac{1}{2} \sum_{k} F^{\alpha}_{xk} Z^{\mathrm{CV}}_{ka} \\ &+ H^{+\beta}_{xa} \left[\mathbf{Z}^{\mathrm{CO}} \right] + H^{+\alpha}_{xa} \left[\mathbf{Z}^{\mathrm{OV}} \right] + \frac{1}{2} H^{+}_{xa} \left[\mathbf{Z}^{\mathrm{CV}} \right] = -\left(Q_{xa} - Q_{ax} \right). \end{aligned} \tag{A79}$$

Finally, the Z-vector equation for the (core, virt) part is obtained from Eqs. A74 and A76 as

$$\begin{aligned} &\sum_{c} \frac{1}{2} Z^{\mathrm{CV}}_{ic} \left(F^{\alpha}_{ca} + F^{\beta}_{ca} \right) - \sum_{k} \frac{1}{2} \left(F^{\alpha}_{ik} + F^{\beta}_{ik} \right) Z^{\mathrm{CV}}_{ka} + \sum_{z} Z^{\mathrm{CO}}_{iz} F^{\beta}_{za} - \sum_{z} F^{\alpha}_{iz} Z^{\mathrm{OV}}_{za} \\ &+ H^{+}_{ia}[\mathbf{Z}] = -\left(Q_{ia} - Q_{ai} \right). \end{aligned} \tag{A80}$$

Eqs. A78-A80 can be rewritten as

$$\begin{pmatrix} \mathbf{J}^{\mathrm{CO,CO}} & \mathbf{J}^{\mathrm{CO,OV}} & \mathbf{J}^{\mathrm{CO,CV}} \\ \mathbf{J}^{\mathrm{OV,CO}} & \mathbf{J}^{\mathrm{OV,OV}} & \mathbf{J}^{\mathrm{OV,CV}} \\ \mathbf{J}^{\mathrm{CV,CO}} & \mathbf{J}^{\mathrm{CV,OV}} & \mathbf{J}^{\mathrm{CV,CV}} \end{pmatrix} \begin{pmatrix} \mathbf{Z}^{\mathrm{CO}} \\ \mathbf{Z}^{\mathrm{OV}} \\ \mathbf{Z}^{\mathrm{CV}} \end{pmatrix} = - \begin{pmatrix} \mathbf{U}^{\mathrm{CO}} \\ \mathbf{U}^{\mathrm{OV}} \\ \mathbf{U}^{\mathrm{CV}} \end{pmatrix}, \tag{A81}$$

where the orbital Hessian matrix is defined as

$$J^{\mathrm{CO,CO}}_{ix,kz} = F^{\beta}_{xz}\delta_{ik} - F^{\beta}_{ik}\delta_{xz} + 2K^{\mathrm{c}}_{ix,kz} + 2K^{\mathrm{m}}_{ix,kz}, \tag{A82}$$

$$J^{\mathrm{CO,OV}}_{ix,zc} = -F^{\alpha}_{ic}\delta_{xz} + 2K^{\mathrm{c}}_{ix,zc} - 2K^{\mathrm{m}}_{ix,zc}, \tag{A83}$$

$$J^{\mathrm{CO,CV}}_{ix,kc} = \frac{1}{2}F^{\beta}_{xc}\delta_{ik} + 2K^{\mathrm{c}}_{ix,kc}, \tag{A84}$$

$$J^{\mathrm{OV,CO}}_{xa,kz} = F^{\beta}_{ak}\delta_{xz} + 2K^{\mathrm{c}}_{xa,kz} - 2K^{\mathrm{m}}_{xa,kz}, \tag{A85}$$

$$J^{\mathrm{OV,OV}}_{xa,zc} = F^{\alpha}_{ac}\delta_{xz} - F^{\alpha}_{xz}\delta_{ac} + 2K^{\mathrm{c}}_{xa,zc} + 2K^{\mathrm{m}}_{xa,zc}, \tag{A86}$$

$$J^{\mathrm{OV,CV}}_{xa,kc} = -\frac{1}{2}F^{\alpha}_{xk}\delta_{ac} + 2K^{\mathrm{c}}_{xa,kc}, \tag{A87}$$

$$J^{\mathrm{CV,CO}}_{ia,kz} = \frac{1}{2}F^{\beta}_{az}\delta_{ik} + 2K^{\mathrm{c}}_{ia,kz}, \tag{A88}$$

$$J^{\mathrm{CV,OV}}_{ia,zc} = -\frac{1}{2}F^{\alpha}_{iz}\delta_{ac} + 2K^{\mathrm{c}}_{ia,zc}, \tag{A89}$$

$$J^{\mathrm{CV,CV}}_{ia,kc} = \frac{1}{4}\left(F^{\alpha}_{ac} + F^{\beta}_{ac}\right)\delta_{ik} - \frac{1}{4}\left(F^{\alpha}_{ik} + F^{\beta}_{ik}\right)\delta_{ac} + 2K^{\mathrm{c}}_{ia,kc}. \tag{A90}$$

The orbital Hessian matrix is found to be symmetric under the condition that the nondiagonal

blocks of the effective Fock matrix (Eq. A50) vanish. The RHS of Eq. A81 is described as

$$U_{ix}^{\mathrm{CO}} = H_{ix}^{+\beta}\left[\mathbf{T}^{\alpha}\right] + H_{ix}^{+\alpha}\left[\mathbf{T}^{\beta}\right] - 2\sum_{p}^{\mathrm{C}\oplus\mathrm{O}} X_{px}\mathcal{K}_{pi} - 2\sum_{q}^{\mathrm{O}\oplus\mathrm{V}} X_{xq}\mathcal{K}_{qi}$$
$$- 2\sum_{qs}^{\mathrm{O}\oplus\mathrm{V}} X_{iq}F_{qs}^{\beta}X_{xs} - 2\sum_{x} T_{xz}F_{zi}^{\alpha} - 2\sum_{c} T_{xc}^{\beta}F_{ci}^{\beta} - 2\sum_{k} T_{xk}^{\alpha}F_{ki}^{\alpha} - 2\omega T_{ix}^{\alpha}, \tag{A91}$$

$$U_{xa}^{\mathrm{OV}} = H_{xa}^{+\alpha}\left[\mathbf{T}^{\alpha}\right] + H_{xa}^{+\beta}\left[\mathbf{T}^{\beta}\right] + 2\sum_{q}^{\mathrm{O}\oplus\mathrm{V}} X_{xq}\mathcal{K}_{qa} - 2\sum_{q}^{\mathrm{C}\oplus\mathrm{O}} X_{pa}\mathcal{K}_{pa}$$
$$+ 2\sum_{pr}^{\mathrm{C}\oplus\mathrm{O}} X_{px}F_{pr}^{\alpha}X_{ra} + 2\sum_{k} T_{xk}^{\alpha}F_{ka}^{\alpha} - 2\sum_{q}^{\mathrm{O}\oplus\mathrm{V}} T_{aq}^{\beta}F_{qx}^{\beta} + 2\omega T_{xa}^{\beta}, \tag{A92}$$

$$U_{ia}^{\mathrm{CV}} = \frac{1}{2}H_{ia}^{+}\left[\mathbf{T}\right] + \sum_{q}^{\mathrm{O}\oplus\mathrm{V}} X_{iq}\mathcal{K}_{qa} - \sum_{p}^{\mathrm{C}\oplus\mathrm{O}} X_{pa}\mathcal{K}_{pi} + \sum_{k} T_{ik}^{\alpha}F_{ka}^{\alpha} - \sum_{c} T_{ac}^{\beta}F_{ci}^{\beta}. \tag{A93}$$

By differentiating the Lagrangian (Eq. A51) with the nuclear coordinates, one can obtain the same expression for the excitation energy gradient as in the spin-unrestricted case (Eq. A42), whereas the definitions of relaxed difference density matrices $\mathbf{P}^{\alpha/\beta}$, which are described as follows, are different from those in the spin-unrestricted case.

$$\mathbf{P}^{\alpha} = \mathbf{T}^{\alpha} + \mathbf{Z}^{\mathrm{OV}} + \frac{1}{2}\mathbf{Z}^{\mathrm{CV}}, \tag{A94}$$

$$\mathbf{P}^{\beta} = \mathbf{T}^{\beta} + \mathbf{Z}^{\mathrm{CO}} + \frac{1}{2}\mathbf{Z}^{\mathrm{CV}}. \tag{A95}$$

B Details of DFTB Parametrization in Chapter 6

B.1 Overview

In DFTB, the ground-state total energy E_0 is expressed as

$$E_0 = E_{\mathrm{el}} + V_{\mathrm{rep}}. \tag{B1}$$

Here, E_{el} is the energy component depending on the electronic structure, and V_{rep} is a repulsive potential, which is a function of interatomic distance. The DFTB parameter set consists of the electronic part and the repulsive part, which are regarding E_{el} and V_{rep}, respectively. The electronic and repulsive parts are defined for each element and each element pair, respectively. As summarized in Tables B1 and B2, new parameters were constructed for Pb, I, and Cs and the related element pairs. For other elements or element pairs, the 3OB parameter set[2,3] was employed. Table B1 also describes the included basis set shells for each element. Note that the repulsive part is essential only when the interatomic distance is within the bonding region. Hence, the repulsive potential were omitted for element pairs whose interatomic distance does not fall within the bonding region. For parameter construction, the ADPT program was used.[4] The reference DFT calculations including DFT-MD were performed using the PBE exchange–correlation functional[5] and projector augmented-wave method[6] as implemented in VASP program package.[7–10]

Table B1: Electronic part for each element. *new* and *3OB* indicate that the electronic parameter was newly constructed and that the 3OB parameter[2] was adopted, respectively.

element	parameter	shells
Pb	*new*	s,p
I	*new*	s,p
Cs	*new*	s
H	*3OB*	s
N	*3OB*	s,p
C	*3OB*	s,p

Table B2: Repulsive part for each element pair. The labels *new* and *3OB* indicate that the repulsive potential parameter was newly constructed and that the 3OB parameter[2,3] was adopted, respectively. ∅ indicates element pairs where the repulsive potential was not imposed.

	Pb	I	Cs	H	N	C
Pb	∅	*new*	∅	∅	∅	∅
I	-	*3OB*	*new*	*3OB*	*3OB*	*3OB*
Cs	-	-	*new*	∅	∅	∅
H	-	-	-	*3OB*	*3OB*	*3OB*
N	-	-	-	-	*3OB*	*3OB*
C	-	-	-	-	-	*3OB*

B.2 Construction of the Electronic Part

The closed-shell DFTB2 Hamiltonian is described as

$$H_{\mu\nu} = H^0_{\mu\nu} + \frac{1}{2} S_{\mu\nu} \sum_{\xi}^{N_{\text{shell}}} \left(\gamma_{\alpha\xi} + \gamma_{\beta\xi}\right) \Delta q_{\xi}, \tag{B2}$$

where

$$S_{\mu\nu} = \left\langle \phi_\mu \middle| \phi_\nu \right\rangle, \tag{B3}$$

$$H^0_{\mu\nu} = \begin{cases} \epsilon^0_\mu & \mu = \nu \\ \left\langle \phi_\mu \middle| \hat{T} + V_{\text{eff}}\left[\rho_A + \rho_B\right] \middle| \phi_\nu \right\rangle & A \neq B \wedge \mu \neq \nu \cdot \\ 0 & \text{otherwise} \end{cases} \tag{B4}$$

ϕ_μ denotes μ-th AO basis function that expands the MOs. $\gamma_{\alpha\beta}$ depends on the interatomic distance and the Hubbard parameter (chemical hardness, U) of the atoms to which shells α and β belong. U is calculated as a derivative of the energy level of highest occupied AO in the isolated atom with respect to its occupation number. ϵ^0_μ is the orbital energy of the μ-th AO calculated in the isolated single atom. The calculated values of ϵ^0_μ and U for the atoms whose electronic part was newly constructed, i.e., Pb, I, and Cs, are listed in Table C1. For other elements, these values were taken from ref. S8. $\hat{T}$ is the kinetic energy operator with respect to electrons. $V_{\text{eff}}\left[\rho_A + \rho_B\right]$ is the Kohn–Sham potential according to the superposition of atomic electron den-

sities, $\rho_A + \rho_B$. In this work, V_{eff} was calculated using the PBE exchange–correlation potential. The AO wavefunction, ϕ_μ, is obtained by solving the following Kohn–Sham-like equation for an isolated atom:

$$\left[\hat{T} + V_{\text{eff}}\left[\rho_A\right] + V_{\text{conf}}\right]\phi_\mu = \epsilon_\mu \phi_\mu, \tag{B5}$$

where the confining potential V_{conf} is imposed to mimic the environment of the atoms in compounds. V_{conf} is optimized in an empirical manner for each element and shell. For Pb, I, and Cs, the modified Woods–Saxon type confining potential[4,11] was employed:

$$V_{\text{conf}}(R) = \frac{W}{1 + \exp\left[-a\left(R - r\right)\right]}, \tag{B6}$$

where W, a, and r are the parameters to be optimized, and R is the distance from the nucleus. The parameters for Pb and Cs were optimized to reproduce the band structures of pure metals calculated with PBE. Regarding I, the parameters were fitted to the set of PBE-calculated band gaps of $CsPbI_3$ with various cell parameters. The optimized parameters are listed in Table C2. The parameters for the s and p shells are specified by the subscripts s and p, respectively. The parameters for the calculation of the atomic electron density (ρ_A) is indicated by the subscript "den." Regarding other elements, namely, H, N, and C, the settings of 3OB parameter set[2] was employed, where the confining potential is expressed as a quadratic form:

$$V_{\text{conf}}(R) = \left(\frac{R}{r}\right)^2. \tag{B7}$$

The optimized values of the parameter r are listed in ref. S8. The band gaps of cubic $CsPbI_3$ calculated using DFTB with the optimized parameter are compared in Fig. B1 with the reference PBE results. The horizontal axis indicates the cell parameter referenced to that relaxed with PBE. In the PBE-optimized structure, which is indicated by "100" at the horizontal axis, the DFTB band gap is in excellent agreement with the PBE result. Fig. B1 also shows that the discrepancy between the DFTB and PBE results are within an acceptable level when the cell

parameters are expanded or shrunk by 5%, suggesting that the constructed parameter set can cover the deformed structures in the dynamics simulations.

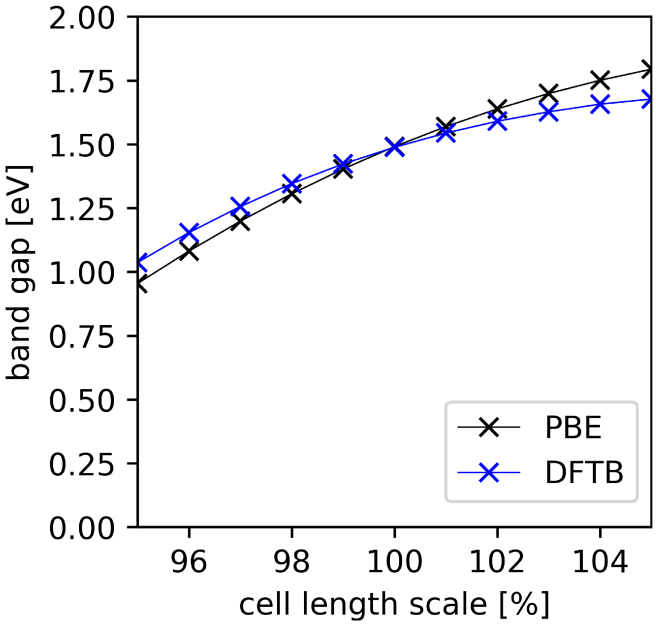

Fig. B1: Calculated band gaps of cubic $CsPbI_3$ with DFTB (blue) and PBE (black) on varying the cell length. The cell length (horizontal axis) is indicated as ratio to the optimized value with PBE.

B.3 Construction of the Repulsive Part

The combined exponential and spline forms of the repulsive potentials, which is a piecewise-defined function, were employed:

$$V_{\mathrm{rep}}^{AB}(d) = \begin{cases} \exp\left[-a_1 d + a_2\right] + a_3 & d < d_0 \\ \sum_{i=0}^{Z} c_i^n (d - d_n)^i & d_n \leq d < d_{n+1} \wedge n < N \cdot \\ 0 & d_N \leq d \end{cases} \tag{B8}$$

Here, the spline order Z is 4 or 3, and d is the distance between the atom A and atom B. d_0, d_1,..., d_N are the positions of spline knots, where $d_0 < d_1 < ... < d_N$. The parameters a_k ($k = 1, 2, 3$), c_l (l = 1,...,Z), and d_m (m = 1,...,N) are determined in such a way that the function $V_{\mathrm{rep}}^{AB}(d)$ becomes continuous and smooth at arbitrary d. For the newly constructed repulsive potentials (Table B2), $Z = 4$ is used. The constructed I–Pb (Pb–I), I–Cs (Cs–I), and Cs–Cs

repulsive potential parameters are listed in the Tables C3, C4, and C5, respectively. For the element pairs where the 3OB parameters were adopted (Table B2), the spline order was set to 3 ($Z = 3$) following the original literature.[2,3] The optimized cell parameters of cubic $CsPbI_3$, where the cell parameter is α, and tetragonal $MAPbI_3$, where the cell is an $\alpha \times \alpha \times \beta$ cuboid, are listed in Table B3. Table B3 compares the DFTB and PBE results, revealing that the deviation is around 1%, which suggests satisfactory agreement. In addition, Fig. B2 shows the VDOS via Fourier transformation of velocity autocorrelation functions obtained from DFTB-MD runs (blue), with comparison to the corresponding DFT-MD results (black). The MD simulations were conducted under the *NVE* ensemble with a time step of 0.25 fs after thermalization runs at 298.15 K with velocity rescaling. Fig. B2(a) indicates that the DFTB result was consistent with the DFT result in the case of $CsPbI_3$. For $MAPbI_3$ (Fig. B2(b)), while the intensity of the DFTB result is somewhat deviated from that of the DFT result, the positions and shape of the peaks are consistent. Hence, it can be concluded that the constructed parameter set reproduces the structural dynamics with reasonable quality.

Table B3: Optimized cell parameters with DFTB and PBE.

compound	crystal system	α / Å (DFTB)	α / Å (PBE)	dev. (%)	β / Å (DFTB)	β / Å (PBE)	dev. (%)
$CsPbI_3$	cubic	6.4743	6.3977	1.2	-	-	-
$MAPbI_3$	tetragonal	9.0073	8.9326	0.8	13.1117	13.1103	0.01

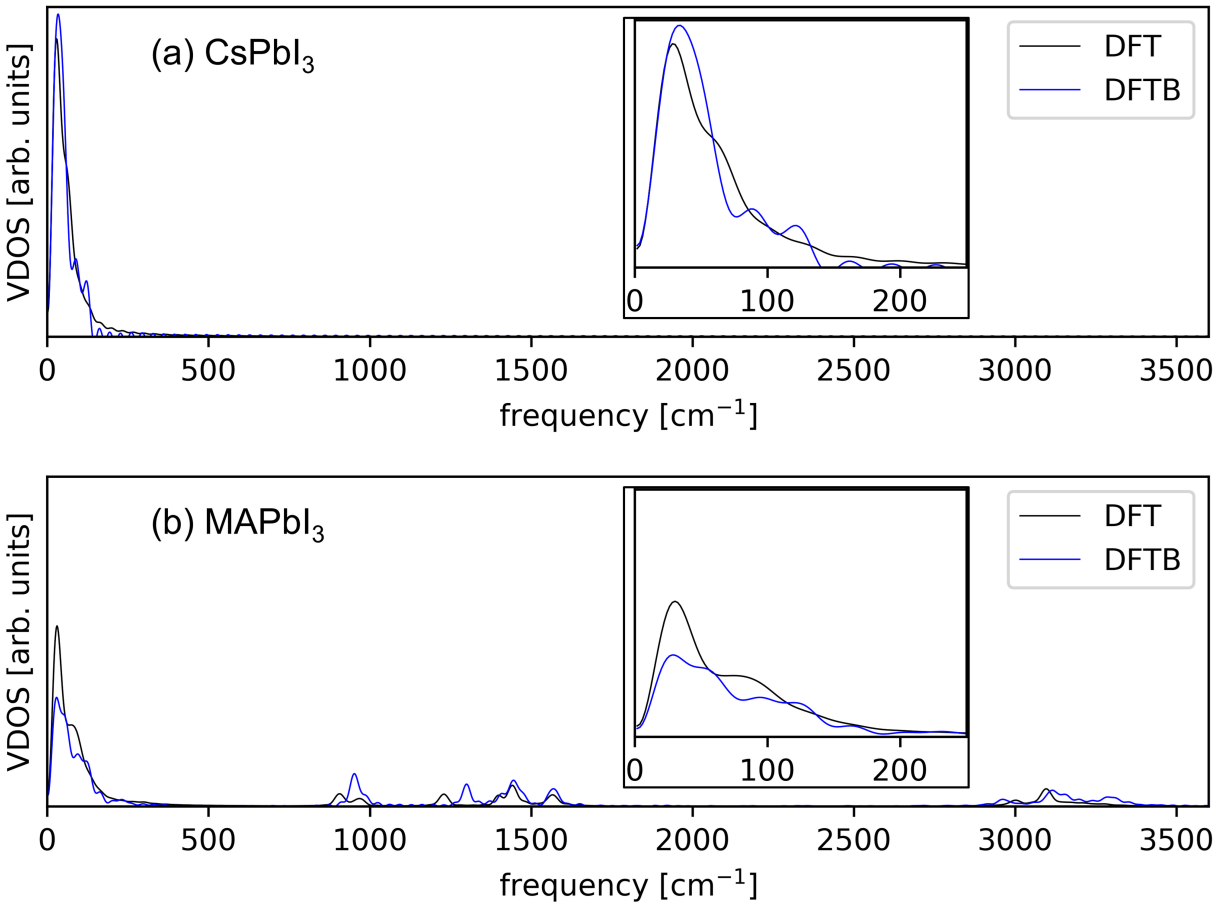

Fig. B2: VDOS of (a) $CsPbI_3$ and (b) $MAPbI_3$ obtained from DFTB-MD (blue) and DFT-MD (black). Enlarged views of the low-frequency range are shown in the insets.

C Tables of DFTB Parameters

C.1 For Chapter 6

Table C1: Calculated AO energy values, ϵ_s^0 and ϵ_p^0, for s and p shells, respectively, and Hubbard parameters (U, in Hartree atomic units). The subscripts s and p indicate that the value is regarding s-shell and p-shell, respectively.

	Pb	I	Cs
ϵ_s^0	-0.44019521	-0.63889433	-0.07666100
ϵ_p^0	-0.13254749	-0.26128390	-
U	0.210323662338	0.284106077922	0.120564649351

Table C2: Optimized electronic parameters (in Hartree atomic units except dimensionless quantities).

parameter	Pb	I	Cs
r_s	4.5159813652382921	4.7328576867979359	7.0652390787826107
a_s	10.479037924020117	16.226632944172614	6.1164101159663158
w_s	14.578966029615868	19.924746482182726	5.1165651133884182
r_p	4.7393160961205529	5.3930212738958705	-
a_p	14.200977710672456	4.7313131571249842	-
w_p	12.804412006327981	7.5979906375433588	-
r_{den}	5.6718184437141685	5.7860785683446556	8.9467680558691178
a_{den}	5.0127951382518257	9.1806798848075744	6.8343175057981425
w_{den}	9.3173909273039293	5.4381510083721301	0.45554964026034445

Table C3: Optimized I–Pb (Pb–I) repulsive parameters (in Hartree atomic units except dimensionless quantities).

a_1	a_2	a_3
1.895029E+00	5.867450E+00	-2.454019E-02

n	d_n	c_0^n	c_1^n	c_2^n	c_3^n	c_4^n
0	4.400000	5.998730428165E-02	-1.601820622742E-01	1.517748332588E-01	-6.080821796801E-02	8.932801133142E-03
1	6.100000	2.163940000845E-03	4.192528891709E-03	-3.452306729325E-03	-6.517026263925E-05	-2.491790159566E-03
2	6.300000	2.859845283657E-03	2.724048483356E-03	-4.089438525205E-03	-2.058602390292E-03	4.090061099110E-03
3	6.500000	3.231152717956E-03	9.721227416100E-04	-4.342985295594E-03	1.213446488996E-03	-8.859608245139E-04
4	6.700000	3.260147889048E-03	-6.478085443323E-04	-3.827548000079E-03	5.046778293849E-04	-4.810481214887E-03
5	7.000000	2.695987409293E-03	-3.327606301654E-03	-5.970997809672E-03	-5.267899628479E-03	2.424077824916E-02
6	7.300000	1.214432729776E-03	-5.714533836237E-03	2.377912779242E-03	2.382103427051E-02	-3.197806393003E-02
7	7.600000	9.823033650729E-05	-1.309737820097E-03	6.548689100486E-03	-1.455264244552E-02	1.212720203794E-02
8	7.900000	-	-	-	-	-

Table C4: Optimized I–Cs (Cs–I) repulsive parameters (in Hartree atomic units except dimensionless quantities).

a_1	a_2	a_3
5.904081E-01	1.136443E+00	-9.435844E-02

n	d_n	c_0^n	c_1^n	c_2^n	c_3^n	c_4^n
0	4.000000	1.993436555017E-01	-1.734041003186E-01	5.118959450787E-02	-5.117972788196E-03	-9.272613132359E-07
1	4.500000	1.247991994171E-01	-1.260534490325E-01	4.351124443361E-02	-5.119827310823E-03	5.211672798013E-08
2	5.000000	7.201031085266E-02	-8.638204902363E-02	3.583158164247E-02	-5.119723077367E-03	-1.401179155146E-08
3	5.500000	3.713721549105E-02	-5.439026669509E-02	2.815197600873E-02	-5.119751100950E-03	-9.584208282441E-06
4	6.000000	1.633950824505E-02	-3.008289611621E-02	2.045797304488E-02	-5.138919517515E-03	8.529568485306E-05
5	6.500000	5.775519488781E-03	-1.343646486705E-02	1.287753729589E-02	-4.968328147809E-03	2.221624094918E-06
6	7.000000	1.655769212260E-03	-4.284062869968E-03	5.428377510316E-03	-4.963884899619E-03	2.359330441096E-03
7	7.500000	3.978046949709E-04	-1.398933813818E-03	1.521545822532E-03	-2.452240174265E-04	-3.232639277740E-04
8	8.000000	2.786724603045E-05	-2.229379682436E-04	6.688139047309E-04	-8.917518729745E-04	4.458759364873E-04
9	8.500000	-	-	-	-	-

Table C5: Optimized Cs–Cs repulsive parameters (in Hartree atomic units except dimensionless quantities).

a_1	a_2	a_3
9.23887	74.9819	-0.00107706

n	d_n	c_0^n	c_1^n	c_2^n	c_3^n	c_4^n
0	8.70000	3.456565616244E-03	-4.188560129835E-02	1.934877639489E-01	-2.899459963340E-01	0.000000000000E+00
1	8.80000	9.129371295643E-04	-1.188642839859E-02	1.065039650487E-01	-2.899459963340E-01	1.707058984628E-02
2	8.90000	5.010950028433E-04	7.842670805199E-04	2.054440153929E-02	-2.831177603955E-01	7.367734570233E-01
3	9.05000	4.984532208385E-04	-2.216419614575E-03	-7.394173940541E-03	1.589463138185E-01	-3.611019698167E-01
4	9.25000	4.532096991429E-04	2.344205433290E-03	1.309141594528E-03	-1.299352620349E-01	3.308709063991E-01
5	9.40000	5.632680870100E-04	-1.566925039320E-03	-1.249415395730E-02	6.858728180456E-02	-9.695914473357E-02
6	9.60000	1.436805437167E-04	-1.436805437167E-03	5.388020389378E-03	-8.980033982296E-03	5.612521238935E-03
7	10.00000	-	-	-	-	-

C.2 For Chapter 7

Table C6: Electronic parameters for Pb (in atomic units).

orbital type	W	a	r_0
s	6.76254	5.60847	4.54346
p	5.33981	9.14422	4.42425
d	4.58160	5.96026	4.80418
f	2.40562	2.83573	5.82248
density	7.01658	5.55764	4.23132

Table C7: Pb–I repulsive potential parameters (in atomic units).

a_1	a_2	a_3
2.067509E+00	5.616456E+00	-7.032404E-03

R_0	c_0	c_1	c_2	c_3	c_4
4.300000	3.082860992619E-02	-7.827799356081E-02	8.092023408549E-02	-3.003160069907E-02	5.128927793232E-05
4.609800	1.345202267925E-02	-3.678065883753E-02	5.303839964651E-02	-2.996804302586E-02	2.414304304420E-03
4.826300	7.676232444769E-03	-1.793104068906E-02	3.425313895081E-02	-2.787725549823E-02	1.727706606781E-04
4.831400	7.585671363570E-03	-1.758383384233E-02	3.382664390428E-02	-2.787373097675E-02	7.729573645229E-03
5.622500	4.072295874378E-03	-1.089048277048E-03	-3.301260240250E-03	-3.414268133792E-03	7.967429589431E-03
5.898700	3.494087064850E-03	-3.022546521069E-03	-2.483481779939E-03	5.388148076612E-03	-4.197780308028E-03
6.171900	2.569449999077E-03	-3.515425857717E-03	5.275477906474E-05	8.008137559991E-04	7.202015661719E-04
6.572200	1.240538476683E-03	-2.903436228347E-03	1.706883001333E-03	1.954000503753E-03	-3.804023645709E-03
6.778900	7.236369074490E-04	-2.081734329285E-03	1.943399762789E-03	-1.191166246519E-03	9.471375980340E-04
7.166000	1.611817555858E-04	-8.928732587616E-04	1.411649413755E-03	2.753816102771E-04	-1.765618955388E-03
*7.431500	2.001209625241E-05	-2.172276391035E-04	8.842373369206E-04	-1.599705720345E-03	1.085282035512E-03

*The last distance range ends at 7.800000 a.u..

References

[1]N. Minezawa and M. S. Gordon, *J. Chem. Phys.* **137**, 034116 (2012).

[2]M. Gaus, A. Goez, and M. Elstner, *J. Chem. Theory Comput.* **9**, 338 (2013).

[3]M. Kubillus, T. Kubař, M. Gaus, J. Řezáč, and M. Elstner, *J. Chem. Theory Comput.* **11**, 332 (2015).

[4]C.-P. Chou, Y. Nishimura, C.-C. Fan, G. Mazur, S. Irle, and H. A. Witek, *J. Chem. Theory Comput.* **12**, 53 (2016).

[5]J. P. Perdew, K. Burke, and M. Ernzerhof, *Phys. Rev. Lett.* **77**, 3865 (1996).

[6]P. E. Blöchl, *Phys. Rev. B* **50**, 17953 (1994).

[7]G. Kresse and J. Hafner, *Phys. Rev. B* **47**, 558 (1993).

[8]G. Kresse and J. Hafner, *Phys. Rev. B* **49**, 14251 (1994).

[9]G. Kresse and J. Furthmüller, *Comp. Mater. Sci.* **6**, 15 (1996).

[10]G. Kresse and J. Furthmüller, *Phys. Rev. B* **54**, 11169 (1996).

[11]H. A. Witek, C. Köhler, T. Frauenheim, K. Morokuma, and M. Elstner, *J. Phys. Chem. A* **111**, 5712 (2007).

Acknowledgements

This research project has been conducted under the supervision of Professor Hiromi Nakai, Waseda University. The author acknowledges his valuable advice and gracious support in all aspects of being a scientist.

The author also thanks Professor Kohei Imura and Professor Yukio Furukawa for their thorough reading and careful evaluation of the thesis.

This work would not have been realized without the professional cooperation of Dr. Chien-Pin Chou and Professor Takeshi Yoshikawa. In addition, this study stems from the author's master's and undergraduate course projects under the supervision of Professor Koichi Yamashita of the University of Tokyo, and Professor Hironori Kaji of Kyoto University, respectively. The author would sincerely like to thank these researchers.

Further, the author acknowledges that he has been able to smoothly conduct the research project owing to much assistance from all the current and former members of the laboratory. In particular, the author appreciates the kind support of Dr. Masaki Okoshi and Dr. Mikito Fujinami throughout the doctoral course.

For financial support, the author is grateful for having received the Japan Society for the Promotion of Science Research Fellowship for Young Scientists.

The author owes his parents and grandparents for giving him the opportunity for academic education. Finally, the author would like to conclude the thesis by expressing gratitude to his wife, Mika Yoshimoto, for her generous cooperation.

List of Achievements

Original Articles

1. ○"Trajectory Surface Hopping Approach to Condensed-Phase Nonradiative Relaxation Dynamics Using Divide-and-Conquer Spin-Flip Time-Dependent Density-Functional Tight Binding"
   Hiroki Uratani, Takeshi Yoshikawa, and Hiromi Nakai
   J. Chem. Theory Comput. in press.

2. ○"Fast Nonadiabatic Molecular Dynamics via Spin-Flip Time-Dependent Density-Functional Tight-Binding Approach: Application to Nonradiative Relaxation of Tetraphenylethylene with Locked Aromatic Rings"
   Hiroki Uratani, Toshiki Morioka, Takeshi Yoshikawa, and Hiromi Nakai
   J. Chem. Theory Comput. **16**, 7299 (2020).

3. ○"Non-adiabatic molecular dynamics with divide-and-conquer type large-scale excited-state calculations"
   Hiroki Uratani and Hiromi Nakai
   J. Chem. Phys. **152**, 224109 (2020).

4. ○"Simulating the Coupled Structural–Electronic Dynamics of Photoexcited Lead Iodide Perovskites"
   Hiroki Uratani and Hiromi Nakai
   J. Phys. Chem. Lett. **11**, 4448 (2020).

5. ○“Quantum mechanical molecular dynamics simulations of polaron formation in methylammonium lead iodide perovskite”
   Hiroki Uratani, Chien-Pin Chou, and Hiromi Nakai
   Phys. Chem. Chem. Phys. **22**, 97 (2020).

6. “Inorganic Lattice Fluctuation Induces Charge Separation in Lead Iodide Perovskites: Theoretical Insights”
   Hiroki Uratani and Koichi Yamashita
   J. Phys. Chem. C **121**, 26648 (2017).

7. “Charge Carrier Trapping at Surface Defects of Perovskite Solar Cell Absorbers: A First-Principles Study”
   Hiroki Uratani and Koichi Yamashita
   J. Phys. Chem. Lett. **8**, 742 (2017).

8. “Detailed analysis of charge transport in amorphous organic thin layer by multiscale simulation without any adjustable parameters”
   Hiroki Uratani, Shosei Kubo, Katsuyuki Shizu, Furitsu Suzuki, Tatsuya Fukushima, and Hironori Kaji
   Sci. Rep. **6**, 39128 (2016).

Review

1. “ペロブスカイト太陽電池材料におけるポーラロン形成の量子力学的分子動力学シミュレーション”
   浦谷 浩輝, 周 建斌, 中井 浩巳
   J. Comput. Chem. Jpn. **18**, 142 (2019).

Conference Presentations

International Conferences

1. “Large-Scale Quantum Mechanical Molecular Dynamics Simulations of Polaron Formation Process in a Lead Halide Perovskite Material Using Divide-and-Conquer Type Density-Functional Tight-Binding Method”
   Hiroki Uratani, Chien-Pin Chou, and Hiromi Nakai
   The Ninth Conference of the Asia-Pacific Association of Theoretical and Computational Chemists (APCTCC-9), Sydney, Australia (Oct 2019).

2. “Divide-and-conquer DFTB-MD simulations of polaron formation process in a lead halide perovskite material”
   Hiroki Uratani, Chien-Pin Chou, and Hiromi Nakai
   10th Triennal Congress of the International Society for Theoretical Chemical Physics (ISTCP-X), Tromsø, Norway (Jul 2019).

3. “Inorganic Lattice Fluctuation Induces Charge Separation in Lead Iodide Perovskites: Theoretical Insights”
   Hiroki Uratani and Koichi Yamashita
   APS March Meeting 2018, Los Angeles, USA (Mar 2018).

4. “Inorganic Lattice Fluctuation Induces Charge Separation in Lead Iodide Perovskites: Theoretical Insights”
   Hiroki Uratani and Koichi Yamashita
   International Conference Asia-Pacific Hybrid and Organic Photovoltaics Conference (AP-HOPV18), Yokohama, Japan (Jan 2018).

5. “Inorganic Lattice Fluctuation Induces Charge Separation in Lead Iodide Perovskites: Theoretical Insights”

Hiroki Uratani and Koichi Yamashita

CPMD2017 Workshop, Tsukuba, Japan (Oct 2017).

6. “Design Principles for Perovskite Solar Cells: Insights from Density Functional Theory Calculations”

   Hiroki Uratani and Koichi Yamashita

   Interdisciplinary Symposium for Up-and-coming Materials Scientists 2017 (ISUMS 2017), Osaka, Japan (Jun 2017).

7. “First-principles investigation of charge carrier trapping at surface defects of organic-inorganic hybrid perovskites as photovoltaic materials”

   Hiroki Uratani and Koichi Yamashita

   APS March Meeting 2017, New Orleans, USA (Mar 2017).

8. “Charge Carrier Trapping at Surface Defects of Perovskite Solar Cell Absorbers: A First-Principles Study”

   Hiroki Uratani and Koichi Yamashita

   International Conference Asia-Pacific Hybrid and Organic Photovoltaics Conference (AP-HOPV17), Yokohama, Japan (Feb 2017).

Domestic Conferences

1. “分割統治型励起状態計算に基づく大規模非断熱分子動力学手法の開発”

   浦谷 浩輝, 中井 浩巳

   分子科学会オンライン討論会, オンライン開催（2020年9月）.

2. “鉛ハライドペロブスカイト材料におけるポーラロン形成過程の量子分子動力学シミュレーション”

   浦谷 浩輝, 周 建斌, 中井 浩巳

   第13回分子科学討論会, 名古屋（2019年9月）.

3. “ペロブスカイト太陽電池材料におけるポーラロン形成の量子的分子動力学シミュレーション”

   浦谷 浩輝, 周 建斌, 中井 浩巳

   日本コンピュータ化学会春季年会2019, 東京（2019年6月）.

4. “分割統治型密度汎関数強束縛法によるペロブスカイト太陽電池材料におけるポーラロン形成動力学シミュレーション”

   浦谷 浩輝, 周 建斌, 中井 浩巳

   第22回理論化学討論会, 北海道（2019年5月）.

5. “密度汎関数強束縛法に基づくペロブスカイト太陽電池におけるキャリア特性の研究”

   浦谷 浩輝, 周 建斌, 中井 浩巳

   第12回分子科学討論会, 福岡（2018年9月）.

6. “ペロブスカイト太陽電池における構造揺らぎと電荷分離の関係：第一原理シミュレーションと理論解析”

   浦谷 浩輝, 山下 晃一

   第11回分子科学討論会, 仙台（2017年9月）.

7. “第一原理計算に基づくペロブスカイト型太陽電池の動作機構および性能向上指針に関する研究”

   浦谷 浩輝, 山下 晃一

   第20回理論化学討論会, 京都（2017年5月）.

8. “Monte Carlo シミュレーションによる非晶質有機膜内の電荷輸送解析”

   浦谷 浩輝, 志津 功將, 鈴木 不律, 福島 達也, 梶 弘典

   第63回応用物理学会春季学術講演会, 東京（2016年3月）.

Awards

1. 分子科学会オンライン討論会 学生優秀講演賞 (Sep 2020).

2. Poster Award, 10th Triennal Congress of the International Society for Theoretical Chemical Physics (ISTCP-X) (Jul 2019).

3. 日本コンピュータ化学会 奨学賞（Jun 2019）.